Analysis and Interpretation of Transverse Spin Dependent Azimuthal Asymmetries in SIDIS at the COMPASS Experiment

Bakur Parsamyan

Università degli Studi di Torino,
Dipartimento di Fisica Generale "A. Avogadro"

CERN-THESIS-2009-105
27/11/2007

Turin, 28 November 2007

Analysis and Interpretation of Transverse Spin Dependent Azimuthal Asymmetries in SIDIS at the COMPASS Experiment

Dissertation

University of Turin
General Physics Department *"A.Avogadro"*
XX-th cycle, 2004-2007

Candidate: Bakur Parsamyan

Scientific Supervisor: Prof. Aram Kotzinian
Tutor: Prof. Ferruccio Balestra

Opponent: Prof. Enzo De Sanctis

Date of oral examination:	28-th November 2007
Examining Board:	Prof. M. Anselmino (chairman)
	Prof. T. Suomijarvi
	Prof. H. Borel

Abstract

In general, eight target transverse spin-dependent azimuthal modulations are allowed in semi-inclusive deep inelastic scattering (SIDIS) of polarized leptons on a transversely polarized target. In the QCD parton model four of these asymmetries can be interpreted within the leading order approach and other four are twist-three level contributions. Two leading twist transverse spin asymmetries, namely Collins and Sivers effects were already published by HERMES and COMPASS collaborations. While the remaining six *new* asymmetries have been measured for the first time in COMPASS using a high energy longitudinally polarized muon beam and a transversely polarized deuterium target.

In the introductory chapter of this thesis we describe the general expression of the cross-section of polarized SIDIS and review the aspects of the QCD parton model with transverse momentum dependent distribution and fragmentation functions. Then we define the target transverse spin asymmetries arising in SIDIS and motivate the importance of their measurement.

The two subsequent chapters are dedicated to our study of the double spin asymmetries A_{LT} and A_{LL}; calculations and the prediction plots for x,y,z and P_{hT} dependence of asymmetries for COMPASS, HERMES and JLab experiments are presented.

In chapters 5–7 we describe the COMPASS experimental setup, review the general aspects of the data analysis procedure (event selection, analysis methods, systematic studies and cross-checks) and present the results on target transverse spin dependent azimuthal asymmetries extracted from COMPASS 2002-2004 data. Asymmetries are evaluated as a functions of x,y,z and P_{hT} kinematic variables for positive and negative *unidentified* hadrons and for positive and negative pions and kaons.

At the end of the thesis we summarize the obtained results and draw some conclusions.

Contents

Chapter 1

Introduction

One of the important aspects in the investigation of the structure of the nucleon is the partonic origin of the nucleon spin which still remains mysterious. According to the naïve quark model the nucleon spin sums from the spins of it constituent partons (quarks). However in late eighties the results obtained by the European Muon Collaboration (EMC) has shown that the contribution of the valence quarks spins to the total spin of the nucleon is of less than 30% Ref. [1]. This puzzle has stimulated a further theoretical and experimental investigations in order to find the missing component of the nucleon spin.

The contribution of the spins of the partons into the overall spin of the nucleon is described by helicity and transversity distributions. The helicity distributions are defined by the difference between the numbers of partons with their spins parallel and antiparallel to the spin of the longitudinally polarized nucleon (spin is parallel to the momentum of the nucleon). While the transversity distribution is defined similarly but for the nucleons with spin polarized transversely to its direction of motion. Both type of distributions are defined in a frame in which the nucleon has a very large momentum and its direction breaks rotational symmetry (infinite nucleon momentum frame). Considering the transverse structure of the nucleon one have to mention another an important degree of freedom – the intrinsic transverse momentum of the partons $\boldsymbol{k_T}$ which plays an essential role in spin-physics.

Another possible contributions in the formation of the nucleon spin can be expected from orbital momentum of the partons and from gluons (due to the helicity conservation gluons can contribute only to the longitudinal polarization of nucleon) and gluon orbital momentum.

In the past years a lot of progress and understanding has been achieved concerning the longitudinal structure of a fast moving proton – the $Bjørken\ x$ - dependence of the unpolarized parton distribution functions and of the helicity distributions, but still very little is known about the transverse structure – both the transverse spin distributions and the parton intrinsic motion. These factors cannot be considered as minor details in the investigation of spin structure of the nucleon. Without a good knowledge of the total intrinsic momentum carried by the partons, and its connection with the spin, one could never explore the parton orbital motion and progress towards a more complex picture beyond the simple collinear partonic representation.

One powerful method to study three-dimensional [1] QCD picture of nucleon is the measurement of azimuthal asymmetries in polarized SIDIS[2]

$$\ell(l, P_l) + N(P, \mathbf{S}_T) \to \ell(l') + h(P_h) + X, \tag{1.1}$$

where l indicates the beam lepton, N the target nucleon, and h the produced hadron, and four-momenta are given in parentheses. The P_l and $\mathbf{S}_T$ are the longitudinal polarization of lepton and polarization of target, respectively.

The description of SIDIS includes a set of transverse momentum dependent (TMD) distribution and fragmentation functions (DFs and FFs) Refs. [2, 3]. The definitions of these functions and QCD factorization for inclusive processes including both a large momentum scale, like the mass of a virtual photon in e^+e^- annihilation or in Drell–Yan lepton pair production, and a small transverse momentum of the produced particles, was established by Collins and Soper Ref. [4] already in the early 80s. Recent data on single spin azimuthal asymmetries in SIDIS obtained by the COMPASS Refs. [5, 6], HERMES Ref. [7] and CLAS at JLab Refs. [8, 9] collaborations triggered a new interest in TMD DFs and FFs. The gauge invariant definitions of TMD and factorization theorems for polarized SIDIS were carefully studied in Ref. [10] and Ref. [11]. It was demonstrated that the general expression for the SIDIS cross-section can be factorized into TMD DFs and FFs and soft and hard parts arising from soft gluon radiation and QCD contributions to hard scattering, respectively. However, it is difficult to apply the complete formalism of the QCD factorized approach in performing a phenomenological analysis of data or making predictions. The current common practice (see, for example, the recent analysis of Cahn, Sivers and Collins asymmetries in Refs. [12] – [13]) is to use the leading order (LO) expressions for soft and hard parts which is equivalent to using the simple parton model expression including twist-two TMD DFs and FFs. This approach allows to capture the main features of considered effects and make predictions for different processes. In our calculations in Sec. 3 and 4 we followed the same line.

In general, eight target transverse polarization dependent asymmetries are allowed in reaction Eq. (1.1). At leading twist of the QCD parton model the polarized nucleon is described by eight transverse momentum dependent distribution functions four of which induce the specific target transverse polarization dependent azimuthal asymmetries.

The data concerning two asymmetries, namely, Collins and Sivers effects in reaction Eq. (1.1) are now available from HERMES Ref. [7] and COMPASS Refs. [5, 6], experiments. The interpretation of these asymmetries within the QCD parton model includes transversity and Sivers distribution function and the ordinary unpolarized and transversely polarized quark fragmentation functions. Using these data the phenomenological analysis and extraction of Sivers DF were performed, see Ref. [14] and references therein.

The Collins FF can be studied via azimuthal asymmetries in the reaction $e^+e^- \to h_1 h_2\, X$. The new measurements were reported from Belle Collaboration at KEK Ref. [15]. The global analysis of these and SIDIS data from HERMES and COMPASS experiments were performed in Ref. [16] and, for the first time, the transversity function for light quarks and Collins fragmentation functions were extracted.

[1] Longitudinal momentum fraction + transverse momentum dependent distribution functions

[2] Here only spinless or unpolarized hadron production is considered.

It is very important to measure all possible TMD spin-dependent asymmetries and perform a 'global' phenomenological analysis by simultaneous extraction of TMD DF's parameters from experimental data taking into account the general TMD positivity constraints Ref. [17]. The comparison of extracted DFs with models based on Lorenz Invariance relation will alow to check the self-consistency of the LO QCD picture of polarized SIDIS (see discussion and predictions in Ref. [18] and in Sec. 3 and 4).

COMPASS (COmmon Muon and Proton Apparatus for Structure and Spectroscopy) is a high-energy physics experiment at the Super Proton Synchrotron (SPS) at CERN in Geneva, Switzerland. The purpose of this experiment is the study of hadron structure, in particular the investigation of spin structure of the nucleon and hadron spectroscopy with high intensity muon and hadron beams and a polarized deuteron or proton target. In the longitudinal target spin mode, the main goal of the experiment is the measurement of $\Delta G/G$, the polarization of the gluons in a longitudinally polarized nucleon, in the same time very precise data in the flavor decomposition of the longitudinal helicity distribution functions (g_1^d) was collected. Approximately twenty percent of the running time COMPASS was running with the transversely polarized target. With the data collected in this mode the transverse spin effects in particular the single- and the double- spin azimuthal asymmetries are extracted and investigated.

The last mentioned aspect – the extraction and interpretation of target transverse spin dependent asymmetries in COMPASS is the main goal of this thesis.

Chapter 2

Target Transverse Spin Dependent Asymmetries

2.1 General formalism and QCD parton model

Following Ref. [2], we consider the polarized SIDIS in the simple quark-parton model within one-photon exchange approximation and neglecting the lepton mass. In the sequel the standard notations for DIS variables are used: l and l' are four-momenta of the initial and the final state lepton; $q = l - l'$ is the exchanged virtual photon four-momenta and $Q^2 = -q^2$; P is the target nucleon four-momenta while M and S are its mass and spin respectively; P_h is the final hadron four-momenta;

$$x = \frac{Q^2}{2\,P\cdot q}, \qquad y = \frac{P\cdot q}{P\cdot l}, \qquad z = \frac{P\cdot P_h}{P\cdot q}. \tag{2.1}$$

The kinematics and defined reference frame of DIS process is presented in Fig. 2.1.

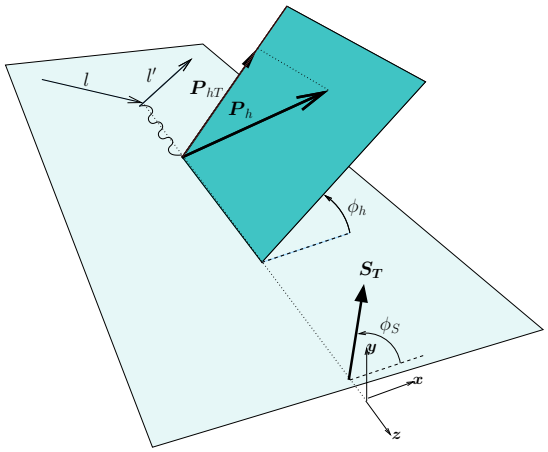

Figure 2.1: Definition of azimuthal angles for semi-inclusive deep inelastic scattering. P_{hT} and S_T are the transverse components of hadron momentum P_h and the target polarization with respect to the photon momentum.

The reference frame is defined with the z-axis along the virtual photon momentum direction and x-axis in the lepton scattering plane, with positive direction chosen along lepton transverse momentum. The azimuthal angles of the produced hadron (with transverse momentum, P_{hT}), ϕ_h, and of the nucleon spin, ϕ_S, are counted around z-axis (for more details see Refs. [2] or [3]).

Based on the general principles of quantum field theory it can be shown in the model independent way that in the one photon exchange approximation the cross-section of the process Eq. (1.1) includes set of 18 structure functions Refs. [2], [19]:

$$
\begin{aligned}
&\frac{d\sigma}{dx\,dy\,d\psi\,dz\,d\phi_h\,dP_{hT}^2} = \\
&\quad \frac{\alpha^2}{xyQ^2}\,\frac{y^2}{2\,(1-\varepsilon)}\left(1+\frac{\gamma^2}{2x}\right)\Bigg\{F_{UU,T} + \varepsilon\,F_{UU,L} + \sqrt{2\,\varepsilon(1+\varepsilon)}\,\cos\phi_h\,F_{UU}^{\cos\phi_h} \\
&\qquad + \varepsilon\cos(2\phi_h)\,F_{UU}^{\cos 2\phi_h} + P_l\,\sqrt{2\,\varepsilon(1-\varepsilon)}\,\sin\phi_h\,F_{LU}^{\sin\phi_h} \\
&\qquad + S_L\left[\sqrt{2\,\varepsilon(1+\varepsilon)}\,\sin\phi_h\,F_{UL}^{\sin\phi_h} + \varepsilon\sin(2\phi_h)\,F_{UL}^{\sin 2\phi_h}\right] \\
&\qquad + S_L P_l\left[\sqrt{1-\varepsilon^2}\,F_{LL} + \sqrt{2\,\varepsilon(1-\varepsilon)}\,\cos\phi_h\,F_{LL}^{\cos\phi_h}\right] \\
&\qquad + |\boldsymbol{S}_T|\Bigg[\sin(\phi_h-\phi_S)\left(F_{UT,T}^{\sin(\phi_h-\phi_S)} + \varepsilon\,F_{UT,L}^{\sin(\phi_h-\phi_S)}\right) \\
&\qquad\quad + \varepsilon\,\sin(\phi_h+\phi_S)\,F_{UT}^{\sin(\phi_h+\phi_S)} + \varepsilon\,\sin(3\phi_h-\phi_S)\,F_{UT}^{\sin(3\phi_h-\phi_S)} \\
&\qquad\quad + \sqrt{2\,\varepsilon(1+\varepsilon)}\,\sin\phi_S\,F_{UT}^{\sin\phi_S} + \sqrt{2\,\varepsilon(1+\varepsilon)}\,\sin(2\phi_h-\phi_S)\,F_{UT}^{\sin(2\phi_h-\phi_S)}\Bigg] \\
&\qquad + |\boldsymbol{S}_T|P_l\Bigg[\sqrt{1-\varepsilon^2}\,\cos(\phi_h-\phi_S)\,F_{LT}^{\cos(\phi_h-\phi_S)} + \sqrt{2\,\varepsilon(1-\varepsilon)}\,\cos\phi_S\,F_{LT}^{\cos\phi_S} \\
&\qquad\quad + \sqrt{2\,\varepsilon(1-\varepsilon)}\,\cos(2\phi_h-\phi_S)\,F_{LT}^{\cos(2\phi_h-\phi_S)}\Bigg]\Bigg\},
\end{aligned}
\tag{2.2}
$$

where the standard SIDIS notations are used, and the ratio ε of longitudinal and transverse photon fluxes is given by

$$
\varepsilon = \frac{1-y-\frac{1}{4}\gamma^2y^2}{1-y+\frac{1}{2}y^2+\frac{1}{4}\gamma^2y^2}, \tag{2.3}
$$

where $\gamma = \frac{2Mx}{Q}$. The notations for the structure functions F_{sub}^{sup} which on the r.h.s. depend on x, Q^2, z and P_hT (transverse component of the momentum of the produced hadron) have the following meaning: the superscript corresponds to the azimuthal asymmetry

described by the given structure function, whereas the first and second subscripts indicate the respective ("U"-unpolarized,"L"-longitudinal and "T"-transverse) polarization of beam and target and the third one specifies the polarization of the virtual photon. Integrating these structure functions over the produced hadron momentum and summing over all hadrons in the final state one can find relations between the polarized SIDIS structure functions and ordinary DIS structure functions. For more details see Refs. [2],[19].

The azimuthal angles in Eq. (2.2) are defined as presented in the Fig. 2.1. The angle ψ is the laboratory azimuthal angle of the scattered lepton and in DIS kinematics $d\psi \approx d\phi_S$.

Taking into account expression Eq. (2.3) the depolarization factors entering in the cross-section can be written as

$$\frac{y^2}{2\,(1-\varepsilon)} = \frac{1}{1+\gamma^2}\left(1-y+\tfrac{1}{2}y^2+\tfrac{1}{4}\gamma^2y^2\right) \approx \left(1-y+\tfrac{1}{2}y^2\right), \tag{2.4}$$

$$\frac{y^2}{2\,(1-\varepsilon)}\,\varepsilon = \frac{1}{1+\gamma^2}\left(1-y-\tfrac{1}{4}\gamma^2y^2\right) \approx (1-y), \tag{2.5}$$

$$\frac{y^2}{2\,(1-\varepsilon)}\,\sqrt{2\,\varepsilon(1+\varepsilon)} = \frac{1}{1+\gamma^2}\,(2-y)\,\sqrt{1-y-\tfrac{1}{4}\gamma^2y^2} \approx (2-y)\,\sqrt{1-y}, \tag{2.6}$$

$$\frac{y^2}{2\,(1-\varepsilon)}\,\sqrt{2\,\varepsilon(1-\varepsilon)} = \frac{1}{\sqrt{1+\gamma^2}}\,y\,\sqrt{1-y-\tfrac{1}{4}\gamma^2y^2} \approx y\,\sqrt{1-y}, \tag{2.7}$$

$$\frac{y^2}{2\,(1-\varepsilon)}\,\sqrt{1-\varepsilon^2} = \frac{1}{\sqrt{1+\gamma^2}}\,y\left(1-\tfrac{1}{2}y\right) \approx y\left(1-\tfrac{1}{2}y\right). \tag{2.8}$$

As one can see from this general expression of the cross-section there are only eight target transverse polarization dependent azimuthal modulations: five single target spin dependent and three double beam-target spin dependent asymmetries. Up to now only $\sin(\phi_h-\phi_S)$ (so called Sivers asymmetry) and $\sin(\phi_h+\phi_S)$ (so called Collins asymmetry) are measured and interpreted within leading order QCD parton model. In the next sections we will present the parton model interpretation of all eight modulations and first measurement of corresponding asymmetries by COMPASS.

2.1.1 Parton model interpretation

The high energy polarization phenomena which include the hard scale can be described using QCD factorization theorem. According to this theorem the cross section can be factorized into a hard photon-quark scattering process and parton distribution functions describing the distribution of quarks in the target and fragmentation functions describing the fragmentation of a quark into the observed hadron. Within this approach the cross section for hadron produced in the current fragmentation region of SIDIS can be represented as a convolution of initial quark distribution in nucleon

$$d\sigma^{l+N\to l'+h+X} \propto DF \otimes d\sigma^{l+q\to l'+q'} \otimes FF, \tag{2.9}$$

where $d\sigma^{l+q(k)\to l'+q'(k')}$ – is the polarized lepton-quark elastic hard scattering cross section and symbol $\otimes$ stands for convolution over quark intrinsic transverse momentum. A first

proof of factorization to all orders in α_s for the (similar but simpler) case of two-hadron production in e^+e^- collisions was given in Ref. [20]. The recent works on factorization in SIDIS can be found in Refs. [21, 22] and in Ref. [23].

Limiting ourselves to the leading and first sub-leading term in the $1/Q$ expansion of the cross section we end up with eight (six time reversal even and two time reversal odd) twist-two TMD quark distribution functions DFs describing the nucleon:

$$\begin{aligned}
\mathcal{P}_N^q(x,k_T^2) &= f_1^q(x,k_T^2) + f_{1T}^{\perp q}(x,k_T^2)\frac{[\mathbf{k}_T\times\hat{\mathbf{S}}_N]\cdot\mathbf{S}_T}{M},\\
\mathcal{P}_N^q(x,k_T^2)\, s_L^q(x,k_T) &= g_{1L}^q(x,k_T^2)\, S_L + g_{1T}^q(x,k_T^2)\,\frac{\mathbf{k}_T\cdot\mathbf{S}_T}{M}\,, \qquad (2.10)\\
\mathcal{P}_N^q(x,k_T^2)\,\mathbf{s}_T^q(x,k_T) &= h_{1T}^q(x,k_T^2)\,\mathbf{S}_T + \left[h_{1L}^{q\perp}(x,k_T^2)S_L + h_{1T}^{q\perp}(x,k_T^2)\frac{\mathbf{k}_T\cdot\mathbf{S}_T}{M}\right]\frac{\mathbf{k}_T}{M}\\
&\quad + h_1^{\perp q}(x,k_T^2)\frac{[\mathbf{k}_T\times\hat{\mathbf{S}}_N]}{M}.
\end{aligned}$$

In this equations M is the nucleon mass, k_T is the transverse momentum of quark, $\mathbf{S}_T$ and S_L are the transverse and longitudinal components of target polarization with respect to nucleon momentum and $\hat{\mathbf{S}}_N$ the unit vector along this momentum. The probabilistic interpretation of distribution functions is as follows:

- $\mathcal{P}_N^q(x,k_T^2)$ is a number density of quarks which is defined by ordinary unpolarized TMD DF $f_1^q(x,k_T^2)$ and naive T-odd DF $f_{1T}^{\perp q}(x,k_T^2)$ – the Sivers function. In the notation of our published papers Refs. [5],[6] $\Delta_0^T q(x,k_T^2) = -\frac{k_T}{M} f_{1T}^{\perp q}(x,k_T^2)$.

- The quark longitudinal polarization, $s_L^q(x,k_T)$, is defined by DFs $g_{1L}^q(x,k_T^2)$ – the TMD helicity distribution and $g_{1T}^q(x,k_T^2)$ – the distribution of longitudinally polarized quarks in transversely polarized nucleon.

- The quark transverse polarization, $\mathbf{s}_T^q(x,k_T)$, contains four different terms, corresponding DFs are:

  1. $h_{1T}^q(x,k_T^2)$ describes quark transverse polarization along target transverse polarization,
  2. $h_{1L}^{q\perp}(x,k_T^2)$ describes quark transverse polarization along quark intrinsic transverse momentum in the longitudinally polarized target,
  3. $h_{1T}^{q\perp}(x,k_T^2)$ describes quark transverse polarization along quark intrinsic transverse momentum in the transversely polarized target,
  4. $h_1^{\perp q}(x,k_T^2)$ (T-odd Boer-Mulders function) describes quark transverse polarization along normal to the plane defined by quark intrinsic transverse momentum and nucleon momentum in the unpolarized target.

These partonic functions are often referred to as unintegrated functions, as they are not integrated over the transverse momentum.

Very often the combination

$$h_1(x,k_T^2) = h_{1T}^q(x,k_T^2) + \frac{\mathbf{k}_T^2}{2M} h_{1T}^{q\perp}(x,k_T^2)$$

is used and referred as TMD transversity distribution. In the notation of papers published by COMPASS collaboration Refs. [5],[6]

$$\Delta_T q(x) = \int d^2k_T \Delta_T q(x,k_T^2) = h_1(x) = \int d^2k_T h_1(x,k_T^2).$$

The TMD "k_T-unintegrated" distribution functions are related with the ordinary parton DFs via integration over intrinsic transverse momentum of the quarks. After the integration over k_T only the unpolarized $f_1^q(x)$, helicity $g_1^q(x)$ and transversity $h_1^q(x)$ ordinary distributions do not vanish.

$$f_1^q(x) = \int d^2k_T\, f_1^q(x,k_T^2), \tag{2.11}$$

$$g_1^q(x) = \int d^2k_T\, g_{1L}^q(x,k_T^2), \tag{2.12}$$

$$h_1^q(x) = \int d^2k_T \left[h_{1T}^q(x,k_T^2) - \frac{k_T^2}{2M^2} h_{1T}^{q\perp}(x,k_T^2) \right]. \tag{2.13}$$

For production of unpolarized (spinless) hadron the quark FFs entering in Eq. (2.9) contain the ordinary spin independent and fragmenting quark transverse polarization, $\mathbf{s}_T^{q'}$, dependent parts:

$$D_{q\uparrow}^h(z,P_{h\perp}^2) = D_{1q}^h(z,P_{h\perp}^2) + H_{1q}^{\perp h}(z,P_{h\perp}^2) \frac{[\mathbf{P}_{h\perp} \times \hat{\mathbf{k}}'] \cdot \mathbf{s}_T^{q'}}{m}, \tag{2.14}$$

here $D_{1q}^h(z,P_{h\perp}^2)$ is the ordinary unpolarized FF, $H_{1q}^{\perp h}(z,P_{h\perp}^2)$ – the Collins FF, $\hat{\mathbf{k}}'$ – unit vector collinear with fragmenting quark momentum, m is a produced hadron mass and $P_{h\perp}$ is the transverse to this vector component of produced hadron momentum. The probabilistic interpretation of FF is the following:

- $D_{1q}^h(z,P_{h\perp}^2)$ is the probability density that a struck quark of a flavor q fragments into a certain hadron of type h carrying energy fraction z;
- $H_{1q}^{\perp h}(z,P_{h\perp}^2)$ (Collins FF) is the difference of the probability densities for quarks with opposite transverse spin states to fragment to a hadrons h.

The relation with the notation used in Refs. [5],[6] is: $\Delta_T^0 D_q^h(z,P_{h\perp}^2) = -\frac{P_{h\perp}}{m} H_{1q}^{\perp h}(z,P_{h\perp}^2)$.

The leading order QCD parton model calculations Refs. [2] – [3] shows that the structure functions entering in amplitudes of transverse polarization dependent azimuthal modulations in Eq. (2.2) are given by the following convolutions:

$$F_{UT}^{\sin(\phi_h-\phi_S)} \propto f_{1T}^{\perp q} \otimes D_{1q}^{h}, \tag{2.15}$$

$$F_{UT}^{\sin(\phi_h+\phi_S)} \propto h_{1}^{q} \otimes H_{1q}^{\perp h}, \tag{2.16}$$

$$F_{UT}^{\sin(3\phi_h-\phi_S)} \propto h_{1T}^{\perp q} \otimes H_{1q}^{\perp h} \tag{2.17}$$

$$F_{LT}^{\cos(\phi_h-\phi_S)} \propto g_{1T}^{q} \otimes D_{1q}^{h}, . \tag{2.18}$$

The spin independent part of the cross section is given by

$$F_{UU,T} \propto f_{1}^{q} \otimes D_{1q}^{h}. \tag{2.19}$$

The Eq. (2.15) and Eq. (2.16) describe now the well known Sivers and Collins effects, respectively. The new leading twist modulations $\cos(\phi_h-\phi_S)$ and $\sin(3\phi_h-\phi_S)$ according to Eq. (2.18) and Eq. (2.17) give us access to DFs g_{1T}^{q} and $h_{1T}^{\perp q}$. Note that the first of these modulations is double spin effect related to the longitudinal polarization of quark in the transversely polarized nucleon. Our study performed for this effect is presented in Sec. 3 (see also Ref. [18]).

Within the QCD parton model the nonzero contributions arise also for the remaining four transverse azimuthal modulations at twist-three level. It is important to note, that using only twist-two DFs and FFs and taking into account the order $|\mathbf{k}_T|/Q$ kinematic corrections one also obtain the nonzero contributions to all these asymmetries Ref. [2], Ref. [19]. This approximation was successfully used to describe the (twist-three) Cahn effect in unpolarized SIDIS Ref. [24] and also to make predictions for the $\cos(\phi_h)$ dependence of SIDIS A_{LL} asymmetry (see Sec. 4 and Ref. [25]). Within this approximation

$$F_{UT}^{\sin(\phi_S)} \propto \frac{M}{Q}\left(h_{1}^{q} \otimes H_{1q}^{\perp h} + f_{1T}^{\perp q} \otimes D_{1q}^{h}\right), \tag{2.20}$$

$$F_{UT}^{\sin(2\phi_h-\phi_S)} \propto \frac{M}{Q}\left(h_{1T}^{\perp q} \otimes H_{1q}^{\perp h} + f_{1T}^{\perp q} \otimes D_{1q}^{h}\right). \tag{2.21}$$

$$F_{LT}^{\cos(\phi_S)} \propto \frac{M}{Q} g_{1T}^{q} \otimes D_{1q}^{h}, \tag{2.22}$$

$$F_{LT}^{\cos(2\phi_h-\phi_S)} \propto \frac{M}{Q} g_{1T}^{q} \otimes D_{1q}^{h}, \tag{2.23}$$

Note, that the convolutions in these equations include different combination of intrinsic transverse momentum of quarks in nucleon and produced hadron transverse momentum in the quark fragmentation. For exact definitions of all convolutions presented in Eqs. (2.15) – (2.23) see Ref. [19]. All DFs and FFs entering in these equations are now parameterized (extracted from experimental data) or can be modeled (as g_{1T}^{q} in Ref. [18] or in quark-diquark model of nucleon, see for example Ref. [26]). The measurement of the corresponding asymmetries will allow us to conclude about importance of twist-three DFs and FFs. It is worthwhile to remind here that for longitudinally polarized target the twist-two $A_{UL}^{\sin(2\phi)}$ asymmetry appears to be much smaller than twist-three $A_{UL}^{\sin(\phi)}$ asymmetry at HERMES Ref. [27] and JLab Ref. [9].

Let us briefly mention some experimental results and phenomenological analyses for the structure functions entering in the SIDIS cross-section Eq. (2.2). For simplicity we do not distinguish between measurements of the structure functions and of the associated spin or angular asymmetries, which correspond to the ratio of the appropriate structure functions and $F_{UU,T} + \epsilon F_{UU,L}$ (see next section).

1. $F_{UU}^{\cos\phi_h}$ – measurements of the cross-section components containing these structure function have been reported in Refs. [28, 29, 32, 33]. A description of the $\cos\phi_h$ modulation by the Cahn effect alone has been given in Ref. [24].

2. $F_{LL}^{\cos\phi_h}$ – described by g_{1L}^q helicity distribution function, corresponds to the polarized Cahn effect. In Sec. 4 we will present our phenomenological analysis on this subject (see also corresponding publication Ref. [25]).

3. $F_{UU}^{\cos 2\phi_h}$ – contains the functions $h_1^\perp$ (Boer-Mulders function Ref. [30]) and $H_1^\perp$ (Collins function Ref. [31]). It has been measured in Refs. [32, 33].

4. $F_{LU}^{\sin\phi_h}$ – this structure function has been recently measured by the CLAS collaboration Ref. [34].

5. $F_{UL}^{\sin\phi_h}$ – has been measured by HERMES Ref. [27]. The precise extraction of this observable requires care because in experiments the target is polarized along the direction of the lepton beam and not of the virtual photon Refs. [35, 36, 37, 38]. This implies that the longitudinal target-spin asymmetries measured in Refs. [39, 40, 41] receive contributions not only from $F_{UL}^{\sin\phi_h}$, but at the same order in $1/Q$ also from $F_{UT,T}^{\sin(\phi_h-\phi_S)}$ and $F_{UT}^{\sin(\phi_h+\phi_S)}$ (see also the phenomenological studies of Refs. [42, 43, 44, 45, 46, 47, 48]). In Ref. [27] the HERMES collaboration has separated the different contributions to the experimental $\sin\phi_h$ asymmetry with longitudinal target polarization and shown that $F_{UL}^{\sin\phi_h}$ is dominant in the kinematics of the measurement.

6. $F_{UL}^{\sin(2\phi_h)}$ – corresponding twist-two $A_{UL}^{\sin(2\phi)}$ asymmetry have been measured at HERMES Ref. [27] and JLab Ref. [9].

7. $F_{UT,T}^{\sin(\phi_h-\phi_S)}$ – contains the Sivers function Ref. [49] and has been recently measured for a proton target at HERMES Ref. [52] and for a deuteron target at COMPASS Refs. [5, 6]. Extractions of the Sivers function from the experimental data were performed in Refs. [53, 54, 55] (see Ref. [14] for a comparison of the various extractions).

8. $F_{UT}^{\sin(\phi_h+\phi_S)}$ – structure function contains the transversity distribution function Refs. [50, 51] and the Collins function. As the previous structure function, it has been measured by HERMES Ref. [52] on the proton and by COMPASS Ref. [5, 6] on the deuteron. Phenomenological studies have been presented in Ref. [54], where information about the Collins function was extracted, and in Ref. [56], where constraints on the transversity distribution function were obtained by using additional information from a Collins asymmetry measured in e^+e^- annihilation Ref. [57].

9. $F_{UT}^{\sin(3\phi_h-\phi_S)}$, $F_{LT}^{\cos(\phi_h-\phi_S)}$, $F_{UT}^{\sin(\phi_S)}$, $F_{UT}^{\sin(2\phi_h-\phi_S)}$, $F_{LT}^{\cos(\phi_S)}$, $F_{LT}^{\cos(2\phi_h-\phi_S)}$ – The preliminary results on the corresponding asymmetries for deuteron target are the main results of our work, they have been recently presented by COMPASS collaboration Ref. [58, 59]. The analysis procedure and results for these six *new* asymmetries as well as phenomenological analysis performed for $A_{LT}^{\cos(\phi_h-\phi_S)}$ asymmetry (Ref. [18]) will be presented in the following sections.

Thereby with last six *new* azimuthal asymmetries extracted for the first time in COMPASS for deuteron target we make complete the set of measurements of transverse-spin asymmetries and supplement access to six more structure functions in addition to already measured ones.

2.2 Definition of asymmetries

Our goal is the measuring of the structure functions corresponding to target transverse spin dependent azimuthal asymmetries to provide data which can be interpreted, for example, within QCD parton model. As it can be seen from the master equation for polarized SIDIS cross section, Eq. (2.2), in total eight azimuthal modulation are allowed:

$$w_1(\phi_h,\phi_S) = \sin(\phi_h-\phi_S), \tag{2.24}$$
$$w_2(\phi_h,\phi_S) = \sin(\phi_h+\phi_S), \tag{2.25}$$
$$w_3(\phi_h,\phi_S) = \sin(3\phi_h-\phi_S), \tag{2.26}$$
$$w_4(\phi_h,\phi_S) = \sin(\phi_S), \tag{2.27}$$
$$w_5(\phi_h,\phi_S) = \sin(2\phi_h-\phi_S), \tag{2.28}$$
$$w_6(\phi_h,\phi_S) = \cos(\phi_h-\phi_S), \tag{2.29}$$
$$w_7(\phi_h,\phi_S) = \cos(\phi_S), \tag{2.30}$$
$$w_8(\phi_h,\phi_S) = \cos(2\phi_h-\phi_S) \tag{2.31}$$

and the cross section can be represented in the terms of asymmetries as:

$$\begin{aligned} d\sigma(\phi_h,\phi_S,...) \;&\propto\; (1+|\boldsymbol{S}_T|\sum_{i=1}^{5} D^{w_i(\phi_h,\phi_S)} A_{UT}^{w_i(\phi_h,\phi_S)} w_i(\phi_h,\phi_S) \\ &+\; P_l|\boldsymbol{S}_T|\sum_{i=6}^{8} D^{w_i(\phi_h,\phi_S)} A_{LT}^{w_i(\phi_h,\phi_S)} w_i(\phi_h,\phi_S) + ...\big). \end{aligned} \tag{2.32}$$

Here, we factored out the explicitly calculable depolarization factors, $D^{w_i(\phi_h,\phi_S)}$, and defined the asymmetries as the ratios of corresponding structure functions to unpolarized one:

$$A_{BT}^{w_i(\phi_h,\phi_S)} \equiv \frac{F_{BT}^{w_i(\phi_h,\phi_S)}}{F_{UU,T}}, \tag{2.33}$$

where $B = L$ or $B = U$ corresponds to beam polarization dependent (DSA) or independent (SSA) part of asymmetry.

In $\mathcal{O}(1/Q)$ approximation these depolarization factors entering in Eq. (2.32) depend only on y and are given by (see Eqs. (2.2) – (2.8))

$$D^{\sin(\phi_h-\phi_S)}(y) = 1, \tag{2.34}$$

$$D^{\sin(\phi_h+\phi_S)}(y) = D^{\sin(3\phi_h+\phi_S)}(y) = D_{NN}(y) = \frac{2(1-y)}{1+(1-y)^2}, \tag{2.35}$$

$$D^{\sin(2\phi_h-\phi_S)}(y) = D^{\sin(\phi_S)}(y) = \frac{2(2-y)\sqrt{1-y}}{1+(1-y)^2}, \tag{2.36}$$

$$D^{\cos(\phi_h-\phi_S)}(y) = D(y) = \frac{y(2-y)}{1+(1-y)^2}, \tag{2.37}$$

$$D^{\cos(2\phi_h-\phi_S)}(y) = D^{\cos(\phi_S)}(y) = \frac{2y\sqrt{1-y}}{1+(1-y)^2}. \tag{2.38}$$

Defined in such a way asymmetries have very simple interpretation in the QCD parton model and are given by the ratio of convolutions of spin-dependent to spin-independent DFs and FFs, see Eqs. (2.15) – (2.23).

In the QCD parton model four of the eight transverse asymmetries are given by the ratio of convolutions of spin-dependent to spin-independent twist two DFs and FFs:

$$A_{UT}^{\sin(\phi_h-\phi_S)} \propto \frac{f_{1T}^{\perp q}\otimes D_{1q}^h}{f_1^q\otimes D_{1q}^h}, \tag{2.39}$$

$$A_{UT}^{\sin(\phi_h+\phi_S)} \propto \frac{h_1^q\otimes H_{1q}^{\perp h}}{f_1^q\otimes D_{1q}^h}, \tag{2.40}$$

$$A_{LT}^{\cos(\phi_h-\phi_S)} \propto \frac{g_{1T}^q\otimes D_{1q}^h}{f_1^q\otimes D_{1q}^h}, \tag{2.41}$$

$$A_{UT}^{\sin(3\phi_h-\phi_S)} \propto \frac{h_{1T}^{\perp q}\otimes H_{1q}^{\perp h}}{f_1^q\otimes D_{1q}^h} \tag{2.42}$$

As an example, the $A_{LT}^{\cos(\phi_h-\phi_S)}$ and $A_{UT}^{\sin(3\phi_h-\phi_S)}$ leading-twist asymmetries can be used for extraction of DFs g_{1T}^q and $h_{1T}^{\perp q}$ describing the quark longitudinal and transverse (along the quark transverse momentum) polarization in the transversely polarized nucleon. The other four asymmetries can be interpreted as Cahn kinematic corrections to spin effects on the transversely polarized nucleon Ref. [2]:

$$A_{LT}^{\cos(\phi_S)} \propto \frac{M}{Q}\frac{g_{1T}^q\otimes D_{1q}^h}{f_1^q\otimes D_{1q}^h}, \tag{2.43}$$

$$A_{LT}^{\cos(2\phi_h-\phi_S)} \propto \frac{M}{Q}\frac{g_{1T}^q\otimes D_{1q}^h}{f_1^q\otimes D_{1q}^h}, \tag{2.44}$$

$$A_{UT}^{\sin(\phi_S)} \propto \frac{M}{Q}\frac{h_1^q \otimes H_{1q}^{\perp h} + f_{1T}^{\perp q} \otimes D_{1q}^h}{f_1^q \otimes D_{1q}^h}, \tag{2.45}$$

$$A_{UT}^{\sin(2\phi_h-\phi_S)} \propto \frac{M}{Q}\frac{h_{1T}^{\perp q} \otimes H_{1q}^{\perp h} + f_{1T}^{\perp q} \otimes D_{1q}^h}{f_1^q \otimes D_{1q}^h}. \tag{2.46}$$

According to Eq. (2.32) the counting rate asymmetries extracted from the data as amplitudes of corresponding azimuthal modulations (*raw* asymmetries) are then given by

$$A_{UT,\,raw}^{w_i(\phi_h,\phi_S)} = D^{w_i(\phi_h,\phi_S)}(y) f |S_T| A_{UT}^{w(\phi_h,\phi_S)}, \quad (i = 1,5), \tag{2.47}$$

$$A_{LT,\,raw}^{w(\phi_h,\phi_S)} = D^{w(\phi_h,\phi_S)}(y) f P_l |S_T| A_{LT}^{w(\phi_h,\phi_S)}, \quad (i = 6,8), \tag{2.48}$$

where f is the target polarization dilution factor (the fraction of polarisable material inside the target see Sec. 7.1.5).

Chapter 3

Predictions for A_{LT} asymmetry

This section is dedicated to our phenomenological analysis performed for $A_{LT}^{\cos(\phi_h-\phi_s)}$ asymmetry (see also Ref. [18]).

As it was already noted in previous sections within this LO QCD parton model approach the polarized nucleon is described by eight twist-two TMD DFs. One of these DFs, $g_{1T}^q(x,k_T^2)$, describes longitudinal polarization of quarks in the transversely polarized target and lead to a specific double-spin $\mathcal{A}_{LT}$. asymmetry (Eq. (2.42)). The rough estimates of this asymmetry has been performed in Ref. [60] using the so called Lorentz invariance (LI) relation Ref. [61, 3] between the first k_T-momentum of the twist-two DF $g_{1T}^q(x,k_T^2)$ and the twist-three DF $g_2^q(x)$. In its turn the twist-three DF $g_2^q(x)$ was expressed through the twist-two helicity DF $g_1^q(x)$ using Wandzura and Wilczek Ref. [62] (WW) relation. Thus the corresponding k_T^2 weighted distribution function $g_{1T}^{(1)}$ was related to the ordinary helicity distribution $g_1(x)$ measured in DIS.

Now using the recent parameterizations for (un)polarized distribution and for fragmentation functions and applying the same LI and WW relations as in Ref. [60] we performed a more detailed analysis and calculated A_{LT} asymmetry on transversely polarized proton and deuteron targets for different types hadron production. The predictions were given for COMPASS, HERMES and JLab energies.

The chapter is organized as follows. First in Sec 3.1 we calculate hadron-transverse-momentum weighted asymmetries. The resulting values obtained for COMPASS, HERMES and JLab energies are rather small. Then in next section (Sec 3.2), we assume gaussian parametrization for intrinsic transverse momentum and calculate the asymmetries without weighting by hadron transverse momentum. In this case, with appropriate choice of cuts, asymmetry can reach 2–7 % depending on the width of intrinsic transverse momentum distribution of $g_{1T}^q(x,k_T^2)$. We present results for different sets of cuts and indicate the regions of kinematical variables where asymmetry can be sizable.

Finally, in Sec. 3.3 we discuss the obtained results and draw some conclusions.

3.1 Hadron-transverse-momentum weighted asymmetry

In the LO QCD parton model the twist-to parton distribution function $g_{1T}^q(x,k_T^2)$ describes the longitudinal quark polarization in a transversely polarized nucleon. Such a polariza-

tion can be non-vanishing only if the quark transverse momentum is nonzero. This DF can be measured in polarized SIDIS as first shown in Ref. [2], where it leads to a specific azimuthal asymmetry. The DF $g_{1T}^q(x, k_T^2)$ does not contribute to helicity distribution $g_1^q(x)$, but it does contribute to the twist-three DF $g_T^q(x) = g_1^q(x) + g_2^q(x)$, which gives $\mathcal{O}(1/Q)$ contribution to the inclusive polarized lepto-production cross section Ref. [61].

Following Ref. [2], we consider in our calculations the polarized SIDIS in the simple quark-parton model. We will use standard notations for DIS variables and azimuthal angles presented already in Sec. 2.1: l and l' are momenta of the initial and the final state lepton; $q = l - l'$ is the exchanged virtual photon momentum; P (M) is the target nucleon momentum (mass), S its spin; P_h is the final hadron momentum; $Q^2 = -q^2$; $s = Q^2/xy$; $x = Q^2/2P \cdot q$; $y = P \cdot q/P \cdot l$; $z = P \cdot P_h/P \cdot q$. The reference frame is defined with the z-axis along the virtual photon momentum direction and x-axis in the lepton scattering plane, with positive direction chosen along lepton transverse momentum. The azimuthal angles of the produced hadron (with transverse momentum, P_{hT}), ϕ_h, and of the nucleon spin, ϕ_S, are counted around z-axis (for more details see Refs. [2] or [3]). As independent azimuthal angles we choose $\phi_h^S \equiv \phi_h - \phi_S$ and ϕ_S and we will give cross-sections integrated over ϕ_S (which corresponds to integration over laboratory azimuthal angle of lepton) at fixed value of ϕ_h^S.

We are interested in $\cos\phi_h^S$ asymmetry arising due to g_{1T} DF and thus we do not consider the contributions to cross section arising from DFs $h_{1T}, h_{1T}^\perp, h_{1L}^\perp$ and time reversal odd DFs $h_1^\perp$ and $f_{1T}^\perp$. These contributions are either vanishing after ϕ_h^S integration or projected out in $\cos\phi_h^S$ weighted asymmetries.

Keeping only relevant terms at leading order the SIDIS cross section for polarized leptons and transversely polarized hadrons has the form

$$\frac{d\sigma(\ell N \to \ell' h X)}{dx dy dz\, d^2P_{hT}} = \frac{2\pi\alpha^2}{Q^2\, y}\left\{[1 + (1-y)^2]\,\mathcal{H}_{f_1} + y(2-y)\, P_l\, |S_T|\, \cos\phi_h^S\, \mathcal{H}_{g_{1T}}\right\}. \quad (3.1)$$

The structure functions $\mathcal{H}_f$ entering in Eq. (3.1) are given by quark-charge-square weighted sums of definite k_T-convolutions of the DF's and the spin-independent fragmentation function $D_q^h(z, P_{h\perp}^2)$ with $P_{h\perp} = P_{hT} - zk_T$ being the transverse momentum of hadron with respect to fragmenting quark. The explicit form of the structure functions can be found in Refs. [2, 3]:

$$\mathcal{H}_{f_1} = \sum_q e_q^2 \int d^2k_T\, f_1^q(x, k_T^2) D_q^h(z, (P_{hT} - zk_T)^2), \quad (3.2)$$

$$\mathcal{H}_{g_{1T}} = \sum_q e_q^2 \int d^2k_T \frac{\mathbf{k}_T \cdot \mathbf{P}_{hT}}{M\,|\mathbf{P}_{hT}|}\, g_{1T}^q(x, k_T^2) D_q^h(z, (P_{hT} - zk_T)^2). \quad (3.3)$$

Note, that these structure functions include only unpolarized FFs, $D_q^h(z, P_{h\perp}^2)$.

The target transverse spin asymmetry for SIDIS of 100 % longitudinally polarized lepton (P_l=1) is defined as

$$A_{LT}(x, y, z, P_{hT}, \phi_h^S) = \frac{d\sigma^\uparrow - d\sigma^\downarrow}{d\sigma^\uparrow + d\sigma^\downarrow}. \quad (3.4)$$

with $\uparrow$ ($\downarrow$) denoting the transverse polarization of the target nucleon with S_L = 0 and $|S_T|$ = 1. From Eq. (3.1) we get

$$A_{LT}(x,y,z,P_{hT},\phi_h^S) = \frac{\frac{2-y}{xy}\,\mathcal{H}_{g_{1T}}}{\frac{1+(1-y)^2}{xy^2}\,\mathcal{H}_{f_1}}\,\cos(\phi_h-\phi_S). \tag{3.5}$$

In Ref. [60] the P_{hT}-weighted asymmetries were introduced for the first time. It was demonstrated that it is possible to express these asymmetries trough the corresponding moments of DFs and FFs for arbitrary dependence on intrinsic transverse momentum. The transverse-spin asymmetry weighted with $\mathbf{S}_T\cdot\mathbf{P}_{hT}/M = (|\mathbf{P}_{hT}|/M)\cos(\phi_h-\phi_S)$ (see Ref. [60]) can be expressed as

$$\begin{aligned} A_{LT}^{\frac{|\mathbf{P}_{hT}|}{M}\cos(\phi_h-\phi_S)}(x,y,z) &= 2\frac{\int d^2P_{hT}\frac{|\mathbf{P}_{hT}|}{M}\,\cos\phi_h^S\,(d\sigma^\uparrow - d\sigma^\downarrow)}{\int d^2P_{hT}(d\sigma^\uparrow + d\sigma^\downarrow)} \\ &= 2\frac{\frac{2-y}{xy}\,z\,\sum_q e_q^2\,g_{1T}^{q\,(1)}(x)\,D_q^h(z)}{\frac{1+(1-y)^2}{xy^2}\,\sum_q e_q^2\,f_1^q(x)\,D_q^h(z)}, \end{aligned} \tag{3.6}$$

where

$$g_{1T}^{q\,(1)}(x) = \int d^2k_T\,\frac{\mathbf{k}_T^2}{2M^2}\,g_{1T}^q(x,k_T^2). \tag{3.7}$$

As is shown in Refs. [61, 3] this $(k_T^2/2M^2)$–weighted k_T-integrated function $g_{1T}^{q\,(1)}(x)$, which appears in Eq. (3.6) is directly related to the DF $g_2^q(x)$,

$$g_2^q(x) = \frac{d}{dx}\,g_{1T}^{q\,(1)}. \tag{3.8}$$

This relation arises from constraints imposed by Lorentz invariance on the antiquark-target forward scattering amplitude and the use of QCD equations of motion for quark fields Ref. [3]. Using Wandzura and Wilczek Ref. [62] approximation for $g_2^q(x)$

$$g_2^q(x) \approx -g_1^q(x) + \int_x^1 dy\,\frac{g_1^q(y)}{y}, \tag{3.9}$$

the following relation was derived in Ref. [60]

$$g_{1T}^{q(1)}(x) \approx x\int_x^1 dy\,\frac{g_1^q(y)}{y}. \tag{3.10}$$

For numerical estimations of asymmetries we used the LO GRV98 Ref. [63] unpolarized and corresponding GRSV2000 Ref. [64] polarized (standard scenario) DFs and Kretzer Ref. [65] FFs. In Fig 3.1 we present the ratio $g_{1T}^{q(1)}(x)/f_1^q(x)$ for u-, d- and s-quarks and antiquarks calculated using these DFs and Eq. (3.10). From this figure one can see that contribution of u and d quarks have opposite signs and are small in low x region. Thus the effect is expected to be small at low x and moreover it have to be smaller for deuterium target compared to the proton one due to the more effective cancelation between the u and d quark contributions.

The predictions for x, y and z dependence of $A_{LT}^{(|\mathbf{P}_{hT}|/M)\cos(\phi_h-\phi_S)}$ are obtained by performing integration of numerator and denominator of Eq. (3.6) and presented in Figs. 3.2, 3.3 and 3.4. The following selections and cuts are imposed

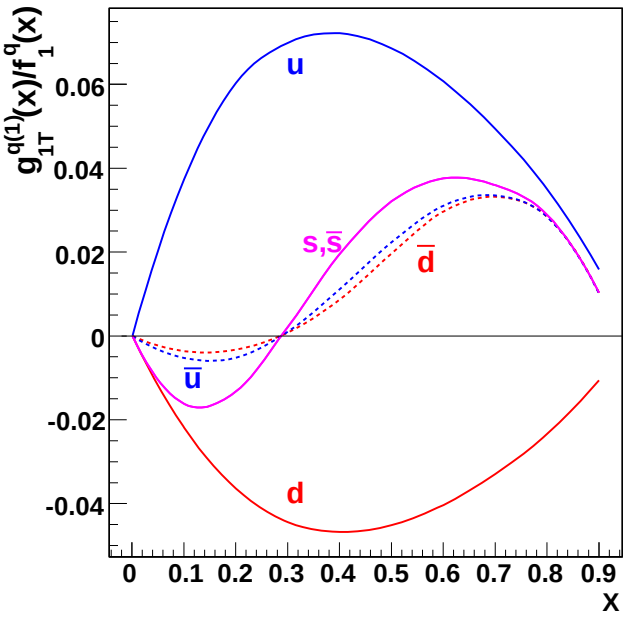

Figure 3.1: The ratio $g_{1T}^{q(1)}(x)/f_1^q(x)$ for different types of quarks at $Q^2 = 5$ (GeV/c)^2.

- COMPASS: positive (h^+), all (h) and negative (h^-) hadron production, $Q^2 > 1.0$ (GeV/c)^2, $W^2 > 25$ GeV^2, $0.05 < x < 0.6$, $0.5 < y < 0.9$ and $0.4 < z < 0.9$
- HERMES: π^+, π^0 and π^- production, $Q^2 > 1.0$ (GeV/c)^2, $W^2 > 10$ GeV^2, $0.1 < x < 0.6$, $0.45 < y < 0.85$ and $0.4 < z < 0.7$
- JLab at 6 GeV: π^+, π^0 and π^- production, $Q^2 > 1.0$ (GeV/c)^2, $W^2 > 4$ GeV^2, $0.2 < x < 0.6$, $0.4 < y < 0.7$ and $0.4 < z < 0.7$.

As one can see from these figures the predicted $|\mathbf{P}_{hT}|/M$-weighted asymmetries are quite small even for high x, y and z values both for proton and deuteron targets. This is related to dominant contribution of low $|\mathbf{P}_{hT}|$ integration region into denominator and negligible contribution to numerator in Eq. (3.6). We have done also calculations for JLab at 12 GeV beam energy with the same kinematic cuts as for 6 GeV. The results are almost identic to that of Fig. 3.4 and we do not present them in the following too.

3.2 Transverse momentum dependence

Usually, for reconstruction of produced hadron azimuthal angle in data analysis some cut on minimal value of $|\mathbf{P}_{hT}|$ of order 50 – 100 MeV/c is applied. On the other hand as we have demonstrated in the previous section the expected $|\mathbf{P}_{hT}|/M$-weighted asymmetries are very small due to integration over all available hadron transverse momentum phase space. Thus, it is very interesting to have a model and make predictions for transverse

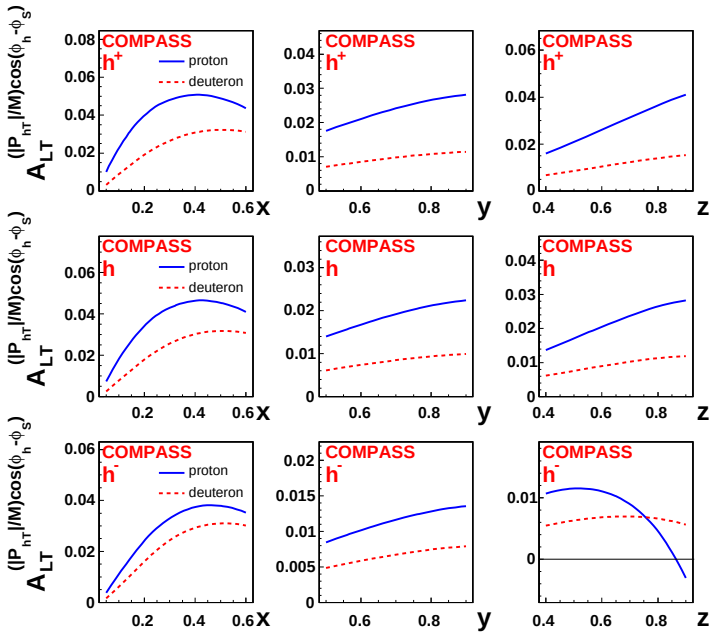

Figure 3.2: Predicted dependence of $A_{LT}^{(|\mathbf{P}_{hT}|/M)\cos(\phi_h-\phi_S)}$ on x, y and z for production of positive (h^+), all charged (h) and negative (h^-) hadrons at COMPASS for SIDIS on transversely polarized proton (the solid line) and deuteron (the dashed line) targets.

momentum dependence of A_{LT}. For this end let us assume that transverse momentum dependencies of DFs and FFs are given by factorized gaussian form:

$$f_1^q(x,k_T^2) = f_1^q(x)\frac{1}{\pi\mu_0^2}\,\exp(-\frac{\mathbf{k}_T^2}{\mu_0^2}), \tag{3.11}$$

$$D_q^h(z,P_{h\perp}^2) = D_q^h(z)\frac{1}{\pi\mu_D^2}\,\exp(-\frac{\mathbf{P}_{h\perp}^2}{\mu_D^2}), \tag{3.12}$$

$$g_{1T}^q(x,k_T^2) = g_{1T}^q(x)\,N\,\exp(-\frac{\mathbf{k}_T^2}{\mu_1^2}), \tag{3.13}$$

where $f_1^q(x)$ and $D_q^h(z)$ are ordinary transverse momentum integrated DFs and FFs. DF $g_{1T}^q(x)$ can be related to $g_{1T}^{(1)}(x)$ by using the definition Eq. (3.7)

$$g_{1T}^q(x) = \frac{2M^2}{N\pi\mu_1^4}\,g_{1T}^{(1)}(x), \tag{3.14}$$

thus, the Eq. (3.13) can be rewritten as

$$g_{1T}^q(x,k_T^2) = g_{1T}^{q(1)}(x)\,\frac{2M^2}{\pi\mu_1^4}\,\exp(-\frac{\mathbf{k}_T^2}{\mu_1^2}). \tag{3.15}$$

Note, that normalization coefficient N in Eq. (3.13) is fixed by the relation Eq. (3.14).

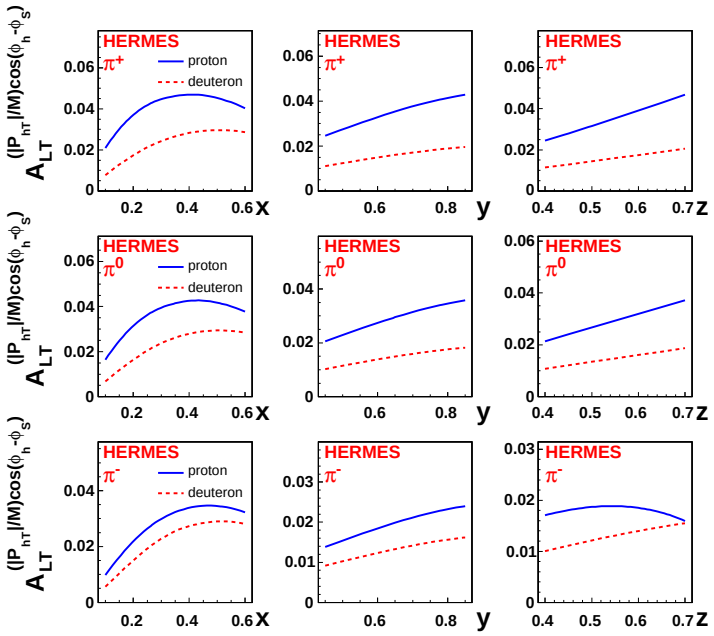

Figure 3.3: Predicted dependence of $A_{LT}^{(|\mathbf{P}_{hT}|/M)\cos(\phi_h-\phi_S)}$ on x, y and z for π^+, π^0 and π^- production at HERMES for SIDIS on transversely polarized proton (the solid line) and deuteron (the dashed line) targets.

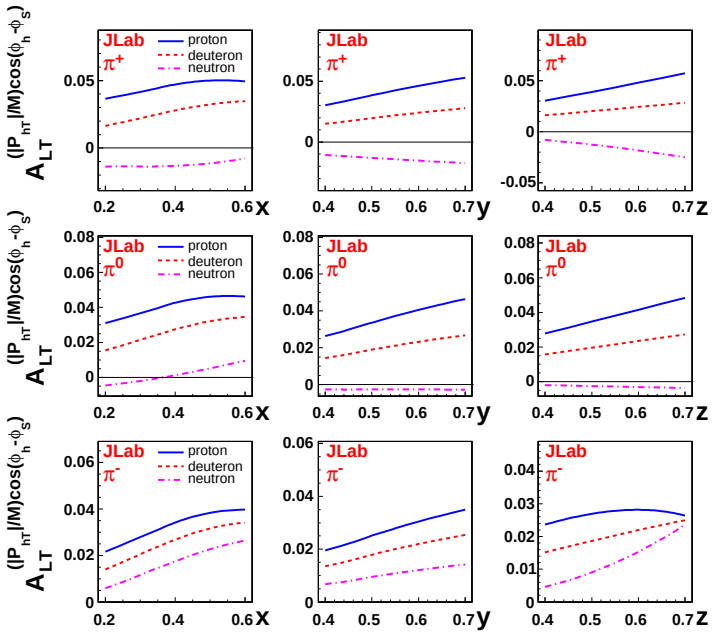

Figure 3.4: Predicted dependence of $A_{LT}^{(|\mathbf{P}_{hT}|/M)\cos(\phi_h-\phi_S)}$ on x, y and z for π^+, π^0 and π^- production at JLab for SIDIS on transversely polarized proton (the solid line), deuteron (the dashed line) and neutron (dot-dashed line) targets.

Now using Eqs. 3.2 and 3.3 and performing integration over intrinsic transverse momentum one obtains for $\cos\phi_h^S$ weighted asymmetry

$$A_{LT}^{\cos\phi_h^S}(x,y,z,P_{hT}) = 2\frac{\int_0^{2\pi} d\phi_h^S\,(d\sigma^\uparrow - d\sigma^\downarrow)\cos\phi_h^S}{\int_0^{2\pi} d\phi_h^S\,(d\sigma^\uparrow + d\sigma^\downarrow)}$$
$$= 2\frac{\frac{2-y}{xy}\frac{Mz|\mathbf{P}_{hT}|}{(\mu_D^2+\mu_1^2z^2)^2}\exp\left(-\frac{\mathbf{P}_{hT}^2}{\mu_D^2+\mu_1^2z^2}\right)\sum_q e_q^2\,g_{1T}^{q(1)}(x)\,D_q^h(z)}{\frac{1+(1-y)^2}{xy^2}\frac{1}{\mu_D^2+\mu_0^2z^2}\exp\left(-\frac{\mathbf{P}_{hT}^2}{\mu_D^2+\mu_0^2z^2}\right)\sum_q e_q^2\,f_1^q(x)\,D_q^h(z)}. \quad (3.16)$$

The numerator for asymmetry expression contains factors proportional to z, P_{hT} and $g_{1T}^{q(1)}(x)$ which are small at small x. At the same time the denominator gets the maximal contribution at small values of this variables. The same is valid for y dependence. Thus, the interesting region where asymmetry can be large corresponds to relatively large values of kinematic variables x, y, z and P_{hT}.

The dependence of asymmetry on the lower limit of $P_{hT,min}$ is calculated as

$$A_{LT}^{\cos\phi_h^S}(P_{hT,min}) = 2\frac{\int_{\mathbf{P}_{hT,min}^2}^{\mathbf{P}_{hT,max}^2} dP_{hT}^2\int dx\int dy\int dz\int_0^{2\pi} d\phi_h^S(d\sigma^\uparrow - d\sigma^\downarrow)\cos\phi_h^S}{\int_{\mathbf{P}_{hT,min}^2}^{\mathbf{P}_{hT,max}^2} dP_{hT}^2\int dx\int dy\int dz\int_0^{2\pi} d\phi_h^S(d\sigma^\uparrow + d\sigma^\downarrow)} \quad (3.17)$$
$$= 2\frac{\iiint dxdydz\,\frac{2-y}{xy}\frac{Mz}{\sqrt{\mu_D^2+\mu_1^2z^2}}\left[\Gamma\left(\frac{3}{2},\,\frac{\mathbf{P}_{hT,min}^2}{\mu_D^2+\mu_1^2z^2}\right)-\Gamma\left(\frac{3}{2},\,\frac{\mathbf{P}_{hT,max}^2}{\mu_D^2+\mu_1^2z^2}\right)\right]\sum_q e_q^2\,g_{1T}^{q(1)}(x)\,D_q^h(z)}{\iiint dxdydz\,\frac{1+(1-y)^2}{xy^2}\left[\exp\left(-\frac{\mathbf{P}_{hT,min}^2}{\mu_D^2+\mu_0^2z^2}\right)-\exp\left(-\frac{\mathbf{P}_{hT,max}^2}{\mu_D^2+\mu_0^2z^2}\right)\right]\sum_q e_q^2\,f_1^q(x)\,D_q^h(z)},$$

where

$$\Gamma(a,x) = \int_x^\infty dt\,t^{a-1}\exp(-t)$$

is incomplete Gamma function and we choose $|\mathbf{P}_{hT,max}|$ =2.0, 1.5 and 1.0 GeV/c for COMPASS, HERMES and JLab, respectively.

In Figs. 3.5 and 3.6 we show our predictions for $A_{LT}^{\cos(\phi_h-\phi_S)}(|\mathbf{P}_{hT,min}|)$ for COMPASS, HERMES on proton and deuteron targets and proton, deuteron and neutron targets for JLab. The same kinematic cuts as in previous section has been used. The width of the transverse momentum distribution for unpolarized DFs and FFs can be obtained by analyzing the data on $\cos\varphi$-azimuthal dependence (Cahn effects) and $|\mathbf{P}_{hT}|$-dependence of unpolarized SIDIS cross-section. The corresponding analysis performed in Ref. [12] shows that the following values $\mu_0^2 = 0.25$ (GeV/c)^2 and $\mu_D^2 = 0.2$ (GeV/c)^2 satisfactory describes the data up to $|\mathbf{P}_{hT}| \leq 1$ GeV/c.

It is easy to check that with our choice of distribution function the naive positivity constraint $\frac{|\mathbf{k}_T|}{M}\,|g_{1T}^q(x,k_T^2)| \leq f_1^q(x,k_T^2)$ holds when $\mu_1^2 < 0.246$ (GeV/c)^2 in whole range of variables x and $|\mathbf{k}_T|$. We present the results for three different choices of the transverse momentum width parameter μ_1^2 of the $g_{1T}^q(x,k_T^2)$ DF: 0.1, 0.15 and 0.2 (GeV/c)^2. As one can see in Figs. 3.5 and 3.6, the asymmetry reveals a strong dependence upon this parameter and increases with μ_1 for $|\mathbf{P}_{hT,min}|$ higher than 0.5 (GeV/c).

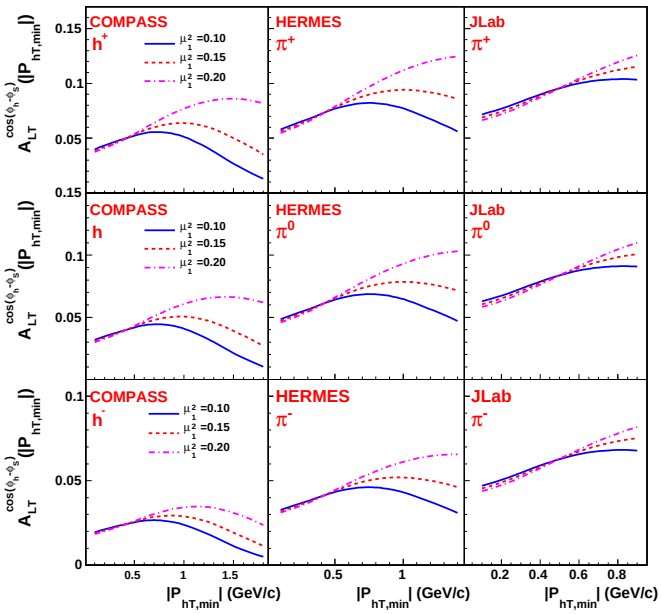

Figure 3.5: Predicted dependence of $A_{LT}^{\cos(\phi_h-\phi_S)}(|\mathbf{P}_{hT,min}|)$ on $|\mathbf{P}_{hT,min}|$ for proton target.

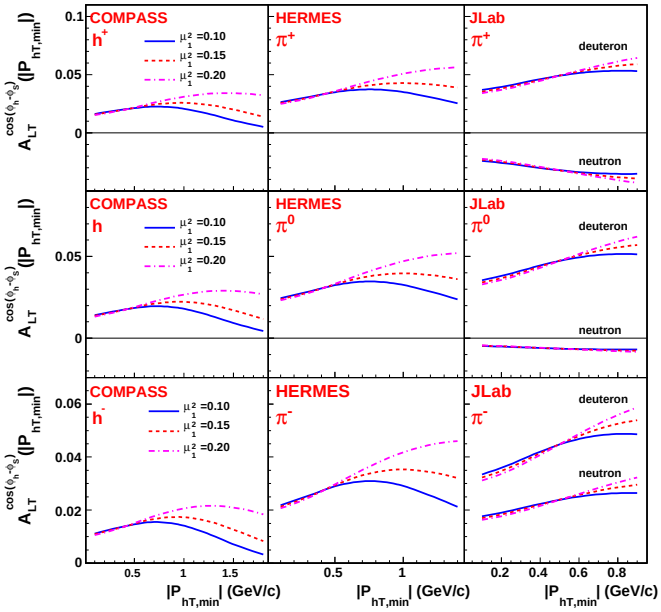

Figure 3.6: Predicted dependence of $A_{LT}^{\cos(\phi_h-\phi_S)}(|\mathbf{P}_{hT,min}|)$ on $|\mathbf{P}_{hT,min}|$ for deuteron (and neutron for JLab) target.

In Figs. 3.7, 3.8 and 3.9 we present the x-, y- and z-dependencies of $A_{LT}^{\cos(\phi_h-\phi_S)}$ integrated over $|\mathbf{P}_{hT}|$ with $|\mathbf{P}_{hT,min}| = 0.5$ GeV/c and μ_1^2 =0.15 (GeV/c)^2. As it is

expected these asymmetries due to the avoided small $|\mathbf{P}_{hT}|$ region are almost twice larger than $\frac{|\mathbf{P}_{hT}|}{M}$-weighted asymmetries in Figs. 3.2, 3.3 and 3.4.

Finally, we have checked that the value of the predicted asymmetry depends on the widths of the transverse momentum dependence of the DFs and FFs. For example, with the following choice of parameters: $\mu_0^2 = 0.09$ (GeV/c)^2 and $\mu_D^2 = 0.13$ (GeV/c)^2 and $\mu_1^2 = 0.08$ (GeV/c)^2, the asymmetry increases by ≈ 1.5 times and, naturally, the azimuthal and transverse momentum distributions of unpolarized SIDIS are changed too. Thus, it is desirable to extract these widths from the same set of data. First, the parameters μ_0^2 and μ_D^2 have to be fixed from unpolarized SIDIS azimuthal and $|\mathbf{P}_{hT}|$-dependencies, then, μ_1^2 can be extracted from the measured $A_{LT}^{\cos(\phi_h - \phi_S)}$ asymmetry.

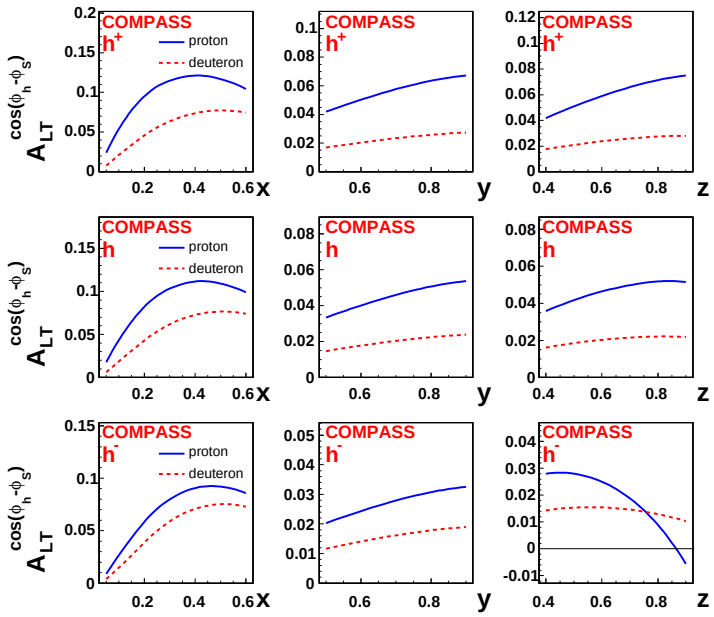

Figure 3.7: Predicted dependence of $A_{LT}^{\cos(\phi_h - \phi_S)}$ on x-, y- and z with $|\mathbf{P}_{hT,min}| = 0.5$ GeV/c for COMPASS.

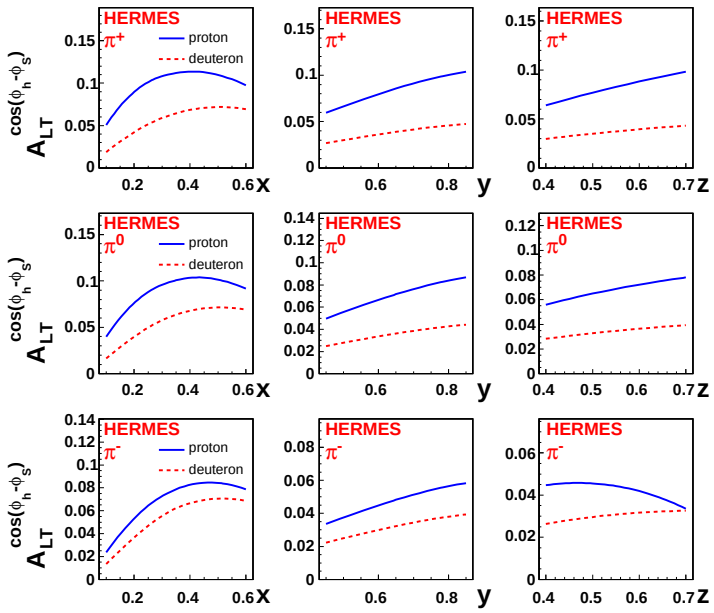

Figure 3.8: Predicted dependence of $A_{LT}^{\cos(\phi_h-\phi_S)}$ on x-, y- and z with $|\mathbf{P}_{hT,min}| = 0.5$ GeV/c for HERMES.

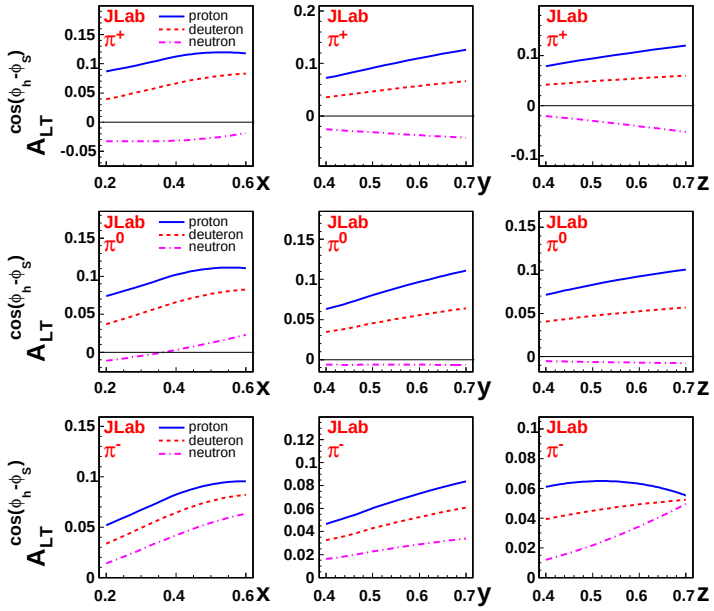

Figure 3.9: Predicted dependence of $A_{LT}^{\cos(\phi_h-\phi_S)}$ on x-, y- and z with $|\mathbf{P}_{hT,min}| = 0.5$ GeV/c for JLab.

3.3 Discussion and Conclusions

We have performed the detailed calculations of double spin azimuthal asymmetry for SIDIS induced by longitudinal polarization of quarks in transversely polarized nucleon. The results presented in the Sec. 3.1 show that the hadron-transverse-momentum weighted asymmetries are quite small and maybe difficult to measure. In Sec. 3.2 it is demonstrated that unweighted asymmetry can be enhanced and reach few percents with the cut on minimal value of hadron transverse momentum $|\mathbf{P}_{hT,min}| \simeq 0.1 \div 0.5$ GeV/c [2].

We have used the conventional LO QCD approach for SIDIS in the current fragmentation region. One of the main ingredients used for asymmetry calculations is the Lorentz invariance relation between twist-two and twist-three DFs $g_{1T}^{q(1)}(x)$ and $g_2^q(x)$ Eq. (3.8) and the Wandzura-Wilczek approximation for $g_2^q(x)$ Eq. (3.9). The recent measurements of $g_2(x)$ structure function Ref. [66] demonstrated that the WW-relation is not strongly violated in high $x > 0.05$ and $Q^2 > 2 \sim 3$ (GeV/c)^2 region. On the other hand it was demonstrated that the Lorentz invariance relations are violated in some QCD based model (so called dressed quark target model) for DFs Ref. [67]. Then it was shown Refs. [68, 69] that the same Wilson link in the definition of DFs which makes possible the existence of nonzero Sivers effect leads to violation of Lorentz invariance relations among DFs. Thus, experimental verification of our predictions for double spin $\cos(\phi_h - \phi_S)$ asymmetry will allow us to check if there exists a strong violation of Lorentz invariance relation.

In our calculations we have used the ordinary formalism of factorized QCD picture of SIDIS. The possible effects of polarized hadronization Ref. [70] has been neglected. This polarization dependence of hadronization is expected to be enhanced at low energies. For this reason, it is important to perform measurements at different energies with different accessible range of W^2.

As it is mentioned in Sec. 3.2 the naive positivity bound is satisfied for the width of transverse momentum distribution of $g_{1T}^q(x, k_T^2)$ DF $\mu_1 \lesssim \mu_0$. However, as it was shown in Ref. [17] the positivity bounds which takes into account all twist two TMD DFs are more complicated and involve also other polarized DFs. For $g_{1T}^q(x, k_T^2)$ distribution function of interest the following inequality (or even more sharpened, see for details Ref. [17]) was derived

$$\frac{\mathbf{k}_T^2}{M^2}\left(g_{1T}^q(x,k_T^2)\right)^2 + \frac{\mathbf{k}_T^2}{M^2}\left(f_1^{q\perp}(x,k_T^2)\right)^2 \leq \left(f_1^q(x,k_T^2)\right)^2 - \left(g_{1L}^q(x,k_T^2)\right)^2, \qquad (3.18)$$

where $f_1^{q\perp}(x, k_T^2)$ is a DF leading to Sivers effect. Note that in Ref. [12][1] the naive positivity constraint $\frac{|\mathbf{k}_T|}{M}|f_1^{q\perp}(x,k_T^2)| < f_1^q(x,k_T^2)$ was used during fitting of the Sivers DF. The resulting DF for d-quark can reach the upper limit allowed by this relation at $x \approx 0.24$ and $|\mathbf{k}| \approx 0.57$ GeV/c for the best choice of parameters. This will violate the relation Eq. (3.18) even if $g_{1T}^d(x, k_T^2) = 0$ unless very improbable value for d-quark helicity TMD DF $g_{1L}^q(x, k_T^2) = 0$ holds at this values of x and $|\mathbf{k}|$. One has to note, however, that extracted in Ref. [12] and other analyzes (see Ref. [13] references therein) parameters for Sivers function have large errors and it is possible to fulfill the constraint Eq. (3.18) taking into account that at moderate x the following inequality takes place $\left(g_{1L}^q(x,k_T^2)\right)^2 \ll \left(f_1^q(x,k_T^2)\right)^2$.

[1] The relation between notations of this article with that used here can be found in Ref. [13]

These considerations demonstrate that to check the self-consistency of the LO QCD picture of polarized SIDIS it is very important to measure all possible TMD spin-dependent asymmetries, for example, the azimuthal angle and $|\mathbf{P}_{hT}|$-dependence of SIDIS A_{LL} asymmetry which will give us a possibility to extract the k_T-dependence of $g_{1L}^q(x, k_T^2)$ (see next section), and perform 'global' phenomenological analysis by simultaneous extraction of TMD DF's parameters from experimental data taking into account the positivity constraints Ref. [17].

In the following sections we will show the results on $A_{LT}^{\cos(\phi_h-\phi_s)}$ asymmetry extracted from the COMPASS data. The definition of the A_{LT} as an amplitude of $\cos(\phi_h - \phi_s)$ modulation in the cross-section which we used in our calculations differs from one given by Eq. (2.32) by the factor of $D^{\cos(\phi_h-\phi_s)}(y)$. In order to calculate asymmetry according to the *COMPASS-definition* we have to use expression Eq. (3.16) divided by the depolarization factor $D^{\cos(\phi_h-\phi_s)}(y)$ from Eq. (2.37):

$$A_{LT,exp}^{\cos\phi_h^S}(x,y,z,P_{hT}) = 2\frac{\frac{Mz|\mathbf{P}_{hT}|}{(\mu_D^2+\mu_1^2z^2)^2}\exp\left(-\frac{\mathbf{P}_{hT}^2}{\mu_D^2+\mu_1^2z^2}\right)\sum_q e_q^2\, g_{1T}^{q(1)}(x)\, D_q^h(z)}{\frac{1}{\mu_D^2+\mu_0^2z^2}\exp\left(-\frac{\mathbf{P}_{hT}^2}{\mu_D^2+\mu_0^2z^2}\right)\sum_q e_q^2\, f_1^q(x)\, D_q^h(z)}. \tag{3.19}$$

In addition cutting away the events with small x, y, z and P_{hT} in order to get sizable asymmetry values we will loose the most part of statistics in COMPASS, since the favorable kinematic for this experiment corresponds to low values of kinematic variables (see Sec. 6.3.9). With this reason we recalculated our predictions for whole COMPASS kinematical range, which bring as to smaller effect but at least we don't loose the statistics. The comparison of the extracted asymmetries with the predictions are given in Figures 8.1-8.2 presented in the conclusion part of the thesis (Sec. 8).

Chapter 4

Predictions for A_{LL} asymmetry

In this section we present our study of double longitudinal-spin asymmetry A_{LL} and present obtained results (see also Ref. [25]).

Analogously to the previous sections we consider here polarized SIDIS processes, at twist-two in the parton model, with transverse momentum dependent distribution and fragmentation functions. Such processes can be described in terms of six time reversal even Refs. [2, 3] and two (naïvely) time reversal odd PDFs. The dependence on partonic intrinsic motion induces a dependence on P_{hT}. In addition, at $\mathcal{O}(k_T/Q)$, kinematic corrections induce a dependence of the unpolarized cross section on the azimuthal angle ϕ_h between the leptonic and the hadron production planes – the so called Cahn effect Refs. [71, 72]. It was shown in Ref. [12] that a careful study of the dependence of the cross section on the final hadron momentum allows to extract the average values of intrinsic momenta in unpolarized PDFs and FFs.

We expand on the work of Ref. [12] and evaluate the role of partonic intrinsic motion in polarized SIDIS; in particular, on the double spin asymmetry (DSA) for the scattering of longitudinally polarized leptons off a longitudinally polarized target, A_{LL}, where longitudinal refers to the incoming lepton direction, in the laboratory frame. We show that a study of A_{LL} and of the weighted asymmetry $A_{LL}^{\cos\phi_h}$ allows to extract the transverse momentum dependence of the unintegrated helicity distribution function $g_{1L}^q(x, k_T^2)$ [or $\Delta q(x, k_T^2)$].

The chapter is organized as follows. In Sec 4.1 we shortly recall the relevant formalism for polarized SIDIS. In Sec 4.2 some predictions for the double longitudinal spin asymmetries are presented. The results are given for different sets of kinematical cuts, according to the experimental setups of HERMES, COMPASS and JLab experiments; they indicate the best kinematical regions for the asymmetry to be sizeable. Finally, in Sec. 4.3 we shortly discuss our results and draw some conclusions.

4.1 Polarized cross section

Similarly to the previous section and Ref. [2], we consider the polarized SIDIS in the simple quark-parton model, with unintegrated parton distributions. The standard notations for DIS variables are used: ℓ and ℓ' are, respectively, the four-momenta of the initial and

the final state leptons; $q = \ell - \ell'$ is the exchanged virtual photon momentum; P (M) is the target nucleon momentum (mass), S its polarization; P_h is the final hadron momentum; $Q^2 = -q^2$; $x = Q^2/2P \cdot q$; $y = P \cdot q/P \cdot \ell$; $z = P \cdot P_h/P \cdot q$, $Q^2 = xy(s - M^2)$, $s = (\ell + P)^2$. We work in a frame with the z-axis along the virtual photon momentum direction and the x-axis in the lepton scattering plane, with positive direction chosen along the lepton transverse momentum. The produced hadron has transverse momentum $\boldsymbol{P}_{hT}$; its azimuthal angle, ϕ_h, and the azimuthal angle of the transverse nucleon spin, ϕ_S, are measured around the z-axis (for further details see Ref. [2]).

We consider longitudinally polarized protons and leptons, where longitudinal (according to the laboratory setup) refers to the initial lepton direction. It then results that a proton with longitudinal spin S along the incoming lepton direction, has a transverse – with respect to the γ^* direction – spin component:

$$S_T = S \sin\theta_\gamma, \tag{4.1}$$

where

$$\sin\theta_\gamma = \sqrt{\frac{4M^2x^2}{Q^2 + 4M^2x^2}\left(1 - y - \frac{M^2x^2y^2}{Q^2}\right)} \simeq \frac{2Mx\sqrt{1-y}}{Q}\,. \tag{4.2}$$

This component gives contributions of order M/Q.

Keeping only twist-two contributions and terms up to $\mathcal{O}(M/Q)$ the cross section for SIDIS of longitudinally polarized leptons off a longitudinally polarized target can be written as:

$$\frac{d^5\sigma^{\overrightarrow{\Leftarrow}}}{dx\,dy\,dz\,d^2P_{hT}} = \frac{2\alpha^2}{xy^2s}\left\{\mathcal{H}_{f_1} + P_l\left(S_L\mathcal{H}_{g_{1L}} + S_T\mathcal{H}_{g_{1T}}\right)\right\}, \tag{4.3}$$

where the arrows indicate the direction of the lepton ($\rightarrow$) and target nucleon ($\Leftarrow$) polarizations, with respect to the lepton momentum; P_l, S_L and S_T are the magnitudes of, respectively: the longitudinal beam polarization, the longitudinal and the transverse target polarization. Notice that $\Leftarrow$ stands for a nucleon with a polarization vector, in the laboratory frame where the nucleon is at rest, *opposite* to the initial lepton momentum. For a $\Rightarrow$ polarization one reverses the signs of the S_L and S_T terms.

The three terms have a simple partonic interpretation:

$$\mathcal{H}_{f_1} = \sum_q e_q^2 \int d^2\boldsymbol{k}_T\, f_1^q(x,k_T^2)\,\pi y^2\,\frac{\hat{s}^2 + \hat{u}^2}{Q^4}\,D_q^h(z,P_{h\perp}^2), \tag{4.4}$$

$$\mathcal{H}_{g_{1L}} = \sum_q e_q^2 \int d^2\boldsymbol{k}_T\, g_{1L}^q(x,k_T^2)\,\pi y^2\,\frac{\hat{s}^2 - \hat{u}^2}{Q^4}\,D_q^h(z,P_{h\perp}^2), \tag{4.5}$$

$$\mathcal{H}_{g_{1T}} = -\sum_q e_q^2 \int d^2\boldsymbol{k}_T\,\frac{k_T}{M}\,\cos\varphi\; g_{1T}^q(x,k_T^2)\,\pi y^2\,\frac{\hat{s}^2 - \hat{u}^2}{Q^4}\,D_q^h(z,P_{h\perp}^2)\,, \tag{4.6}$$

and deserve some comments.

- The partonic factorized structure of the above equations is supposed to hold in the large Q^2 kinematic region where $P_{hT} \simeq \Lambda_{\rm QCD} \simeq k_T \ll Q$ Ref. [10]. It neglects terms of $\mathcal{O}(k_T/Q)^2$, in which case

$$\boldsymbol{P}_{h\perp}^2 = \boldsymbol{P}_{hT} - z\boldsymbol{k}_T \,,$$

where $\boldsymbol{P}_{h\perp}$ is the intrinsic transverse momentum of the hadron h with respect to the fragmenting quark direction.

- The first two contributions, Eqs. (4.4) and (4.5), give, respectively, the unpolarized cross section and the helicity asymmetry

$$\frac{d^5\sigma}{dx\,dy\,dz\,d^2P_{hT}} = \frac{2\alpha^2}{x\,y^2 s}\mathcal{H}_{f_1}; \qquad \frac{d^5\sigma^{++}}{dx\,dy\,dz\,d^2P_{hT}} - \frac{d^5\sigma^{+-}}{dx\,dy\,dz\,d^2P_{hT}} = \frac{4\alpha^2}{x\,y^2 s}\mathcal{H}_{g_{1L}}, \tag{4.7}$$

where $+, -$ stand for helicity states. The quark intrinsic motion induces a ***kinematical azimuthal dependence***, via the elementary polarized cross section Ref. [2]

$$\frac{d\sigma^{lq\to lq}}{dQ^2\,d\varphi} \propto \frac{\hat{s}^2 + \hat{u}^2 + P_l\,\lambda_q\,(\hat{s}^2 - \hat{u}^2)}{\hat{t}^2}, \tag{4.8}$$

where λ_q denotes the quark helicity. Keeping the terms up to order of k_T/Q the Mandelstam variables for the non-coplanar $\ell q \to \ell q$ scattering are expressed as

$$\begin{aligned} \hat{s} &\simeq xs\left[1 - 2\sqrt{1-y}\;\frac{k_T}{Q}\;\cos\varphi\right], \\ \hat{t} &= -Q^2 = -xys, \\ \hat{u} &\simeq -xs\,(1-y)\left[1 - \frac{2\,k_T}{Q\,\sqrt{1-y}}\;\cos\varphi\right], \end{aligned} \tag{4.9}$$

where φ is the azimuthal angle of $\boldsymbol{k}_T$, $d^2\boldsymbol{k}_T = k_T\,dk_T\,d\varphi$. Eq. (4.4) then gives the unpolarized Cahn effect Refs. [71, 72], while Eq. (4.5) gives the corresponding effect for the polarized (helicity) cross section, both at $\mathcal{O}(k_T/Q)$.

- Eq. (4.6) contains another $\cos\varphi$ dependence, of different origin. While the distribution functions $f_1^q(x,k_T^2)$ and $g_{1L}^q(x,k_T^2)$ which appear in Eqs. (4.4) and (4.5), are just the k_T dependent unpolarized and longitudinally polarized (helicity) PDFs, which, upon integration over $d^2\boldsymbol{k}_T$, give the usual $f_1^q(x)$ [or $q(x)$] and $g_1^q(x)$ [or $\Delta q(x)$] distributions, the quantity

$$-\frac{k_T}{M}\;\cos\varphi\; g_{1T}^q(x,k_T^2) = \Delta\hat{f}_{s_z/S_T} \tag{4.10}$$

is related to the number of partons longitudinally polarized inside a transversely polarized proton Refs. [2, 3, 73] (see Sec. 2.1.1): it can only depend on the scalar product between the two corresponding polarization vectors, which gives the $\cos(\phi_{S_T} - \varphi) = -\cos\varphi$ factor explicitly shown (see, for example, Eq. (C19) of Ref. [73]). This distribution is a leading-twist one, not suppressed by (k_T/Q) small factors. However, Eq. (4.6) will be multiplied by S_T, which is of $\mathcal{O}(M/Q)$, Eqs. (4.1)–(4.3); for this reason, in Eq. (4.6) we shall not take into account the extra (k_T/Q) kinematical terms contained in $(\hat{s}^2 - \hat{u}^2)$ of Eq. (4.8).

The integrals in Eqs. (4.4)–(4.6) can be analytically performed, if one assumes a simple factorized and gaussian behavior of the involved TMD PDFs and FFs, like it was done in Sec. 3.2:

$$f_1^q(x,k_T^2) = f_1^q(x)\,\frac{1}{\pi\mu_0^2}\,\exp\left(-\frac{k_T^2}{\mu_0^2}\right), \tag{4.11}$$

$$D_q^h(z,P_{h\perp}^2) = D_q^h(z)\,\frac{1}{\pi\mu_D^2}\,\exp\left(-\frac{P_{h\perp}^2}{\mu_D^2}\right), \tag{4.12}$$

$$g_{1T}^q(x,k_T^2) = g_{1T}^q(x)\,\frac{1}{\pi\mu_1^2}\,\exp\left(-\frac{k_T^2}{\mu_1^2}\right), \tag{4.13}$$

$$g_{1L}^q(x,k_T^2) = g_1^q(x)\,\frac{1}{\pi\mu_2^2}\,\exp\left(-\frac{k_T^2}{\mu_2^2}\right), \tag{4.14}$$

here Eqs. (4.11) - (4.13) are the same as Eqs. (3.11) - (3.13) used in calculations of A_LT asymmetry in the previous chapter, while Eq. (4.14) is the *new* one describing the g_{1L}^q DF. From above four equations and Eqs. (4.4) - (4.6) at $\mathcal{O}(P_{hT}/Q)$ we obtain:

$$\mathcal{H}_{f_1} = \left[1+(1-y)^2-4(2-y)\,\sqrt{1-y}\,\frac{z\,\mu_0^2\,P_{hT}}{Q\,(\mu_D^2+z^2\mu_0^2)}\,\cos\phi_h\right]\frac{\exp\left(-\frac{P_{hT}^2}{\mu_D^2+z^2\mu_0^2}\right)}{\mu_D^2+z^2\,\mu_0^2}\times \\ \times\sum_q e_q^2\,f_1^q(x)\,D_q^h(z), \tag{4.15}$$

$$\mathcal{H}_{g_{1L}} = y\left[2-y-4\,\sqrt{1-y}\,\frac{z\,\mu_2^2\,P_{hT}}{Q\,(\mu_D^2+z^2\mu_2^2)}\,\cos\phi_h\right]\frac{\exp\left(-\frac{P_{hT}^2}{\mu_D^2+z^2\mu_2^2}\right)}{\mu_D^2+z^2\,\mu_2^2}\times \\ \times\sum_q e_q^2\,g_1^q(x)\,D_q^h(z), \tag{4.16}$$

$$\mathcal{H}_{g_{1T}} = -y(2-y)\,\frac{z\,\mu_1^2\,P_{hT}}{M(\mu_D^2+z^2\mu_1^2)}\cos\phi_h\,\frac{\exp\left(-\frac{P_{hT}^2}{\mu_D^2+z^2\mu_1^2}\right)}{\mu_D^2+z^2\mu_1^2}\sum_q e_q^2\,g_{1T}^q(x)\,D_q^h(z). \tag{4.17}$$

4.2 Predictions for A_{LL}

We use Eqs. (4.3) and (4.15)–(4.17) to compute observables which depend on partonic intrinsic motions. Notice that we have allowed different average values of $\langle k_T^2\rangle$ for the different distribution functions: $\langle k_T^2\rangle = \mu_0^2$ for the unpolarized distributions, $\langle k_T^2\rangle = \mu_2^2$ for the helicity distributions, and $\langle k_T^2\rangle = \mu_1^2$ for $g_{1T}^q(x,k_T^2)$; each of these value is taken to be constant and flavour independent. For the fragmentation functions we have $\langle p_\perp^2\rangle = \mu_D^2$. Following Ref. [12] we use

$$\mu_0^2 = 0.25\ (\mathrm{GeV}/c)^2 \qquad\qquad \mu_D^2 = 0.20\ (\mathrm{GeV}/c)^2\,, \tag{4.18}$$

while we consider μ_1^2 and μ_2^2 as free parameters, which can give interesting information on the quark transverse motion in polarized protons; the naïve positivity bounds imply that we should have

$$\mu_1^2 \le \mu_0^2 \qquad\qquad \mu_2^2 \le \mu_0^2\,. \tag{4.19}$$

Our approach is supposed to hold up to $P_{hT} \simeq 1$ (GeV/c) Ref. [74]. Above that higher order pQCD corrections must be taken into account, and lead to tiny variations of the values given in Eq. (4.18) Ref. [74]; however, we shall consider experiments which are expected to produce data mainly in the low P_{hT} region, and both our approach and $\mu^2_{0,D}$values are well adequate.

We consider the P_{hT} dependence of the double longitudinal spin asymmetry

$$A_{LL}(x,y,z,P_{hT}) = \frac{\int_0^{2\pi} d\phi_h \, [\, d\sigma^{\overrightarrow{\Leftarrow}} - d\sigma^{\overrightarrow{\Rightarrow}} \,]}{P_l \, S \int_0^{2\pi} d\phi_h \, [\, d\sigma^{\overrightarrow{\Leftarrow}} + d\sigma^{\overrightarrow{\Rightarrow}} \,]} \,, \tag{4.20}$$

and the $\cos\phi_h$ weighted asymmetry, defined as

$$A_{LL}^{\cos\phi_h}(x,y,z,P_{hT}) = \frac{2\int_0^{2\pi} d\phi_h \, [\, d\sigma^{\overrightarrow{\Leftarrow}} - d\sigma^{\overrightarrow{\Rightarrow}} \,] \cos\phi_h}{P_l \, S \int_0^{2\pi} d\phi_h \, [\, d\sigma^{\overrightarrow{\Leftarrow}} + d\sigma^{\overrightarrow{\Rightarrow}} \,]} \cdot \tag{4.21}$$

From Eqs. (4.15)–(4.17) one has

$$A_{LL}(x,y,z,P_{hT}) = \frac{\Delta\sigma_{LL}}{\sigma_0}, \tag{4.22}$$

with

$$\Delta\sigma_{LL} = \frac{y(2-y)}{xy^2} \frac{1}{\mu_D^2 + z^2\mu_2^2} \exp\left(-\frac{P_{hT}^2}{\mu_D^2 + z^2\mu_2^2}\right) \sum_q e_q^2 \, g_1^q(x) \, D_q^h(z) \,. \tag{4.23}$$

and

$$\sigma_0 = \frac{1+(1-y)^2}{xy^2} \frac{1}{\mu_D^2 + z^2\mu_0^2} \exp\left(-\frac{P_{hT}^2}{\mu_D^2 + z^2\mu_0^2}\right) \sum_q e_q^2 \, f_1^q(x) \, D_q^h(z) \,. \tag{4.24}$$

Analogously, Eqs. (4.15)–(4.17) and (4.2) give

$$A_{LL}^{\cos\phi_h}(x,y,z,P_{hT}) = \frac{\Delta\sigma_{LL}^{\cos\phi_h} + \Delta\sigma_{LT}^{\cos\phi_h}}{\sigma_0}, \tag{4.25}$$

where the contribution from the longitudinal part of the target polarization is given by

$$\Delta\sigma_{LL}^{\cos\phi_h} = -4\,\frac{\sqrt{1-y}}{xy} \frac{z\,\mu_2^2\,P_{hT}}{Q\,(\mu_D^2 + z^2\mu_2^2)^2} \exp\left(-\frac{P_{hT}^2}{\mu_D^2 + z^2\mu_2^2}\right) \sum_q e_q^2 \, g_1^q(x) \, D_q^h(z), \tag{4.26}$$

and the contribution from the transverse part of the target polarization by

$$\Delta\sigma_{LT}^{\cos\phi_h} = \frac{-2(2-y)\sqrt{1-y}}{y} \frac{z\,\mu_1^2\,P_{hT}}{Q\,(\mu_D^2 + z^2\mu_1^2)^2} \exp\left(-\frac{P_{hT}^2}{\mu_D^2 + z^2\mu_1^2}\right) \sum_q e_q^2 \, g_{1T}^q(x) \, D_q^h(z). \tag{4.27}$$

Of course, both the numerator and denominator of Eqs. (4.20) and (4.21) can be integrated over some of the variables, according to the range covered by the setups of the experiments we shall consider:

- COMPASS: positive (h^+), all (h) and negative (h^-) hadron production, $Q^2 > 1.0$ (GeV/c)^2, $W^2 > 25$ GeV^2, $0.1 < x < 0.6$, $0.5 < y < 0.9$ and $0.4 < z < 0.9$
- HERMES: π^+, π^0 and π^- production, $Q^2 > 1.0$ (GeV/c)^2, $W^2 > 10$ GeV^2, $0.1 < x < 0.6$, $0.45 < y < 0.85$ and $0.4 < z < 0.7$
- JLab at 6 GeV: π^+, π^0 and π^- production, $Q^2 > 1.0$ (GeV/c)^2, $W^2 > 4$ GeV^2, $0.2 < x < 0.6$, $0.4 < y < 0.85$ and $0.4 < z < 0.7$.

We start by considering Eqs. (4.22)–(4.24). Notice that they are leading-twist quantities, not suppressed by any inverse power of Q. Concerning the usual integrated distribution and fragmentation functions we use the LO GRV98 Ref. [63] unpolarized and the corresponding GRSV2000 Ref. [64] polarized (standard scenario) DFs, and Kretzer Ref. [65] FFs. We can then compute the P_{hT} dependence of A_{LL}, depending on the only unknown quantity μ_2^2. We plot the results of our computations in Figs. 4.1 and 4.2, for a proton and deuteron (+ neutron, for JLab) target, respectively.

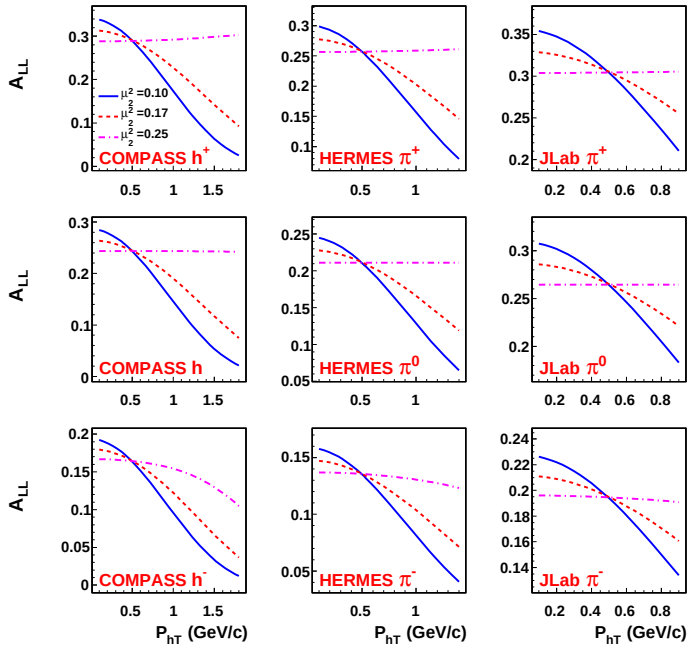

Figure 4.1: Predicted dependence of A_{LL} on P_{hT}, for scattering off a proton target, with different choices of μ_2^2: 0.1 (GeV/c)^2 – continuous, 0.17 (GeV/c)^2 – dashed and 0.25 (GeV/c)^2 – dot-dashed lines.

The results depend clearly on the relative values of $\langle k_T^2 \rangle$ for the unpolarized and helicity distribution, μ_0^2 and μ_2^2 respectively: $A_{LL}(P_{hT})$ is approximately constant if $\mu_2^2 = \mu_0^2 = 0.25$ (GeV/c)^2, whereas it sharply decreases with P_{hT} if $\mu_2^2 < \mu_0^2$. The trend of $A_{LL}(P_{hT})$ is thus a significant indication of the average quark transverse motion inside unpolarized versus longitudinally polarized nucleons. Although our numerical estimates are based on

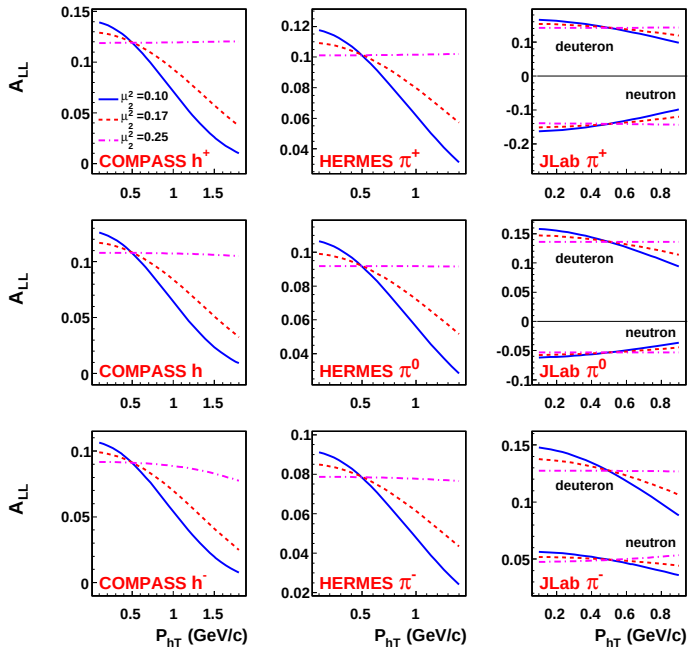

Figure 4.2: Predicted dependence of A_{LL} on P_{hT}, for scattering off a deuteron (and neutron for JLab) target, with different choices of μ_2^2: 0.1 (GeV/c)^2 – continuous, 0.17 (GeV/c)^2 – dashed and 0.25 (GeV/c)^2 – dot-dashed lines.

the gaussian factorization ansatz, Eqs. (11)-(14), we expect them to have a more general interpretation and information content. The P_{hT} dependence of A_{LL} reflects, essentially, the difference between the k_T dependence of $f_1^q(x,k_T)$ and $g_{1L}^q(x,k_T)$, independently of their functional forms; the trend of $A_{LL}(P_{hT})$, whether constant or decreasing, reveals the behavior of $g_{1L}^q(x,k_T)/f_1^q(x,k_T)$ and their relative k_T dependence.

Similarly, we can use Eqs. (4.24)–(4.27) in order to give some estimates of $A_{LL}^{\cos\phi_h}$. Notice that $\Delta\sigma_{LL}^{\cos\phi_h}$ and $\Delta\sigma_{LT}^{\cos\phi_h}$ are (kinematical) higher-twist quantities, proportional to P_{hT}/Q; in addition, $\Delta\sigma_{LT}^{\cos\phi_h}$ contains one unknown function, namely $g_{1T}^q(x)$, related to the helicity distribution of partons inside a transversely polarized proton. In the absence of any better guidance, we adopt the same strategy as in Ref. [18]. Analogously to see Sec. 3.1 we start by noticing that, from Eq. (4.13) we obtain Eq. (3.7)

$$g_{1T}^{q\,(1)}(x) \equiv \int d^2k_T \, \frac{k_T^2}{2M^2} \, g_{1T}^q(x,k_T^2) = \frac{\mu_1^2}{2M^2} \, g_{1T}^q(x) \, .$$

According to Refs. [61, 3] $g_{1T}^{q\,(1)}(x)$ is directly related to the DF $g_2^q(x)$, which has both twist-two and higher-twist contributions (Eq. (3.8),

$$g_2^q(x) = \frac{d}{dx} \, g_{1T}^{q\,(1)}(x).$$

This relation, although much debated, arises from constraints imposed by Lorentz invariance on the antiquark-target forward scattering amplitude and the use of QCD equa-

tions of motion for quark fields Ref. [3]. If, in addition, one uses the Wandzura and Wilczek Ref. [62] approximation for the twist-two part of $g_2^q(x)$ given by Eq. (3.9),

$$g_2^q(x) \simeq -g_1^q(x) + \int_x^1 dx' \, \frac{g_1^q(x')}{x'},$$

the following relation can be derived (Eq. (3.10),

$$g_{1T}^{q(1)}(x) \simeq x \int_x^1 dx' \, \frac{g_1^q(x')}{x'} \, ,$$

which, via Eq. (3.7), allows to express $g_{1T}^q(x)$ through the well known integrated helicity distributions.

Although such a procedure is appealing and convenient, we should stress there are strong arguments Refs. [67]–[69] (see also Sec. 3.3) against the validity of the relation (3.8). Therefore, we should consider the above expression, Eq. (3.10), only as a rough model for the otherwise unknown function $g_{1T}^q(x)$.

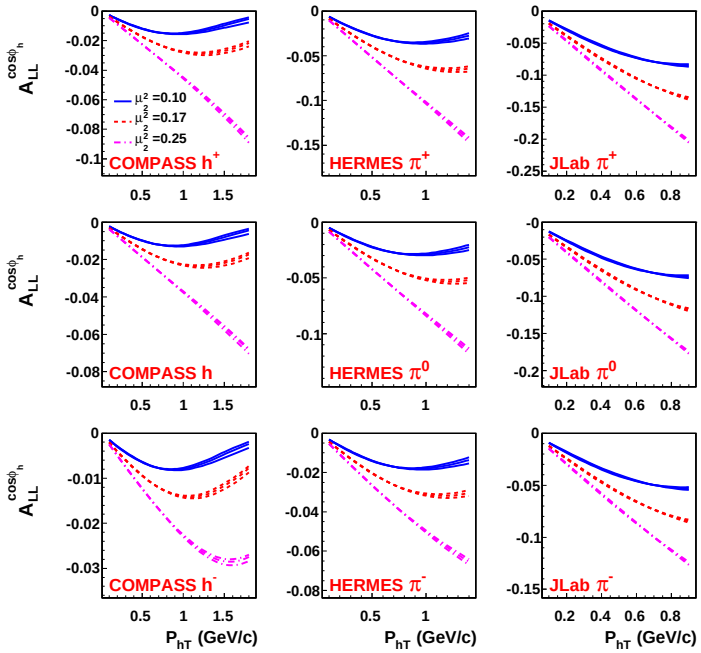

Figure 4.3: Predicted dependence of $A_{LL}^{\cos\phi_h}$ on P_{hT} for scattering off a proton target with different choices of μ_2^2: 0.1 (GeV/c)^2 – continuous, 0.17 (GeV/c)^2 – dashed and 0.25 (GeV/c)^2 – dot-dashed lines. Each line splits into three almost overlapping lines corresponding, for each value of μ_2^2, to three different values of $\mu_1^2 =$ (up-down) 0.1, 0.15 and 0.2 (GeV/c)^2.

In Fig. 4.3 we show our predictions for $A_{LL}^{\cos\phi_h}(P_{hT})$ as measurable by COMPASS, HERMES and JLab collaboration experiments on a proton target. The analogous results,

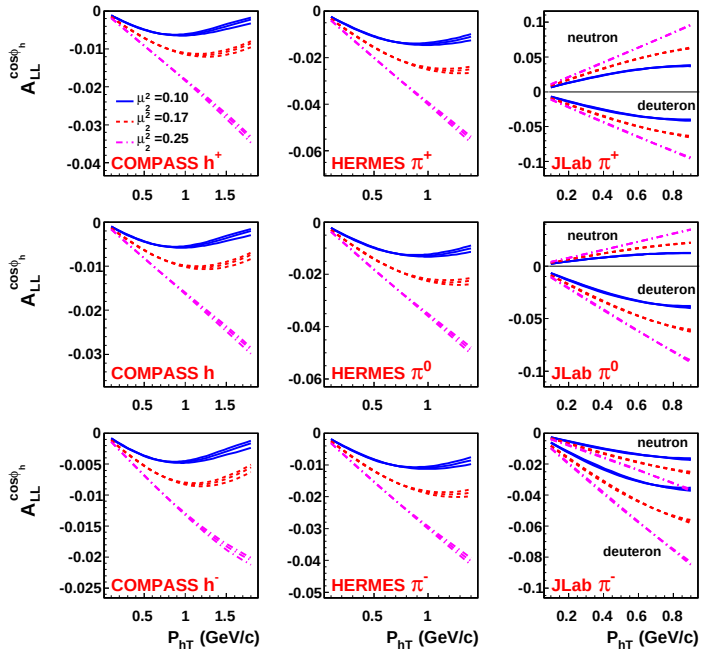

Figure 4.4: Predicted dependence of $A_{LL}^{\cos\phi_h}$ on P_{hT} for scattering off a deuteron (and neutron for JLab) target with different choices of μ_2^2: 0.1 (GeV/c)^2 – continuous, 0.17 (GeV/c)^2 – dashed and 0.25 (GeV/c)^2 – dot-dashed lines. Each line splits into three almost overlapping lines corresponding, for each value of μ_2^2, to three different values of $\mu_1^2 =$ (up-down) 0.1, 0.15 and 0.2 (GeV/c)^2.

for scattering off a deuteron target (and a neutron target as well, for JLab) are shown in Fig. 4.4. Again, we present the results for three different choices of $\mu_2^2 = 0.1$, 0.17 and 0.25 (GeV/c)^2, which turn out to be well different from each other. Instead, when varying the values of μ_1^2 our results hardly change: each line, obtained at a fixed μ_2^2 value, simply splits in three almost overlapping lines (corresponding, from up down, to $\mu_1^2 = 0.1$, 0.15 and 0.2 (GeV/c)^2). This is not surprising, as, when adopting the expression (3.7), there remains little dependence on μ_1^2 in Eq. (4.27). Our computations show instead a clear strong dependence on μ_2^2.

It is interesting also to compute the dependence of $A_{LL}^{\cos\phi_h}$ on each of the other single variables; for example, the x-dependence is computed as

$$A_{LL}^{\cos\phi_h}(x) = \frac{\int_{P^2_{hT,min}}^{P^2_{hT,max}} dP^2_{hT} \int dy \int dz \, (\Delta\sigma_{LL}^{\cos\phi_h} + \Delta\sigma_{LT}^{\cos\phi_h})}{\int_{P^2_{hT,min}}^{P^2_{hT,max}} dP^2_{hT} \int dy \int dz \, \sigma_0} \,, \tag{4.28}$$

while the y- and z-dependencies are calculated in a similar way. In Figs. 4.5, 4.6 and 4.7 we present the x-, y- and z-dependencies of $A_{LL}^{\cos\phi_h}$ integrated over P_{hT} with $P_{hT,min} =$ 0.5 GeV/c and μ_1^2 =0.15 (GeV/c)^2, μ_2^2 =0.25 (GeV/c)^2 for COMPASS ($P_{hT,max} = 2$ GeV/c), HERMES ($P_{hT,max} = 1.5$ GeV/c) and JLab ($P_{hT,max} = 1$ GeV/c) kinematics.

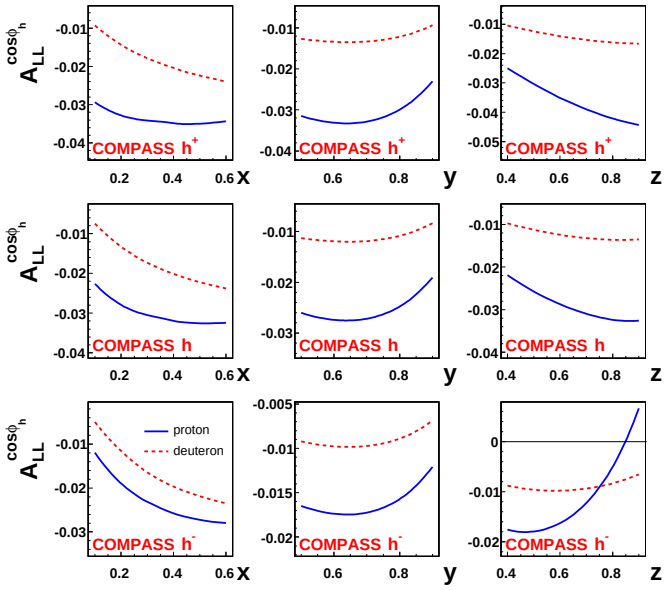

Figure 4.5: Predicted dependence of $A_{LL}^{\cos\phi_h}$ on x, y and z, for proton and deuteron targets, for COMPASS.

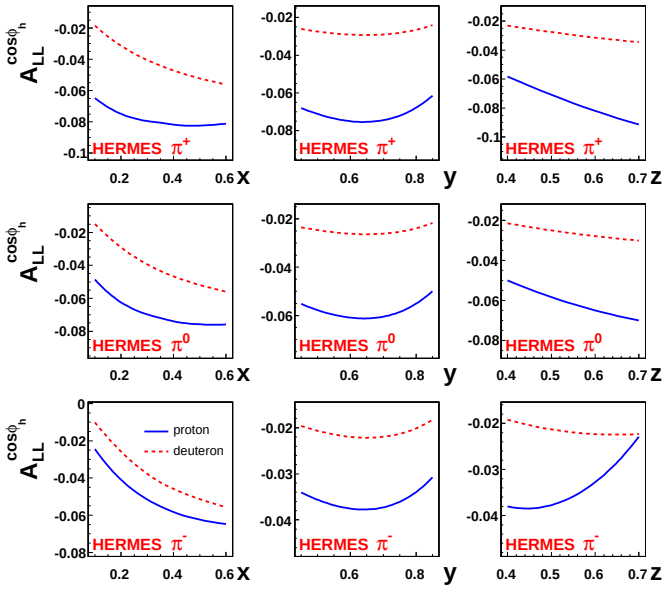

Figure 4.6: Predicted dependence of $A_{LL}^{\cos\phi_h}$ on x, y and z, for proton and deuteron targets, for HERMES.

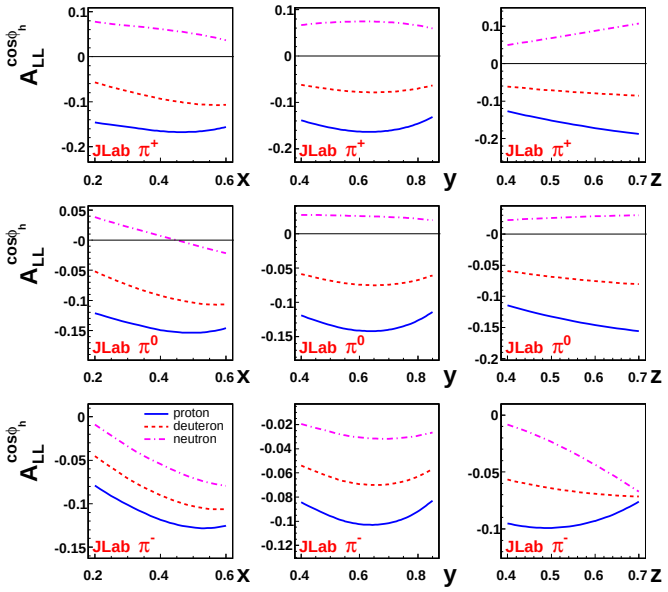

Figure 4.7: Predicted dependence of $A_{LL}^{\cos\phi_h}$ on x, y and z, for proton, neutron and deuteron targets, for JLab.

In order to find the kinematic range most preferable for the measurement of the asymmetry in a sense of available statistics and the significance of the magnitude of the effect the old *"golden rule"* of spin physics can be used. Significance of the figure of the merit of asymmetry can be reached by minimizing the relative statistical error of asymmetry:

$$\frac{\delta A_{LL}^{\cos\varphi}}{A_{LL}^{\cos\varphi}} \propto \frac{1}{\sqrt{N} A_{LL}^{\cos\varphi}} \propto \frac{1}{\sqrt{\sigma_0} A_{LL}^{\cos\varphi}} \tag{4.29}$$

which is equivalent to maximization of the quantity $\sigma_0 \cdot (A_{LL}^{\cos\varphi})^2$. Note, that in the last part of Eq. (4.29) the acceptance was assumed constant over the kinematic variables and number of events, N, is $\propto \sigma_0$. The correct expression that takes into account non-constant acceptance, a, contains $N \propto a \cdot \sigma_0$ and, in principle, a can be calculated using the complete simulation chain for the experiment or simply using measured number of events in different bins of kinematic variables.

As an example, assuming constant a, we performed this exercise for the COMPASS, HERMES and JLab kinematics dividing the accessible interval of each variable into five bins. The optimal region according to this criterion happens to be located at small values of x, y, z and $|\mathbf{P}_{hT}|$ where the asymmetry itself is very small. It has sense to apply this "golden rule" imposing an additional cut $A_{LL}^{\cos\varphi} > A_{min}$ with, for example $A_{min} = 3\delta A_{sys}$, where δA_{sys} is the systematic error of asymmetry measurement. In figure 4.8 the $A_{LL}^{\cos\varphi}(x,y)$ and $\sigma_0(x,y) \cdot (A_{LL}^{\cos\varphi}(x,y))^2$ distributions in $x : y$ phase-space are presented for COMPASS, HERMES and JLab experiments for positive hadron production at $0.4 < z < 0.65$ and $0.5 < |\mathbf{P}_{h,T}| < 0.75$ GeV/c. It can be clearly seen that

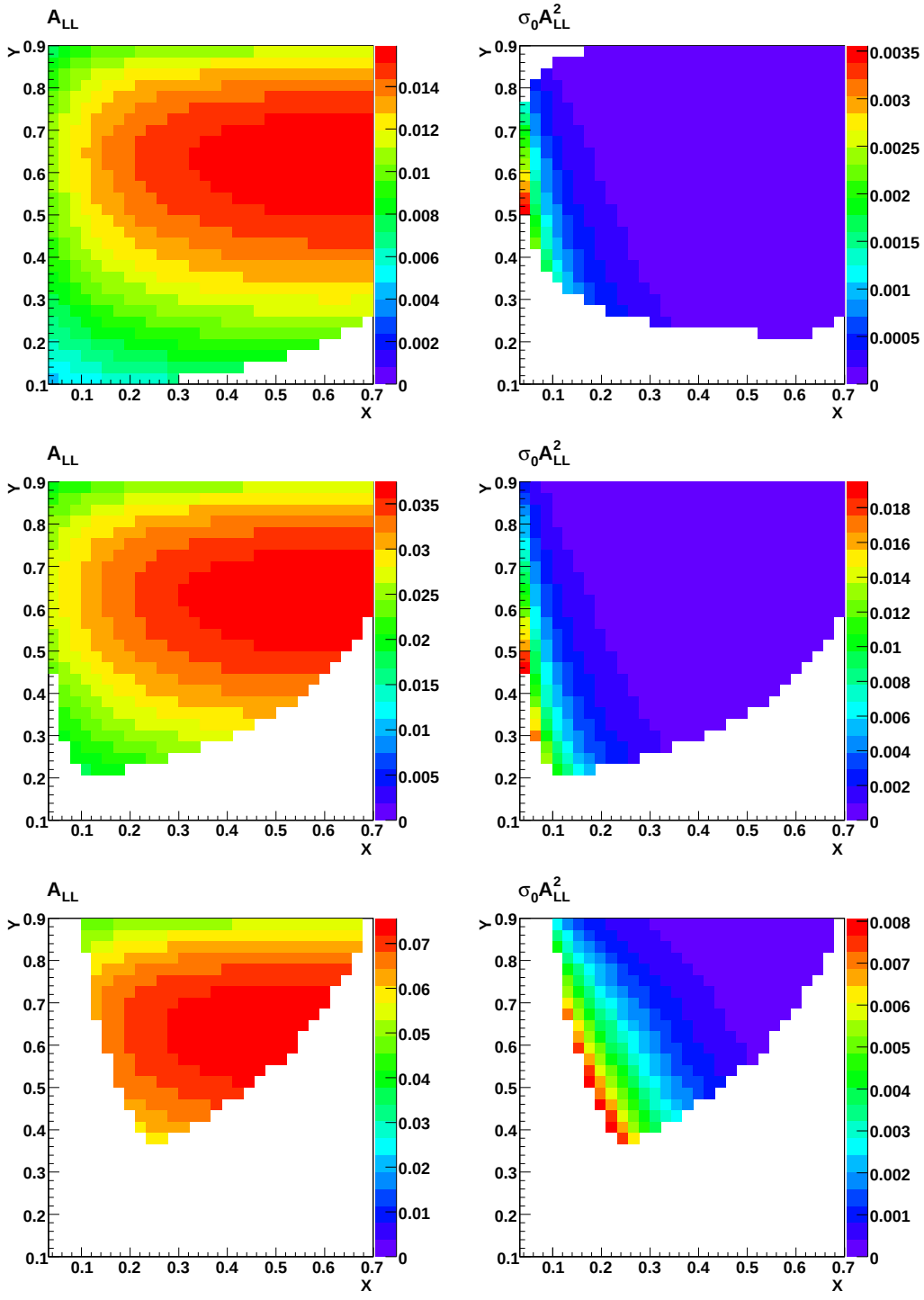

Figure 4.8: Left plots – $A_{LL}^{\cos\varphi}(x,y)$ at COMPASS (top), HERMES (middle) and JLab (bottom) with proton target, h^+ production, cuts: $0.4 < z < 0.65$ and $0.5 < |\mathbf{P}_{h,T}| < 0.75$ GeV/c; Right plots – corresponding $\sigma_0(x,y) \cdot (A_{LL}^{\cos\varphi}(x,y))^2$ in arbitrary units with, additional cut $A_{LL}^{\cos\varphi} > 0.01$ is imposed.

in COMPASS kinematics asymmetry reaches it maximum in the region of large x and y, while preferable for the measurement region is at small x, where effect is small $\simeq 1\%$. Situation is more optimistic for HERMES and much more optimistic for JLab.

4.3 Discussion and Conclusions

We have studied the P_{hT} dependence of A_{LL} and $A_{LL}^{\cos\phi_h}$, measurable in SIDIS processes by COMPASS, HERMES and JLab collaborations. For P_{hT} values up to ~ 1 GeV/c this dependence is entirely generated by intrinsic motion, both of partons inside the nucleons, and of hadrons in the parton fragmentation process Refs. [12, 74].

Within a simple factorized gaussian model for the k_T and $p_\perp$ dependence of the distribution and fragmentation functions, it turns out that $A_{LL}(P_{hT})$ is strongly sensitive to the relative value of $\langle k_T^2\rangle$ in unpolarized (μ_0^2) and helicity (μ_2^2) quark distributions: similar values, $\mu_0^2 \simeq \mu_2^2$, would reflect into an approximately constant $A_{LL}(P_{hT})$, while $\mu_2^2 < \mu_0^2$, would lead to a decreasing trend. Such different behaviors are expected in general, independently of the factorized gaussian assumption, as the shape of $A_{LL}(P_{hT})$ is essentially related to the ratio of the k_T dependence of g_1^q and f_1^q. Notice, however, that we have assumed the same constant values of $\langle k_T^2\rangle$ and $\langle p_\perp^2\rangle$ for all quark flavors; more involved choices might lead to different behaviors. A comparison of the quark intrinsic transverse momentum in unpolarized and longitudinally polarized protons might give new important information concerning the spin and orbital motion of quarks. For example, one expects that parton transverse motion contributes to the longitudinal component of the angular momentum, differently inside unpolarized and longitudinally polarized nucleons.

The P_{hT} dependence of $A_{LL}^{\cos\phi_h}$ is not only related to kinematical non-collinear contributions, but also to a TMD and spin dependent g_{1T}^q function, which gives the number density of longitudinally polarized quarks inside a transversely polarized nucleon. This function induces a $\cos\phi_h$ dependence, but it is unknown; we adopted a much debated relationship, together with the twist-two part the Wandzura-Wilczek sum rule (and the usual Gaussian factorization), in order to link the x-dependent part of g_{1T}^q to the integrated helicity distributions. Within such an approach, it turns out that also $A_{LL}^{\cos\phi_h}(P_{hT})$ has a strong dependence on μ_2^2 alone, thus giving further information on the average transverse motion of quarks inside a longitudinally polarized proton.

We conclude by noticing, as it was done in Ref. [18], that the exact k_T dependence of the distribution functions $f_1^q(x,k_T^2)$, $g_{1L}^q(x,k_T^2)$ and $g_{1T}^q(x,k_T^2)$ is crucial when considering the general positivity bounds of Ref. [17], which involve in one inequality the three previous functions and the Sivers function. The k_T dependence might play an essential role in fulfilling the inequality, and a check of its validity is a fundamental test for the self consistency of the LO QCD description of SIDIS processes.

Chapter 5

The COMPASS experiment

5.1 Introduction

COMPASS (COmmon Muon and Proton Apparatus for Structure and Spectroscopy) is a high-energy physics experiment at the Super Proton Synchrotron (SPS) at CERN in Geneva, Switzerland. Experimental setup is located in SPS North area on the M2 beam line (see Fig. 5.1). The purpose of this experiment is the study of hadron structure and hadron spectroscopy with high intensity muon and hadron beams. Shortly the history of COMPASS experiment can be presented in the following chronological sequence:

- March 1996: The Hadron-Muon Collaboration (HMC) and the CHarm Experiment with Omni purpose Setup (CHEOPS) experimental groups submitted a joint COMPASS proposal.
- February 1997: The experiment was approved conditionally by CERN.
- September 1998: The final Memorandum of Understanding was signed.
- 1999 - 2000: Installation of the experimental setup.
- 2001: Technical run, and commissioning of the setup.
- 2002: COMPASS started data taking.
- 2005: One year of shutdown.
- 2006 - till now: Data taking restarted.

Apart from a two-week pilot run in 2004 with $190\,\mathrm{GeV}/c$ pion beam used for the measurement of the pion polarizability via the Primakoff reaction,the experiment was focused on the investigation of the spin structure of the nucleon using a $160\,\mathrm{GeV}/c$ μ^+ beam and a polarized deuteron target. In the longitudinal target spin mode, the main goal of the experiment is the measurement of $\Delta G/G$ Ref. [76], the polarization of the gluons in a longitudinally polarized nucleon, in the same time very precise A_1^d data was collected Refs. [77, 78], and the polarized valence quark distribution from semi-inclusive DIS was studied Ref. [79].

Approximately 20% of the running time in 2002-2004 data taking period COMPASS was running with the transversely polarized target, and correspondingly transverse spin effects were measured. Our work is dedicated to this last point, namely to the results obtained in the extraction of transverse spin dependent azimuthal asymmetries from COMPASS 2002-2004 data.

With the muon beam COMPASS investigates also spin structure functions, flavor separation, vector meson production, and polarized Λ physics.

Hadron beam experiments are scheduled to start in 2007. Depending on the beam availability the present COMPASS physics programme will be completed around 2010. Future plans involving measurements of generalized parton distribution functions, detailed measurements of transversity and an extension of the spectroscopy studies are presently being discussed.

5.2 The experimental set-up

The COMPASS physics programme imposes specific requirements to the experimental setup. They are: large angle and momentum acceptance, including the request to track particles scattered at extremely small angles, precise kinematic reconstruction of the events together with efficient particle identification and good mass resolution. Operation at high luminosity imposes capabilities of high beam intensity and counting rates, high trigger rates and huge data flows.

The basic layout of the COMPASS spectrometer, as it was used in 2004, is shown in Fig. 5.2. Three parts can be distinguished. The first part includes the detectors upstream of the target, which measures the incoming beam particles. The second and the third part of the setup are located downstream of the target, and extend over a total length of $50\,\mathrm{m}$. These are the Large Angle Spectrometer (LAS) and the Small Angle Spectrometer (SAS), respectively. The LAS starts immediately after the target and serves for the detection of the particles that have been scattered at large polar angles of up to $180\,\mathrm{mrad}$. The SAS placed after the LAS does measurements for the particles at small angles ($\pm 30\,\mathrm{mrad}$) and higher energy (momenta of $5\,\mathrm{GeV}/c$ and higher). Each of the two spectrometers is built around an analyzing magnet, SM1 and SM2 respectively. The first SM1 magnet installed in LAS part has an field integral of $1.0\,\mathrm{Tm}$ and assist in the measurement of lower momentum particles, while the SM2 magnet of SAS deals with the particles with higher momenta and therefore has a higher integrated filed strength of $4.4\,\mathrm{Tm}$. Both spectrometers consist of various tracking detectors and are completed by a hadron calorimeters and by a muon filter stations for high energy muon identification. In addition LAS has A RICH detector for hadron identification and SAS includes an electromagnetic calorimeter. The flexibility required by the broad spectrum of the COMPASS physics programme has been reached by mounting a large set of huge setup elements on rails, allowing them to be positioned at variable distances from the experimental target: the RICH, the first hadron calorimeter, the first muon filter, the second analyzing magnet and the trackers fixed to it can move longitudinally on rails. In the following sections we will describe in more details the COMPASS setup as it was in 2002-2004 years, complete information about the spectrometer (including all upgrades done after 2004 year) can be found in Ref. [80].

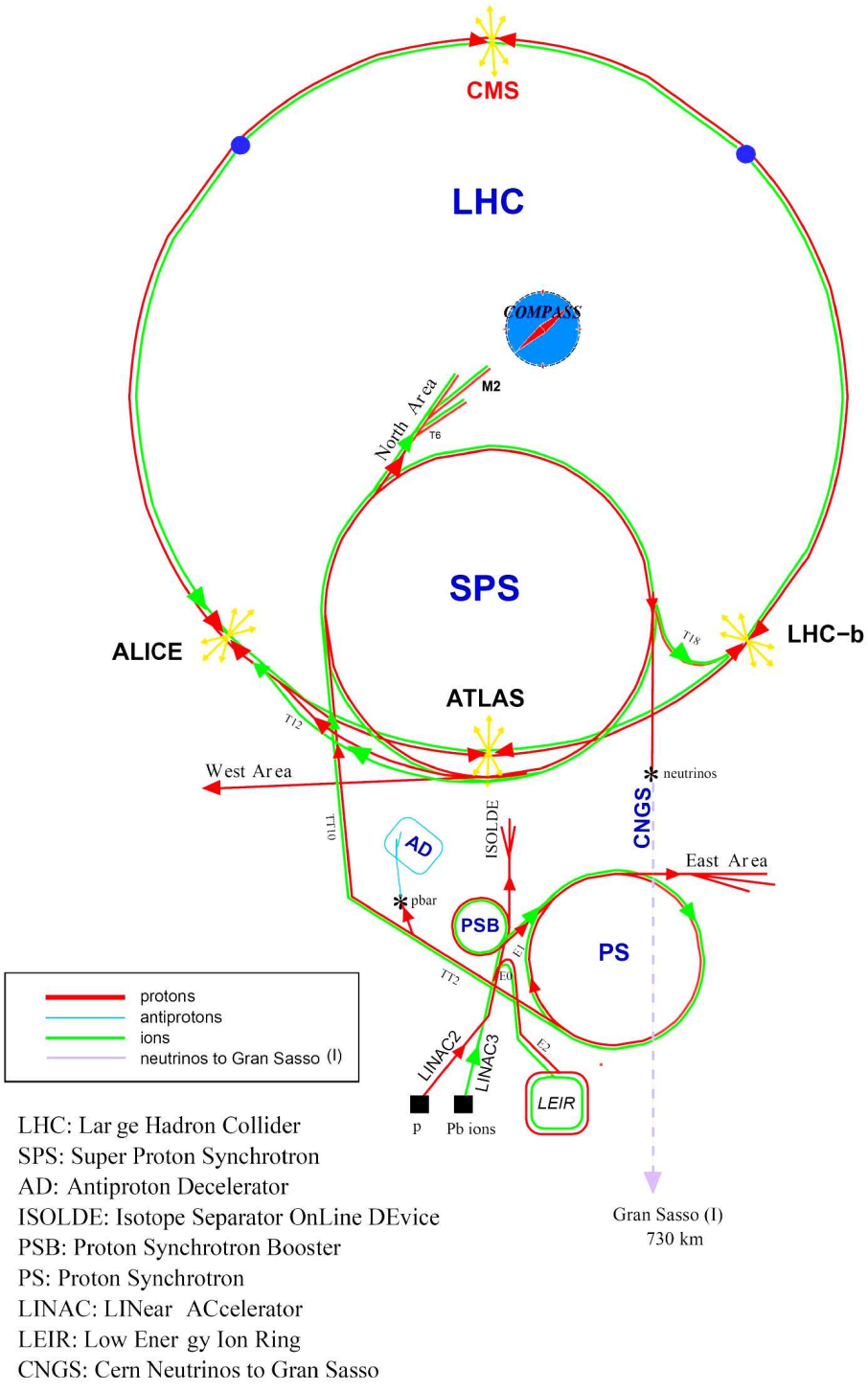

Figure 5.1: CERN accelerators and the COMPASS (NA58) experiment in the SPS North area (M2 beam-line)

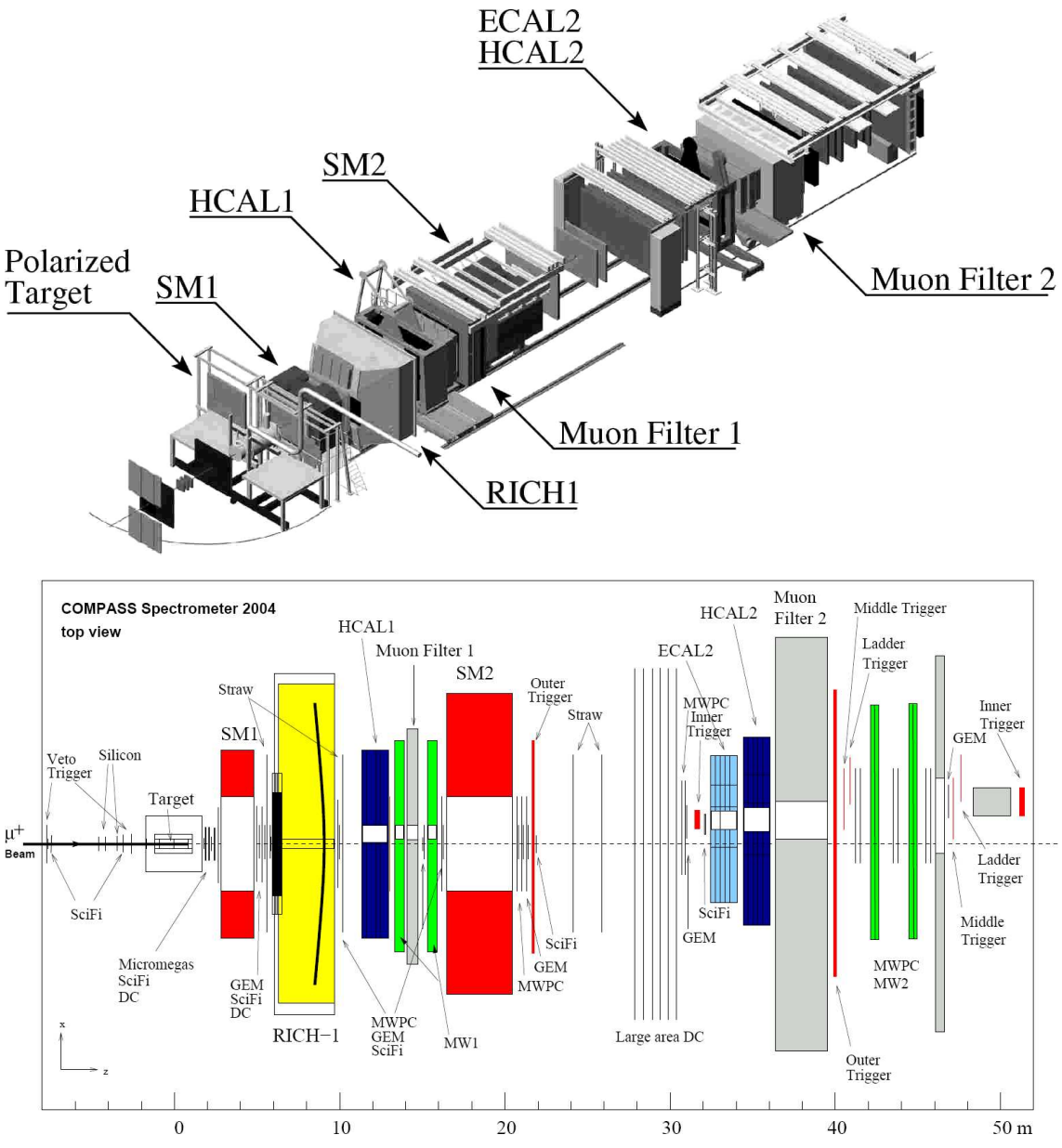

Figure 5.2: Compass 2004 muon setup (top) artistic view, (bottom) top view (for detector names, see corresponding sections).

5.3 The muon beam

The CERN SPS beam line M2 can be tuned for either high-intensity positive muon beams up to $190\,\mathrm{GeV}/c$ or high-intensity hadron (mainly proton or pion, positive or negative) beams up to $280\,\mathrm{GeV}/c$. Negative muon beams are also available, although with lower intensities. On request a low-energy, low-intensity tertiary electron beam can be used for test and calibration purposes. The changes between the various beam modes are fast and fully controlled from a computer terminal.

The muon beam is derived from a very intense primary proton beam, extracted from the CERN SPS at $400\,\mathrm{GeV}/c$ momentum, that impinges on a Beryllium target with $500\,\mathrm{mm}$ thickness. Thinner targets can be selected for lower flux, if required. The nominal proton flux available for COMPASS is $1.2 \cdot 10^{13}$ protons during $4.8\,\mathrm{s}$ long spills, within a $16.8\,\mathrm{s}$ long SPS cycle. A section of six acceptance quadrupoles and a set of three dipoles selects a high pion flux with the small contamination of kaons (about 3.6%), which then transported along a $600\,\mathrm{m}$ long Hadron Decay Section consisting of regularly spaced alternately focusing and defocusing (FODO) quadrupoles where the majority of pions and kaons decay into muon and neutrino. The section of hadron absorbers made from Beryllium modules is then installed in order to absorb the hadron component of the beam. Series of dipole magnets provide an upward deflection of $24\,\mathrm{mrad}$ for a good momentum separation. The dipole section is followed by a series of acceptance quadrupoles for the muons. The accepted muon beam is subsequently cleaned and momentum selected by two horizontal and three vertical magnetic collimators. The muons are transported to the surface level by a second $250\,\mathrm{m}$ long FODO channel. Finally the muons are bent back onto a horizontal axis by three, five meters long dipole magnets, surrounded by four hodoscopes and two scintillating fibres planes for momentum measurement (see next section), and focused onto the polarized target. The muon momentum can be chosen between 60 and $190\,\mathrm{GeV}/c$ with a momentum spread usually between $\pm 3\%$ and $\pm 5\%$ RMS. The nominal COMPASS setting is $160\,\mathrm{GeV}/c$. The maximum authorized muon flux is $2 \cdot 10^8$ muons per SPS cycle, the limitation being imposed by radio-protection guidelines. Due to the parity violating nature of the pion decay, the COMPASS muon beam is naturally polarized. The final muon polarization value of $(-80 \pm 4)\%$ in the 2004 run also includes a tiny correction due to the kaon component of the pion beam. The nominal parameters of the positive muon beam are listed in Table 5.1.

Table 5.1: Parameters and performance of the $160\,\mathrm{GeV}/c$ muon beam.

Beam parameters	**Measured**
Beam momentum (p_μ)/(p_π)	($160\,\mathrm{GeV}/c$)/($172\,\mathrm{GeV}/c$)
Proton flux on T6 per SPS cycle	$1.2 \cdot 10^{13}$
Focussed muon flux per SPS cycle	$2 \cdot 10^8$
Beam polarization	$(-80 \pm 4)\%$
Spot size at COMPASS target ($\sigma_x \times \sigma_y$)	$8 \times 8\,\mathrm{mm}^2$
Divergence at COMPASS target ($\sigma_x \times \sigma_y$)	$0.4 \times 0.8\,\mathrm{mrad}$
Muon halo within $15\,\mathrm{cm}$ from beam axis	16%
Halo in experiment ($3.2 \times 2.5\,\mathrm{m}^2$) at $\lvert x, y\rvert > 15\,\mathrm{cm}$	7%

5.4 Beam Momentum Station (BMS)

The first part of the setup includes the Beam Momentum Station (BMS), located along the beam line about $100\,\mathrm{m}$ upstream of the experimental hall. This beam spectrometer measures the momentum of the incoming muon on an event by event base; it includes an analyzing magnet and two telescopes of tracking stations formed by scintillator hodoscopes and scintillating fibre (SciFi) detectors.

Fig. 5.3 shows the detectors composing the BMS. Three consecutive dipole magnets (B6) compose the last large vertical bend ($30\,\mathrm{mrad}$) that brings the muon beam close to the horizontal direction before entering the experimental hall. The B6 dipoles are surrounded by a system of four quadrupoles and six beam detectors. Four of them (BM01–BM04)) are scintillator hodoscopes with horizontal scintillator strips. The readout is done using fast photomultiplier tubes (PMT). The time resolution achieved is $0.3\,\mathrm{ns}$. In order to cope with the high beam current and multiple-hit environment of the COMPASS experiment, two scintillating fibre hodoscopes (BM05, BM06) were added, one in between each of the existing hodoscope pairs. These two planes provide additional redundancy in the track matching between the beam momentum station and the detectors located in front of the target, thus increasing the overall beam detection efficiency. The design was chosen, such that the maximum rate per channel does not exceed $3 \cdot 10^6\,\mathrm{s}^{-1}$.

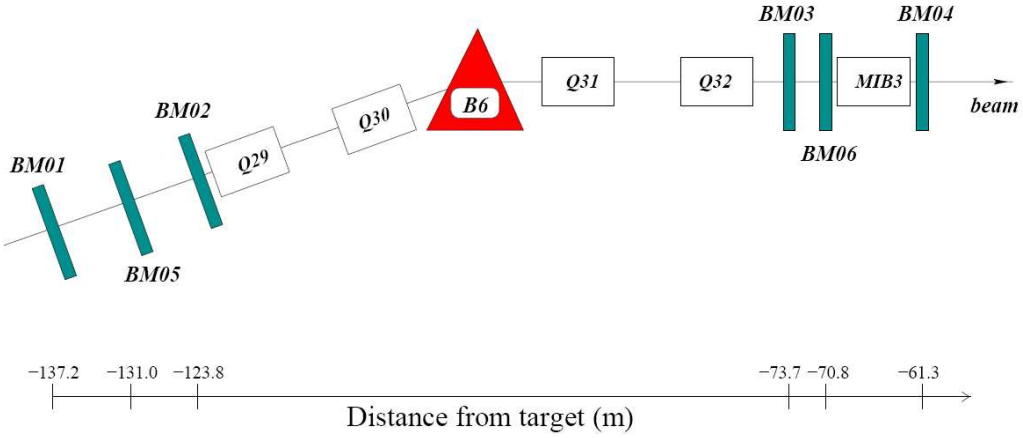

Figure 5.3: Layout of the Beam Momentum Station for the COMPASS muon beam.

5.5 Polarized target

As it will be shown in the next chapters our observable counting rate asymmetries depend linearly on beam and target polarizations, respectively, and on dilution factor f (the fraction of polarisable material inside the target). The use of a polarized target is thus mandatory and, and in addition, all the listed factors must be large as possible in order to optimize the statistical significance of the results. Furthermore, due to the limited muon flux, ($1.2 \cdot 10^7\,\mathrm{s}^{-1}$), a target thickness of about $60\,\mathrm{g/cm}^2$ is needed to reach the luminosity of a high precision experiment ($\approx 4 \cdot 10^{32}\,\mathrm{cm}^{-2}\mathrm{s}^{-1}$).

Deuterated lithium (^{6}LiD) has been chosen as isoscalar target. This material allows to reach a high degree of deuteron polarization ($> 40\%$) and has a very favorable composition Refs. [81, 82, 83]. Indeed, since ^{6}LiD can be considered to a good approximation as a spin-0 ^{4}He nucleus and a deuteron, the fraction of polarisable material f is of the order of 0.35, taking into account also the He content in the target region. The irradiated ammonia (NH_3), which is used as polarized proton target, has a less favorable composition ($f \approx 0.15$) but can be polarized to a higher degree ($> 80\%$).

COMPASS target (see Fig. 5.4) consist of two cylindrical cells with a radius of $1.5\,\mathrm{cm}$ and a length of $60\,\mathrm{cm}$, separated by $10\,\mathrm{cm}$. They are surrounded by longitudinal (along the beam direction) $2.5\,\mathrm{T}$ magnetic field maintained by super-conducting solenoid magnet. Up to 2004, the SMC magnet has been used, limiting the acceptance to $\pm$ 70 mrad for upstream and $\pm$ 170 mrad for downstream cell. The large aperture solenoid designed to match the full COMPASS spectrometer acceptance ($\pm$ 180 mrad) has been put in operation in 2006.

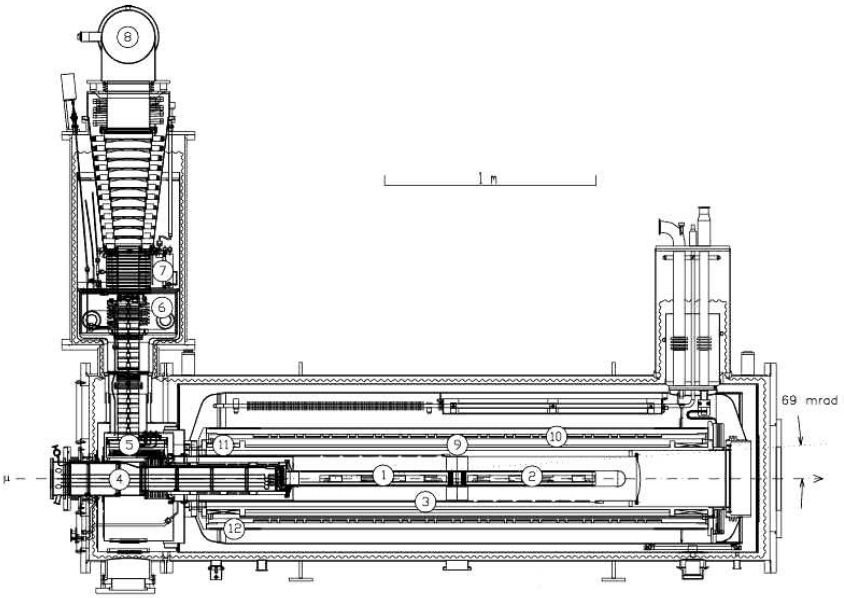

Figure 5.4: Side view of the COMPASS polarized target: (1) upstream target cell and (2) downstream target cell inside mixing chamber, (3) microwave cavity, (4) target holder, (5) still (^{3}He evaporator), (6) ^{4}He evaporator, (7) ^{4}He liquid/gas phase separator, (8) ^{3}He pumping port, (9) solenoid coil, (10) correction coils, (11) end compensation coil, (12) dipole coil. The muon beam enters from the left. The two halves of the microwave cavity are separated by a thin microwave stopper.

In order to polarize the target the dynamic nuclear polarization (DNP) method has been used. The high electron polarization transfer to the protons through microwave irradiation of a suitable frequency close to the spin resonance frequency of the electron. This procedure goes under the temperature of about $200\,\mathrm{mK}$ provided by ^{3}He/^{4}He dilution refrigerator filled with liquid helium. The microwave radiation is generated with two

extended interaction oscillator tubes (EIO). This process continues until the moment when all proton spins are pointing in the same direction as the electron spins. After the needed polarization has been achieved, the spin configuration can be ”frozen” by cooling the target to $50\,\mathrm{mK}$. A deuteron polarization $|P| > 40\%$ is reached within 24 hours in a $2.5\,\mathrm{T}$ field. The maximum polarization difference between the upstream and downstream cells $|P_{\mathrm{up}} - P_{\mathrm{down}}| > 100\%$ is reached in five days. The relaxation time for target polarization is quit long (more than 1000 hours). In order to cancel acceptance effects which could mask the physics asymmetries, the spin directions must be frequently (every 8 hours) inverted or by rotating the solenoid field, or by leaving external magnetic field constant and using irradiation of target cells by the microwaves with exchanged frequencies. During the polarization flip by using the solenoid field rotation, in order to keep the polarization, it must be maintained by a transverse field which is also needed for data taking in so-called “transverse mode”, i.e. with orthogonal directions of the beam and target polarizations. Transverse (with respect to the beam direction) magnetic field of $0.42\,\mathrm{T}$ is produced by a dipole coil.

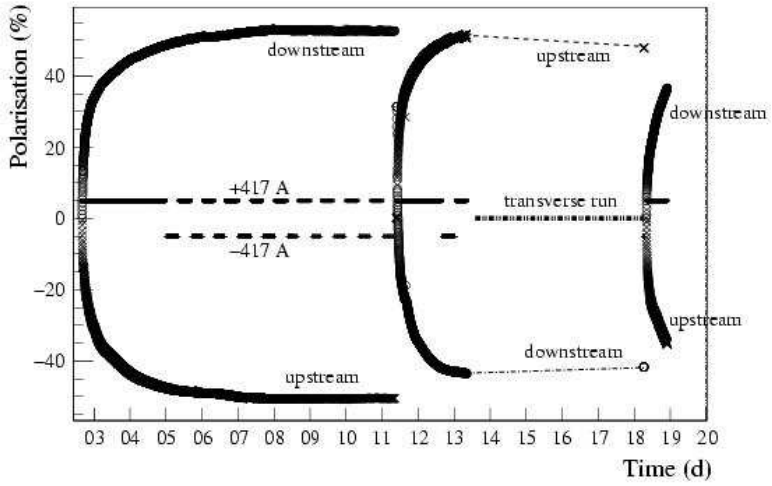

Figure 5.5: Typical average polarizations in the upstream and downstream target cells during 20 days of the 2004 run. After day 11, the polarizations in the target cells are reversed by changing the microwave frequencies. Data are taken in transverse mode from day 13 to day 18 and a new field reversal by microwaves is performed at the end of the period. The current of $\pm 417\,\mathrm{A}$ corresponds to an axial field of $2.5\,\mathrm{T}$.

For the transverse mode the target polarization is first brought up to a stable high level in longitudinal mode before the dipole field is switched on, then taking advantage of long relaxation time data taking can be started with transverse polarization. In this mode, the target material is kept in frozen spin mode below $90\,\mathrm{mK}$, and the polarization is reversed by exchanging the microwave frequencies of the two cells. Reversal process in transverse mode performed usually once per week and takes two days.

Each of the target cell contains five NMR coils used for the local monitoring of the polarization. The relaxation rate in frozen spin mode is $(0.4 - 1.0)\,\%/\mathrm{d}$ in the $0.42\,\mathrm{T}$ field and $(0.05 - 0.10)\,\%/\mathrm{d}$ in the $2.5\,\mathrm{T}$ field. In the Fig. 5.5 you can see the typical average

polarizations in the upstream and downstream target cells during 20 days of the 2004 run and Fig. 5.6 shows the target polarization modes during the longitudinal and transverse data taking periods.

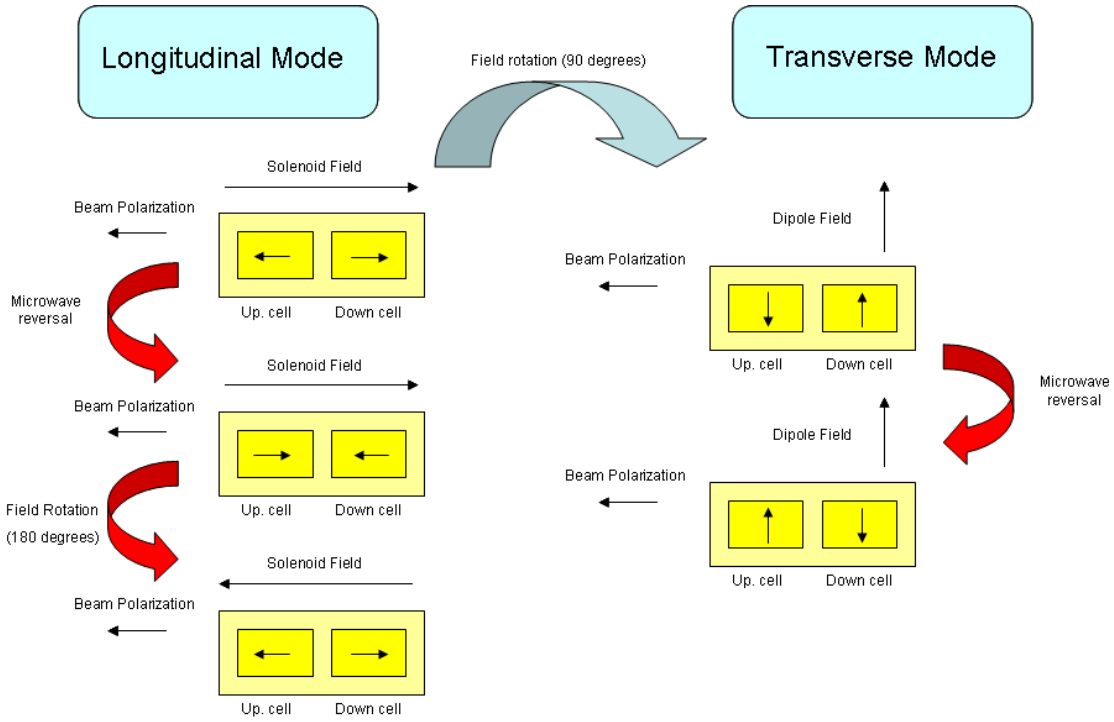

Figure 5.6: Target polarization modes

5.6 Tracking detectors

Set of different tracking detectors are mounted in COMPASS setup. Depending on the location along the beam axis and in transverse to beam direction plane, tracking detectors must fulfill different requirements on space-time resolution, high rate capability and active surface dimension. Working conditions of different detector planes and various requests are specified by the particle flux per unit transverse surface which varies by more than five orders of magnitude in the different regions of spectrometer. Detector stations mounted along the beam, or close to the target, must combine a high particle rate capability (up to a few MHz/channel) with an excellent spatial resolution ($100\,\mu\mathrm{m}$ and better). In order to minimize multiple scattering and secondary interactions the minimal amount of material along the beam axis is required. In close to beam region and particularly in the region upstream SM1 the strong requirements on the beam-time resolution are more strengthened because of the large number of low energy secondary particles coming from the target region. Far from the beam, the resolution constraint can be reduced, but larger areas need to be covered. Different varieties of large gaseous detectors based on wire amplification are used for these regions. The central regions of large area detectors are

deactivated in order to not exceed their rate capability. The near-beam and beam regions are covered by fast scintillating, gaseous and silicon tracking detectors, respectively, with active areas overlapping the dead zones of the larger detectors to guarantee efficient track reconstruction and good relative alignment.

Each tracking station consists of a set of detectors of the same type, located at approximately the same z-coordinate along the beam. In order to determine precisely the interaction point each station measure the trajectory of a charged particle in two or more transverse to beam direction projections. The group of channels within a station measuring the horizontal and vertical coordinates are labeled X- and Y-plane respectively, while the labels U- and V-plane describe all channels measuring projections rotated clockwise and anticlockwise, respectively, with respect to the x-axis. Note that the dipole magnets bend the charged particle trajectories in the horizontal plane.

In general tracking detectors used in COMPASS can be divided in three groups:

- Very Small Area Trackers (VSAT) - These category is presented by covering beam and near beam region eight scintillating fibres hodoscopes (SciFi) and three stations of double-sided silicon micro-strip detectors (SI).

  Two pairs of SciFis are mounted immediately upstream and downstream of the target, the other two pairs before and after SM2 magnet, while the three SIs are installed upstream of the target.

  These small in size detectors (lateral sizes vary from $4\,\mathrm{cm}$ to $12\,\mathrm{cm}$), combine high flux capabilities and excellent space or time resolutions.

- Small Area Trackers (SAT) - The region at a radial distance of $2.5\,\mathrm{cm}$ to $30-40\,\mathrm{cm}$ is covered by medium size detectors fulfilling requests on high space resolution and minimum material budget. These are three Micromegas (Micromesh Gaseous Structure) stations, and 11 GEM (Gas Electron Multiplier) stations.

  Each Micromegas station is composed of four planes and has an active area of $40 \times 40\,\mathrm{cm}^2$. All three stations are located between the target and the SM1 magnet.

  Each GEM station consists of two detectors with an active area of $31 \times 31\,\mathrm{cm}^2$, each measuring two coordinates. The 11 GEM stations cover the region from the downstream side of SM1 to the far end of the COMPASS setup.

  Both Micromegas and GEM detectors have central dead zones with $5\,\mathrm{cm}$ diameter.

- Large Area Trackers (LAT) - At large angles detectors with large active surface, covering experimental setup acceptance and with a good spatial resolution are required. This type of detectors are presented by Drift Chambers (DC), straw drift tubes, and Multi-Wire Proportional Chambers (MWPC). Trackers installed in SAS part detect the particles scattered at relatively small angles comparing with the detectors mounted in LAS.

  Three Drift Chambers has an active area of $1.8 \times 1.3\,\mathrm{m}^2$ with a central hole of $30\,\mathrm{cm}$ diameter, and are located one upstream of SM1 and two immediately downstream of it.

Each of five straw drift tube stations consists of two planes of size $323 \times 280\,\mathrm{cm}^2$ and one plane of size $325 \times 243\,\mathrm{cm}^2$. Both planes have a central dead zone of $20 \times 20\,\mathrm{cm}^2$. Straw drift tubes are mounted, two upstream and one downstream of the RICH counter and two in the outer region downstream of SM2.

Fourteen MWPC stations are located from downstream of the RICH counter to the far end of the setup. The active areas of MWPCs are of $1.8 \times 0.9 - 1.2\,\mathrm{m}^2$ and the diameters of central dead zones increase along the beam line from 16 to $22\,\mathrm{cm}$.

In addition six large area drift chambers of $5.0 \times 2.5\,\mathrm{m}^2$ active surface with a dead zone of $50\,\mathrm{cm}$ or $100\,\mathrm{cm}$ diameter in the center of the planes are installed in the outer region of spectrometer downstream of SM2.

In the following sections more detailed description of all the aforementioned detectors is presented. The complete information can be found in Ref. [80].

5.7 Very Small Area Trackers (VSAT)

In this section we describe the Very Small Area Trackers (VSAT), which cover the beam region up to a radial distance of 2.5 - $3\,\mathrm{cm}$. The very high rate of beam particles in this area (up to about $10^5\,\mathrm{s}^{-1}\mathrm{mm}^{-2}$ in the center of the muon beam) requires excellent time or position resolution of the corresponding detectors in order to identify hits belonging to the same track. Scintillating fibres (see Sec. 5.7.1) and silicon micro-strip detectors (see Sec. 5.7.2) fulfil this task.

5.7.1 Scintillating-Fibre Hodoscopes (SciFi)

The COMPASS spectrometer has eight scintillating-fibre (SciFi) hodoscope stations Refs. [84, 85], two pairs of them being placed immediately in front (no. 1, 2) and behind (no. 3, 4) of the target, and two more pairs upstream (no. 5, 6) and downstream (no. 7, 8) of the second spectrometer magnet (SM2).

The task of SciFis is to detect minimally deflected particles, mainly incoming and scattered beam particles and all other charged reaction products within the narrow region close to the center of the primary beam.

Each station consists of at least two planes measuring (X) and (Y) coordinates. Three stations (no. 3, 4, 6) have an additional projection (U), rotated by $\sim 45^\circ$ w.r.t. beam line.

The fibers have different $0.5\,\mathrm{mm}$, $0.75\,\mathrm{mm}$ and $1\,\mathrm{mm}$ diameter and are disposed like it is shown in Fig. 5.7 in order to avoid dead areas.

The number of fibres in one column is seven for stations 1–4, six for station 5, and four for stations 6–8, and is chosen to achieve the required time resolution and at the same time minimize the amount of material in the beam.

The size of the active surface of each of the (X) (Y) and (U) planes varies from $3.94 \times 3.94\,\mathrm{cm}^2$ to $12.3 \times 12.3\,\mathrm{cm}^2$ for different stations and planes. Parameters of the different stations are given in Table 5.2.

The hit rate can reach $3 \cdot 10^6\,\mathrm{s}^{-1}$ per fibre in the center of the muon beam, so the spatial correlation would be too ambiguous and hits can be assigned to the corresponding track

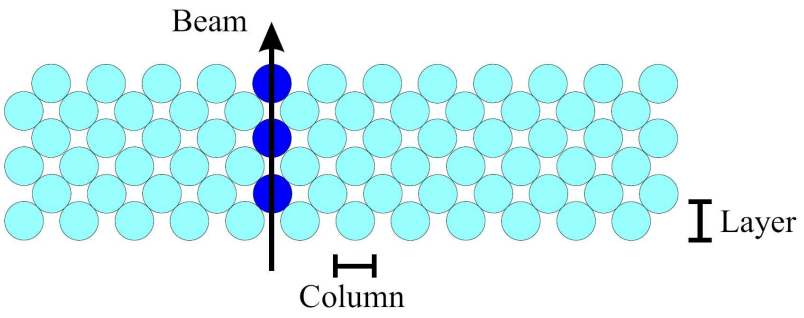

Figure 5.7: Fibre configuration of a SciFi plane (the actual number of fibre layers per plane is 8, 12 or 14, depending on the station).

only by time correlation. The obtained time resolution using one plane is nearly constant for all channels. R.m.s. values between $350\,\mathrm{ps}$ and $450\,\mathrm{ps}$ were obtained for the central regions of the various planes. Stations 1–4 have an r.m.s. spatial resolution of $130\,\mu\mathrm{m}$, station 5 of $170\,\mu\mathrm{m}$ and stations 6–8 of $210\,\mu\mathrm{m}$, with local variations which are consistent with fluctuations of the order of 10% of the fibre diameter.

No.	Proj.	# of layers	Size (cm^2)	Fibre ø (mm)	Pitch (mm)	# of ch.	Thickness (X_0)
1,2	X, Y	14	$3.9^2, 3.9^2$	0.5	0.41	$96, 96$	1.64%
3,4	X, Y, U	14	$5.3^2, 5.3^2, 5.3^2$	0.5	0.41	$128, 128, 128$	2.46%
5	X, Y	12	$8.4^2, 8.4^2$	0.75	0.52	$160, 160$	2.1%
6	X, Y, U	8	$10.0^2, 10.0^2, 12.3^2$	1.0	0.70	$143, 143, 176$	2.79%
7	X, Y	8	$10.0^2, 10.0^2$	1.0	0.70	$143, 143$	1.86%
8	X, Y	8	$12.3^2, 12.3^2$	1.0	0.70	$176, 176$	1.86%

Table 5.2: Parameters of SciFi stations in COMPASS. Column 3 specifies the number of fibre layers per projection, columns 4 and 7 give the size of the square active area and the number of channels for each projection, respectively. Column 8 lists the thickness of the respective station in units of radiation lengths (X_0).

5.7.2 Silicon Micro-Strip Detectors (SI)

In total COMPASS setup includes three silicon micro-strip detectors (SI) which are installed immediately after the target.

Each of three SI detectors is made of the $300\,\mu\mathrm{m}$ thick n-type wafer with an active area of $5\times7\,\mathrm{cm}^2$. The 1280 readout strips on the n-side ($54.6\,\mu\mathrm{m}$ pitch) are perpendicular to the 1024 readout strips on the p-side ($51.7\,\mu\mathrm{m}$ pitch), so that with one wafer two-dimensional position information can be obtained.

The principle of detector is the following: ionizing particles traversing the detector produce the electron-hole pairs along their tracks. Pairs are separated by external field, so instead of recombining immediately they will drift to electrodes and produce electrical pulse in the chain.

Due to the small width of anode strips and small of $15\,\mu\mathrm{m}$ distance between them SIs has a perfect spatial resolution ($8\,\mu\mathrm{m}$ for the p-side, and $11\,\mu\mathrm{m}$ for the n-side).

But as a result of the drift time of the electrons the average time resolution was found to be higher than for SciFis: $\langle\sigma_t\rangle = 2.5\,\mathrm{ns}$. Anyway the silicon micro-strip detectors which has better spatial resolution and SciFi stations which has better time resolution, perfectly supplement each other in the tracking of particles from beam region.

5.8 Small Area Trackers (SAT)

The intermediate region at a radial distance of $2.5\,\mathrm{cm}$ to 30 - $40\,\mathrm{cm}$ is covered by the Small Area Trackers (SAT), and is the domain of micro-pattern gas detectors. Here, two novel devices – Micromegas (see Sec. 5.8.1) and GEM detectors (see Sec. 5.8.2) – are employed successfully for the first time in a large-scale particle physics experiment. These detectors combine high rate capability (up to about $10^4\,\mathrm{s}^{-1}\mathrm{mm}^{-2}$) and good spatial resolution (better than $100\,\mu\mathrm{m}$) with low material budget over fairly large sizes.

5.8.1 Micromega (MICRO-MEsh GAseous Structure) Detectors

COMPASS is the first high energy experiment using Micromegas (Micro-mesh Gaseous Structure) detectors Refs. [86, 87, 88]. A total of twelve detectors combined in three stations of four planes each (X, Y, U, V), are mounted in the $1\,\mathrm{m}$ long region between the polarized target and the SM1 magnet. The principle of operation of Micromega detectors is shown in Fig. 5.8. Detector present by itself a gaseous tracker composed by three electrodes: the drift electrode, the micro-mesh and the micro-strips. The special feature of this detector is the presence of a metallic micro-mesh which separates the gaseous volume into two regions: a conversion region where the ionization takes place and the resulting primary electrons drift in a moderate field (here about $1\,\mathrm{kV/cm}$ over $3.2\,\mathrm{mm}$), and an amplification region where a higher field (here $50\,\mathrm{kV/cm}$ over $100\,\mu\mathrm{m}$) produces an avalanche which then reaches read-out strips in very short time (about $100\,\mathrm{ns}$).

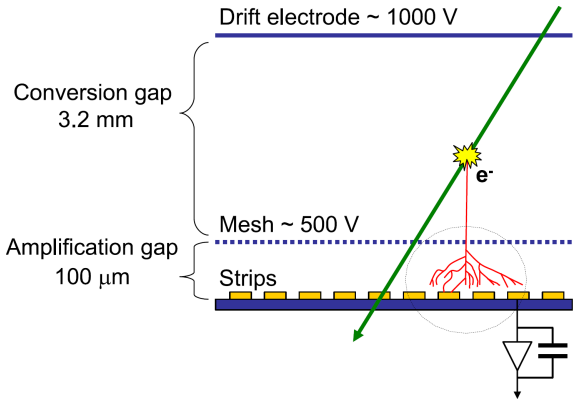

Figure 5.8: Principle of a Micromegas detector.

Due to the thinness of the amplification region avalanches can't enlarge much in transverse w.r.t. to the field direction and track can be determined with high precision. The obtained mean time resolution for Micromegas is $9.3\,\mathrm{ns}$ and the spatial resolution averaged over all Micromega detectors at nominal beam intensity is of $90\,\mu\mathrm{m}$ while the particle detection efficiency reaches 98%.

The gas mixture used in detectors is Ne/C_2H_6/CF_4 (80/10/10), which is optimized for a good time resolution. The detector has an active area of $40 \times 40\,\mathrm{cm}^2$ and a central dead zone of $5\,\mathrm{cm}$ in diameter.

5.8.2 GEM (Gas Electron Multiplier) Detectors

The COMPASS Gas Electron Multipliers (GEM) (Ref. [89]) are also gaseous tracking detectors and are similar in their construction to the Micromegas. The volume of the

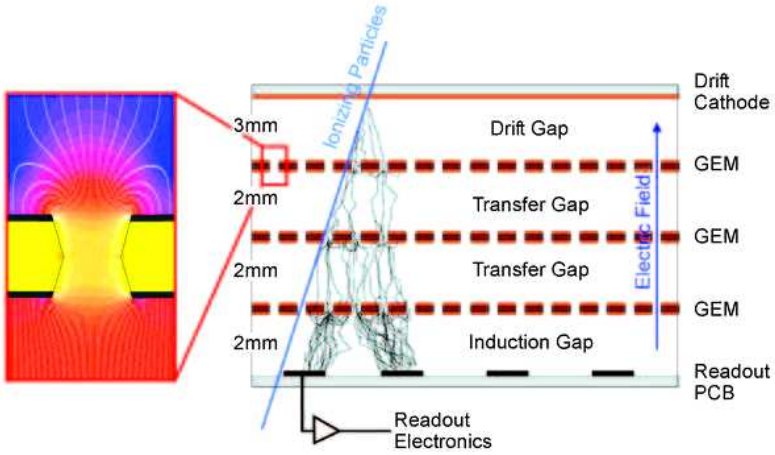

Figure 5.9: Schematic cross section of a triple GEM detector. The insert shows the electric field configuration for typical GEM voltages.

gas-filled (Ar/CO_2 (70/30) mixture) chamber between his two parallel plate electrodes is divided by up to three $50\,\mu\mathrm{m}$ thin polyimide foils with Cu cladding on both sides ($5\,\mu\mathrm{m}$). Foils has about $10^4/\mathrm{cm}^2$ micro-holes (with the diameter of $70\,\mu\mathrm{m}$) which have been chemically etched using photolithographic techniques. The electrons induced in drift region by ionizing particles are then multiplied several times in strong electric field of several $100\,\mathrm{V}$ applied in the transfer regions. Suitable electric fields extract the electrons from the holes on the other side of the foil and guide them to the next amplification stage or to the readout anode, which is segmented in two sets of 768 strips with a pitch of $400\,\mu\mathrm{m}$ each, perpendicular to each other and separated by a thin insulating layer.

In the Fig. 5.9 the principle of operation of GEMs is shown, the insert depicts the electric field lines in the vicinity of a GEM hole for typical voltage settings.

The spatial and time resolution of GEM detectors are $70\,\mu\mathrm{m}$ and $12\,\mathrm{ns}$ respectively. The active area of GEMs is $31 \times 31\,\mathrm{cm}^2$. The central region with a diameter of $5\,\mathrm{cm}$ is deactivated during normal high-intensity physics runs by lowering the voltage in order to avoid too high occupancies on the central strips. GEM detectors are mounted back-to-back (rotated by $45°$), forming one GEM station. So the particle trajectories are measured

in four projections (XY and UV). Partial overlap with a large area tracker located at the same position along the beam guarantees complete track reconstruction and alignment. In total, 11 GEM detector stations, i.e. 22 detectors, are installed in COMPASS.

5.9 Large Area Trackers (LAT)

The reduced flux in the outermost regions is covered by the Large Area Trackers (LAT). In COMPASS detectors of this group are presented by: drift chambers (see Sec. 5.9.1, 5.9.4), straw tube chambers (see Sec. 5.9.2), and multiwire proportional counters (see Sec. 5.9.3).

5.9.1 Drift Chambers (DC)

Three identical Drift Chambers (DC) installed in COMPASS provide reliable tracking in the vicinity of the SM1 magnet. One DC is installed upstream, and two DCs downstream of the SM1 magnet. The chambers fulfil the severe criteria imposed by the experimental conditions in this region and by the required kinematics:

- large active area. All three DCs have an active area of $180 \times 127\,\mathrm{cm}^2$, fully covering the acceptance of the target magnet upstream as well as downstream of SM1. Detectors has a central dead zone of $30\,\mathrm{cm}$ diameter which can be activated for alignment purposes.
- good spatial resolution (better than $200\,\mu\mathrm{m}$).
- minimized material budget. The total material budget of each detector along the beam path, is 0.32% of a radiation length.
- capability to stand high incident rates ($300\,\mathrm{kHz}$/channel and higher) with minimal loss in local efficiency. At nominal COMPASS beam conditions efficiency od DCs is 95% or higher

Each DC consists of eight layers of wires aggregated in four pairs with four different inclinations vertical (X), horizontal (Y) and tilted by $20°$(U) and $-20°$(V) with respect to the vertical direction. Such a construction was chosen in order to minimize the number of fake tracks during the reconstruction.

Each layer of wires consists of 176 sensitive wires of $20\,\mu\mathrm{m}$ diameter, alternated with a total of 177 potential wires with $100\,\mu\mathrm{m}$ diameter, and is enclosed by two cathode foils of $25\,\mu\mathrm{m}$ thickness, coated with about $10\,\mu\mathrm{m}$ of graphite, defining a gas gap of $8\,\mathrm{mm}$ extent. Two consecutive layers of the same pair (inclination) are staggered by $3.5\,\mathrm{mm}$ (half a drift cell) in order to solve left-right ambiguities. During operation of the chamber the cathode foils, the sensitive wires and the potential wires are kept at around $-1700\,\mathrm{V}$,$0\,\mathrm{V}$ and $-1700\,\mathrm{V}$, respectively.

Drift cell boundaries (Fig. 5.10) are defined by the cathode foils, normal to the beam direction, and by two potential wires separated by $7\,\mathrm{mm}$.

The choice of a small drift cell size ($8 \times 7\,\mathrm{mm}^2$) depend on counting rate considerations. Smaller drift cells decrease the incident flux per cell and reduce the electron drift

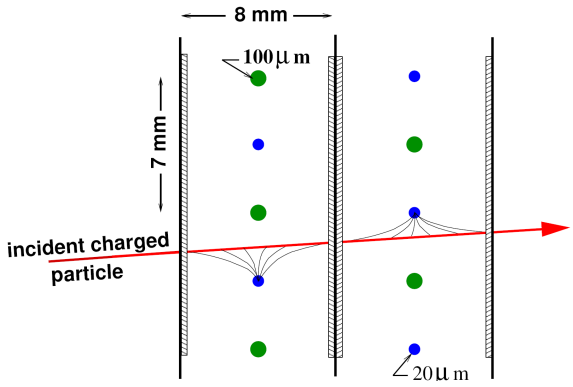

Figure 5.10: Drift cell geometry of the COMPASS drift chambers.

time. The reduced drift time has an additional advantage: it allows the use of a shorter time window and consequently minimizes the number of uncorrelated particles. As a gas mixture $Ar/C_2H_6/CF_4$ (45/45/10) was chosen, because of a good spatial resolution, good efficiency, large "high voltage" plateau and other characteristics.

5.9.2 Straw Tube Drift Chambers

Straw tube drift chambers (Ref. [90]) are installed downstream SM1 magnet and are used for the tracking of charged particles at high angles ($15 - 200\,\mathrm{mrad}$).

The straw tubes consist of two layers of thin plastic films. The inner layer which is a $40\,\mu\mathrm{m}$ thick graphite-coated kapton foil is glued onto the second layer - an aluminized kapton foil of $12\,\mu\mathrm{m}$ thickness. The gold-plated tungsten anodes with $30\,\mu\mathrm{m}$ diameter are held tout in the center of straw tubes. Detectors consist of two shifted by a half the diameter of a tube layers of straws.

Each detector has an active area of about $9\,\mathrm{m}^2$. The central part closest to the beam axis and correspondingly exposed to higher rates is made of 190 long and 64 short straws per layer, all with an outer diameter of $6.14\,\mathrm{mm}$, while the outer two parts each have 96 straws with $9.65\,\mathrm{mm}$ outer diameter. In total 12440 straw tubes are assembled into 15 detectors. Dead region with a size determined by the active area of the neighboring GEM detectors (around 30 cm) covers the immediate beam region. Detector has a rectangular hole without material of about $20 \times 10\,\mathrm{cm}^2$ for the beam. The straw tubes are operated at a high voltage of $1950\,\mathrm{V}$, and as a fast counting gas a mixture of $Ar/CO_2/CF_4$ (74/6/20) is used.

One station consist of three detectors forming X, Y and rotated by 10° with respect to the vertical one U projections. The detectors with vertical (X) and inclined straws (U) are of the same type (called type X), while the ones with horizontal straws have a slightly different geometry (type Y). The corresponding parameters of both types can be found in table 5.3.

For one straw detector (two layers), the average resolution is of $190\,\mu\mathrm{m}$ and the efficiency is higher than 95% with the inefficiencies being concentrated along the mechanical edges of the detector.

Table 5.3: Geometrical properties of X and Y types of straw detectors.

Type	Sensitive area $X \times Y$ (mm^2)	Length of straws (mm)	Number of straws with outer diameter of $6.14\,\mathrm{mm}$	$9.65\,\mathrm{mm}$	Number of readout channels	Overall dimensions $X \times Y$ (mm^2)
X	3232×2802	3202 1523	380 128	384	892	3570×4117
Y	3254×2427	3652 1752	320 128	256	704	4567×3160

5.9.3 Multi-Wire Proportional Chambers (MWPCs)

The multi-wire proportional chambers (MWPC) provide the large-angle scattered particles tracking. A total of 34 wire layers, corresponding to about 25000 detector channels, make part of both LAS and SAS spectrometers.

In COMPASS three different types of MWPC are used, named type-A, type-A* and type-B:

- Type-A stations consist of three anode wire layers X, U and V, where last two are rotated with respect to the first (vertical) one by $\pm 10.14^\circ$. Active area of the station is of $178 \times 120\,\mathrm{cm}^2$.
- Type-A* stations are similar to Type-A stations, with an additional horizontal wire layer (Y).
- Type-B stations have only two wire layers, one vertical and one rotated by 10.14° (U or V). Type-B stations have a smaller active area ($178 \times 80\,\mathrm{cm}^2$).

For all the types of the stations layers are characterized by the following values: wire length of about $1\,\mathrm{m}$, wire diameter of $20\,\mu\mathrm{m}$, wire pitch of $2\,\mathrm{mm}$ and an anode/cathode gap of $8\,\mathrm{mm}$.

Table 5.4: Characteristics of the COMPASS MWPC detectors.

	A-type	A*-type	B-type
# of chambers	7	1	6
Active area	$178 \times 120\,\mathrm{cm}^2$	$178 \times 120\,\mathrm{cm}^2$	$178 \times 80\,\mathrm{cm}^2$
# of layers/chamber	3	4	2
Planes	X, U, V	X, U, V, Y	$X, U/V$
Dead zone $\oslash$	$16 - 20\,\mathrm{mm}$	$16\,\mathrm{mm}$	$22\,\mathrm{mm}$
Wire pitch	$2\,\mathrm{mm}$	$2\,\mathrm{mm}$	$2\,\mathrm{mm}$
Anode/cathode gap	$8\,\mathrm{mm}$	$8\,\mathrm{mm}$	$8\,\mathrm{mm}$
# of wires/plane	752 (X, U, V), 512 (Y)	752 (X, U, V), 512 (Y)	752 (X, U, V), 512 (Y)

Chambers have a dead zone of $16 - 22\,\mathrm{mm}$ diameter, depending on the location of the chamber along the beam axis. The characteristics of all the types of MWPCs used in COMPASS are presented in Table 5.4.

For track detection MWPCs use the principle of formation of avalanches when an ionizing particle pass through a counting gas (mixture of $Ar/CO_2/CF_4$ in proportions 74/6/20). The avalanches induce an electrical pulse in closest anode wires (operated at nominal high voltage of $4250\,\mathrm{V}$) which is than detected in two dimensions by read-out system.

The spatial resolution is around $700\,\mu\mathrm{m}$. The detector efficiency for charged particle detection is higher than 99%.

5.9.4 Large Area Drift Chambers (W45)

The SAS part of COMPASS setup contains six large area drift chambers (called W45). They serve as a trackers for large angle particles. The basic detector characteristics are summarized in Table 5.5.

Table 5.5: Basic characteristics of the COMPASS large area drift chambers.

	XY-type	XV-type	XU-type	YV-type	YU-type
# of chambers	2	1	1	1	1
Active area	$500 \times 250\,\mathrm{cm}^2$	$500 \times 250\,\mathrm{cm}^2$	$500 \times 250\,\mathrm{cm}^2$	$500 \times 250\,\mathrm{cm}^2$	$500 \times 250\,\mathrm{cm}^2$
# of layers/chamber	4	4	4	4	4
Planes	X, Y	X, V	X, U	Y, V	Y, U
Dead zone $\oslash$	$500\,\mathrm{mm}$	$1000\,\mathrm{mm}$	$1000\,\mathrm{mm}$	$1000\,\mathrm{mm}$	$1000\,\mathrm{mm}$
Anode wire pitch	$4\,\mathrm{cm}$	$4\,\mathrm{cm}$	$4\,\mathrm{cm}$	$4\,\mathrm{cm}$	$4\,\mathrm{cm}$
Anode/cathode gap	$10\,\mathrm{mm}$	$10\,\mathrm{mm}$	$10\,\mathrm{mm}$	$10\,\mathrm{mm}$	$10\,\mathrm{mm}$
# of wires/plane	260, 130	260, 288	260, 288	130, 288	130, 288

Chambers consists of 4 sensitive anode wire layers (diameter $20\,\mu\mathrm{m}$, pitch of $4\,\mathrm{cm}$), separated by layers of cathode wires (diameter $100\,\mu\mathrm{m}$, pitch of $2\,\mathrm{mm}$) inclined by 5° with respect to vertical direction for better field homogeneity. The anode/cathode gap is $10\,\mathrm{mm}$. The signal wires are separated with field wires of $200\,\mu\mathrm{m}$ diameter. The signal wires are operated at a high voltage of $1925\,\mathrm{V}$, the field wire potential is kept at $-800\,\mathrm{V}$. The active surface of each detector is of $5 \times 2.5\,\mathrm{m}^2$. The total number of readout channels is 2750.

All chambers have two planes, each plane consisting of two wire layers shifted with respect to each other by half of the wire pitch. Four of the chambers has XY configuration, the other two are of YV-type and YU-type, where V and U are rotated with respect to the X layer by ($+30^\circ$ and (-30° respectively.

Detectors has a dead region with a diameter of $0.5\,\mathrm{m}$ and of $1\,\mathrm{m}$ in the center of each layer of XY-type, and of XV, XU, YV and YU-type chambers, respectively.

A $Ar/CF_4/CO_2$ (85/10/5) gas mixture is used to increase the drift velocity, which is important for efficient track reconstruction. The average layer efficiency was measured to be 93%. A mean spatial resolution of $0.5\,\mathrm{mm}$ was achieved in the 2004 run.

5.10 Detectors for Particle Identification

Described in previous section detectors provide the tracking information which is used for the determination of the momentum of particles. In order to distinguish particles of different types additional information on their energy or velocity is required. A range of different detectors serving for particle identification are mounted in both LAS and SAS parts of COMPASS setup:

- A RICH counter located in the large angle spectrometer (see Sec. 5.11) determines the velocity of the charged particles and separates them into pions, kaons and protons, in the momentum range from few GeV/c up to $43\,\mathrm{GeV}/c$.
- Calorimetry measurements are provided by two hadron calorimeters (HCAL1 (LAS) see Sec. 5.12.1 and HCAL2 (SAS), see Sec. 5.12.2) and electromagnetic calorimeter (ECAL2 (SAS), see Sec. 5.12.3). Hadron calorimeters measure the energy of hadrons and are used in triggering as well.
- Muon identification is done by applying the method of blocking all other charged particles but muons after the momentum measurement. In both LAS and SAS parts, for this purpose to muon wall systems are installed (MW1 and MW2, see Sec. 5.13) both consisting of medium resolution tracking detectors combined with a hadron absorber.

5.11 The RICH Detector

Cherenkov radiation is the process observed when a charged particle passes through the insulator at a speed greater than the speed of light in that medium and emits photons at the angle determined by the following expression:

$$\cos\theta_C = 1/(\beta \cdot n) \tag{5.1}$$

where $\beta = v/c$ and n is refractive index. With known momentum of the particle and refractive index of material by measuring the angle θ_C one can obtain the velocity of the particle and consequently the mass.

The COMPASS RICH Ref. [91] is a large-size Ring Imaging Cherenkov detector which performs hadron identification in the momentum range from $5\,\mathrm{GeV}/c$ to $43\,\mathrm{GeV}/c$. The threshold energy for the Cherenkov light emission is $2.5\ GeV$ for pions, $8.9\ GeV$ for kaons and $17\ GeV$ for protons. Operation in this range imposes the use of C_4F_{10} as a radiator gas, thanks to its low chromaticity, in spite of its high refractive index ($n - 1 = 0.0015$ for $7\,\mathrm{eV}$ photons). The overall length of the radiator vessel (see Fig. 5.11) is required to be of about $3\,\mathrm{m}$ in order to provide sufficient number of Cherenkov photons for this type of radiative gas.

Detector has a large dimensions ($5.3\,\mathrm{m} \times 6.6\,\mathrm{m} \times 3.3\,\mathrm{m}$, see Fig. 5.11) so the whole angular acceptance of the COMPASS LAS is covered by the active surface ($\pm 250\,\mathrm{mrad}$ in the horizontal plane and $\pm 180\,\mathrm{mrad}$ in the vertical plane).

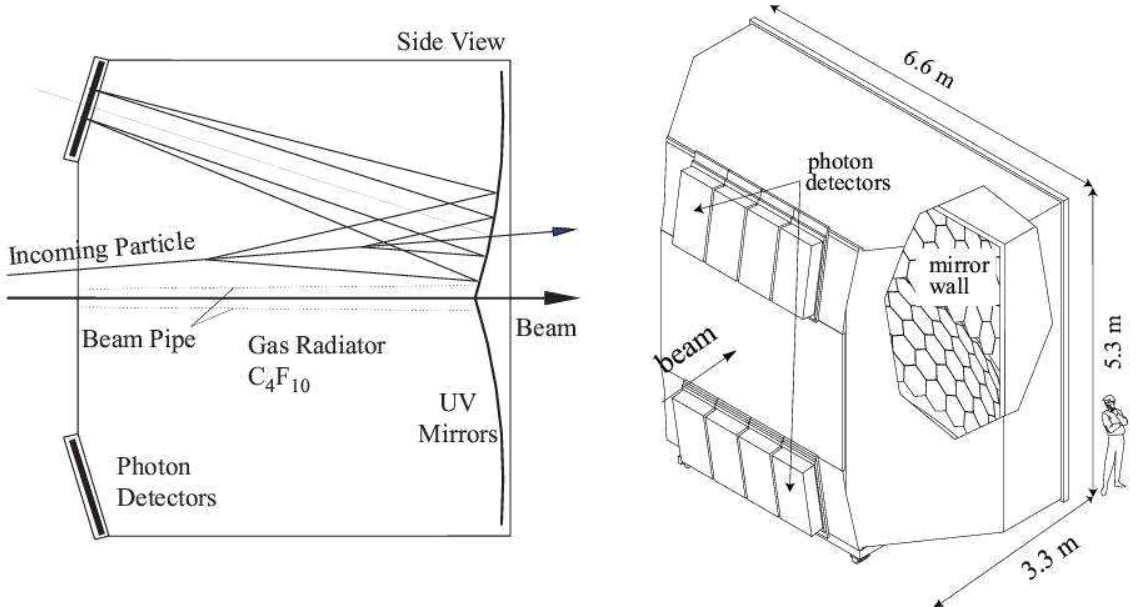

Figure 5.11: COMPASS RICH: principle and artistic view.

Cherenkov photons emitted in the gas at specific angles corresponding to particle type are reflected by two spherical mirror surfaces of total area larger than $21\,\mathrm{m}^2$ and a radius of curvature of $6600\,\mathrm{mm}$. These mirror surfaces has a mosaic structure composed of 116 spherical mirror units: 68 of them are regular hexagons with a side length of $261\,\mathrm{mm}$, the other 48 are pentagons with six different sizes. Such construction was designed to reflect and focus the Cherenkov ring images on photon detectors that are placed far from the beam line and outside the LAS spectrometer acceptance.

There are in total eight photon detectors presented by large-size MWPCs ($576 \times 1152\,\mathrm{mm}^2$) with CsI photocathodes for photon detecting. The RICH geometry results in a photon detector surface of $5.6\,\mathrm{m}^2$. The main parameters of the MWPCs are: $20\,\mu\mathrm{m}$ diameter wires, $4\,\mathrm{mm}$ wire pitch, $2\,\mathrm{mm}$ anode-cathode gap. Photocathode surface is segmented in $8 \times 8\,\mathrm{mm}^2$ pads. The eight photon detectors have 82944 pad channels in total. CsI photon converters shows a good quantum efficiency for wavelengths below $200\,\mathrm{nm}$ only; which automatically put constraint to operate in very ultraviolet (VUV) range of both the mirror system and the gas radiator. The gas radiator is separated from photon detectors by the quartz windows which impose the lower limit of the useful wavelength at $\approx 165\,\mathrm{nm}$. The radiator transparency in the light wavelength region between 160 and $200\,\mathrm{nm}$ is essential for RICH operation, as it influences directly the number of photons observed per ring. A dedicated radiator gas system establishes continuous gas circulation in a closed loop and ensures both optimum VUV transparency and constant relative pressure in the vessel.

Figure 5.12 shows an example of a RICH event. Radiuses of the formed rings are related with velocity of the original charged particle via expression:

$$r = (R_{mirror}/2)\arccos(1/\beta n) \tag{5.2}$$

where the R_{mirror} is the radius of curvature of the spherical mirror surfaces.

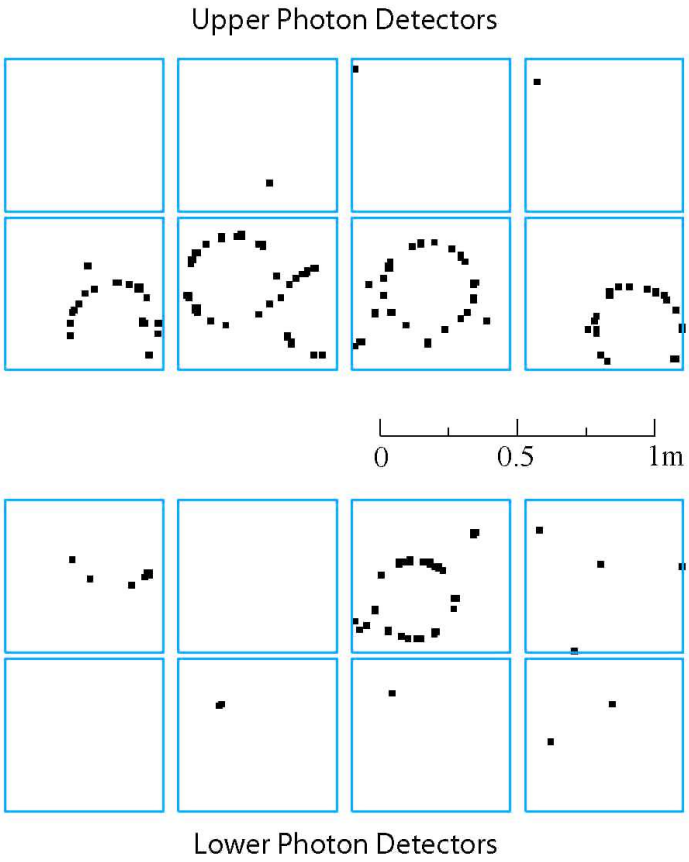

Figure 5.12: Typical event from the online event display of COMPASS RICH.

5.12 Calorimeters

Calorimetric detectors in COMPASS are presented by two hadron calorimeters and one electromagnetic calorimeter. The first hadron calorimeter (HCAL1, see Sec. 5.12.1) is installed in LAS before the muon filters, while electromagnetic calorimeter (ECAL, see Sec. 5.12.3) and the second hadron calorimeter (HCAL2, see Sec. 5.12.2) are installed in SAS part before the second muon filter system (see Fig. 5.2). The hadron calorimeters measure the energy of the hadrons that penetrate into the detector, and the electromagnetic calorimeters detects high energy gamma rays (or electrons). Both hadron calorimeters as well as electromagnetic calorimeters take part also in triggering (see Sec. 5.14).

5.12.1 LAS Hadron Calorimeter (HCAL1)

The first hadron calorimeter (HCAL1) is installed in LAS part before first muon wall (MW1). It consist of 480 calorimeter modules framed in a matrix of 28 (horizontal) $\times$

20 (vertical) with 12 modules removed from each corner and 8×4 modules from the center (for the beam and scattered muons). Each calorimeter module consist of 40 ($142 \times 146\,\mathrm{mm}^2$) alternated layers of iron ($20\,\mathrm{mm}$ thick) and scintillator ($5\,\mathrm{mm}$ thick) plates, equivalent to 4.8 nuclear interaction lengths. The outside dimensions of the HCAL1 are $4.2 \times 3\,\mathrm{m}^2$ with the useful surface $10.8\,\mathrm{m}^2$.The whole detector construction is mounted on the rails and can be moved across the beam axis.

Hadrons passing through iron layer interact with material inelastically and produce the avalanche of secondary particles. Avalanches in their turn generate the Cherenkov radiation in scintillator layers, which is then transported via light guide to photomultipliers and converted to electronic signals. Summarizing all this signals give the measure of the energy deposited by particle in the calorimeter. Since the HCAL1 have been used for trigger purposes small fractions of the signals are fed into the fast summation system.

The main characteristics of the calorimeter were determined using the negative hadron and lepton beams at the CERN X5 beam line with energies between 10 and $100\,\mathrm{GeV}$. Obtained energy resolution of HCAL1 as a function of the energy for pions can be parameterized by $\sigma(E)/E = (59.4 \pm 2.9)\,\%/\sqrt{E} \bigoplus (7.6 \pm 0.4)\,\%$, with the energy E in units of GeV. For the particles with momenta above $5\,\mathrm{GeV}/c$ the efficiency is almost constant and close to 100%. The spatial resolution of the detector is $\sigma_{\mathrm{x,y}} = 14 \pm 2\,\mathrm{mm}$.

5.12.2 SAS Hadron Calorimeter (HCAL2)

The second hadron calorimeter have been installed in the SAS between the electromagnetic calorimeter (ECAL) and second muon wall (MW2). Calorimeter consist of 216 modules assembled in a 22×10 matrix with a 2×2 hole left for the beam. HCAL2 like HCAL1 is mounted on the rails and can be moved across the beam axis.

There are two types of modules used in HCAL2 both of them being sandwich counters with $20 \times 20\,\mathrm{cm}^2$ transverse dimensions. The first type are the most used in detector, it consist of thirty-six $25\,\mathrm{mm}$ thick steel plates, alternated with $5\,\mathrm{mm}$ thick scintillator sheets which is equivalent to five nuclear interaction lengths for pions and seven for protons. Only the central 8×6 cells are filled with thicker modules consisting of forty layers. As well as in the case of HCAL1 small fractions of the signals are fed into the fast summation system for trigger purposes.

The characteristics of the HCAL2 modules were determined using X5 test beam (same as for HCAL1). HCAL2 has a good energy resolution characteristics in the energy range from 10 to $100\,\mathrm{GeV}$, where the energy resolution can be presented by: $\sigma(E)/E = (66/\sqrt{E} \bigoplus 5)\,\%$, with the energy E in units of GeV.

The efficiency of the detector for hadrons with energies above $10\,\mathrm{GeV}$ is close to 100%.

5.12.3 Electromagnetic Calorimeter (ECAL)

The electromagnetic calorimeter ECAL in located in the SAS part of the COMPASS spectrometer before HCAL2 detector. Detector was made of 2972 lead glass modules ($38 \times 38 \times 450\,\mathrm{mm}^3$) assembled in a matrix of 64×48 with a central hole of 10×10 for

beam passage. The amount of detector material distributed over it length is equivalent to 16 radiation lengths.

A high energy gamma ray (or electron) passing through detector initiates an electromagnetic shower inside the lead glass. The secondary electrons and positrons from a shower emit Cherenkov light with intensity proportional to deposited energy. Photomultipliers measure the intensity of the light emitted at that counter.

The matrix of modules is installed inside a frame, which can be moved vertically and horizontally by $2.5\,\mathrm{m}$ for calibration and maintenance. The whole ECAL2 platform can be moved on rails along beam axis.

The calibration of the detector was done in COMPASS experiment for each data taking period using $40\,\mathrm{GeV}$ electron beam. The energy resolution obtained for ECAL is characterized by the relation: $\sigma(E)/E = 5.5\%/\sqrt{E} \bigoplus 1.5\%$, and for space resolution: $\sigma(x) = 6\,\mathrm{mm}/\sqrt{E} \bigoplus 0.5\,\mathrm{mm}$ where the energy E is in units of GeV.

5.13 Muon Identification

Muons are known as highly penetrative particles, in contrast to hadrons. This important feature was used in two muon identification systems installed in COMPASS. Both system are made of hadron absorber mounted between two set of trackers. After the absorber hadrons (as well as electromagnetic radiation) are cleaned out and one can unambiguously distinguish muon tracks from hadronic background by checking coincidence in muon tracking detectors mounted before and after absorber.

The first muon identification system is installed in LAS, it consist of two Muon Wall (MW1) stations and Muon Filter ($60\,\mathrm{cm}$ thick iron absorber - MF1) between them. System track the muons scattered at large angles and it has a central hole for beam passage.

The second (located in SAS) muon identification system consist of $2.4\,\mathrm{m}$ thick concrete absorber (Muon Filter 2) followed by two Muon Wall stations (MW2) and three MWPC-B (see Sec. 5.9.3) stations.

5.13.1 Muon WALL 1 (MW1)

The first Muon Wall station (MW1) installed in LAS use as a basic elements gaseous wire detectors called Mini Drift Tube (MDT). The MDT detector based on plastic Iarocci tubes is working in proportional mode. This in a fact make the detector capable to work under the high-rate background conditions of the COMPASS experiment.

The schematic view of the MW1 system is shown in Fig. 5.13. The system as it was already mentioned consist of two stations separated by a $60\,\mathrm{cm}$ thick iron absorber (Muon Filter 1). Each station in its turn consist of four detectors with two planes (X and Y) of MDTs on both sides, so the two coordinates are measured.

The gas mixture used in the system is Ar/CO_2 (70/30). Detectors active surface is $400\,\mathrm{cm} \times 200\,\mathrm{cm}$, with the hole in the center matching the acceptance of SM2.

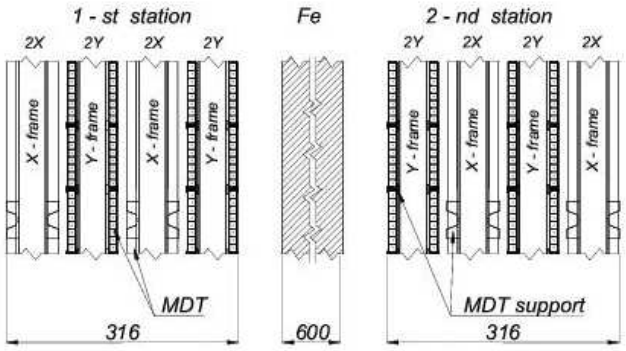

Figure 5.13: Schematic cross–sectional side view of MW1; all dimensions are given in millimetres. Vertically only part ($255\,\mathrm{mm}$) of the stations are shown.

5.13.2 Muon WALL 2 (MW2)

The second Muon Wall station (MW2) located in SAS immediately after the second Muon Filter ($2.4\,\mathrm{m}$ thick concrete absorber). MW2 is build of two identical stations of layers of drift tubes operating with Ar/CH_4 (75/25) gas mixture. Each of the two stations consists of 3 pairs of layers with an active area of $447 \times 202\,\mathrm{cm}^2$. The three double layers have vertical, horizontal and inclined (at -15° w.r.t. to the vertical) tubes, respectively. Each detector plane has a rectangular hole with a size of $1 \times 0.8\,\mathrm{m}^2$ around the beam. The hole is covered by the MWPC-B (see Sec. 5.9.3) stations, which partly overlap with the sensitive area of MW2. Minimally deflected muon tracks which pass through the beam hole in the first Muon Wall can be detected by MW2.

5.14 Trigger System (TS)

In the previous sections the brief description of COMPASS detector stations was done. During the data taking each station perform his functions: detect the particles and collect the information. Having high rate environment and huge number of channels per each detector on one hand, and restricted ability to buffer all data and expenses related with the disk-space on another, the necessity of selective data storing process become obvious. For this purpose the Trigger System (TS) is used. It must fulfill following requirements:

- It must be capable to select event candidates within high rate conditions.
- Decision time and trigger signal should be very fast (below $500\,\mathrm{ns}$), because of limited buffering time of the detectors. As an example buffering time of calorimeters is limited by $600\,\mathrm{ns}$.
- The trigger system must have short dead time.

and perform following tasks:

- Execute fast event candidate selection by checking the necessary requirements on the event to be accepted.
- If event candidate has been selected trigger must provide time window reference and send the signal to detectors readout systems and front-end electronics to process all the data in specified time gate.
- Otherwise if event candidate has not been accepted, trigger system must prevent storage of the data.

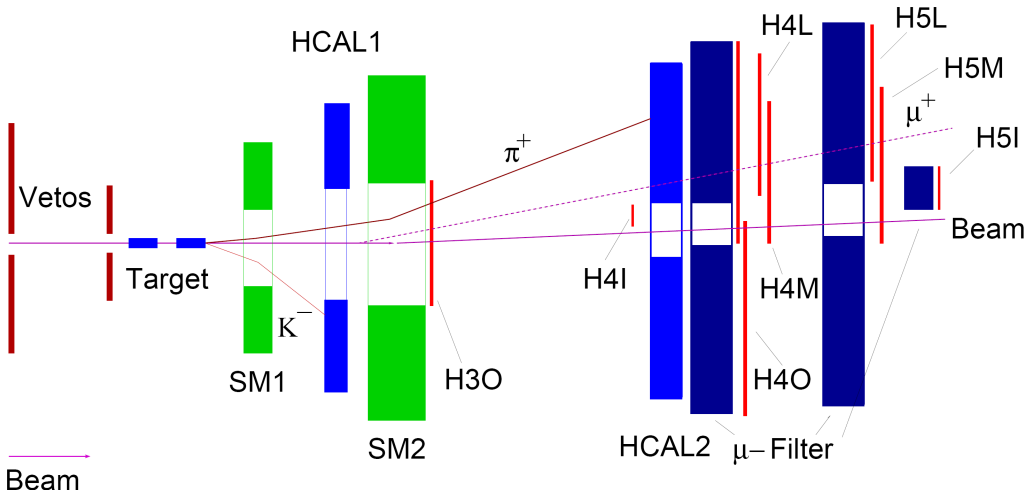

Figure 5.14: Location of the components relevant for the trigger (schematically). For the true scale refer to Fig. 5.2.

In COMPASS event triggering is done mainly by using scattered muon information provided by system of fast trigger hodoscopes (see Sec. 5.14.1). For some events information about energy deposits in calorimeters is also required. Additional veto detectors system (see Sec. 5.14.2) serves for rejection of events with halo muons.

COMPASS trigger hodoscope system consist of four subsystems differentiated by their position is setup and covered kinematical range: Inner Trigger (IT), Ladder Trigger (LT), Middle Trigger (MT) and Outer Trigger (OT). Each of subsystems consist of two hodoscope stations namely: H4I, H5I (Inner trigger), H4L, H5L (Ladder triger), H4M, H5M (Middle trigger) and H3O, H4O (Outer trigger). The location of constituent parts of TS in COMPASS setup is shown in Fig. 5.14.

Events identified by trigger system can be separated in two categories:

- Events with $Q^2 > 0.5\,(\mathrm{GeV}/c)^2$ (Deep Inelastic Scattering (DIS) events), mainly triggered by using the scattered muon information from Middle and Outer triggers (for details on MT and OT see Sec. 5.14.1). Each system (MT and OT) consist of two horizontal scintillator hodoscopes which determine the projection of the muon scattering angle θ in the non-bending plane. The provided information is

then checked for compatibility with the target position (vertical target pointing). The signals are fed into 32×32 coincidence matrices formed by read-out channels of hodoscopes which select only those hit combinations which correspond to muon tracks that point back to the target. In addition muon halo contribution suppressed by making use of veto system (see Sec. 5.14.2).

- Low Q^2 region (quasi-real photon emission events ($Q^2 \simeq 0$)) is characterized by small ($< 10\,\mathrm{mrad}$) muon scattering angles so that target pointing technic is no more applicable. Another requirement for these events is the high degree of polarization of exchange photon, so the reasonable cut on relative energy loss $y > 0.2$ can be applied. Events of this class are thus triggered by measuring energy loss of scattered muon (using the bending of the muon track in the magnetic fields of SM1 and SM2) which should be at least 20% (according to the cut applied on y). For this purpose double vertical scintillator hodoscope planes of Inner (IT), Ladder (LT) and Middle (MT) trigger systems were used (see Sec. 5.14.1). As for the DIS trigger, the signals are fed into 32×32 coincidence matrices formed by read-out channels of hodoscopes which select only those hit combinations which correspond to muon tracks that have suffered a minimum energy loss (see the scheme in Fig. 5.15).

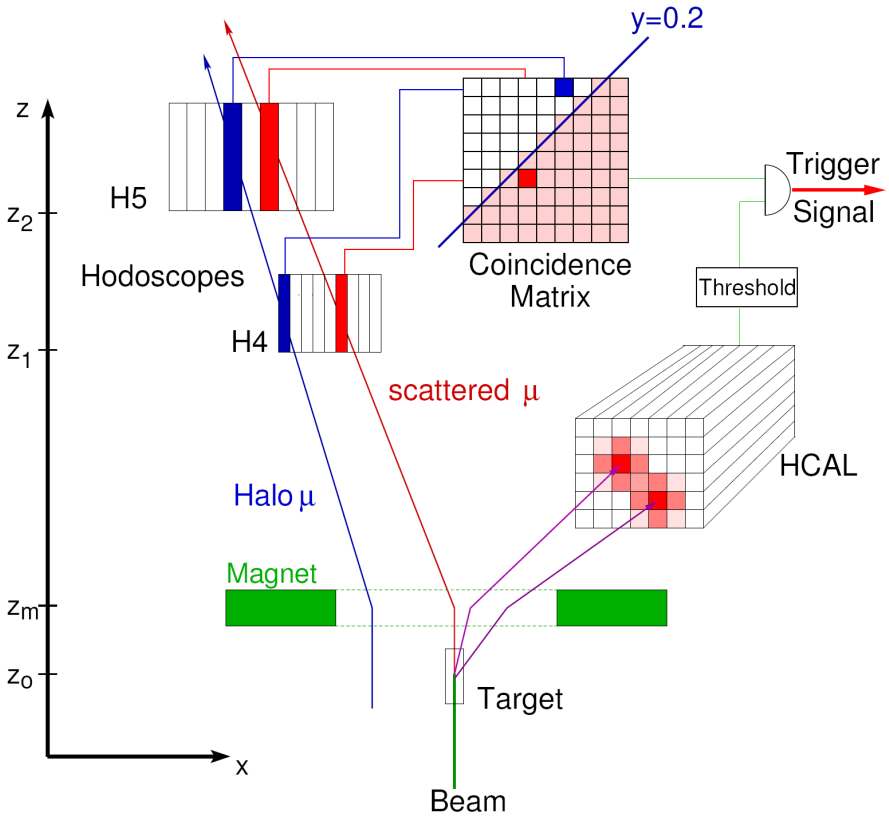

Figure 5.15: Concept of the trigger for quasi-real photo-production with high energy loss. The scattered muon leads to a coincidence in the activated area of the coincidence matrix while the halo muon fails to do so. In addition, a minimum hadron energy can be required in the calorimeter.

In order to suppress the contribution of background processes in the region of small angles (elastic scattering off target electrons, elastic and quasi-elastic radiative scattering off target nuclei and beam halo) the calorimeter trigger have been used as well. For the calorimetric triggering TS requires energy clusters in the hadronic calorimeter, to ensure that hadrons (hadron) are involved in the process which are absent in the background processes.

So summarizing: the quasi-real photon trigger consists of two parts, a trigger on the energy loss by measuring the deflection of the scattered muon in the two spectrometer magnets and a calorimetric trigger selecting hadron energy clusters above a threshold (see Fig. 5.15).

A detailed description of the trigger system can be found in Ref. [92].

5.14.1 Trigger Hodoscopes

The trigger system is subdivided into four subsystems consisting of two hodoscope stations each, the inner (H4I, H5I), the ladder (H4L, H5L) , the middle (H4M, H5M) and the outer system (H3O, H4O).

The inner (H4I, H5I) and the ladder (H4L, H5L) trigger systems determine the horizontal deflection of the scattered muon in the magnetic field of both SM1 and SM2 magnets, by checking the spatial coincidences between the vertical elements in the two hodoscope planes. In order to minimize the possible background effects in muon selection (such as hadrons, electrons...) $1.6\,\mathrm{m}$ Fe absorber is mounted directly in front of the second inner hodoscope. Detectors located between the two inner trigger hodoscopes have a hole that matches the size of these hodoscopes. The strip widths have been chosen according to the y region where the corresponding detector is designed to work. The inner system designed for the y range from 0.2 to 0.5 has a fine grained structure with the element widths of 6 and $12\,\mathrm{mm}$. The ladder system working in the y range between 0.5 and 0.9 uses 20 to $87\,\mathrm{mm}$ strips.

The middle (H4M, H5M) and the outer (H3O, H4O) trigger systems are used for the DIS events triggering, but middle system can be used for quasi-real photon events selection as well. The middle system uses horizontal planes (21.5 to $30\,\mathrm{mm}$ strips) to detect muons with scattering angles between 4 and $12\,\mathrm{mrad}$ (vertical target pointing). For the rough energy loss measurements it uses vertical planes (62 and $77\,\mathrm{mm}$ strips). The outer system designed vertical target pointing measurements by 70 and $150\,\mathrm{mm}$ wide elements. Detector construction and location allows to trigger the muons up to $Q^2 \approx 20\,(\mathrm{GeV}/c)^2$. The upper limit in Q^2 is fixed by the detector position and size of the gap in the SM2 magnet. The kinematic range in y and Q^2 covered by the different constituents of the trigger system (four hodoscope trigger subsystems and the standalone calorimeter trigger) is shown in Fig. 5.16.

The read out of hodoscopes make use of light-guides and photomultipliers. The output signals are fed into 32×32 coincidence matrices which select the events either with muon tracks pointing back to target (Inner and Ladder triggers), or events that fulfilled the energy loss requirements (Middle and Outer triggers).

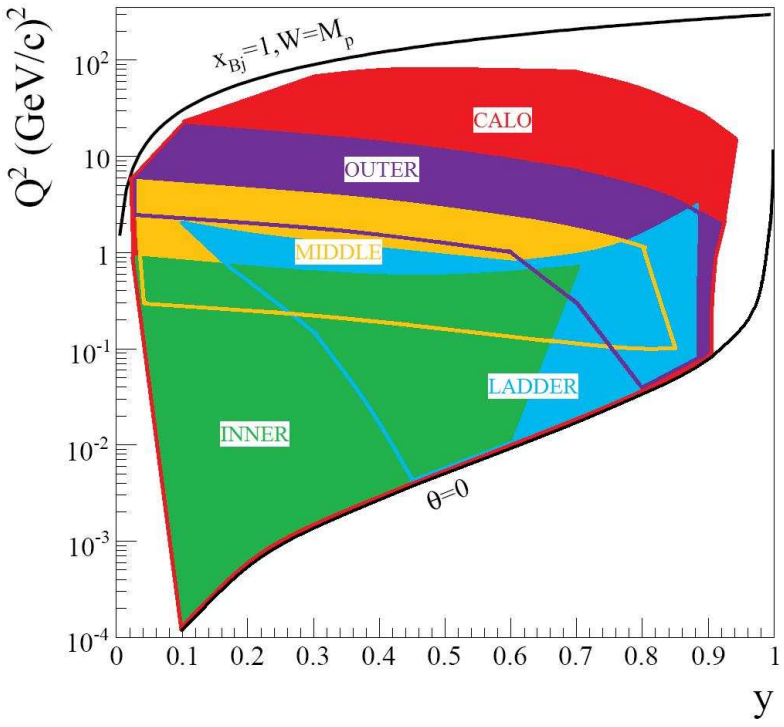

Figure 5.16: The kinematical coverage in y and Q^2 for the four hodoscope trigger subsystems and the standalone calorimetric trigger. The two lines, $x_{\mathrm{Bj}} = 1, W = M_{\mathrm{p}}$ and $\theta = 0$ show the kinematic limits of elastic scattering and forward scattering, respectively.

5.14.2 Veto System

The Veto System makes the part of trigger system which perform the halo muons rejection. veto system has two scintillator counters (Veto 1 and Veto 2) upstream with hole for the beam passage. The Veto 1 detector (larger one) with dimensions $250\,\mathrm{cm} \times 320\,\mathrm{cm}$ is installed at $-800\,\mathrm{cm}$, while the the second detector (Veto 2 – the smaller one) covering $30\,\mathrm{cm} \times 30\,\mathrm{cm}$ is at $-300\,\mathrm{cm}$. Together these stations reject the divergent beam particles which pass through the $4\,\mathrm{cm}$ diameter holes in one of them. Two examples of rejected and one example of a good event are sketched in Fig. 5.17).

Another one veto detector which is not shown in Fig. 5.17, namely Veto BL, $50\,\mathrm{cm} \times 50\,\mathrm{cm}$ with a $10\,\mathrm{cm}$ diameter hole was installed further upstream at $-2000\,\mathrm{cm}$ in order to improve Veto system. Veto is applied only to middle and outer triggers (inclusive triggers) which do not require the calorimetric trigger.

The week point of the veto system is the dead time (about $20\,\%$ at nominal beam intensity) associated to it.

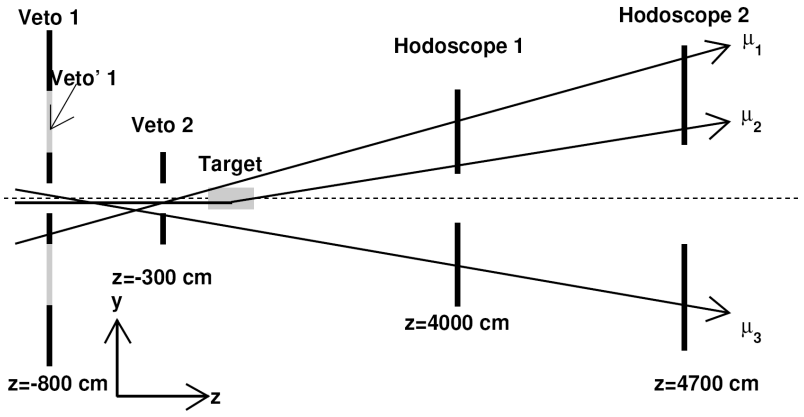

Figure 5.17: Schematical layout of the veto system. The tracks μ_1 and μ_3 are vetoed, whereas the track μ_2 fulfils the inclusive trigger condition.

5.15 Data Acquisition (DAQ) Concept

The COMPASS Data Acquisition system (DAQ) has to be capable to deal with more than 250 000 detector channels and up to $580\,\mathrm{TB}$ data recorded per year. The read-out scheme must be designed for high particle fluxes of $2 \cdot 10^8\,\mu$ per spill of $4.8\,\mathrm{s}$ and high trigger rates of about $10\,\mathrm{kHz}$ with typical event size of $35\,\mathrm{kB}$. In addition the obvious requirement to have nearly dead-time free read-out scheme should be also taken into the account.

In order to fulfill all these requests the entirely new DAQ concept has been implemented. Schematic representation of the data flow in COMPASS DAQ system is shown in Fig. 5.18.

The innovation is that data coming form detectors is digitized and buffered on front-end cards mounted directly in detectors instead of transferring each signal from each channel onto a digitization part. Custom-designed for each detector front-end electronics thus includes preamplifiers and discriminators located close to the detectors and TDC (Time-to-Digital Converter) or ADC (Analog-to-Digital Converter) modules as well.

The Trigger Control Systems (TCS) perform the synchronization of the digitizing and read-out units. By receiving trigger signal the CATCH (COMPASS Accumulate Transfer and Control Hardware) and GeSiCA (GEm and SIlicon Control and Acquisition) readout-driver modules fetch the data buffered within a specified time-window on front-end of detectors. These modules, mounted as close as possible to the detectors, also distribute the trigger signals to the detector front-ends and initialize them during system startup.

The data from up to 16 front-end cards are combined in readout-driver modules in a sub-events pertaining to each trigger and transmitted to central Read-Out Buffers (ROBs) with a maximal speed of $160\,\mathrm{MB/s}$ via S-LINK multiplexer module (SMUX) using the S-LINK protocol developed at CERN.

As read-out buffers (Robs) commercial PCs with a Linux operating system have been used. Each of the ROBs contains four spill-buffers with $512\,\mathrm{MB}$ of memory. Data are written in memory during the beam spill duration time ($4.8\,\mathrm{s}$) and are read out during the

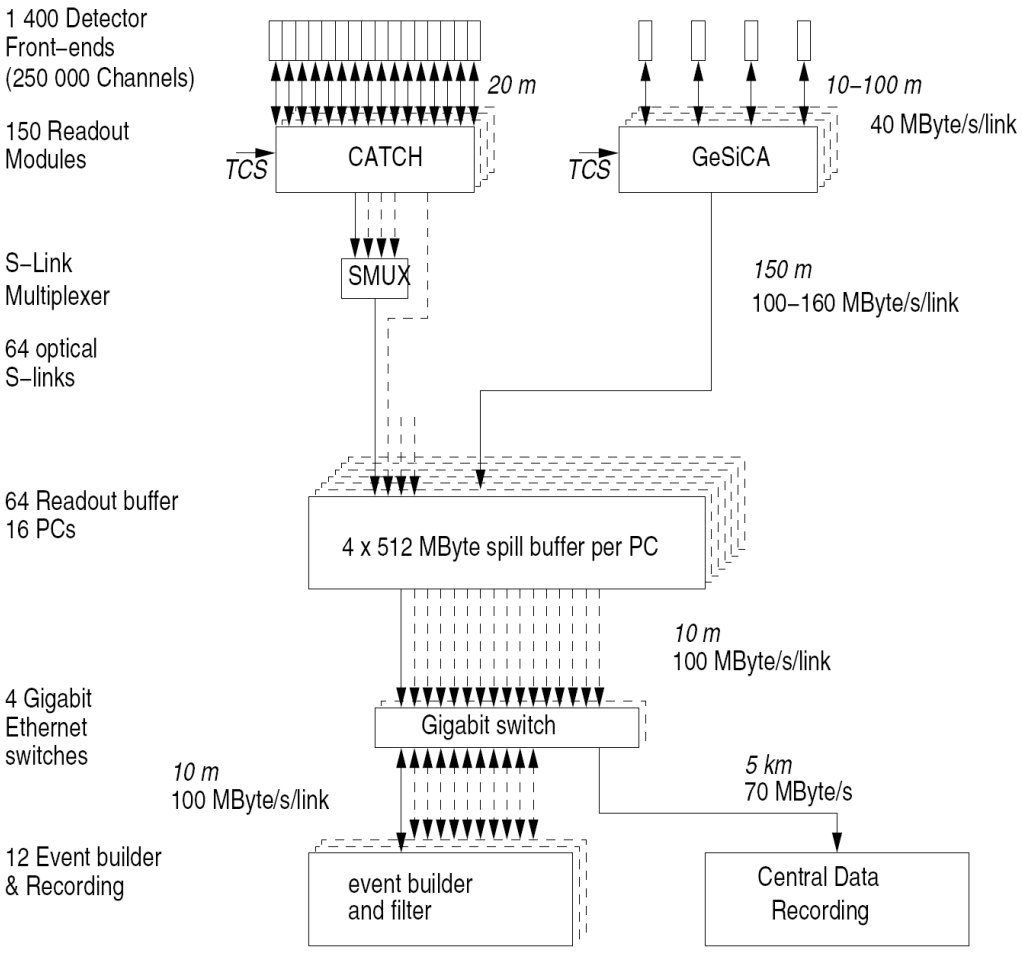

Figure 5.18: General architecture of the DAQ system. Digitized data from the detector front-ends are combined on the readout modules named CATCH and GeSiCA close to the detectors. The storage of the data during the spill and the event building is performed locally. The data are recorded at the CERN computer center.

full SPS cycle of $16.8\,\mathrm{s}$. Each spill buffer can fetch the data of 2-3 spills (the amount of free memory is controlled by DAQ system in order to avoid saturation). Such a configuration allows DAQ system to profit on SPS cycle down-time (interval between two spills) and perform uniform data transfer in system.

From ROBs data are then transported via Gigabit Ethernet to the thirteen parallel event builder computers where the complete events are formed from received sub-events. Event builder system has in total of $7.68\,\mathrm{TB}$ disk space (amount of data collected in one day) available as buffer in case of problems with tape recording. These computers carry out also online filter processes which are called to reject the unfit events useless for the analysis. Rejection of such events save bandwidth, storage space and reconstruction time.

The input for the online filter is the complete event as it is produced in the exit of the event builder. The filtering algorithm check the presence of a reconstructed beam track (standard requirement in muon programme). For this silicon micro-strip and scintillating

fibre detectors upstream of the target together with the beam momentum station must have recorded the sufficient number of hits from the beam particle. Using such a filtering in 2004 a rate reduction by 23% has been achieved.

The amount of data of approximately 100 SPS-spills are combined in one run identified by a unique number. Each run is subdivided to 100 $chunks$ that contain around 25000 events and have a typical size of $\sim 1\,\mathrm{GB}$. During the data taking events formed in chunks and runs are firstly stored in event builder disks. In the same time headers of each event are read and written to a metafile for later storage in an Oracle database. Important pieces of information concerning each run ($\sim 100\,spills$) such as magnetic field strengths and target polarizations as well as special comments made during the data taking, are entered in an online log-book with a database software based on $MySQL$.

At the end of a run chunks with the raw data are registered and copied via Central Data Recording (CDR) system (using CERN-standard RFIO protocol) to the COMPASS Computing Farm (CCF) disk servers (20 servers $500\,\mathrm{GB}$ each (in 2002)) located five kilometers away from the experimental zone. These disk servers are part of the CASTOR (CERN Advanced Storage) hierarchical storage system Ref. [93].

In order to record COMPASS data files on tape in total of 6 tape writers are reserved in CASTOR system. The specific configuration of CASTOR has been developed and optimized for COMPASS purposes so that final performances of more than $8\,\mathrm{TB/d}$ have been reached. This values are close to ones required for the ATLAS and CMS experiments at LHC.

When the CASTOR system is ready it gives the permission to copy the received files to tape. After copying is done successfully the duplicate copies of recorded on tape files which were kept in event builders storage will be deleted by necessity.

In parallel, when the data file is recorded on tape, the corresponding metafile is used to fill the Oracle database with information on the run and on each event. The structure of database allows reconstruction software to have access to each of these events using different selection criteria trigger type or event number.

The main software used for the COMPASS DAQ system is the DATE package Ref. [94] developed by ALICE collaboration at CERN. The package provides components for event building, run control, information logging and event sampling. The run control is supplemented by already mentioned electronic log-book developed for COMPASS.

COMPASS DAQ system has a very flexible architecture which can be expanded in order to satisfy to possible modifications and upgrades. The new detector systems can be implemented in DAQ system simply by including the COMPASS standardized readout-driver modules and ROB PCs. Higher rates can be handled by increasing number of event-builders and making use of online filter capabilities (develop and implement new filtering algorithms).

In the first three years of data taking (2002–2004) COMPASS used of about $12 \cdot 10^5$ SPS spills and collected of 30 billion events which is equivalent to data sample of more than 1 PByte. About 20% of these data have been taken in the transverse target spin mode.

5.16 Data Production Process and CORAL

The data files produced by DAQ system and recorded on tape, contain the raw information from the detector channels digitized by the front-end electronics. The process during which the raw data is converted to events containing the information about the particles that have hit the detectors and associated to each particle vertices and tracks is called data production process (event reconstruction). The amount of data collected by experiment is of $350\,\mathrm{TB/y}$. In order to process such a huge amount of data making event reconstruction at a rate comparable to the data acquisition rate, sufficient computing power of 200k SPECint2000 units is required. Currently this requirement is fulfilled by 200 Linux Dual-CPU PCs out of the CERN shared batch system.

The production procedure begins from ”good” run selection. The following criteria available from corresponding metafile are checked for each run: reasonable number of spills, correct timing from the BMS, target polarization, magnetic fields etc. Only chunks of the good runs are downloaded from the tape. Access to data files is maintained by CASTOR system which has his own commands for the manipulation with files (reading, writing.. etc.). After the good run is downloaded from tape, reconstruction procedure can be started.

The software used by COMPASS for the event reconstruction is the internally-developed **CORAL** (COmpass Reconstruction and AnaLysis) software. CORAL is a fully object oriented programm with a modular architecture, written in C++. The schematic representation of the reconstruction process by CORAL is shown in Fig. 5.19.

CORAL has two different modes: first is reconstruction of the events from raw data collected by the experiment (real data), second is reconstruction from Monte-Carlo simulated data (MC data) when as input to CORAL the output files of COMGeant (COMPASS Geant) COMPASS spectrometer performance simulation software (see Sec. 5.16.4).

In the case of real data the first phase for the event reconstruction is the **decoding** process when the information on the fired detector channel is extracted from the raw data. Next stage is **clustering** process, here the detector planes that are fired by the same particle are grouped together using special algorithms and detector geometry information.

If CORAL process simulated data the procedure is different. The reason for this is the different structure of real and simulated data, in contrast to raw data Monte Carlo data simulated by COMGeant contain the exact coordinates of the interaction point where the particle hits the detector plane. The response of detector in this case is simulated already inside the CORAL during the so-called **digitization** phase which replace the **decoding** process used for real data. Next to this clustering is performed for MC data as well.

After decoding (digitization) and clustering CORAL uses information from tracking detectors and magnetic field maps in order to reconstruct the trajectories of the charged particles through the spectrometer and determine their momenta (see Sec. 5.16.1). Using of hadron calorimeter clusters data allows to separate muons and hadrons, electromagnetic calorimeter clusters provide information about energy and impact coordinate of photons and electrons.

The hadron identification is performed by using RICH detector facilities. The special software calculates the most probable Cherenkov angle and assign probabilities (likelihood) to all possible particle hypotheses (see Sec. 5.16.2), by combining the information

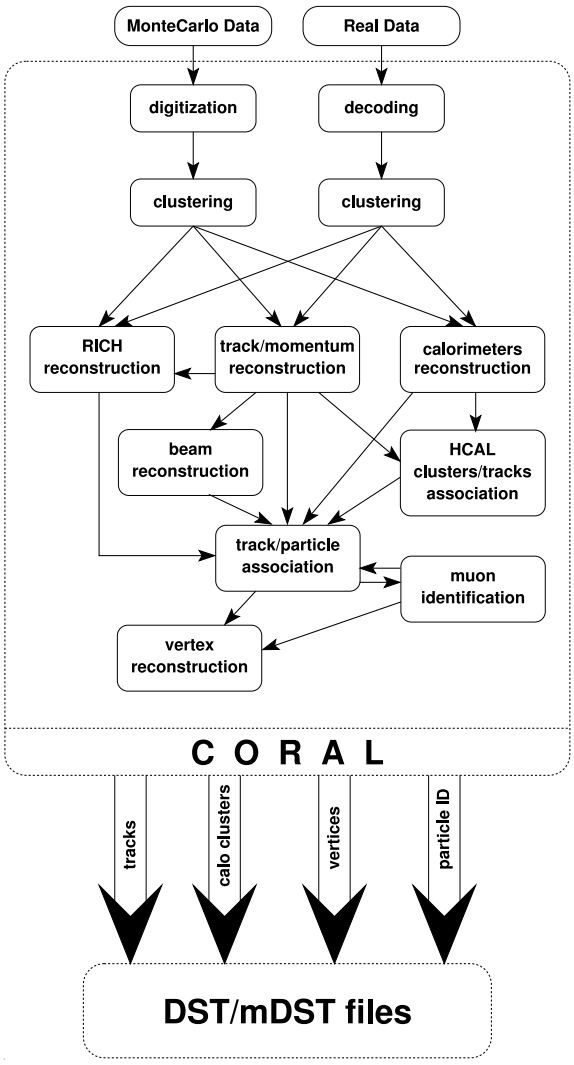

Figure 5.19: Schematic representation of the COMPASS reconstruction software.

from RICH photon detectors and reconstructed particle tracks and momenta.

In order to determine the primary interaction point (primary vertex) and neutral particles decay-points (secondary vertices) the vertex identification procedure is performed for all reconstructed tracks (see Sec. 5.16.3)

Final output of CORAL are the ROOT Ref. [95] trees, called mini Data Summary Tapes (mDST) which contain all the information obtained during the reconstruction process (track parameters, vertices, calorimeter clusters, Particle Identification (PID) probabilities, detector hit patterns,etc.). The data reduction factor between the input raw data and the output mDSTs is about 100. Large DST files which in addition to the tracking, vertex, and PID information contains the detector digits and clusters are also created and kept at CERN on tape.

Next sections are dedicated to track and vertex reconstruction, particle identification

and Monte-Carlo simulation procedures, while the last part introduces the PHAST software tool used in COMPASS data analysis.

5.16.1 Track Reconstruction

Integrated in CORAL track reconstruction algorithm (TRAFFIC/TRAFDIC) has three working phases. **1) pattern recognition** – finding track segments in the various zones of the spectrometer. Spectrometer is divided in five zones along beam axes, where track segments are expected to be approximately straight lines (upstream target, target-SM1, SM1-SM2, SM2-MF2, downstream MF2). **2) bridging** – investigating segments from several distinct zones in order to find parts corresponding to same track and merging them into the full trajectories using special algorithms. **3) fitting** – computing the best estimators for the parameters of the reconstructed tracks (x and y positions, $\mathrm{d}x/\mathrm{d}z$ and $\mathrm{d}y/\mathrm{d}z$ slopes, inverse momentum $1/p$) using information about magnetic fields and material maps. For this purpose, the **Kalman fit** method is used Refs. [96, 97].

5.16.2 Particle Identification

The package named RICHONE serves for the Particle Identification (PID) with RICH detector. The coordinates of the Photon Detectors (PD) pads with signal above threshold and a signal amplitude are combined with track information obtained from tracking reconstruction. With this input RICHONE calculates the probabilities to all possible particle hypotheses and include this information in the track parameters.

CORAL make use of several algorithms which serve for identification of track as a beam or scattered muon or as a neutral particle.

Beam muon tracks are identified mainly by using BMS, SciFis and Silicon Detectors (SI) information. Incoming muon track has to be reconstructed in SciFis and Sis with the momentum being reconstructed in BMS stations, in addition the time of the track should be within a time window of 3σ of BMS and trigger time. In case if several tracks are associated with the trigger time window, a backtracking algorithm is used in order to find the exact one.

A track is identified as a scattered muon if it is associated to a positively charged particle with momentum larger than $1\,\mathrm{GeV}/c$ passing through SM1, and if its trajectory is compatible with the hodoscope hits as given in the trigger matrix corresponding to particular event. In addition extrapolated scattered muon track must cross the entrance and the exit of the polarized target within a radial distance from beam axis smaller than $5\,\mathrm{cm}$. In the case of a standalone calorimetric trigger scattered muon track must have number of hits downstream either first or second hadron absorbers not less than specified minimal value, and the amount of material traversed in the spectrometer must be larger than 66 radiation lengths for tracks reconstructed in LAS and 74 radiation lengths for tracks reconstructed in SAS.

As an evidence of a neutral particle interaction can serve fired calorimeter clusters with no track associated.

5.16.3 Vertex Reconstruction

During the last phase of the event reconstruction the location in space of the primary interaction (primary vertex) or of the two-body decays of neutral particles (so-called V^0 vertices) is performed. Vertex is a common point where (or very near) various tracks are assumed to originate or to come to an end. Using different fitting algorithms (Point Of Closest Approach (POCA), inverse Kalman filter algorithm) CORAL gets the best estimate of the three coordinates of the vertex position, the track parameters at the vertex (momentum components.. etc) and the corresponding error matrices are calculated as well.

A vertex is called primary when it contains a beam track. Since more than one beam track can exist for one event, few primary vertices corresponding to existing beam tracks can be reconstructed. In such cases "best primary vertex" is defined as the one with the maximum number of tracks and, if the number of tracks is the same, the one with smaller vertex χ^2. The selection of the Best Primary Vertex (BPV) is performed later at the level of physics data analysis.

The V^0 vertices (K^0_S, Λ and $\overline{\Lambda}$ decays into charged particles) are searched by combining all pairs of tracks with opposite charge, regardless of their association to the primary vertex. The most probable decay position, the track parameters at the vertex and the corresponding error matrices are calculated using the Kalman filter technique.

5.16.4 Monte-Carlo simulation

The COMPASS spectrometer performance simulation programm called COMGeant (COMPASS Geant) is a Geant 3.21 Ref. [98] based software which can be linked to any generator of lepton, photon or hadron interactions such as Lepto Ref. [99], Aroma Ref. [100] or Pythia Ref. [101].

In order to generate the beam muons and halo parameters from extracted from the real data events recorded with randomly generated triggers have been used. Beam-target interactions are randomly generated inside the target volume, corresponding secondary tracks are then propagated through the spectrometer.

The detector response simulation is performed applying the information about the efficiency and resolution of each station and then is tuned by using real data samples.

Special attention is payed to the realistic description of the regions of the spectrometer with high material densities. With this purpose three dimensional material maps that describe the type and amount of material of each of the spectrometer elements (including frames and supporting structures) have been used. The simulated detector hits are written out and subsequently processed as for real events. This way reconstruction algorithms and data analysis algorithms as well as different detector properties can be tested.

5.17 Data Analysis Tool (PHAST)

For the data analysis purposes the **PHAST** (PHysics Analysis Software Tools) internally-developed software is used. The programm consist of various classes and ROOT-based routines using which user can: 1) access to reconstructed events information stored in

mDSTs, 2) develop his own physics analysis code (select desired for analysis events, calculate necessary physical quantities such as x, y, z, Q^2 etc., apply cuts, fill and plot histograms.. etc.), 3) process new mDSTs containing filtered sub-samples of selected for analysis events.

The PHAST software also provides mDST output data stream at the stage of event reconstruction.

In this work all the data analysis was performed using PHAST.

Chapter 6

Data Selection

In our analysis done for the transverse spin dependent asymmetries we used the COMPASS data collected in years 2002-2004 with the $160\,\mathrm{GeV}/c$ longitudinally polarized muon beam and a transversely polarized ^6LiD target. The following sections are devoted to data quality checks and event selection procedure. After the description of the cuts applied to the data sample the final statistics used in the analysis and distributions of the important kinematical variables are presented.

6.1 Transverse Data Production

In the 2002-2004 years COMPASS spent about 20% of the running-time on measurements with transversely polarized target (see Sec. 5.5). The whole data taking in this mode was separated in five periods: two periods in 2002 (11 days in total), one period in 2003 (9 days) and two periods in 2004 (14 days in total). In transverse mode target cells are polarized oppositely to each other and transversely with respect to the beam direction, so the two cell-spin configuration are possible: (⇑⇓) and (⇓⇑).

The typical cycle (data taking period) with transversely polarized target consist of three stages: first stage ($\sim$ five days) goes with one of the possible cell-spin configurations (⇑⇓ or ⇓⇑), during the second phase the polarization is flipped in both cells by using the microwave frequency exchange (it takes two days to achieve nominal $\sim 50\%$ polarization) and in last stage ($\sim$ five days) measurement is continued with reversed configuration, opposite to initial one. Two data taking stages of the cycle are named sub-periods, so each data taking period includes two sub-periods with opposite cell-spin configurations.

In principle one could avoid microwave reversal and perform measurement using only one cell-spin configuration (⇑⇓ or ⇓⇑) and then calculate the asymmetries from the difference in the counting-rates from the two cells making a profit on COMPASS target feature that allows simultaneous measurement with two spin polarizations. But such a method would be influenced by systematic effects caused by differing acceptance of the two cells.

In a contrary aforementioned sub-periods technic coupling with "double ratio" method used in the analysis (see Sec. 7.2.1 and Sec. 7.7.1) where the counting-rate asymmetry is calculated for two target cells separately in two sub-periods with opposite spin configurations, allows to reduce to a minimum such a systematic effects.

The polarization reversal cannot be done fast in transverse mode, and in order to use effectively the beam time data taking is performed during the long sub-periods, for this reason, the transverse spin measurement usually is scheduled at the end of the run, when the spectrometer is fully operational and stable.

The list of sub-periods processed in 2002-2004 and cell-spin configuration for each of them are given in Table 6.1, while the schematic representation of data taking cycle in transverse mode (and longitudinal as well) is given in Fig. 5.6. During the 2002-2004 in total of ten sub-periods merged in five periods have been processed (P2B-P2C, P2H1-P2H2, P1G-P1H, W33-W34, W35-W36). The sub-periods of one period have opposite cell-spin configuration this was achieved by corresponding field reversal after the first sub-period.

Year	Sub-Period	cell-spin configuration	Duration days/year
2002	P2B	⇓⇑	11
2002	P2C	⇑⇓	
2002	P2H.1	⇓⇑	
2002	P2H.2	⇑⇓	
2003	P1G	⇓⇑	9
2003	P1H	⇑⇓	
2004	W33	⇑⇓	14
2004	W34	⇓⇑	
2004	W35	⇓⇑	
2004	W36	⇑⇓	

Table 6.1: Cell-spin configuration for data taking sub-periods in 2002-2004, and total duration days/year.

All the data collected in transverse mode have been processed using CORAL software, according to the procedure described in Sec. 5.16.

For the physics analysis of transverse spin effects the miniDSTs containing only the events with at least one primary vertex reconstructed and with at least one more outgoing track have been used.

6.2 Data Quality Checks

The data quality checks and spectrometer stability testing must be performed first, before accepting the data for the physics analysis. For this reason each data taking period has been checked run-by-run for the time stability of distributions of various parameters using the histogram files created online during production or produced after in the reconstruction phase or extracted from the ready mDST files.

The data quality analysis has three main aspects:

- **Detector Stability checks**

  The detector performance stabilities were performed analyzing the hit distributions in the about 360 detector planes. Malfunctioning detector planes which have not

been noted in online logbook and could harm the data quality are detected in this stage.

- **Reconstruction and Detector Time Stability checks** The time stability of the detector and reconstruction efficiencies was checked run-by-run looking at stability of the following quantities:
  - the number of clusters per plane and per event;
  - the number of tracks per event;
  - the number of track segments in the different spectrometer regions per event (upstream SM1, between SM1 and SM2, downstream SM2);
  - the number of primary vertices per event;
  - the number of secondary vertices per event.

  Using the miniDST events, the stability was checked monitoring run per run
  - the number of reconstructed K^0 per primary vertex;
  - the reconstructed K^0 mass distribution;
  - the energy measured in the two hadronic calorimeters $HCAL1$ and $HCAL2$;
  - the distributions of the x and y coordinates of the vertex in the two cells;
  - the vertex χ^2 distribution.

- **Kinematic Stability checks**.

  The time stability of the distributions of several kinematical observables was investigated in details:
  - the Bjorken scaling variable x;
  - the relative energy loss of scattered muon y;
  - the negative squared four-momentum of exchanged photon Q^2;
  - the azimuthal angle of the produced hadron ϕ_h and the azimuthal angle of the nucleon spin ϕ_S;
  - the momenta of the scattered muons;
  - the momenta of the produced hadron and it's transverse component.

One of the most informative and objective ways to check the global stability of the production is the extraction of a known physical quantity from data. In COMPASS in order to perform such a test the extraction of K^0 mass was used. The analysis was performed run-by-run with the COMPASS analysis program PHAST using the available mDST data. The invariant mass of V0 vertices (vertices with two outgoing tracks associated) is reconstructed making hypothesis of neutral kaon decay in two charged pions:

$$\begin{aligned} K^0_S &\rightarrow \pi^+\pi^- \ (\Gamma_i/\Gamma \ 69.20 \pm 0.05\%) \\ K^0_S &\rightarrow \pi^0\pi^0 \ (\Gamma_i/\Gamma \ 30.69 \pm 0.05\%) \end{aligned} \tag{6.1}$$

The second by significance decay mode (to two neutral pions), produces no measurable tracks in the COMPASS spectrometer, so only the first-channel reactions are detected. The invariant mass of the $\pi^+\pi^-$ is compared with the K0-mass from the Particle Data Group (PDG) of 497.672 MeV.

As an example, the mean $\pi\pi$ invariant mass in the K^0 region from the data collected in the first sub-period of the 2004 run is shown in Fig. 6.1 as a function of time.

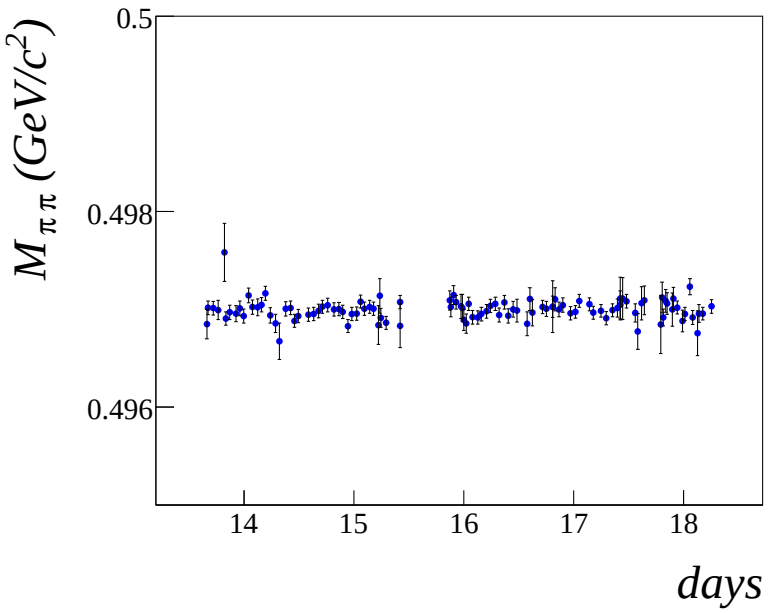

Figure 6.1: $\pi\pi$ invariant mass in the K^0 region as a function of time from August 13 to August 19, 2004.

The number of the runs not used in physics analysis due to some revealed instabilities is: 9 (over a total 462) for the 2002 data, 28 (over a total of 458) for the 2003 data, and 44 (over 462) for the 2004 data.

6.3 Event Selection

The data sample selected for the analysis of target transverse spin dependent asymmetries includes only the deep inelastic scattering events with reconstructed at least one primary vertex and at least one outgoing hadron track. In the following sections the description of kinematical and other cuts applied in physics data selection procedure are given.

6.3.1 DIS Events (Q^2 cut)

Several aspects of large physics analysis program of COMPASS such as ΔG researches use for their purposes the whole kinematical range of Q^2 up to very small values $Q^2 \approx 0$ which corresponds to a quasi-real photon regime. For the transverse spin effects which are the subject of this work, only the events from deep-inelastic scattering region are used. The corresponding $Q^2 > 1$ cut thus have been applied to select the DIS events. Since the COMPASS data are mostly concentrated at low Q^2 this cut represents considerable reduction in data. The reasonable decision to store in miniDST files used for physics analysis, already reduced sample, with applied $Q^2 > 1$, "at least one primary vertex reconstructed" and "at least one outgoing hadron track reconstructed" cuts, was taken. In

fact the stored events makes about 1% of the initial raw sample, which allows to spent less time and computing power on further analysis.

6.3.2 Selection of the Primary Vertex and Muons

Primary Vertex Selection: During the vertex reconstruction by CORAL the events with more than one beam track associated can be reconstructed. For such an events few primary vertices corresponding to existing beam tracks can be reconstructed as well. The selection of Best Primary Vertex (BPV) is performed in PHAST by **event.iBestPrimaryVertex()** function. Named function identifies the BPV from all the primary vertex candidates on the basis of their reduced χ^2 and the number of associated outgoing tracks. Usually the primary vertex with the maximum number of outgoing tracks and smallest χ^2 is the BPV.

Beam Muon Cuts: The beam muon is defined by the beam track belonging to the best primary vertex. A cut on maximum momentum of $P_{beam} < 200$ GeV is applied for the beam particles.

During the reconstruction process, the summed probability (χ^2) that each hit associated to the track indeed belongs to it is calculated by performed global fit. The reduced χ^2 is then obtained by:

$$\chi^2_{red} = \frac{\chi^2_{tot}}{N_{D.O.F}} = \frac{\chi^2_{tot}}{N_{hits} - 5} \tag{6.2}$$

where $N_{D.O.F}$ is the number of degrees of freedom corresponding to track, equal to number of data points (number of hits N_{hits}) minus the number of fitting parameters which are the five: two coordinates (x, y; z is pre-determined by the first hit on the track), two direction cosines ($\frac{dx}{dz}$, $\frac{dy}{dz}$) and the momentum of the track particle.

Events with χ^2_{red} of the beam muon larger than 10 are discarded in order to reject cases with a poorly reconstructed beam track.

In addition, a special cut was applied to ensure an identical beam flux in both cells (see Sec. 6.3.4).

The beam muons momentum distribution for the final data sample is shown in Fig. 6.2.

Scattered Muon Cuts: The outgoing tracks of the primary vertex which corresponds to the scattered muons μ' are identified as such by CORAL during the event reconstruction process. This is done mainly by using the information from trigger hodoscopes system. In the miniDST files such μ' track candidates has a special mark (flag) which can be identified by PHAST thats why we will call this events further on as *flagged*.

Since the trigger hodoscope system do not cover the whole kinematic region of the large angle spectrometer, some of the muons scattered at large angles are not recognized by system as such. In order to identify these μ' tracks, all the outgoing tracks of the primary vertex in each event are checked for the number of hits in the first Muon Wall (MW1) detector planes. Let us remind that MW1 consist of two planes (MA01 and MA02) separated by 60cm hadron absorber (see Sec. 5.13.1). Any outgoing particle from the best primary vertex which causes more than four hits in MA01 and more than six in MA02 is considered as scattered muon candidate.

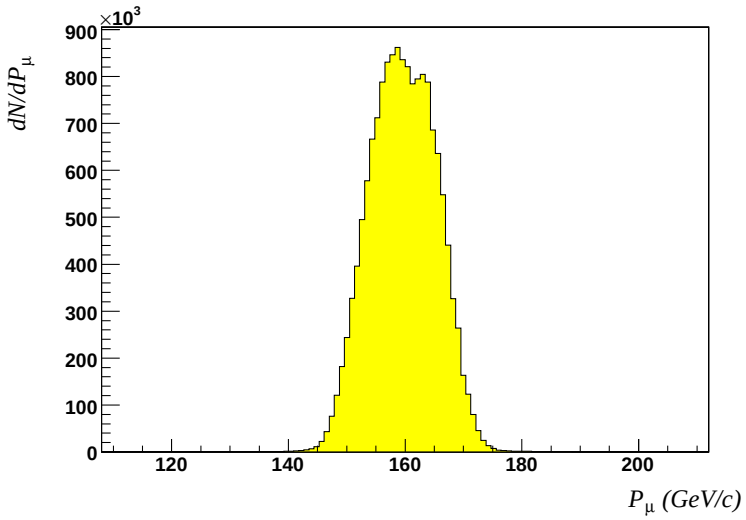

Figure 6.2: Momentum distribution of the reconstructed incoming muons for the final sample of events.

Firstly in order to achieve clean identification both type of scattered muon track candidates (identified by CORAL (*flagged*) and *recovered* ones) are checked for two criteria:

- requirement on the quality of the track: the reduced χ^2 of the track must be smaller than 10 ($\chi^2_{red} < 10$);
- the amount of material traversed by particle must be larger than 30 radiation lengths ($nX/X_0 > 30$).

The tracks which did not pass the test are discarded. Than if only one scattered muon candidate survives (*flagged* or *recovered*) it will be accepted as a real one and event will enter the following steps of the analysis. Otherwise event will be discarded:

- If more than one *recovered* muon is found in an event,
- If a *flagged* μ' and a *recovered* μ' are found in the same event,
- If more than one flagged μ' is found in an event.

6.3.3 Cuts on the Variables y and W

Events with the values of the kinematic variable y below 0.1 and larger than 0.9 are discarded from the analysis. The region $y < 0.1$ corresponds to the events from the elastic region and also includes events with halo and background (multiple scattering.. etc.) muons identified by trigger system as scattered muons. Events with $y > 0.9$ are excluded due to the fact that trigger system can only reliably identify events up to approximately $y = 0.9$.

Events from the resonance region are excluded by a cut on the invariant mass of the final hadronic state $W > 5\,\mathrm{GeV}$. This reduction also enhances the rejection of elastic events corrected mostly by $y < 0.1$ cut.

6.3.4 Target Cuts

The COMPASS target (Sec. 5.5) consist of two $60\,\mathrm{cm}$ long cylindrical with a radius $r > 1.5\,\mathrm{cm}$ cells, separated by $10\,\mathrm{cm}$. In order to ensure that interaction occur between the beam particle and target nucleons, inside the target volume, the special cut on primary vertices is needed. In addition one must take into the account that in transverse mode the dipole field shifts the target cells on x and y axes, so the cylinders are not centered at zero as during the longitudinal mode, operated by solenoid field. In order to fulfill these requirements all primary vertices with a radial distance $r > 1.3\,\mathrm{cm}$ from adjusted for transverse mode central axis are discarded (see Fig. 6.3).

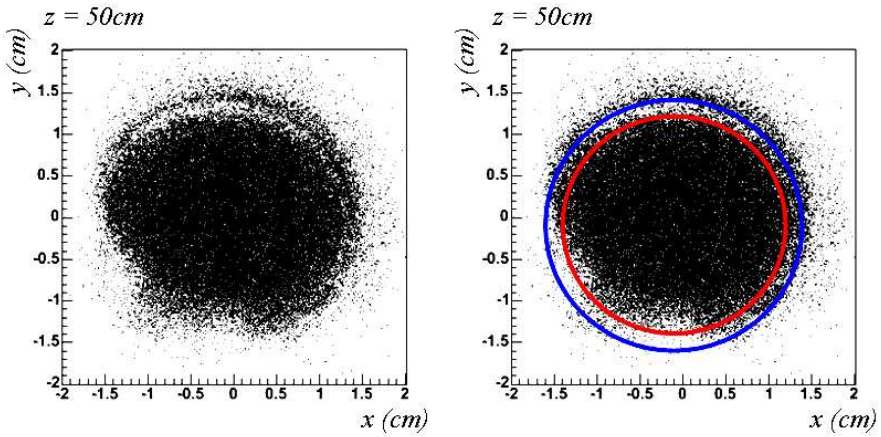

Figure 6.3: Target cut. Left: Distribution of primary vertices with $-50\,\mathrm{cm} \leq z \leq -45\,\mathrm{cm}$. The contour of the target cylinder is evident. Right: Same distribution with the overlayed contour of the cylinder (blue circle), and red circle indicating radial cut $r > 1.3\,\mathrm{cm}$

At the same time cut on z-coordinate of the primary vertices (z_{vtx}) have been applied corresponding to the projection of the target cells on z-axis: -100 cm $<$ z_{vtx} $<$ -40 cm (vertex is in upstream cell) or -30 cm $<$ z_{vtx} $<$ 30 cm (vertex is in downstream cell). Both radial and z cut on the primary vertex coordinate are performed by using the PHAST routine **PaAlgo::InTarget**.

A further cut was applied to ensure an identical beam flux in both target cells, and thus nearly identical luminosity. Only those events were accepted, where the projection of the incoming muon beam track on xy plane at $z = -100$ cm (beginning of the target) and $z = 30$ cm (end of the target) lies within the radial distance determined by aforementioned cut of $r < 1.3\,\mathrm{cm}$. This cut was applied by PHAST routine **PaAlgo::CrossCellst**.

The distribution of the z-coordinates of the primary vertices for the final sample is shown in Fig. 6.4. The difference in geometrical acceptance for two cells ($\pm$ 70 mrad for

upstream and $\pm$ 170 mrad for downstream cell) causes increase in the number of events with z_{vtx}. The two target cells are clearly separated in this plot. The events outside the target cell volume are produced in helium bath or in peripherals, as an example, the peak at z= 500 mm corresponds to the aluminium window, part of the magnet construction.

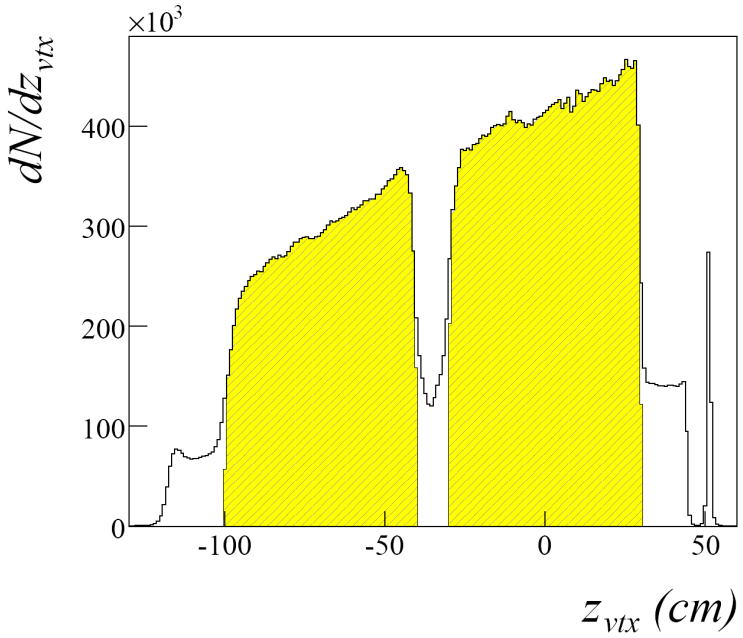

Figure 6.4: Distribution of the primary vertex z-coordinate for the final sample.

6.3.5 Hadron Identification

All the outgoing particles originating from the best primary vertex which are neither flagged nor recovered muons are considered as hadrons. The asymmetries need to be evaluated for positive and negative hadrons separately in order to give access to flavor dependence of corresponding parton distribution functions and fragmentation functions. The flavor of the outgoing quark knocked out by the photon in DIS reaction play essential role in the determination of produced hadron type and charge. For example, the production of a π^+ ($u\overline{d}$) or π^- ($\overline{u}d$) contains a differing contributions from the transverse u and d quark distributions, and thus the investigation of the azimuthal effects on produced positive or negative hadrons will allow to draw some conclusions about the distribution of initial quarks with corresponding flavor inside the nucleon and the fragmentation process by itself. For this reason the information about the charge of hadrons is extracted from miniDST files and two, positive and negative hadron samples are created in the analysis.

In order to reject tracks reconstructed in the fringe field of SM1 which have a poorer momentum resolution, only the particles with the at least one hit after the first spectrometer magnet were used in the analysis. This requirement is fulfilled by applying the cut on the last measured coordinate of the track of outgoing hadron ($z_{last} > 350$ cm).

In addition particles identified as hadrons must satisfy the following criteria:

1. Track quality cut: the reduced χ^2 of the hadron track must be smaller than 10 ($\chi^2_{red} < 10$).

2. the amount of material traversed by hadron in the spectrometer had to be smaller than 10 radiation lengths $nX/X_0 < 10$;

3. Hadron tracks are discarded if they have associated clusters in both calorimeters.

4. if the particle produced the signal in only one hadron calorimeter (the first or the second), the energy deposited by hadron in the associated cluster of HCAL1 or HCAL2 has to exceed some minimal value, specified for each calorimeter in each data-taking year. The cuts on minimum energy deposition in cluster are the following: for HCAL1 $E^{HCAL1} > 5(2002, 2003)\ 4(2004)$ GeV and for HCAL2 $E^{HCAL2} > 8(2002, 2003)\ 5(2004)$ GeV. The correlation between the energy measured in HCAL and that measured by the spectrometer is shown in Fig. 6.5.

5. the hadron track is still accepted if it did not produce signal in none of the two calorimeters.

The first requirement is a general request on the track quality. The second requirement reduces the muon contamination in hadron sample, while the third and the fourth reduces muons and electrons contamination as well.

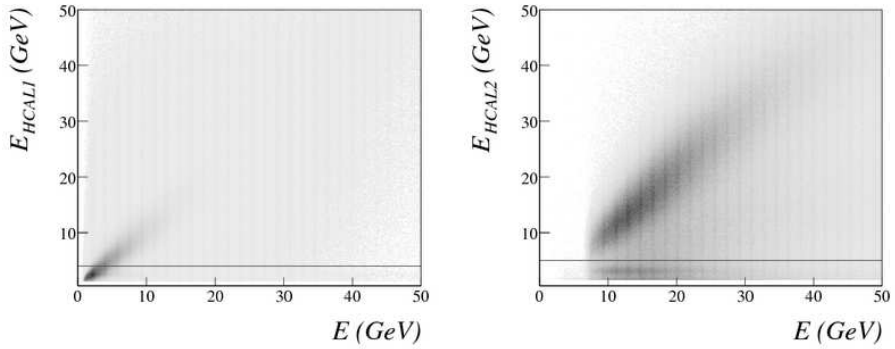

Figure 6.5: Correlation between the energy measured in HCAL1 (left) and HCAL2 (right) and the energy measured by the spectrometer for the 2004 data. Lines indicate applied cuts.

6.3.6 Kinematic Cuts on All Hadrons: z and P_{hT}

The following two kinematic cuts have been applied for the all hadrons sample.

- Cut on the fraction of the photon energy transferred to the hadron to be larger than 0.2, $z > 0.2$. The cut is applied in order to avoid the impurities at lower values of z, such as the secondary interaction of the hadrons. In a fact the greater values of z are of more interest in physics analysis because in this case most probably the hadron

is produced directly from the stuck quark fragmentation and thus carry useful information about the spin structure of the nucleon and fragmentation process. But since the COMPASS kinematics are concentrated mainly at lower z region stronger cut will bring to a sufficient loss in statistics (the requirement $z > 0.2$ by itself reduces the all hadrons sample remaining after previous cuts by 30 to 40%).

- Cut on the transverse momentum of the hadron with respect to the virtual photon direction to be larger than 0.1, $P_{hT} > 1$. This cut ensures a good resolution in the measured azimuthal angle.

6.3.7 Extra Cut on All Hadrons *(y-peak)*

The hadron sample obtained after applying all the aforementioned cuts, have been scrutinized by monitoring the distributions of the different parameters and variables. During this process an unidentified peak has been noticed in the y distribution of the positive hadrons, located in the region of high y in the last z bin ($0.8 < z < 1$) figure 6.6. Following checks revealed the similar behavior: in the z distribution of the first x bin, in the distribution of the energy of positive hadrons at high z and in the distribution of the momentum of the scattered muon.

The first hint giving an idea that hadron-muon misidentification took place, was the fact that none of these peaks does not appear in negative hadron sample.

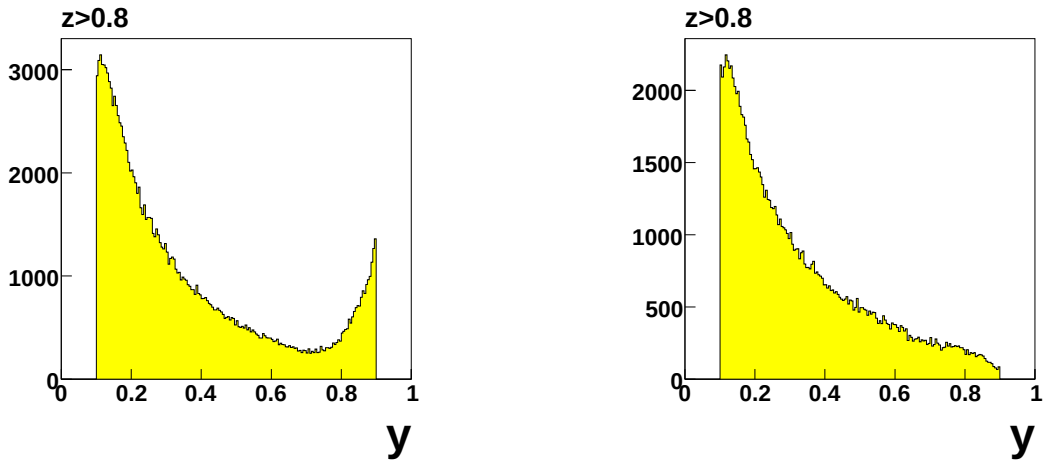

Figure 6.6: y-distribution of hadrons with z in the range of ($0.8 < z < 1$), both for positive (left) and negative (right) hadrons.

It was checked that scattered muons related to the y-peak events are the particles that have passed through the amount of material more than 100 radiation lengths. The distribution of x and y coordinates of corresponding muon tracks have not shown any evidence of holes in the muon wall (figure 6.7(left)) so the reconstructed tracks indeed correspond to positive muons and moreover it was checked that these tracks come from the primary vertex of the event. So if they are not the ”true” scattering muons they should be the muons coming from decays of π or K produced in the primary vertex.

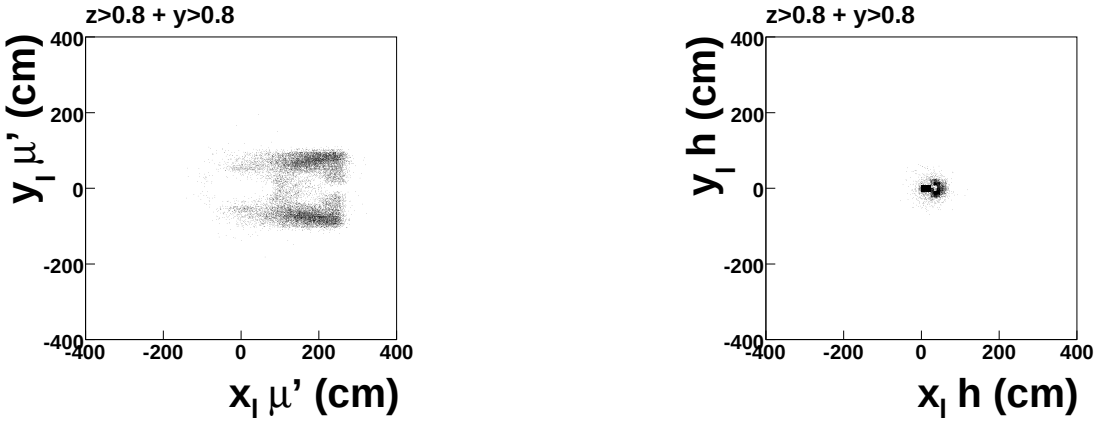

Figure 6.7: x_l vs. y_l distribution of scattered muons for positive hadrons with $z > 0.8$ and $y > 0.8$ (left). x_l vs. y_l distribution of hadrons with $z > 0.8$ and $y > 0.8$ (right).

The analysis done for the positive hadrons corresponding to the peak have shown one peculiarity, i.e. the distribution of the last x and y coordinates (x_l and y_l correspondingly) of the reconstructed hadron tracks is concentrated at a very small area (a square with sides less than 50 cm), while the last z_l coordinate was not focused anywhere. As it was checked the $x_l : y_l$ distribution (figure 6.7(right)) indicates the hole of the hadron absorber. The muon track which pass through that region do not cross the large amount of material which brings to $nX_0 < 10$, and thus track will be identified as a hadron by our selection rules (see Sec. 6.3.5). So lets summarize:

- the scattered muon is identified as a positive hadron, because it goes through the hole and does not cross large amount of the material and thus matches to the hadron selection criteria $nX_0 < 10$;
- a positive muon being the decay product from the primary vertex is reconstructed and wrongly considered as scattered muon.

The reconstruction of these events is wrong and in order to reject them the following cuts have been optimized by analyzing the distribution of extrapolated after the iron absorber coordinates of the track x_e and y_e for different interval in z_l:

1. $\sqrt{(x_e - 45\ \mathrm{cm})^2 + \mathrm{y_e^2}} < 10$ cm for $z_l < 2000\ \mathrm{cm}$;
2. $|y_e| < 25$ cm and $|x_e - 45\ \mathrm{cm}| < 25$ cm for $z_l > 4000\ \mathrm{cm}$;
3. $\sqrt{(x_e - 35\ \mathrm{cm})^2 + \mathrm{y_e^2}} < 15$ cm and ($|y_e| < 3$ cm and $|x_e - 55\ \mathrm{cm}| < 13\ \mathrm{cm}$) for $2000\ \mathrm{cm} < \mathrm{z_l} < 4000\ \mathrm{cm}$;
4. $|y_e| < 25\ \mathrm{cm}$ and $|x_e - 45\ \mathrm{cm}| < 25\ \mathrm{cm}$ for $4000\ \mathrm{cm} < \mathrm{z_l} < 5000\ \mathrm{cm}$

After rejecting these events the y and z distribution looks like (figure 6.8), where the peak has vanished and no good events are rejected. The loss of events due to this cut is negligible as it is less than 1% in overall statistics.

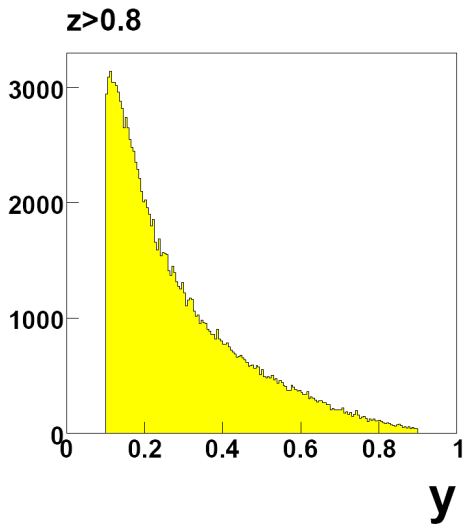

Figure 6.8: y distribution for hadrons with $0.8 < z < 1$ in case of the rejection of the events based on x_e and y_e (as described before).

6.3.8 Final Statistics for *unidentified* hadrons

In Table 6.2 the final statistics for positive and negative hadrons after all aforementioned cuts are presented for all the periods in 2002,2003 and 2004 years.

Year	Period	Positive hadrons	Negative hadrons
2002	P2B/P2C	704840	594138
2002	P2H	472244	399692
2003	P1G/P1H	2429420	2029588
2004	W33/W34	2093759	1739317
2004	W35/W36	2716216	2258956
Sum		$8.4 \cdot 10^6$	$7.0 \cdot 10^6$

Table 6.2: Final statistics for the years 2002,2003 and 2004 for all positive and negative hadrons.

6.3.9 Kinematical distributions

In this section the distributions of some kinematical variables are shown. All the plots included in Fig. 6.9 are produced using the final 2004 charged hadron sample after all the cuts listed in previous sections.

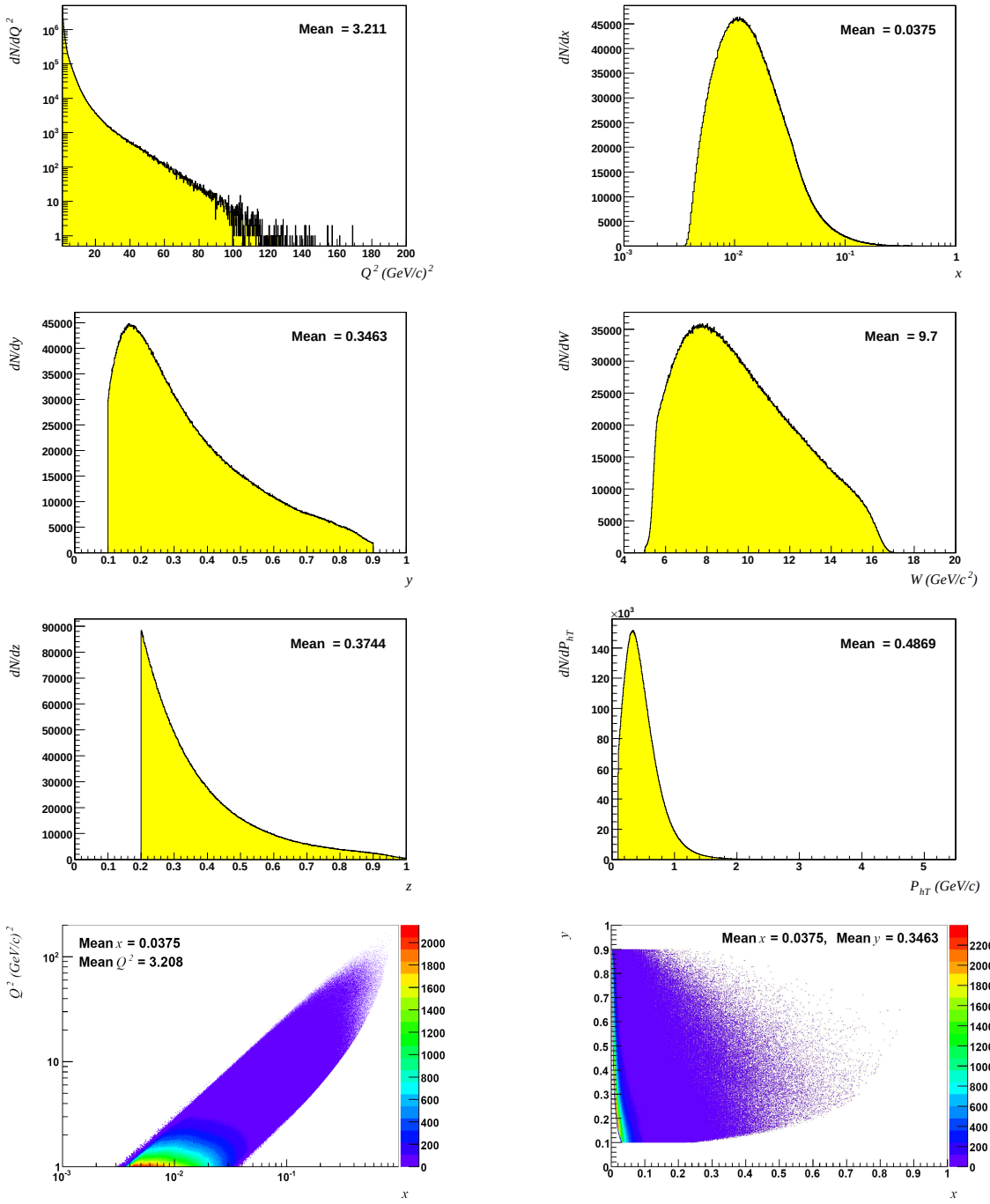

Figure 6.9: All the plots correspond to the final charged hadron sample from the COMPASS 2002-2004 transverse data. Upper plots: Q^2 distribution (left) and x distribution (right), Middle Upper plots: y distribution (left) and W distribution (right), Middle Lower plots: z distribution (left) and P_{hT}-distribution (right) Lower plots: Scatter-plot of Q^2 vs x (left) and Scatter-plot of x vs y (right).

6.3.10 Identification of Hadrons as Pions and Kaons

The transverse spin asymmetries have been evaluated for charged hadrons and for identified charged pions and kaons. Since the RICH (Sec. 5.11) information for transverse mode has been available only for 2003 to 2004 years, only that data has been used in the analysis of identified hadron asymmetries. After the required additional data-quality checks (see below) the event selection procedure have been applied in the same chronology and with the same cuts as in the case of *unidentified* hadrons. Only after this the cuts used for the identification of pions and kaons have been applied (see below).

Data quality checks

For the selection of *unidentified* hadron event sample the RICH information was not used, thus in this case data was not scrutinized for RICH detector stabilities. In the contrary the identification of pions and kaons is performed using the RICH information, and thus some specific studies on the stability in time of this detector are required.

For the RICH detector time performance reasons data from all the six transverse periods have been run-by-run and then spill-by-spill analyzed by exploring the stability of following quantities:

- the calculated likelihood distributions for π and K;
- the number of identified π and K;

The number of ”bad” runs rejected by some of these criteria from each period are presented in the table 6.3.

period	number of bad runs	corresponding number of spills	percentage in spills (%)
P1G	16	905	4.5
P1H	15	1302	7
W33	4	288	2
W34	7	335	2.6
W35	2	111	0.5
W36	2	45	0.3

Table 6.3: The number of runs (and the corresponding number of spills) rejected by the stability checks, for the six periods of transverse data-taking.

The remaining after the first selection good runs have been checked spill-by-spill by the same stability monitoring. The percentage of spills classified as bad after this procedure and rejected from the analysis is shown in table 6.4.

RICH identification of pions and kaons

The hadron identification in event reconstruction process is performed by the RICHONE package (see Sec. 5.16.2) which converts the event-information from RICH photon detectors pads and calculates the probabilities (likelihood) to all possible particle hypotheses.

period	bad spills found in the good runs (%)
P1G	1.05
P1H	0.97
W33	0.96
W34	1.16
W35	0.98
W36	0.96

Table 6.4: The percentage of spills classified as ”bad” and rejected from the analysis for the six periods of transversity data.

At this first step, hadrons are identified with a particular mass hypothesis if the corresponding likelihood is the maximum one. This information is then included in the track parameters and used in further analysis. At the event selection level in order to improve the identification some cuts on hadron momentum and on likelihood distributions have been applied.

Cut on momentum

As an upper limit for the particle momenta the value $50\,\mathrm{GeV}/c$ has been chosen, which corresponds to 1.5σ separation between K and π. As a lower limit the cut little above Cherenkov threshold corresponding to the particle have been applied in order to avoid particles with no Cherenkov photons emitted. The constraints applied are the following:

- $p > p_{th_\pi}$ + $0.5\,\mathrm{GeV}/c$ for pions;
- $p > p_{th_K}$ + $1.0\,\mathrm{GeV}/c$ for kaons.

The Cerenkov threshold $p_{th_{\pi/K}}$ have been calculated for for a particular particle mass using the expression:

$$p_{th_{\pi/K}} = \frac{m_{\pi/K}}{\sqrt{n^2-1}}. \tag{6.3}$$

where n is the corresponding refractive index stored in the miniDST for each run.

Cut on likelihood distributions

The hadron identification using the RICH detector is based on a likelihood method. The detailed examination of the data has shown that some special cuts on $\frac{LH_{max}}{LH_{back}}$ and $\frac{LH_{max}}{LH_{2nd_{max}}}$ quantities can improve the identification. The first quantity expose the separation of the background hypothesis. For example if the value of $\frac{LH_{max}}{LH_{back}}$ is near one, it means that the likelihoods of the identified particle and the background are nearly the same and the distinction between particle and background hypothesis is not so straightforward.

The second quantity shows the separation between the examined particle and another type of particle which hypothesis has the second maximum likelihood. In other words that shows how much close are these two mass hypothesis. Again a value around one means that two likelihoods are nearly equal and the distinction is not clear.

The following likelihood cuts for the π/K identification have been finally adopted in addition to the mentioned above requirements on particles momenta.

Particle is identified as pion if:

- $\frac{LH_\pi}{LH_{back}} > 1.03$;
- $\frac{LH_\pi}{LH_{2^{nd}max}} > 1.002$.

Particle is identified as kaon if:

- $\frac{LH_K}{LH_{back}} > 1.04$;
- $\frac{LH_K}{LH_{2^{nd}max}} > 1.003$.

6.3.11 Final Statistics for Identified Pions and Kaons

In Table 6.5 the final statistics for positive and negative pions and kaons after all aforementioned cuts are presented for all the periods in 2003 and 2004 years.

Year	Period	Positive pions	Negative pions	Positive kaons	Negative kaons
2003	P1G/P1H	1707142	1485228	309563	203485
2004	W33/W34	1536076	1328755	272068	176838
2004	W35/W36	2024054	1752848	359420	234662
Sum		5267272	4566831	941051	614985

Table 6.5: Final statistics for the years 2003 and 2004 for all positive and negative pions and kaons

6.4 Binning

The asymmetries have been evaluated as a functions of x, z and P_{hT} kinematical variables. Binning for each variable has been done by dividing corresponding range into the bins and integrating over the other two variables. Bins have been chosen so that they contain a comparable statistics. Finally asymmetries were extracted in 9 x-bins, 8 z-bins and 9 P_{hT}-bins:

$$
\begin{array}{lll}
0.003 < & x_{Bj} & < 0.008 \\
0.008 \leq & x_{Bj} & < 0.013 \\
0.013 \leq & x_{Bj} & < 0.020 \\
0.020 \leq & x_{Bj} & < 0.032 \\
0.032 \leq & x_{Bj} & < 0.050 \\
0.050 \leq & x_{Bj} & < 0.080 \\
0.080 \leq & x_{Bj} & < 0.130 \\
0.130 \leq & x_{Bj} & < 0.210 \\
0.210 \leq & x_{Bj} & < 1.000
\end{array}
$$

$$
\begin{array}{lll}
0.20 \leq & z & < 0.25 \\
0.25 \leq & z & < 0.30 \\
0.30 \leq & z & < 0.35 \\
0.35 \leq & z & < 0.40 \\
0.40 \leq & z & < 0.50 \\
0.50 \leq & z & < 0.65 \\
0.65 \leq & z & < 0.80 \\
0.80 \leq & z & < 1.00
\end{array}
$$

$$
\begin{array}{lll}
0.10 < & P_{hT} & \leq 0.20 \\
0.20 < & P_{hT} & \leq 0.30 \\
0.30 < & P_{hT} & \leq 0.40 \\
0.40 < & P_{hT} & \leq 0.50 \\
0.50 < & P_{hT} & \leq 0.60 \\
0.60 < & P_{hT} & \leq 0.75 \\
0.75 < & P_{hT} & \leq 0.90 \\
0.90 < & P_{hT} & \leq 1.30 \\
1.30 < & P_{hT} & \leq \text{end.}
\end{array}
$$

Chapter 7

Extraction of Transverse Spin Asymmetries at COMPASS

In this chapter we describe the procedure applied in COMPASS for extraction of the transverse-spin asymmetries from experimental data.

Firstly we introduce the relations between the experimentally measured (*raw*) asymmetries and real physics asymmetries defined in Sec. 2.2. The relevant azimuthal angles and scaling factors are described in corresponding sections.

After this we review two analysis methods used in COMPASS for the extraction of transverse spin asymmetries and present the results obtained using each method. Asymmetries were evaluated as a functions of x, z and P_{hT} kinematic variables for *unidentified* charged hadrons, and *identified* charged pions and kaons. In subsequent sections the corresponding systematic checks, cross-checks and other performed studies are presented.

7.1 Asymmetry Calculation

The real physics asymmetries are evaluated from experimentally extracted ones using some special scaling factors. In this section we define the corresponding relations between the extracted and real asymmetries and describe the respective correction factors. All these relations and quantities are general for both one- and two-dimensional analysis procedures and do not need to be changed according to the method.

7.1.1 Calculation of the raw asymmetries

As it was shown in the Sec. 2.2 the transverse spin dependent part of the SIDIS cross-section can be represented by Eq. (2.32):

$$\begin{aligned} d\sigma(\phi_h, \phi_S, ...) \;&\propto\; (1 + |\boldsymbol{S}_T| \sum_{i=1}^{5} D^{w_i(\phi_h,\phi_S)} A_{UT}^{w_i(\phi_h,\phi_S)} w_i(\phi_h, \phi_S) \\ &+\; P_l |\boldsymbol{S}_T| \sum_{i=6}^{8} D^{w_i(\phi_h,\phi_S)} A_{LT}^{w_i(\phi_h,\phi_S)} w_i(\phi_h, \phi_S) + ...\big). \end{aligned}$$

where $\mathbf{S}_T$ is the target transverse polarization, $w_i(\phi_h, \phi_S)$ are the eight azimuthal modulations, $D^{w_i(\phi_h,\phi_S)}$ are the factored out depolarization factors, and $A_{BT}^{w_i(\phi_h,\phi_S)}$ are the azimuthal asymmetries defined as the ratios of corresponding structure functions to unpolarized one:

$$A_{BT}^{w_i(\phi_h,\phi_S)} \equiv \frac{F_{BT}^{w_i(\phi_h,\phi_S)}}{F_{UU,T}},$$

where $B = L$ or $B = U$ corresponds to beam polarization dependent Double Spin Asymmetry (DSA) or independent Single Spin Asymmetry (SSA) terms. The respective eight modulations presented in Eqs. (2.25–2.31) are the following ones:

$$\begin{aligned}
w_1(\phi_h, \phi_S) &= \sin(\phi_h - \phi_S),\\
w_2(\phi_h, \phi_S) &= \sin(\phi_h + \phi_S),\\
w_3(\phi_h, \phi_S) &= \sin(3\phi_h - \phi_S),\\
w_4(\phi_h, \phi_S) &= \sin(\phi_S),\\
w_5(\phi_h, \phi_S) &= \sin(2\phi_h - \phi_S),\\
w_6(\phi_h, \phi_S) &= \cos(\phi_h - \phi_S),\\
w_7(\phi_h, \phi_S) &= \cos(\phi_S),\\
w_8(\phi_h, \phi_S) &= \cos(2\phi_h - \phi_S)
\end{aligned}$$

These transverse spin modulations lead to respective counting rate asymmetries of the form:

$$\frac{d\sigma^{\Uparrow} - d\sigma^{\Downarrow}}{d\sigma^{\Uparrow} + d\sigma^{\Downarrow}} = A_{UT,\,raw}^{w_i(\phi_h,\phi_S)} \qquad i = 1,..,5 \tag{7.1}$$

$$\frac{d\sigma^{\Uparrow} - d\sigma^{\Downarrow}}{d\sigma^{\Uparrow} + d\sigma^{\Downarrow}} = A_{LT,\,raw}^{w_i(\phi_h,\phi_S)} \qquad i = 6,..,8 \tag{7.2}$$

where $\Uparrow$ ($\Downarrow$) defines up (down) target polarization.

The number-of-event asymmetries extracted from the data as an amplitudes of corresponding azimuthal modulations (raw asymmetries) are then given by Eqs. (2.48 – 2.48):

$$\begin{aligned}
A_{UT,\,raw}^{w_i(\phi_h,\phi_S)} &= D^{w_i(\phi_h,\phi_S)}(y) f |S_T| A_{UT}^{w(\phi_h,\phi_S)}, \quad (i = 1,5),\\
A_{LT,\,raw}^{w(\phi_h,\phi_S)} &= D^{w(\phi_h,\phi_S)}(y) f P_l |S_T| A_{LT}^{w(\phi_h,\phi_S)}, \quad (i = 6,8),
\end{aligned}$$

where P_l is the beam polarization and f is the target polarization dilution factor.

One can see that aforementioned eight modulations are based on just five combinations of azimuthal hadron (ϕ_h) and spin (ϕ_S) angles which are:

$$\Phi_1 = \phi_h - \phi_S \tag{7.3}$$
$$\Phi_2 = \phi_h + \phi_S \tag{7.4}$$
$$\Phi_3 = 3\phi_h - \phi_S \tag{7.5}$$
$$\Phi_4 = \phi_S \tag{7.6}$$
$$\Phi_5 = 2\phi_h - \phi_S \tag{7.7}$$

Two of these combinations, are presented only with *sin* modulations, while the other three have both *sin* and *cos* terms. Therefore, we can define the following five Φ_j dependent modulations:

$$\begin{aligned}
W_1(\Phi_1) &= A_{raw}^{w_1(\phi_h,\phi_S)} \sin(\Phi_1) + A_{raw}^{w_6(\phi_h,\phi_S)} \cos(\Phi_1) \\
W_2(\Phi_2) &= A_{raw}^{w_2(\phi_h,\phi_S)} \sin(\Phi_2) \\
W_3(\Phi_3) &= A_{raw}^{w_3(\phi_h,\phi_S)} \sin(\Phi_3) \\
W_4(\Phi_4) &= A_{raw}^{w_4(\phi_h,\phi_S)} \sin(\Phi_4) + A_{raw}^{w_7(\phi_h,\phi_S)} \cos(\Phi_4) \\
W_5(\Phi_5) &= A_{raw}^{w_5(\phi_h,\phi_S)} \sin(\Phi_5) + A_{raw}^{w_8(\phi_h,\phi_S)} \cos(\Phi_5)
\end{aligned} \tag{7.8}$$

The azimuthal angles ϕ_h and ϕ_S on which the Φ_j angles and corresponding $\mathrm{W}_j(\Phi_j)$ modulations are based, were defined for each event according to the procedure described in next section.

7.1.2 Calculation of the Azimuthal Angles ϕ_h and ϕ_S

In the previous section five combinations of ϕ_h and ϕ_S azimuthal angles on which the transverse spin dependent modulations are based have been listed Eqs. (7.4 – 7.7). In order to calculate this combinations firstly one need to obtain the azimuthal angles of produced hadron momentum (ϕ_h) and nucleon-spin vector in the initial state (ϕ_S) from the data. The coordinate system in which azimuthal angles are calculated is presented in the Fig. 2.1. The x-axis is defined from the difference of the momentum vectors of beam and scattered muon $\vec{l} - \vec{l'}$, the z-axis is defined by the virtual photon momentum $\vec{q}$, and the y-axis orthogonal to these two completes the definition of the frame of reference. The azimuthal angles are calculate around z-axis like it is shown on the plot.

With $\vec{l}$, $\vec{q}$, $\vec{p_h}$ being the momenta of the incident muon, virtual photon and outgoing hadron and with $\vec{S}$ being the nucleon spin one can calculate azimuthal ϕ_h and ϕ_S angles in the following way:

$$\cos\phi_h = \frac{\vec{p}_h \times \vec{q}}{|\vec{p}_h \times \vec{q}|} \cdot \widehat{k} \tag{7.9}$$
$$\cos\phi_S = \frac{\vec{S} \times \vec{q}}{|\vec{S} \times \vec{q}|} \cdot \widehat{k} \tag{7.10}$$

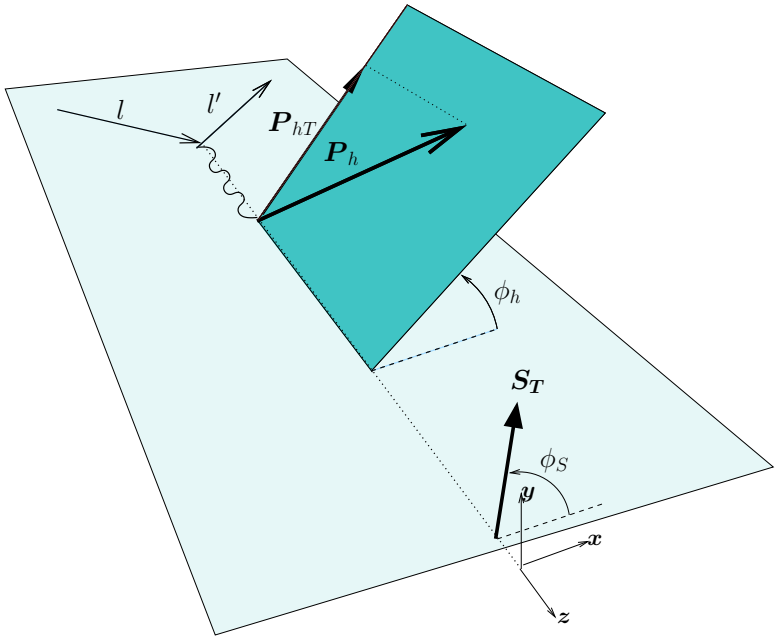

Figure 7.1: Definition of azimuthal angles for semi-inclusive deep inelastic scattering. P_{hT} and S_T are the transverse components of hadron momentum P_h and the target polarization with respect to the photon momentum.

where the $\widehat{k}$ is the unit-vector defined as:

$$\widehat{k} = \frac{\vec{l} \times \vec{q}}{|\vec{l} \times \vec{q}|}. \tag{7.11}$$

The ϕ_h and ϕ_S can then be easily derived by calculating the $\arccos$. The proper sign of the azimuthal angles can be defined according to:

$$sign(\phi_h) = sign(\widehat{k} \cdot \vec{p_h}) \tag{7.12}$$

$$sign(\phi_S) = sign(\widehat{k} \cdot \vec{S}) \tag{7.13}$$

The Φ_j angles from Eqs. (7.4 – 7.7) may by definition be obtained from these two angles. The distributions of the ϕ_h and ϕ_S in COMPASS are shown in Fig. 7.2. The distribution of the azimuthal angle of the produced hadron looks almost uniform while the ϕ_S shows deep hole in the region near $-\pi/2$.

The non-uniformity of the acceptance in ϕ_S is caused by the fraction of muons that have been scattered in horizontal plane at small angles to the right. The magnet field bend such muons to the left and they pass through the beam hole without giving a signal in detectors, and thus such an events most probably are lost.

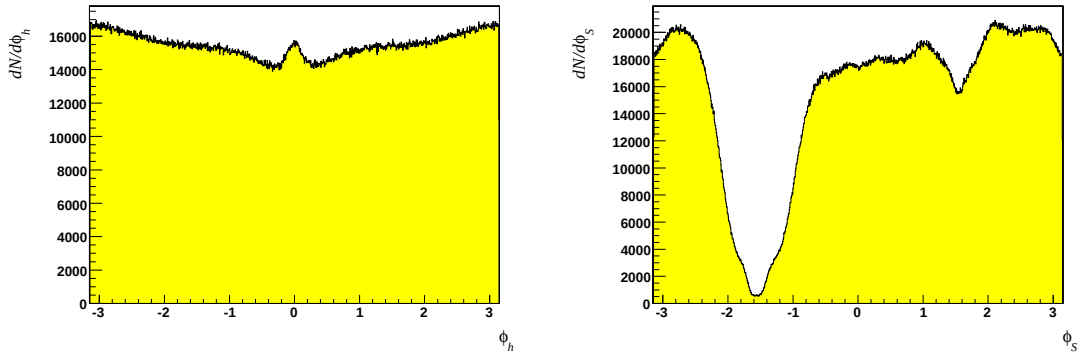

Figure 7.2: Distribution of the azimuthal angles of produced hadron - ϕ_h (left) and nucleon spin - ϕ_S (right). Shown distributions contains events from both cells collected for both polarization states from COMPASS 2002-2004 transverse data.

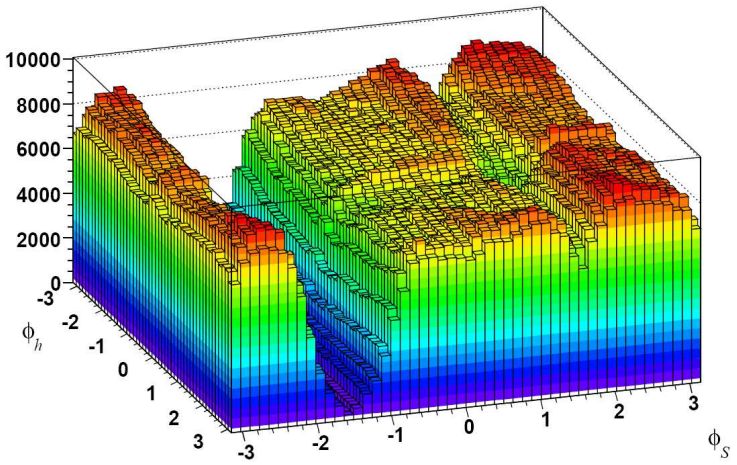

Figure 7.3: Scatter plot of ϕ_h vs. ϕ_S distributions from COMPASS 2002-2004 transverse data.

7.1.3 From the Raw Asymmetry to the Physics Asymmetry

The raw asymmetries extracted from the data as amplitudes of corresponding azimuthal modulations are related with the real physics asymmetries through the expressions Eqs. (2.48 – 2.48):

$$\begin{aligned} A_{UT,\,raw}^{w_i(\phi_h,\phi_S)} &= D^{w_i(\phi_h,\phi_S)}(y) f |S_T| A_{UT}^{w(\phi_h,\phi_S)}, \quad (i=1,5), \\ A_{LT,\,raw}^{w(\phi_h,\phi_S)} &= D^{w(\phi_h,\phi_S)}(y) f P_l |S_T| A_{LT}^{w(\phi_h,\phi_S)}, \quad (i=6,8), \end{aligned}$$

The scaling factors are: the target polarization dilution factor f, the target polarization S_T, the beam polarization P_l and the depolarization factor $D^{w(\phi_h,\phi_S)}(y)$. The f, S_T and

P_l are described in the next sections, while below the full set of transverse momentum dependent asymmetries with the corresponding depolarization factors is presented.

- $\mathbf{A_{UT}^{\sin(\phi_h+\phi_S-\pi)}}$ **asymmetry (**$Collins$**):** The Collins single-spin asymmetry is extracted from the raw asymmetry through the expression

$$A_{UT}^{\sin(\phi_h+\phi_S-\pi)} = \frac{A_{UT,raw}^{\sin(\phi_h+\phi_S-\pi)}}{D^{\sin(\phi_h+\phi_S)}(y)\cdot f\cdot|S_T|}, \tag{7.14}$$

  where $D^{\sin(\phi_h+\phi_S)}(y)$ is the depolarization factor calculated as

$$D^{\sin(\phi_h+\phi_S)}(y) = \frac{2(1-y)}{1+(1-y)^2}. \tag{7.15}$$

  The Collins angle ($\Phi_C = \phi_h + \phi_S - \pi$) is defined according to the notation applied in our published papers Refs. [5],[6].

- $\mathbf{A_{UT}^{\sin(3\phi_h-\phi_S)}}$ **asymmetry:** This single-spin asymmetry is extracted from the raw asymmetry through the expression

$$A_{UT}^{\sin(3\phi_h-\phi_S)} = \frac{A_{UT,raw}^{\sin(3\phi_h-\phi_S)}}{D^{\sin(3\phi_h+\phi_S)}(y)\cdot f\cdot|S_T|}. \tag{7.16}$$

  where $D^{\sin(3\phi_h+\phi_S)}(y)$ is the depolarization factor calculated with the same formula as for Collins effect:

$$D^{\sin(3\phi_h+\phi_S)}(y) = D^{\sin(\phi_h+\phi_S)}(y) = \frac{2(1-y)}{1+(1-y)^2}. \tag{7.17}$$

- $\mathbf{A_{UT}^{\sin(\phi_h-\phi_S)}}$ **asymmetry (**$Sivers$**):** The Sivers single-spin asymmetry is extracted from the raw asymmetry through the expression

$$A_{UT}^{\sin(\phi_h-\phi_S)} = \frac{A_{UT,raw}^{\sin(\phi_h-\phi_S)}}{D^{\sin(\phi_h-\phi_S)}(y)\cdot f\cdot|S_T|}, \tag{7.18}$$

  where the depolarization factor $D^{\sin(\phi_h-\phi_S)}(y)$= 1, In the measurement of Sivers asymmetry the photon couples to an unpolarized quark in a transversely polarized nucleon. Here the kinematical factor is $(1-y+y^2/2)$ which is identical to one of unpolarized scattering. Thus $D^{\sin(\phi_h-\phi_S)}(y)$ becomes

$$D^{\sin(\phi_h-\phi_S)}(y) = \frac{1+(1-y)^2}{1+(1-y)^2} = 1. \tag{7.19}$$

- $\mathbf{A_{LT}^{\cos(\phi_h-\phi_S)}}$ **asymmetry (**A_{LT}**):** The ALT double-spin asymmetry (see Sec. 3) is extracted from the raw asymmetry through the expression

$$A_{LT}^{\cos(\phi_h-\phi_S)} = \frac{A_{LT,raw}^{\cos(\phi_h-\phi_S)}}{D^{\cos(\phi_h-\phi_S)}(y)\cdot f\cdot|S_T|\cdot P_{beam}}, \tag{7.20}$$

where $D^{\cos(\phi_h-\phi_S)}(y)$ is the depolarization factor calculated as

$$D^{\cos(\phi_h-\phi_S)}(y) = \frac{y(2-y)}{1+(1-y)^2}. \tag{7.21}$$

- $\mathbf{A_{UT}^{\sin(\phi_S)}}$ **asymmetry:** This single-spin asymmetry is extracted from the raw asymmetry through the expression

$$A_{UT}^{\sin(\phi_S)} = \frac{A_{UT,raw}^{\sin(\phi_S)}}{D^{\sin(\phi_S)}(y)\cdot f\cdot|S_T|}, \tag{7.22}$$

where $D^{\sin(\phi_S)}(y)$ is the depolarization factor calculated as

$$D^{\sin(\phi_S)}(y) = \frac{2(2-y)\sqrt{1-y}}{1+(1-y)^2}. \tag{7.23}$$

- $\mathbf{A_{UT}^{\sin(2\phi_h-\phi_S)}}$ **asymmetry:** This single-spin asymmetry is extracted from the raw asymmetry through the expression

$$A_{UT}^{\sin(2\phi_h-\phi_S)} = \frac{A_{UT,raw}^{\sin(2\phi_h-\phi_S)}}{D^{\sin(2\phi_h-\phi_S)}(y)\cdot f\cdot|S_T|}, \tag{7.24}$$

where $D^{\sin(2\phi_h-\phi_S)}(y)$ is the depolarization factor calculated with the same formula as for $A_{UT}^{\cos(\phi_S)}$:

$$D^{\sin(2\phi_h-\phi_S)}(y) = \frac{2(2-y)\sqrt{1-y}}{1+(1-y)^2}. \tag{7.25}$$

- $\mathbf{A_{LT}^{\cos(\phi_S)}}$ **asymmetry:** This double-spin asymmetry is extracted from the raw asymmetry through the expression

$$A_{LT}^{\cos(\phi_S)} = \frac{A_{LT,raw}^{\cos(\phi_S)}}{D^{\cos(\phi_S)}(y)\cdot f\cdot|S_T|\cdot P_{beam}}, \tag{7.26}$$

where $D^{\cos(\phi_S)}(y)$ is the depolarization factor calculated as

$$D^{\cos(\phi_S)}(y) = 2\cdot\frac{y\sqrt{1-y}}{1+(1-y)^2}, \tag{7.27}$$

and P_{beam} is the beam polarization.

- $\mathbf{A_{LT}^{\cos(2\phi_h-\phi_S)}}$ **asymmetry:** This double-spin asymmetry is extracted from the raw asymmetry through the expression

$$A_{LT}^{\cos(2\phi_h-\phi_S)} = \frac{A_{LT,raw}^{\cos(2\phi_h-\phi_S)}}{D^{\cos(2\phi_h-\phi_S)}(y)\cdot f\cdot|S_T|\cdot P_{beam}}, \tag{7.28}$$

where $D^{\cos(2\phi_h-\phi_S)}(y)$ is the depolarization factor calculated with the same formula as for $A_{LT}^{\cos(\phi_S)}$:

$$D^{\cos(2\phi_h-\phi_S)}(y) = 2\cdot\frac{y\sqrt{1-y}}{1+(1-y)^2}. \tag{7.29}$$

The depolarization factors $D^{w(\phi_h,\phi_S)}(y)$ are calculated from the kinematics of each event using the corresponding formula.

7.1.4 Target polarization S_T

The direct measurement of the target polarization is not possible in transverse running mode. Thus the polarization values are obtained through the interpolation of the target polarization curve over the whole beam-time with both running modes (longitudinal and transverse). The uncertainties in the target polarization is of 5%. In Table 7.1 we present the polarization values for both cells defined for different sets of runs of 2002-2004 transverse data.

Period	Runs	Upstream cell	Downstream cell
P2B	21178-21207	-49.79	54.58
P2B	21333-21393	-47.79	47.40
P2B	21407-21495	-47.09	46.33
P2C	21670-21765	52.50	-44.09
P2C	21777-21878	50.36	-43.06
P2H.1	23490-23575	-49.83	52.11
P2H.2	23664-23839	47.45	-41.41
P1G	30772-31038	-49.70	+52.78
P1H	31192-31247	+49.39	-42.60
P1H	31277-31524	+51.31	-44.63
W33	38991-39168	+50.70	-43.52
W34	39283-39290	-44.80	+45.97
W34	39325-39430	-38.60	+40.35
W34	39480-39545	-46.14	+47.41
W35	39548-39780	-46.44	+47.44
W36	39850-39987	+49.89	-42.76

Table 7.1: Target transverse polarization values in 2002 - 2004 data taking sub-periods. The numbers in second row indicates the unique IDs given to each run.

7.1.5 Target Dilution Factor f

The target dilution factor f (the fraction of polarisable material inside the target) for the pure ^{6}Li is equal to 0.5, since ^{6}Li can be considered to a good approximation as a spin-0 ^{4}He nucleus and a deuteron so that one-half of all nucleolus are polarisable. Anyway due to the presence of non-polarizable materials in the target cells the actual value of f is smaller. In the analysis the constant dilution factor $f = 0.38$ was assumed. The error on the dilution factor, which takes into account the uncertainty on the target composition, is of the order of 6%.

7.1.6 Beam Polarization P_l

The beam polarization is defined for each event by the **PaAlgo::GetBeamPol** PHAST routine. It provides the average muon beam polarization using as input parameters the

momentum of the beam muon track and the year of data taking (2002, 2003 or 2004).

7.2 One-Dimensional Analysis *(1D)*

This section is dedicated to the *one-dimensional* analysis procedure that makes use of so-called "Ratio Product" (RPM) or "Double Ratio" (DR) method. The method combines the information from both target-cells, collected in two sub-periods with opposite cell-spin configuration during the one transverse data taking period. It allows to reduce to a minimum possible systematic effects originating from the difference in acceptances of two cells.

Actually method is the same as the one applied for already published Collins and Sivers asymmetries Ref. [6]. Anyway the results of the newly obtained Collins and Sivers effects are slightly different from the ones that have been published. The reason is that in the recent analysis the event selection procedure have been changed by applying the new "y-peak" cut (see Sec. 6.3.7).

All the eight asymmetries have been evaluated separately, in each kinematical bin, for each "transverse" data taking period, for positive and negative $"unidentified"$ hadrons as well as for positive and negative hadrons identified as pions and kaons. Results have been checked for the systematic instabilities and "cross-checked" with COMPASS-Bonn group.

7.2.1 Ratio Product Method (RPM)

According to Eq. (2.32) and Eq. (7.8) for each subperiod of our measurement and each target cell, we can describe the counting rate dependence on Φ_j by

$$N^{\pm}_{u/d}(\Phi_j) = F^{\pm}_{u/d} n^{\pm}_{u/d} a^{\pm}_{u/d}(\Phi_j)\sigma(1 \pm W_j(\Phi_j)) \tag{7.30}$$

where +(-) indicates up (down) target polarization and u(d) the upstream and downstream target cells, σ is the unpolarized cross-section, $F^{\pm}_{u/d}$ is the flux and $n^{\pm}_{u/d}$ the target density for the given cell (u/d) and polarization ($\pm$). Finally, $a^{\pm}_{u/d}(\Phi_j)$ is the Φ_j dependent acceptance for the corresponding cell and polarization state.

For the evaluation of the raw asymmetries the so-called Ratio Product (RPM) or Double Ratio (DR) method have been used. We used for one measurement period (i.e. two subperiods with opposite spin direction) the information of both target cells (u, d) and both sub-periods simultaneously by constructing the estimator:

$$R(\Phi_j) = \frac{N^+_u(\Phi_j)N^+_d(\Phi_j)}{N^-_u(\Phi_j)N^-_d(\Phi_j)}, \tag{7.31}$$

with the corresponding error propagation:

$$\sigma_R(\Phi_j) = \sqrt{\frac{1}{N^+_u(\Phi_j)} + \frac{1}{N^+_d(\Phi_j)} + \frac{1}{N^-_u(\Phi_j)} + \frac{1}{N^-_d(\Phi_j)}}. \tag{7.32}$$

By substituting Eq. (7.30) in double ratio quantities Eq. (7.31) we obtain:

$$R(\Phi_j) = \frac{F_u^+ n_u^+ a_u^+(\Phi_j)\sigma(1+W_j(\Phi_j)) \cdot F_d^+ n_d^+ a_d^+(\Phi_j)\sigma(1+W_j(\Phi_j))}{F_u^- n_u^- a_u^-(\Phi_j)\sigma(1-W_j(\Phi_j)) \cdot F_d^- n_d^- a_d^-(\Phi_j)\sigma(1-W_j(\Phi_j))}. \tag{7.33}$$

Which can be rewritten like:

$$R(\Phi_j) = C_F \cdot C_a \cdot \frac{(1+W_j(\Phi_j))(1+W_j(\Phi_j))}{(1-W_j(\Phi_j))(1-W_j(\Phi_j))}. \tag{7.34}$$

where

$$C_F = \frac{F_u^+ \cdot F_d^+}{F_u^- \cdot F_d^-}, \tag{7.35}$$

$$C_a = \frac{a_u^+(\Phi_j) \cdot a_d^+(\Phi_j)}{a_u^-(\Phi_j) \cdot a_d^-(\Phi_j)}. \tag{7.36}$$

According to the "target cuts" applied during the event selection (see Sec. 6.3.4) the beam flux is constant in both cells, so the C_F is equal to one. Making the Taylor expansion of equation Eq. (7.34) at the first order we obtain:

$$R(\Phi_j) \simeq C_a \cdot (1 + 4W_j(\Phi_j)). \tag{7.37}$$

At next step we accept the reasonable assumption on the ratio of acceptances of the upstream and downstream cells $a_u^+(\Phi_j)/a_d^-(\Phi_j)$ to be equal to corresponding ratio $a_u^-(\Phi_j)/a_d^+(\Phi_j)$ after the spin reversal in each Φ_j bin:

$$\frac{a_u^+(\Phi_j)}{a_d^-(\Phi_j)} = \frac{a_u^-(\Phi_j)}{a_d^+(\Phi_j)}. \tag{7.38}$$

In this case the acceptance differences in two cells cancel out so that $C_{a,j}$ is equal to one. Therefore finally we obtain:

$$R(\Phi_j) = const \cdot (1 + 4W_j(\Phi_j)). \tag{7.39}$$

The double ratio quantities are calculated in 16 bins over the $(-\pi, \pi)$ range of Φ_j. The amplitudes of the corresponding to $W_j(\Phi_j)$ modulations can be extracted then by performing a fit with appropriate functions:

$$R(\Phi_j) = par(0)(1 + 4par(1)\sin(\Phi_j)). \tag{7.40}$$

if $W_j(\Phi_j)$ contains only a $sin(\Phi_j)$ term, and

$$R(\Phi_j) = par(0)(1 + 4[par(1)\sin(\Phi_j) + par(2)\cos(\Phi_j)]). \tag{7.41}$$

if $W_j(\Phi_j)$ contains both $sin(\Phi_j)$ and $cos(\Phi_j)$ terms. The $par(0)$ in both of the cases correspond to the constant factor from Eq. (7.39) and it should be equal to one if the acceptance assumption Eq. (7.38) is indeed valid (see Sec. 7.4), while the $par(1)$ and $par(2)$ give the *raw asymmetries* as an amplitudes of the sin and cos terms respectively,

like it was defined in Eq. (7.8). Fit have been performed with χ^2-minimization method using the MINUIT package embedded into ROOT.

The main advantages of the RPM method is that: it combines all the data from the two target cells, it has "soft" requirements on the acceptance stability, it is independent of the relative luminosity in cells and in addition in RPM at first order (for small values of the involved asymmetries) all spin-independent effect, e.g. Cahn asymmetry, are factored out. Anyway the method has some systematic deviations due to the nonuniform acceptance in ϕ_S in COMPASS (see Sec. 7.1.2). This issue will be discussed separately in Sec. 7.5.

7.2.2 Evaluation of the Asymmetries and Results

The target transverse spin dependent asymmetries were evaluated as a functions of x, z and P_{hT} kinematical variables separately for positive and negative *unidentified* hadrons and positive and negative *RICH-identified* pions and kaons. For *unidentified* hadron asymmetries the whole COMPASS "transverse" 2002-2004 data-sample have been used, while for the *RICH-identified* pion and kaon asymmetries only the COMPASS 2003-2004 data which have passed the RICH-stability criteria described in Sec. 6.3.10 could be used (in 2002 data RICH information required for π/K identification was not yet available). The extraction was done with the RPM method using the information from both target cells collected in two sub-periods of one data-taking cycle.

Now let us review and summarize the asymmetry evaluation procedure aspects presented in above sections and define the sequence of steps. The sequence of operations is the same for *unidentified* and *RICH-identified* hadrons, thus we will explain it only in the example of *unidentified* hadrons. After the event selection for one data-taking period (cycle of two sub-periods with opposite cell-spin configuration separated by polarization reversal) is finished and sample is separated in positive and negative hadron sub-samples, from each of them 26 event-sets corresponding to 9 x-bins, 8 z-bins and 9 P_{hT}-bins are selected. Binning for each variable has been done by dividing corresponding kinematic range into the bins and integrating over the other two variables. Bins have been chosen so that they contain a comparable statistics (see Sec. 6.4). At this point we have 52 ($2(\pm charge)\times 26(x,z,P_{hT})$) samples with which two different operations are performed:

- First operation: Each of obtained 52 ($2(\pm charge)\times 26(x,z,P_{hT})$) samples is then divided into two sub-samples each including events from only one of two sub-periods with different cell-spin configuration ($\Uparrow\Downarrow$ and $\Downarrow\Uparrow$). Obtained data sets are then again sub-divided into two samples with events only from *Upstream* or *Downstream* cell. Constructed four sub-samples contain events only from one cell with one polarization state: $up\ \Uparrow$, $down\ \Downarrow$, $up\ \Downarrow$ and $down\ \Uparrow$. Now in each of this sub-samples the "raw" asymmetry correction-factors (we will label them α) corresponding to each of eight asymmetries are calculated event-by-event:

$$\alpha_{n,event}^{w_i(\phi_h,\phi_S)} = D_{n,event}^{w_i(\phi_h,\phi_S)}(y) f\,|S_T^{run}| \tag{7.42}$$

  for the (UT) asymmetries, and

$$\alpha_{n,event}^{w_i(\phi_h,\phi_S)} = D_{n,event}^{w_i(\phi_h,\phi_S)}(y) f\,|S_T^{run}|\,P_l^{event} \tag{7.43}$$

for the (LT) asymmetries. Here n indicates the particular sample (specified by charge of the hadrons, kinematical bin, target cell and polarization state), the target polarization values S_T^{run} are given run-by-run, beam polarization P_l^{event} is defined event-by-event as well as depolarization factors $D_{n,event}^{w_i(\phi_h,\phi_S)}(y)$, while the dilution factor f is constant. After this, the average value for each of eight factors is evaluated in each of four samples separately:

$$\left\langle \alpha_n^{w_i(\phi_h,\phi_S)} \right\rangle = \frac{\sum_{event=1}^{N_{events}} \alpha_{n,event}^{w_i(\phi_h,\phi_S)}}{N_{events}}, (i = 1, .., 8), \tag{7.44}$$

where the N_{events} is the number of the events in n-th sample. At the next step the mean of these four average values for each of eight factors is calculated:

$$\left\langle \alpha_{\pm,bin}^{w_i(\phi_h,\phi_S)} \right\rangle = \frac{\left\langle \alpha_{\pm,bin}^{w_i(\phi_h,\phi_S)} \right\rangle^{u,\Uparrow} + \left\langle \alpha_{\pm,bin}^{w_i(\phi_h,\phi_S)} \right\rangle^{d,\Downarrow} + \left\langle \alpha_{\pm,bin}^{w_i(\phi_h,\phi_S)} \right\rangle^{u,\Downarrow} + \left\langle \alpha_{\pm,bin}^{w_i(\phi_h,\phi_S)} \right\rangle^{d,\Uparrow}}{4},$$

where (i=1,..,8), u and d are the upstream and downstream target cell labels respectively, $\Uparrow$ and $\Downarrow$ indicates cell polarization, $\pm$ denotes hadron charge, and bin indicates the kinematical bin. This procedure is performed for all the 52 sub-samples and obtained 416 ($(2(\pm charge) \times 26(x, z, P_{hT}) \times 8(asymmetries)$) correction factors correspond to same number of raw asymmetry values which will be calculated in 26 kinematical bins for positive and negative hadrons.

- Second operation: Each of obtained 52 ($2(\pm charge) \times 26(x, z, P_{hT})$) samples is divided into 16 equal bins over the $(-\pi, \pi)$ range of each of five Φ_j angles. After that events from each bin are filled into two sub-samples corresponding to two sub-periods with different cell-spin configuration ($\Uparrow\Downarrow$ and $\Downarrow\Uparrow$) which are then subdivided into two samples with events only from *Upstream* or *Downstream* cell. Constructed four sub-samples contain events only from one cell with one polarization state: $up \Uparrow$, $down \Downarrow$, $up \Downarrow$ and $down \Uparrow$. At this point using the number of the events in each of these four sub-samples, the double ratio quantities ($\frac{N_u^+(\Phi_j)N_d^+(\Phi_j)}{N_u^-(\Phi_j)N_d^-(\Phi_j)}$) can be constructed in each Φ_j bin. Performing the fit with appropriate functions (Eq. (7.40) or Eq. (7.41)) we obtain the raw asymmetry value with its error for the corresponding charged hadron sample and kinematical bin. This procedure is then evaluated for five Φ_j angles with each of constructed 52 samples in order to evaluate all eight transverse asymmetries for positive and negative hadrons in each kinematical bin.

At next stage the evaluated 416 raw asymmetry values and their errors are divided by the corresponding mean correction factors calculated in each kinematical bin of positive and negative hadrons in order to obtain the real physics asymmetries.

The described procedure is then performed for all data-taking periods separately since the data from different periods can not be merged in one analysis because of somehow

different acceptance, experimental conditions and collected statistics. While the two subperiods of one period usually are produced with comparable statistics and within approximately same conditions. Anyway after the asymmetries are evaluated for different periods, the final results can be combined with an appropriate weighting. For the simplicity we will label periods like: 1 for P2B-P2C, 2 for P2H1-P2H2, 3 for P1G-P1H, 4 for W33-W34, 5 for W35-W36. In each period eight transverse spin asymmetries are evaluated separately for positive and negative *unidentified* hadrons, pions and kaons in each kinematical bin over x,z and P_{hT} (9+8+9=26 bins), this makes in total of $2 \times 26 \times 8 = 416$ asymmetry values (marked by index m) in each period for each type of particle. The weighted mean over all the periods is evaluated for each of this values using the formula:

$$A_w^m = \frac{\sum_{k=1}^{5} \frac{A_k^m}{\sigma^2_{A_k^m}}}{\sum_{k=1}^{5} \frac{1}{\sigma^2_{A_k^m}}}, \tag{7.45}$$

where A_w^m is the weighted mean asymmetry value, k is the number of period and A_k^m corresponds to an specific asymmetry value extracted from the whole data of k-th period.

The statistical error of weighted mean asymmetry - $\sigma_{A_w^m}$ must be calculated from the statistical errors of separate asymmetries - $\sigma_{A_k^m}$ in the following way:

$$\sigma_{A_w^m} = 1/\sqrt{\sum_{k=1}^{5} \frac{1}{\sigma^2_{A_k^m}}} \tag{7.46}$$

The above expressions are written for *unidentified* hadron asymmetries, while for the *RICH-identified* asymmetries summation should start not from the first but from the third period, since in first two periods RICH information was not yet available in COMPASS. The weighted mean asymmetries and respective statistical errors have been calculated for each x, z and P_{hT} bin of positive and negative: *unidentified* hadrons, identified pions and kaons.

In the figures 7.4 - 7.11 the extracted eight transverse momentum dependent asymmetries for positive and negative unidentified hadrons, pions and kaons are plotted as a function of x, z and P_{hT}. All results presented in this section have been evaluated by using the above described one-dimensional analysis procedure.

The red circles indicates the results for positive hadrons, (pions and kaons) whereas blue triangles shows the results for negative hadrons, (pions and kaons). The error bars shown in all the plots are statistical only. In all the plots the blue triangles are slightly shifted horizontally with the respect to the measured value.

The general observation from this plots is that all the transverse spin asymmetries extracted using the one-dimensional analysis method, from COMPASS data with transversely polarized deuteron target are small, which in a fact can be explained by the partial cancelation of u and d -quarks contributions into the deuteron asymmetry as it was shown on example of A_{LT} asymmetry in Sec. 3.1.

The results of experimentally measured A_{LT} asymmetry have been found to be in agrement with the predictions presented in Sec. 3 and Ref. [18] (see Sec. 8 and Figures 8.1

- 8.2). Other asymmetries obtained with TMD DFs from quark-diquark model are also in agreement with extracted ones Ref. [102].

$A_{UT}^{-\sin(\phi_h+\phi_S)}$ **(Collins) asymmetry with COMPASS data. One-dimensional fit.**

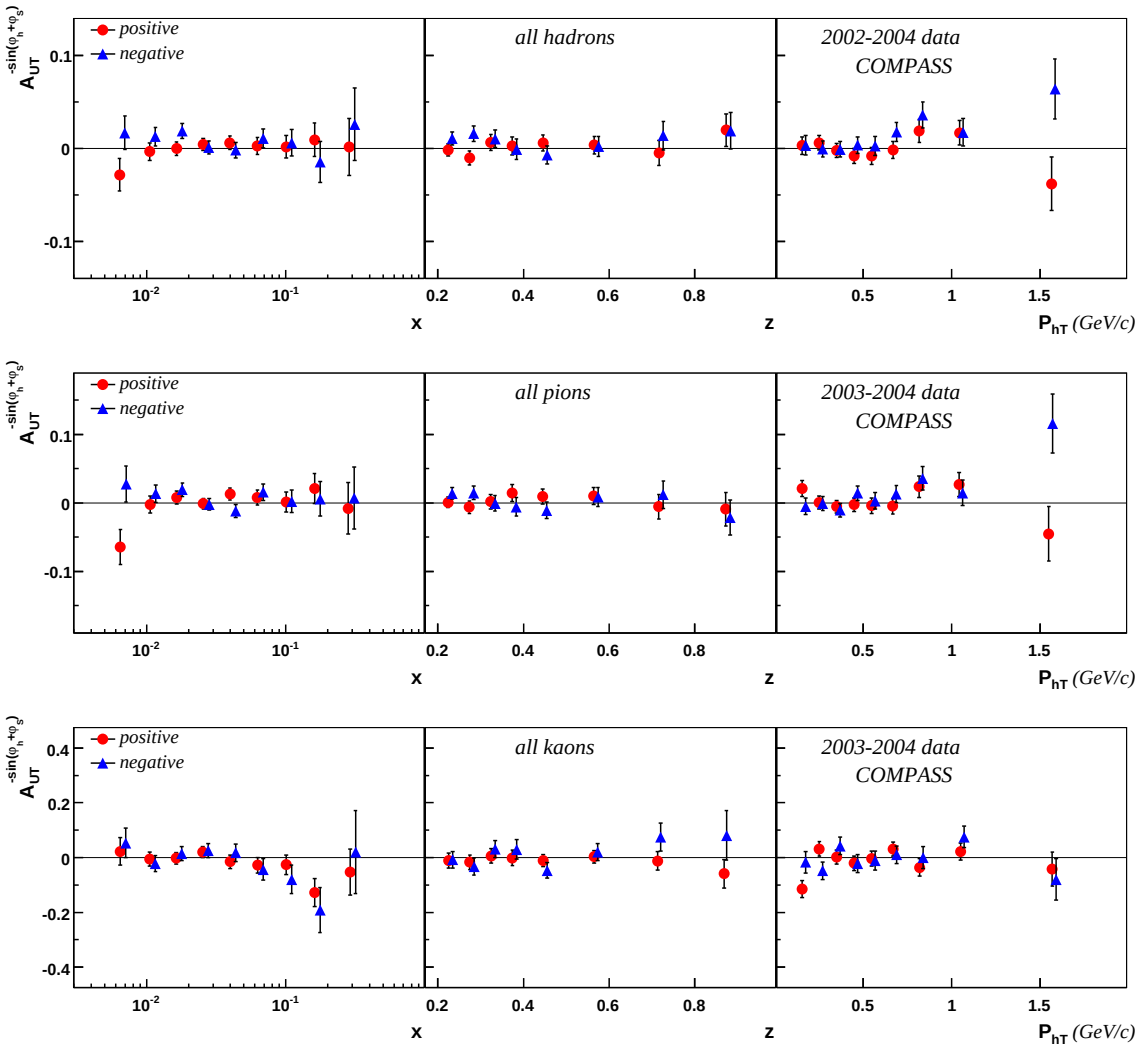

Figure 7.4: Extracted $A_{UT}^{-\sin(\phi_h+\phi_S)}$ (Collins) asymmetry for unidentified hadrons (top row), pions (middle row) and kaons (bottom row) as a function of x, z and P_{hT}

$A_{UT}^{\sin(3\phi_h-\phi_S)}$ asymmetry with COMPASS data. One-dimensional fit.

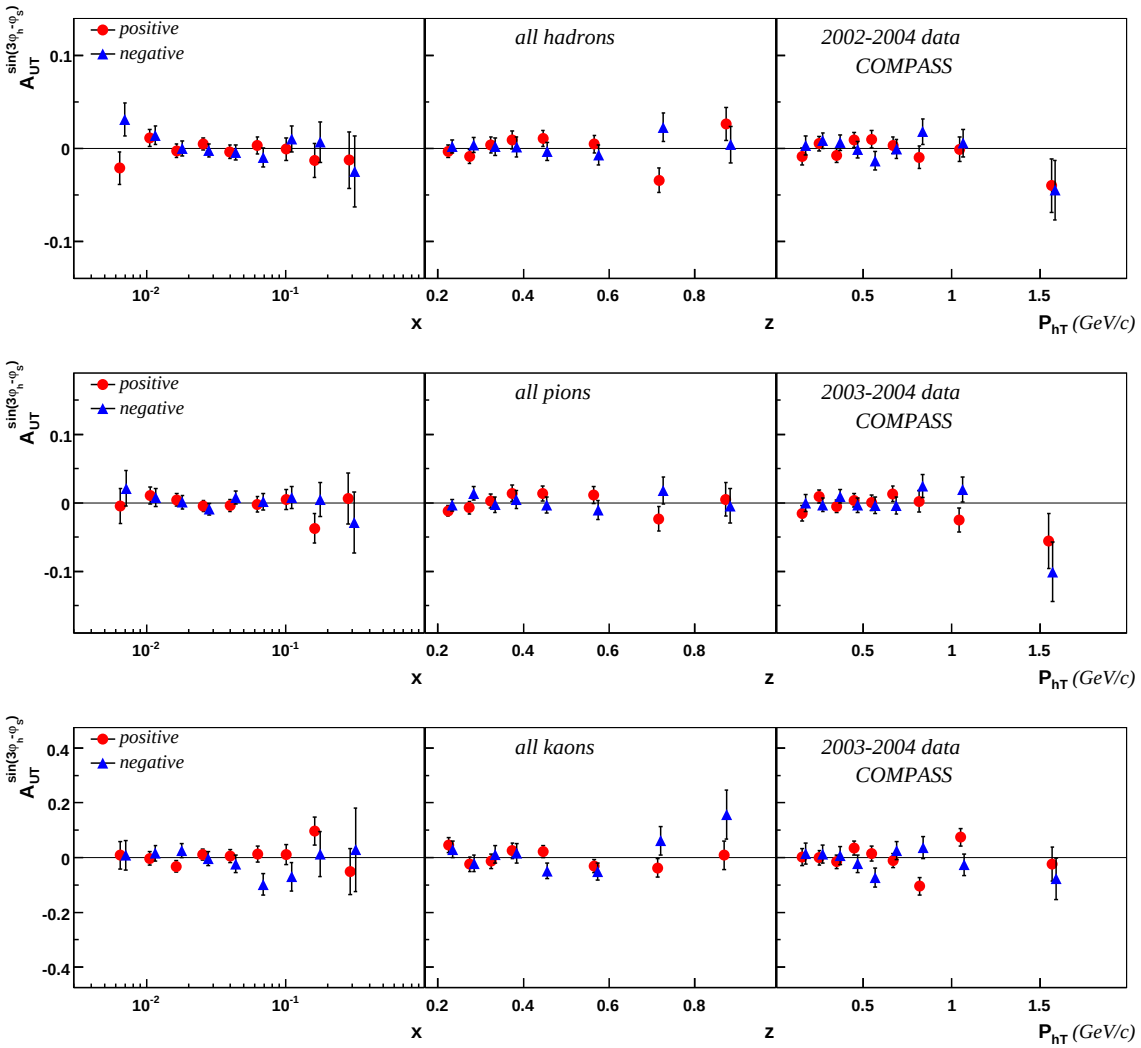

Figure 7.5: Extracted $A_{UT}^{\sin(3\phi_h-\phi_S)}$ asymmetry for unidentified hadrons (top row), pions (middle row) and kaons (bottom row) as a function of x, z and P_{hT}

$A_{UT}^{\sin(\phi_h-\phi_S)}$ **(Sivers) asymmetry with COMPASS data. One-dimensional fit.**

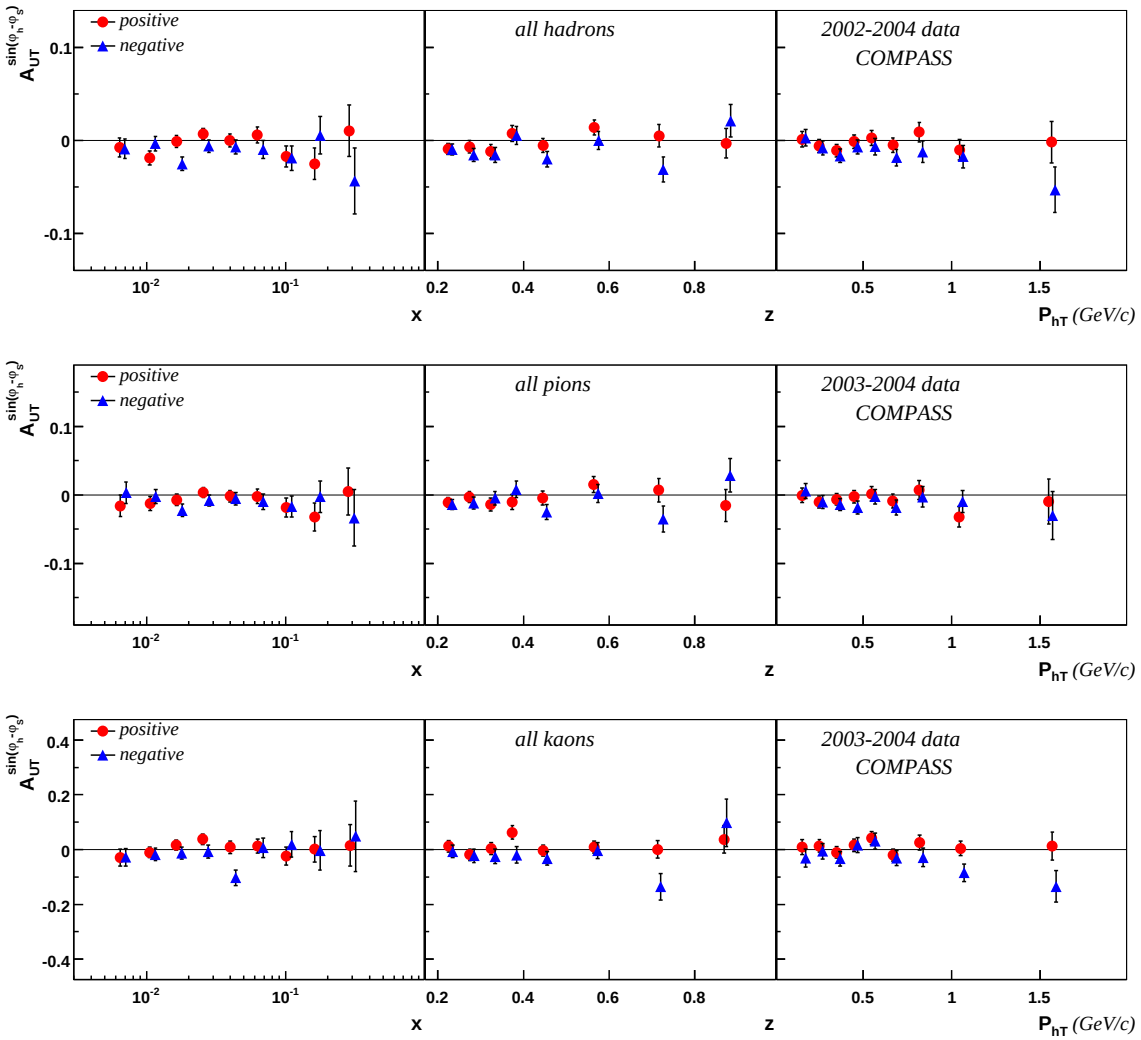

Figure 7.6: Extracted $A_{UT}^{\sin(\phi_h-\phi_S)}$ (Sivers) asymmetry for unidentified hadrons (top row), pions (middle row) and kaons (bottom row) as a function of x, z and P_{hT}

$A_{LT}^{\cos(\phi_h-\phi_S)}$ asymmetry with COMPASS data. One-dimensional fit.

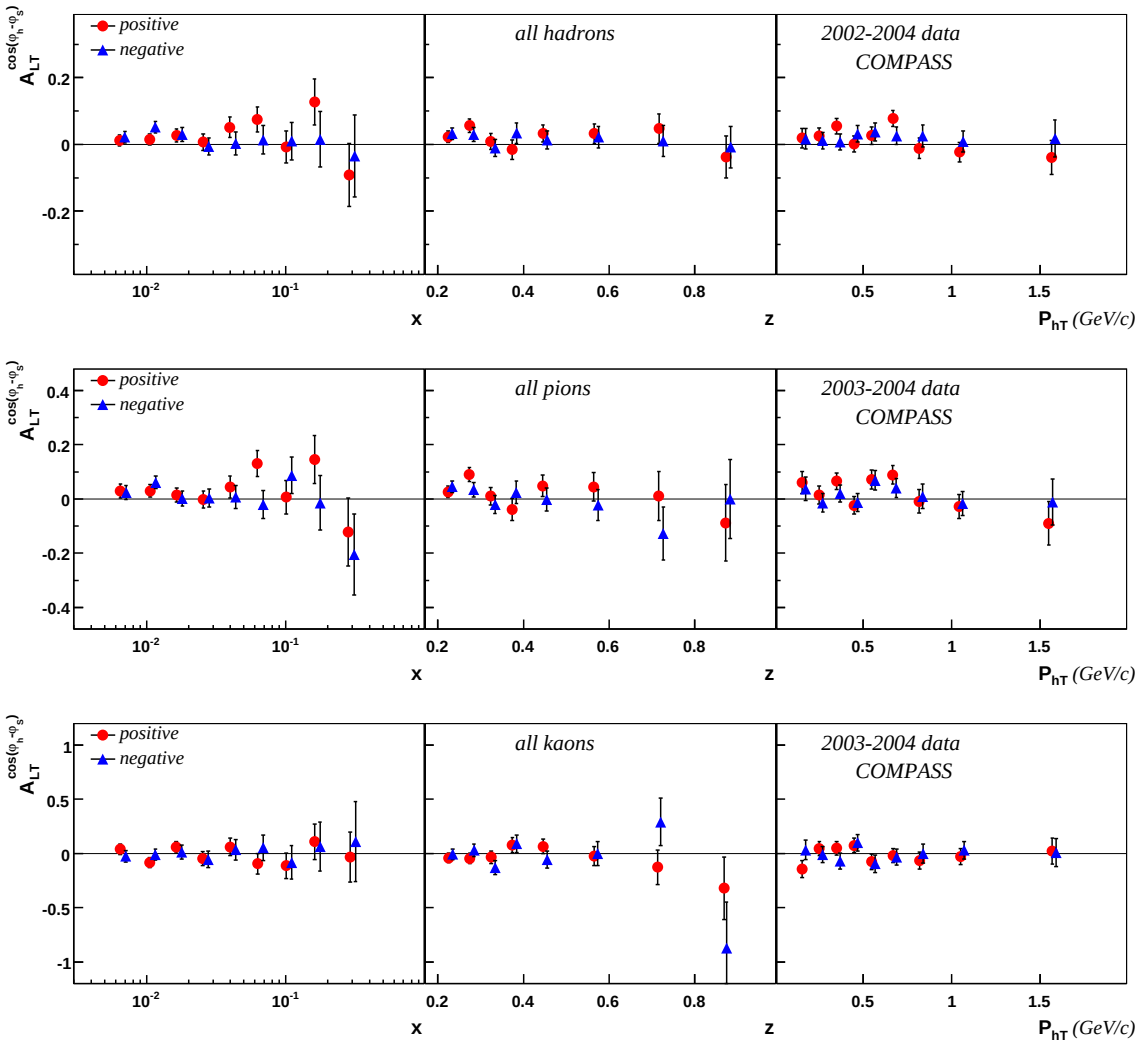

Figure 7.7: Extracted $A_{LT}^{\cos(\phi_h-\phi_S)}$ asymmetry for unidentified hadrons (top row), pions (middle row) and kaons (bottom row) as a function of x, z and P_{hT}

$A_{UT}^{\sin(\phi_S)}$ asymmetry with COMPASS data. One-dimensional fit.

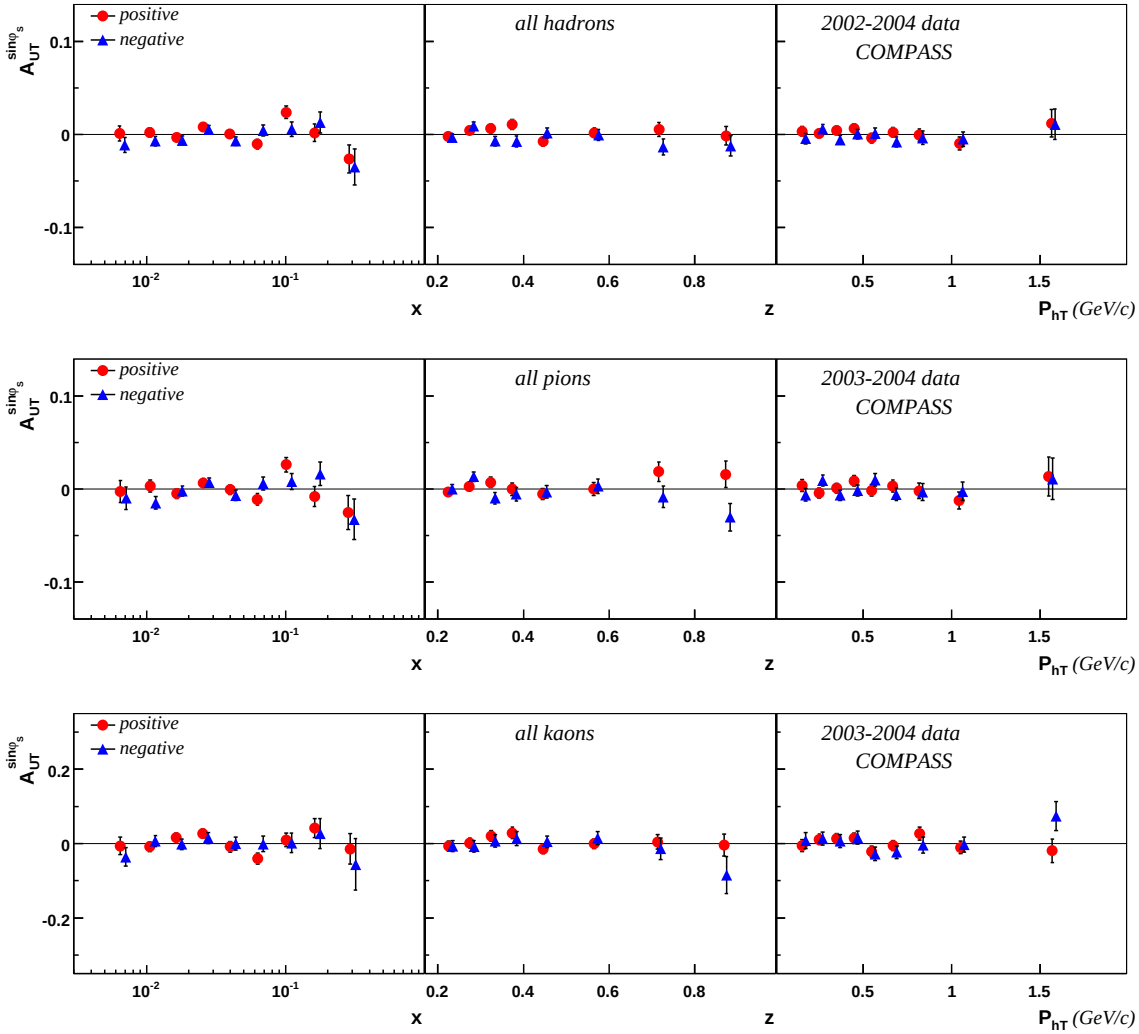

Figure 7.8: Extracted $A_{UT}^{\sin(\phi_S)}$ asymmetry for unidentified hadrons (top row), pions (middle row) and kaons (bottom row) as a function of x, z and P_{hT}

$A_{UT}^{\sin(2\phi_h-\phi_S)}$ asymmetry with COMPASS data. One-dimensional fit.

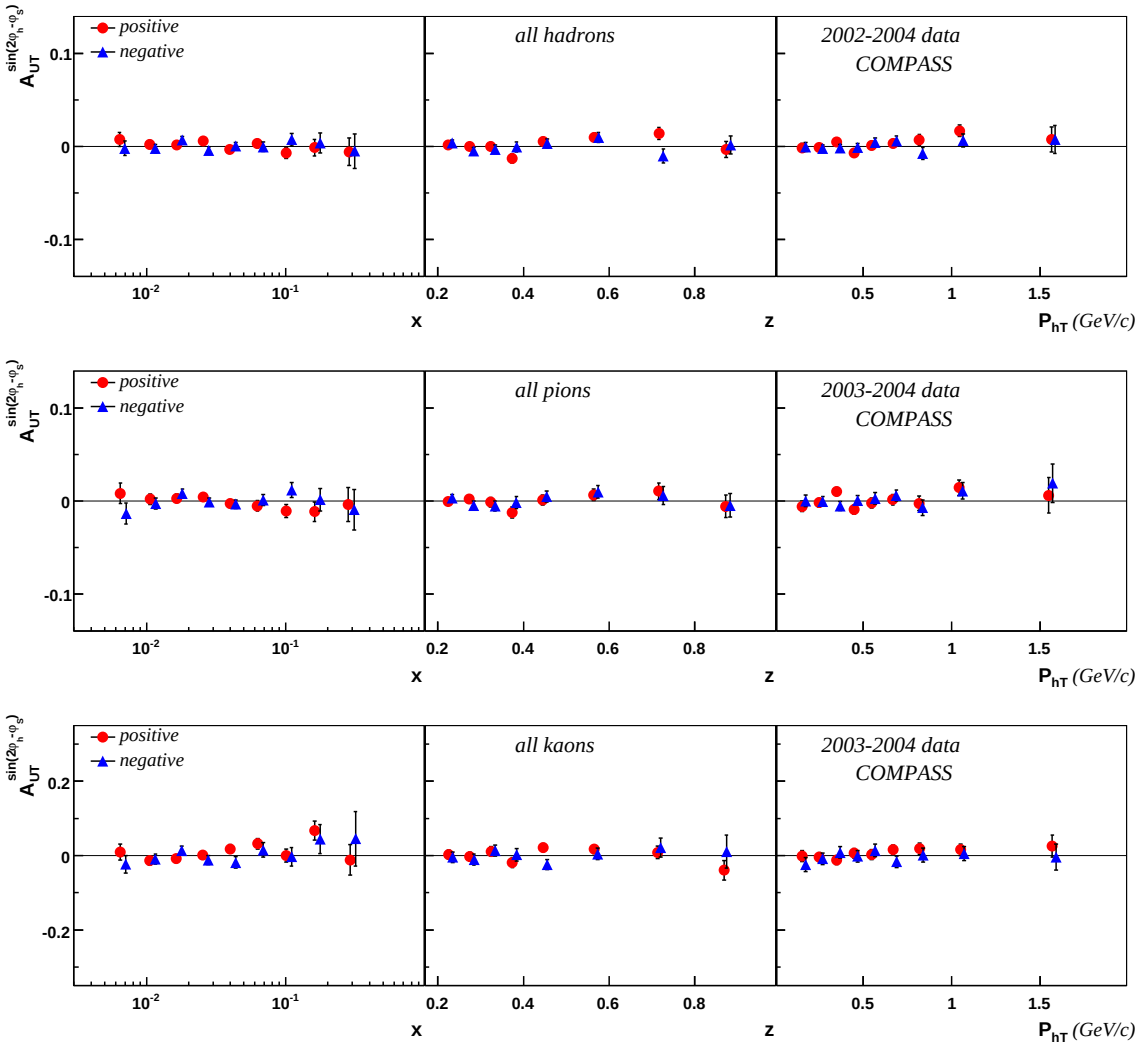

Figure 7.9: Extracted $A_{UT}^{\sin(2\phi_h-\phi_S)}$ asymmetry for unidentified hadrons (top row), pions (middle row) and kaons (bottom row) as a function of x, z and P_{hT}

$A_{LT}^{\cos(\phi_S)}$ asymmetry with COMPASS data. One-dimensional fit.

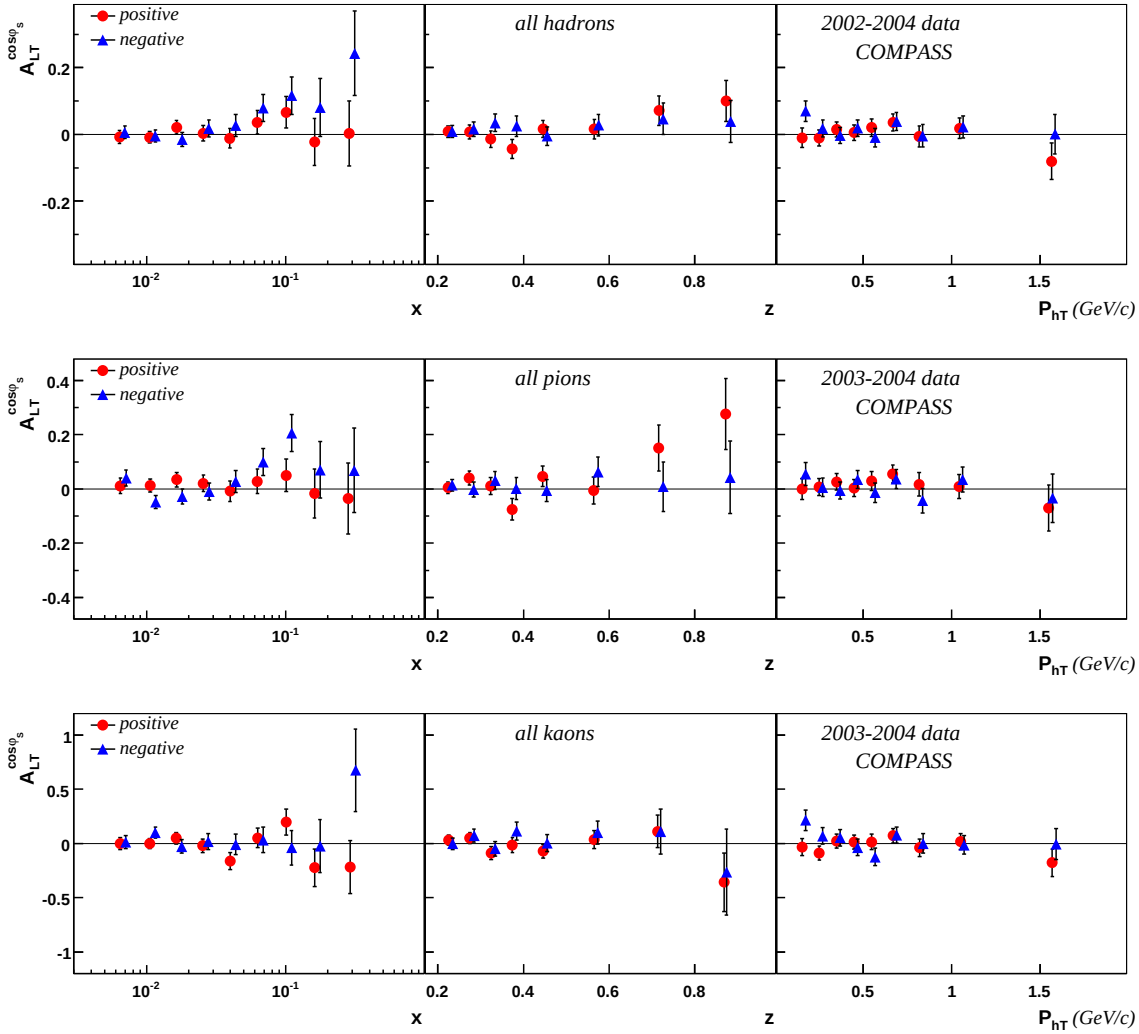

Figure 7.10: Extracted $A_{LT}^{\cos(\phi_S)}$ asymmetry for unidentified hadrons (top row), pions (middle row) and kaons (bottom row) as a function of x, z and P_{hT}

$A_{LT}^{\cos(2\phi_h-\phi_S)}$ asymmetry with COMPASS data. One-dimensional fit.

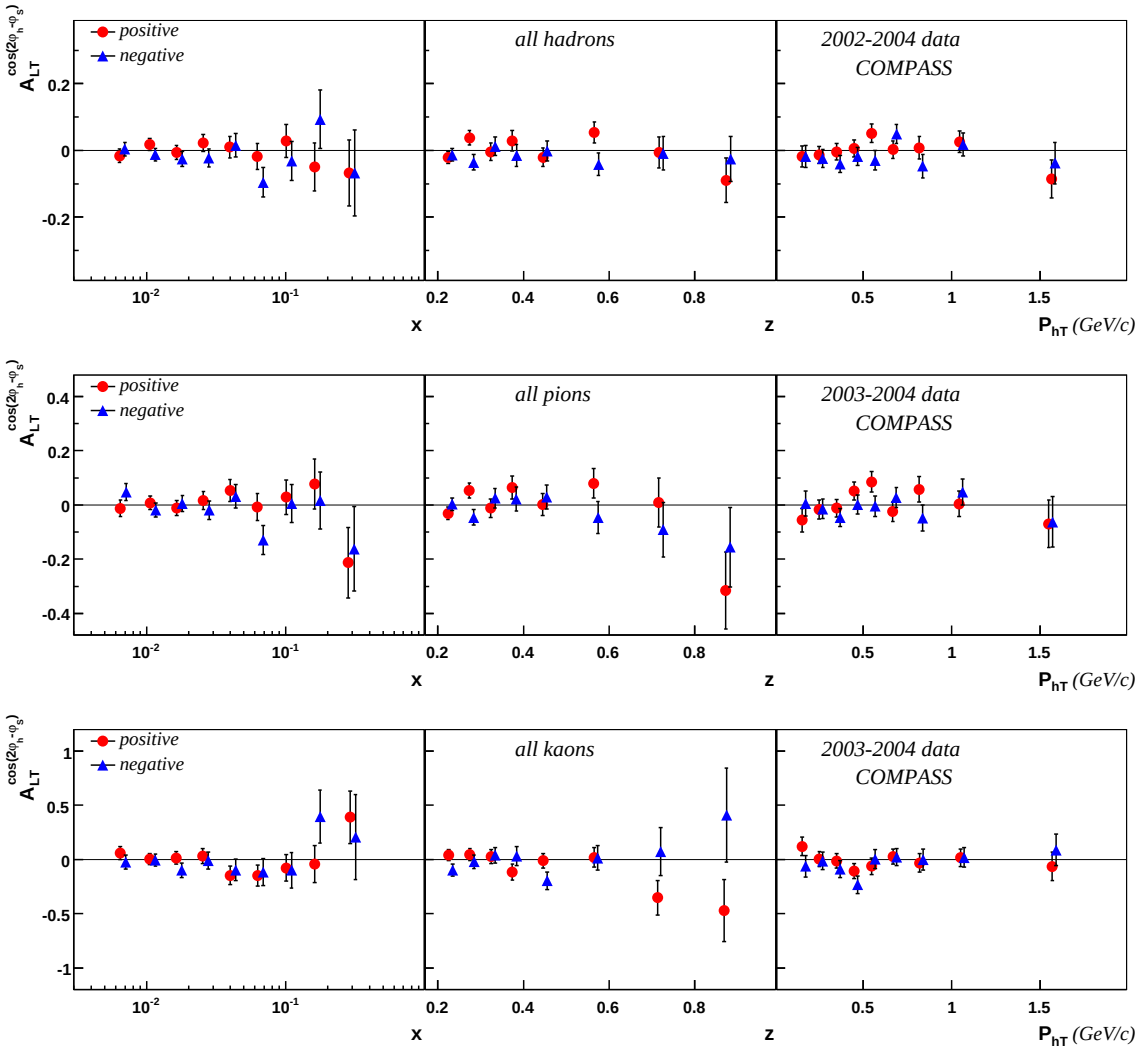

Figure 7.11: Extracted $A_{LT}^{\cos(2\phi_h-\phi_S)}$ asymmetry for unidentified hadrons (top row), pions (middle row) and kaons (bottom row) as a function of x, z and P_{hT}

7.3 Cross-check Between the Independent Analyses *(1D)*

According to the general COMPASS collaboration policy any result obtained from the COMPASS data before being released must be first cross-checked between two independent analyses. In order to fulfill this requirement the independent analysis has been performed by COMPASS group in Bonn (Germany). Then results obtained in Bonn have been cross-checked with ours (results obtained in two groups are labeled correspondingly "Torino" and "Bonn"). As an example figures 7.12 - 7.14 show the cross check between Torino and Bonn analysis for $A_{LT}^{\cos(\phi_h-\phi_S)}$ asymmetry for the weighted mean of 2002–2004 data for *unidentified* hadrons and weighted mean of 2003–2004 data for pions and kaons. Plots demonstrate the excellent agreement between the two results, which is of the same level for all the other measured asymmetries as well. In order to estimate the level of agreement between two analysis the "pulls" distributions were calculated with the given formula:

$$\frac{A^m_{To} - A^m_{Bn}}{\sigma_{A^m_{To}}} \tag{7.47}$$

where A^m_{To} is the asymmetry value extracted by Torino group and A^m_{Bn} is the same value extracted by Bonn group, the difference of these two numbers is divided by the statistical error calculated by Torino (or by Bonn). This quantity is calculated for each asymmetry from all periods (five for *unidentified* hadrons, three for pions and kaons) and evaluated for positive and negative *unidentified* hadrons (pions and kaons) in each kinematical bin in x,z and P_{hT}. Obtained values are filled in histogram giving a "pull" distribution, which is then fitted by the gaussian function. This way the repetition of cross-check plots can be avoided and the clear estimation of the agreement can be done. The figures 7.15 - 7.16 shows the gauss-fitted "pulls" distributions for all eight asymmetries for *unidentified* hadrons and combined pions and kaons. The number of entries is equal to 260 for *unidentified* hadron asymmetries which corresponds to 5 (number of data-taking periods) $\times$ 2 (positive and negative hadrons) $\times$ 26 (total number of kinematical bins (9 x, 8 z and 9 P_{hT})), and 312 for *RICH-identified* pion and kaon asymmetries, which is 3 (number of data-taking periods) $\times$ 2 (positive and negative particles) $\times$ 2 (pions and kaons) $\times$ 26 (total number of kinematical bins (9 x, 8 z and 9 P_{hT})). For all the asymmetries the RMS values given by gauss-fits are approximately of 0.0004, which is an indication of excellent agreement between two analysis. Such a small difference can be explained by the fact that though two groups used the same sequence of cuts and same analysis method, the programming codes and the procedure of evaluating the asymmetries is different.

As an alternative cross-check the published by COMPASS collaboration Collins and Sivers asymmetries have been compared with newly extracted ones. Figure 7.17 shows the corresponding "pull" distribution. As it was expected the difference between the results is more sizable not only because of different evaluation processes but also due to the difference in number of the events accepted for the analysis (in "old" calculations the "y-peak" cut (see Sec. 6.3.7) was not yet implemented").

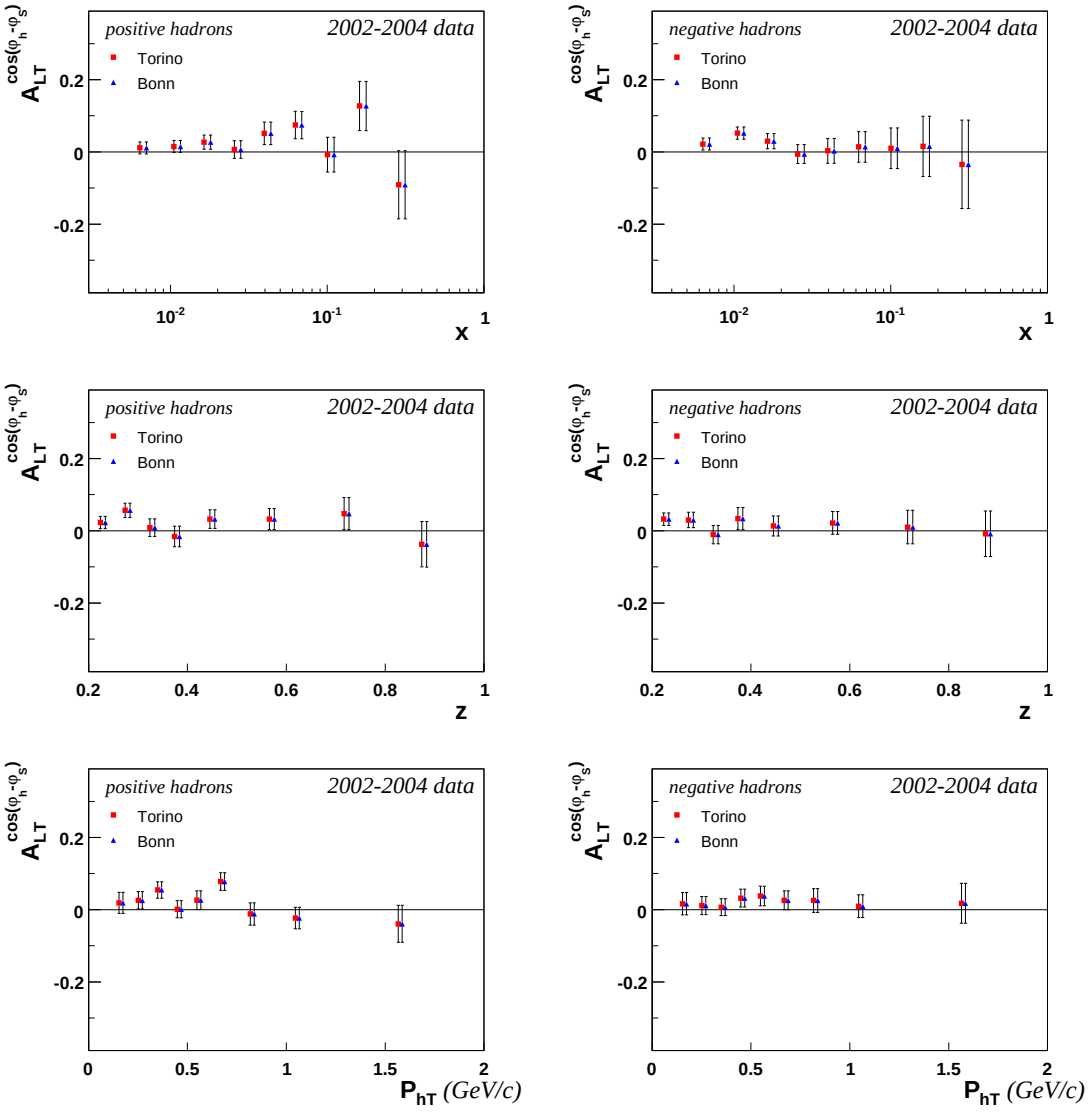

Figure 7.12: Cross check between Torino and Bonn analysis for $A_{LT}^{cos(\phi_h-\phi_S)}$ asymmetry for all periods(2002 - 2004), all positive hadrons vs. x, z and P_{hT}(left) and all negative hadrons vs. x, z and P_{hT}(right).

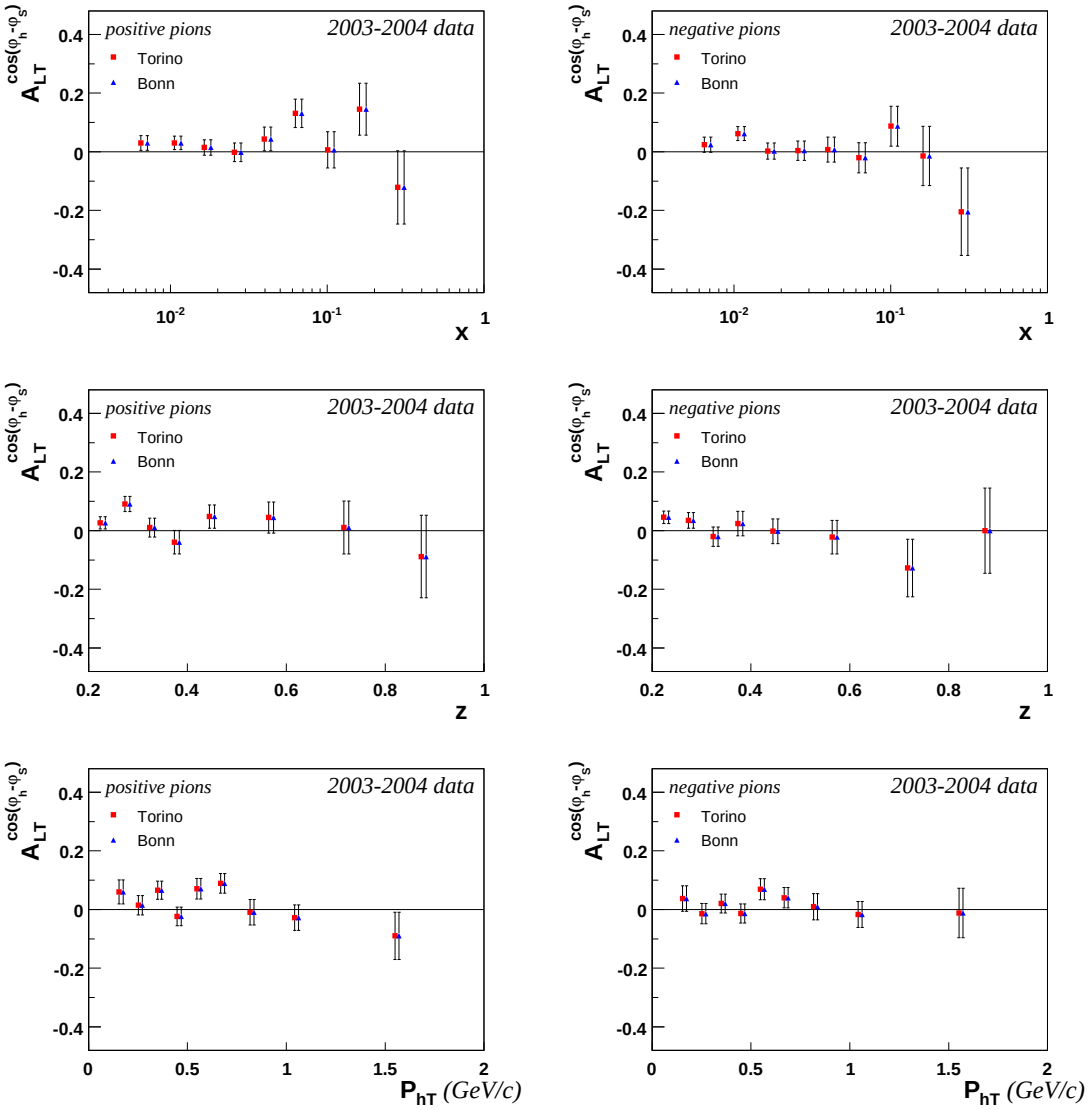

Figure 7.13: Cross check between Torino and Bonn analysis for $A_{LT}^{cos(\phi_h-\phi_S)}$ asymmetry for all periods(2003 - 2004), all positive pions vs. x, z and P_{hT}(left) and all negative pions vs. x, z and P_{hT}(right).

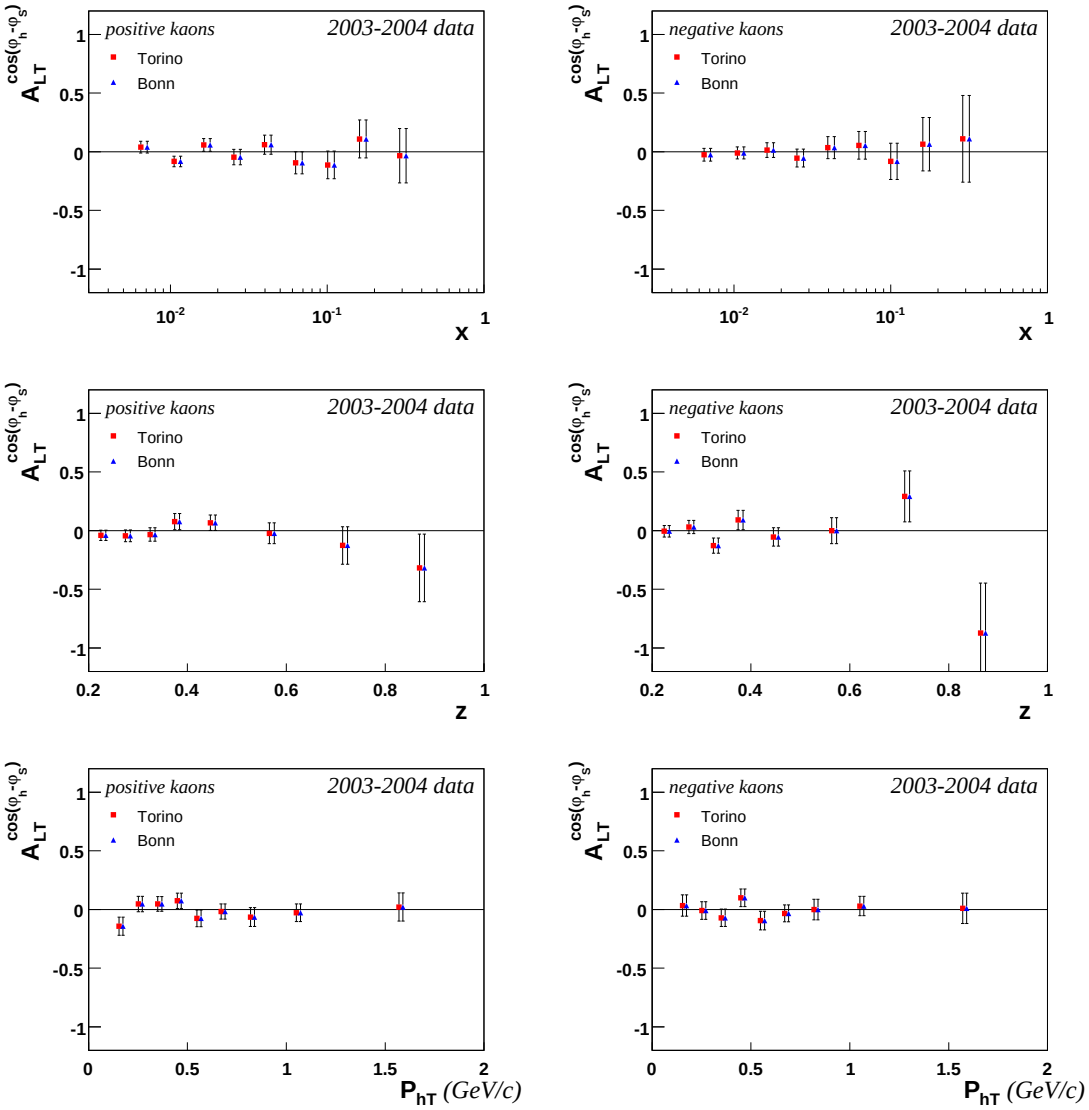

Figure 7.14: Cross check between Torino and Bonn analysis for $A_{LT}^{cos(\phi_h-\phi_S)}$ asymmetry for all periods(2003 - 2004), all positive kaons vs. x, z and P_{hT}(left) and all negative kaons vs. x, z and P_{hT}(right).

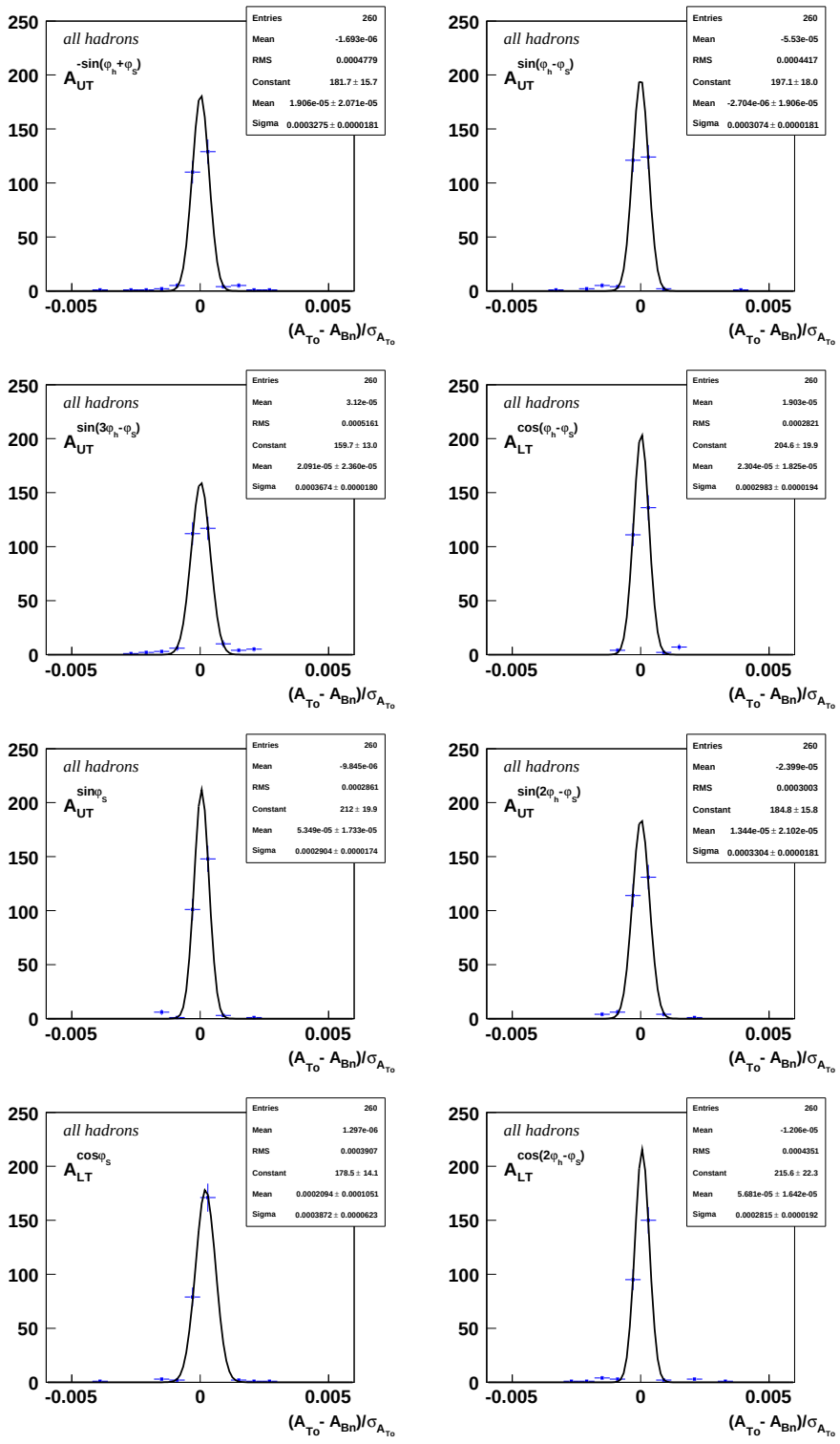

Figure 7.15: Cross check between Torino and Bonn results obtained with one-dimensional analysis for *unidentified* hadron asymmetries: "pulls" distribution for $A_{UT}^{-sin(\phi_h+\phi_S)}$(top left), $A_{UT}^{sin(\phi_h-\phi_S)}$(top right), $A_{UT}^{sin(3\phi_h-\phi_S)}$($2^{nd}$ left), $A_{LT}^{cos(\phi_h-\phi_S)}$($2^{nd}$ right), $A_{UT}^{sin(\phi_S)}$(3^{rd} left), $A_{UT}^{sin(2\phi_h-\phi_S)}$($3^{rd}$ right), $A_{LT}^{cos(\phi_S)}$(bottom left), $A_{LT}^{cos(2\phi_h-\phi_S)}$(bottom right).

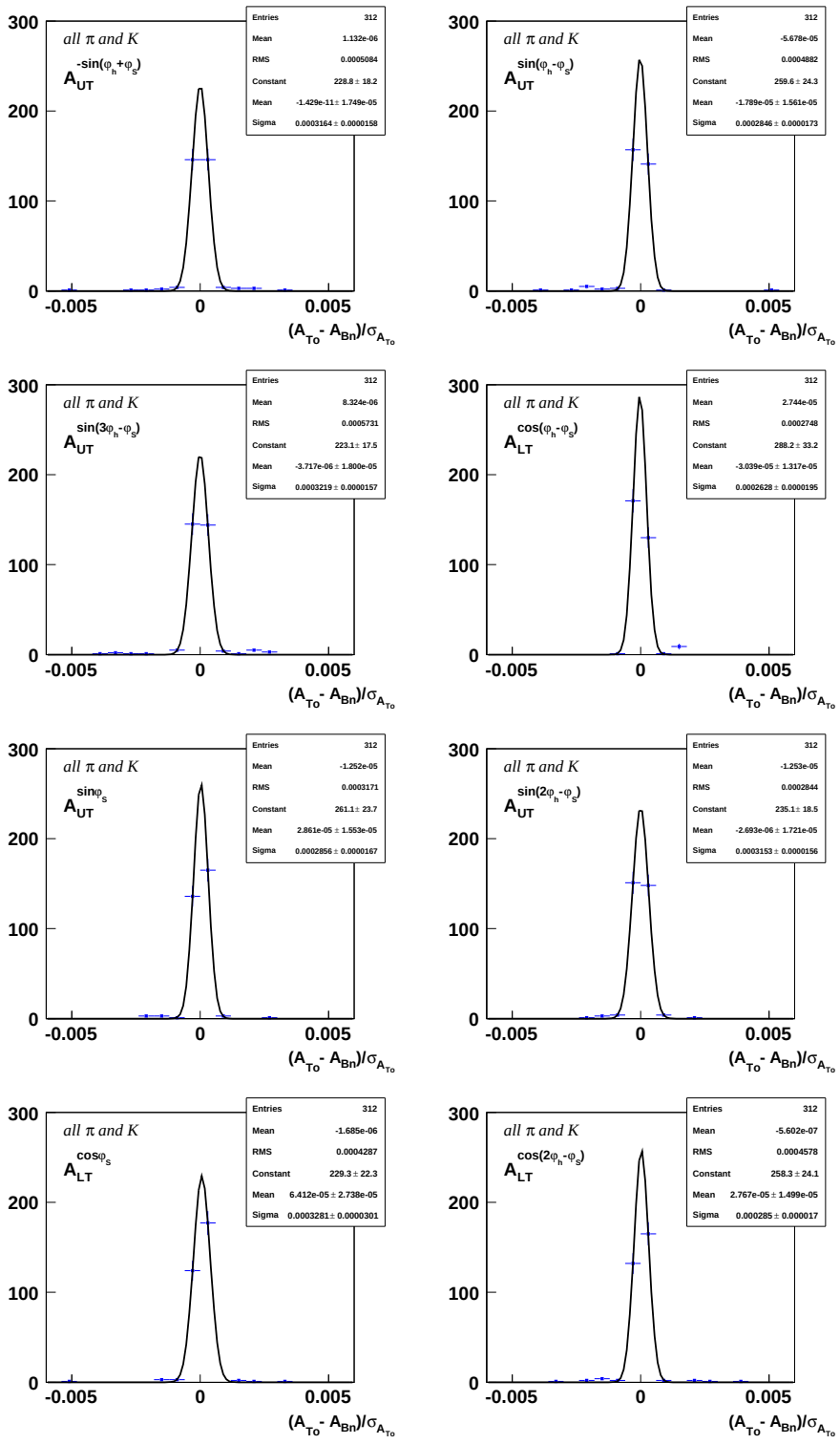

Figure 7.16: Cross check between Torino and Bonn results obtained with one-dimensional analysis for pion and kaon asymmetries: "pulls" distribution for $A_{UT}^{-sin(\phi_h+\phi_S)}$(top left), $A_{UT}^{sin(\phi_h-\phi_S)}$(top right), $A_{UT}^{sin(3\phi_h-\phi_S)}$($2^{nd}$ left), $A_{LT}^{cos(\phi_h-\phi_S)}$($2^{nd}$ right), $A_{UT}^{sin(\phi_S)}$(3^{rd} left), $A_{UT}^{sin(2\phi_h-\phi_S)}$($3^{rd}$ right), $A_{LT}^{cos(\phi_S)}$(bottom left), $A_{LT}^{cos(2\phi_h-\phi_S)}$(bottom right).

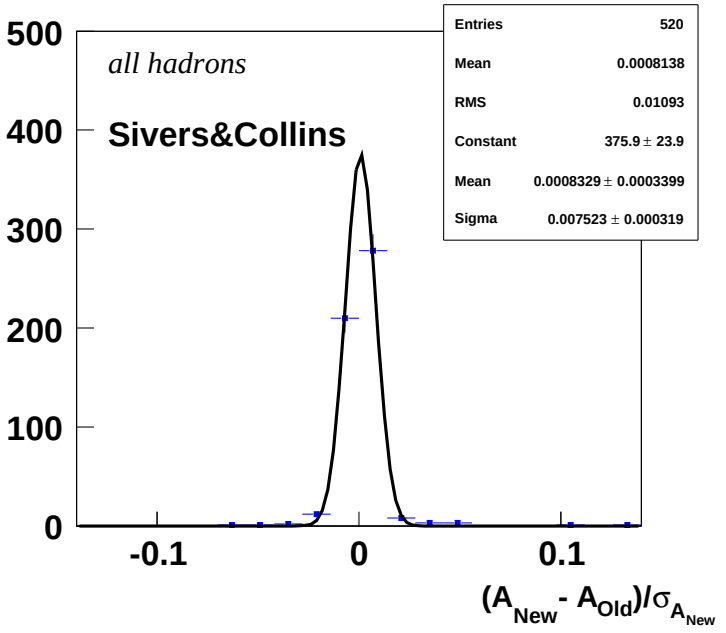

Figure 7.17: ”pulls” distribution for newly extracted Collins and Sivers asymmetry with the published ones

7.4 Systematic Studies *(1D)*

In this section we present several tests performed in order to reveal the possible systematic deviations and estimate their size. The performed studies are:

- Check on compatibility of the results obtained in different data-taking periods.
- So-called *"par(0)-test"* verifies the assumption on the ratio of the acceptances of the upstream and downstream target cells to be constant in two sub-periods processed before and after the polarization reversal.
- So-called *"R'-test"* is a more stringent test checking the stability of the acceptance ratios.
- Testing the quality of the fits by looking at the χ^2 distribution.
- Studying the systematic effects originating from the non-uniformity of the acceptance on the azimuthal angles ϕ_S. This issue will be discussed separately in Sec. 7.5

The systematic checks have been performed for *unidentified* hadron asymmetries from COMPASS 2002-2004 data as well as for pion and kaon asymmetries from COMPASS 2003-2004 data.

7.4.1 Compatibility of the Results from Different Periods

The first systematic test is the check on compatibility of the results from different periods. The agreement between the results obtained from different data-taking periods is an important requirement which ensures that spectrometer was stable during the whole data-taking and the data analysis chain from data production to asymmetry evaluation was identical for all periods.

For each asymmetry value - A_i^m, calculated for positive or negative particle in some particular kinematical bin over x,z or P_{hT}, using data of i-th period, the following P_i^m quantities are constructed:

$$P_i^m = \frac{A_i^m - < A^m >}{\sqrt{\sigma^2_{A_i^m} - \sigma^2_{<A^m>}}} \tag{7.48}$$

where $< A^m >$ is the weighted mean of A_i^m values over all periods. The variances $\sigma^2_{A_i^m}$ and $\sigma^2_{<A^m>}$ are used in the denominator in order to take into account the correlation between A_i^m and $< A^m >$. The P_i^m values evaluated for positive and negative *unidentified* hadrons, from five data-taking periods in 2002-2004 are filled in the histograms separately for x, z and P_{hT} asymmetries, and in one common histogram for all three variables. The same was done for P_i^m values for positive and negative combined pion and kaon asymmetries from three $RICH$-periods in 2003-20004. The histograms were fitted by gaussian and as it was expected they follow the standard normal distribution demonstrating that the differences between the results from different periods has only a statistical origin. Figures 7.18 and 7.19 shows the resulting plots on compatibility test for *unidentified*

hadron asymmetries and for pion and kaons asymmetries. For *unidentified* hadrons total number of entries in x histogram is 720 which corresponds to eight asymmetries evaluated separately from data of five periods for positive and negative hadrons in nine x bins - $8 \times 5 \times 2 \times 9 = 720$. Similarly in P_{hT} histogram number of entries is 720, while in case of z histogram number of entries is 640 since the number of z bins is not nine but eight and correspondingly $8 \times 5 \times 2 \times 8 = 640$. Total number of events in combined x,z and P_{hT} histogram is $720 + 640 + 720 = 2080$.

For pions and kaons total number of entries in x histogram is 864 which corresponds to eight asymmetries evaluated separately from data of three periods for positive and negative pions and kaons in nine x bins - $8 \times 3 \times 2 \times 2 \times 9 = 864$. Similarly in P_{hT} histogram it's the same - 864, and in z histogram it's 768. In the combined x,z and P_{hT} number of entries thus will be $864 + 768 + 864 = 2496$.

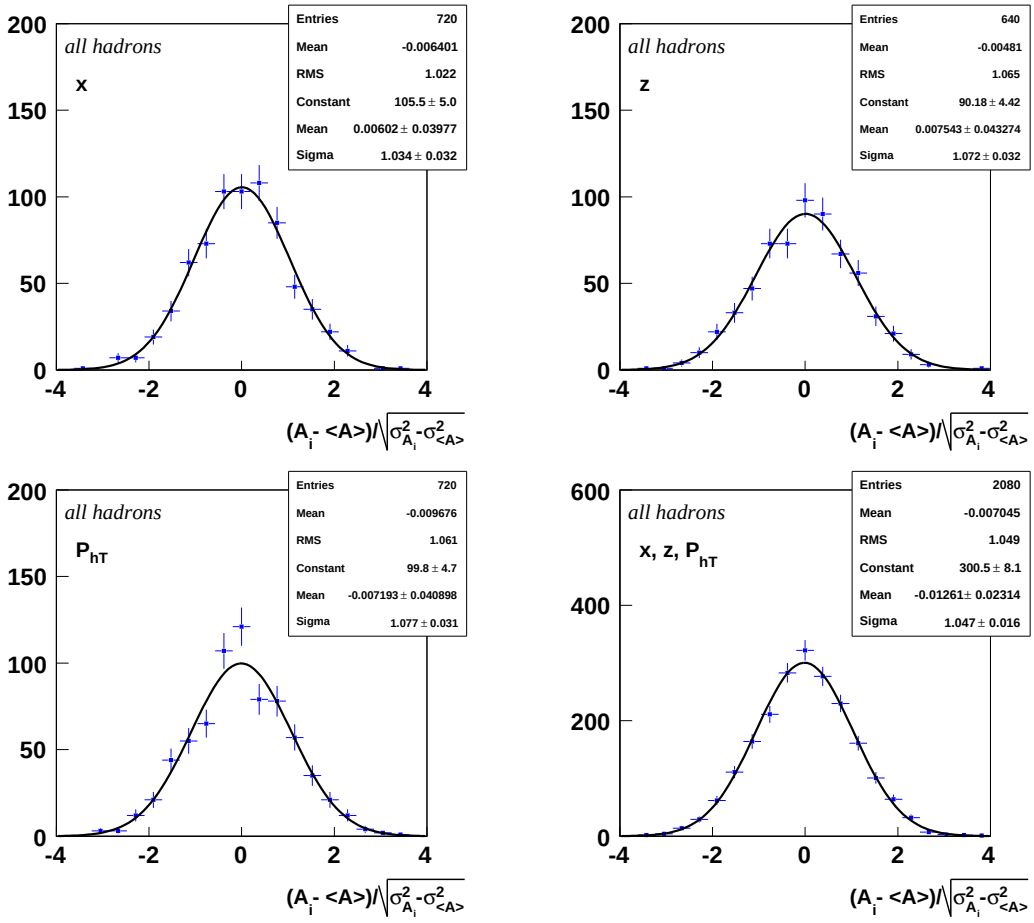

Figure 7.18: Compatibility of the results from different periods: "pulls" distribution to see the compatibility of results from different periods with x (top left), z (top right), P_{hT} (bottom left) and combined x, z, P_{hT} (bottom right).

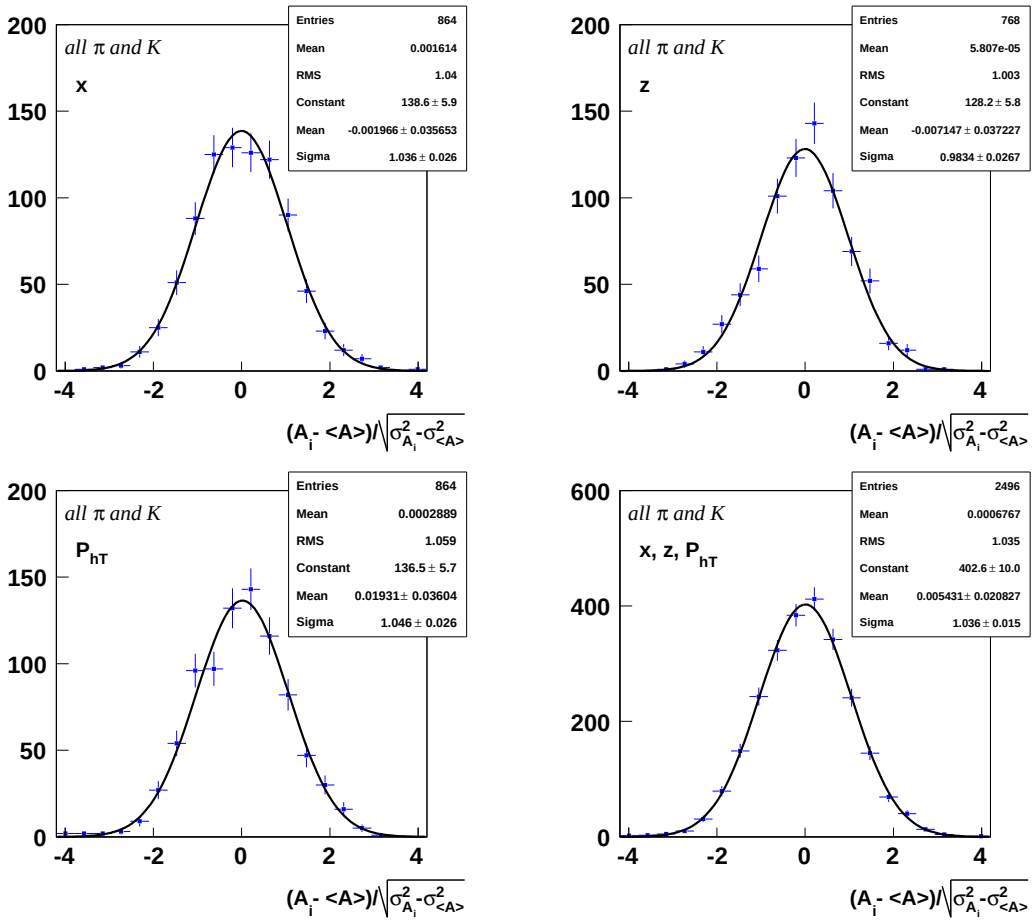

Figure 7.19: Compatibility of the results from different periods: "pulls" distribution to see the compatibility of results from different periods with x (top left), z (top right), P_{hT} (bottom left) and combined x, z, P_{hT} (bottom right)..

7.4.2 par(0) Calculation

Both fitting functions (7.40, 7.41) used in one-dimensional analysis contain free parameter *par(0)*. As it was shown in Sec. 7.2.1 this parameter is required to be close to one in case if assumption on acceptance ratios Eq. (7.38) is correct. The $par(0)$ values have been extracted from the fit for all five $W_j(\Phi_j)$ modulations (Eq. (7.8)), for positive and negative *unidentified* hadrons, pions and kaons, from all available data (five periods or three periods respectively) in all x, z and P_{hT} kinematical bins. Obtained values have been filled in histograms which then have been fitted by gaussian.

The number of entries in "$par(0)$" histogram for *unidentified* hadrons is 1300 ($5(modulations)\times 2(\pm)\times 5(periods)\times 26(9-x, 8-z\ and\ 9-P_{hT}\ bins)$), while for the pion kaon histogram the number of entries is 1560 ($5(modulations)\times 2(\pm)\times 2(\pi/K)\times 3(periods)\times 26(9-x, 8-z\ and\ 9-P_{hT}\ bins)$).

The "$par(0)$" histograms for *unidentified* hadrons and pions and kaons are presented in left and right plot of figure 7.20 respectively, in both of the cases the distribution has a

narrow peak at one, proving the validity of the acceptance assumption.

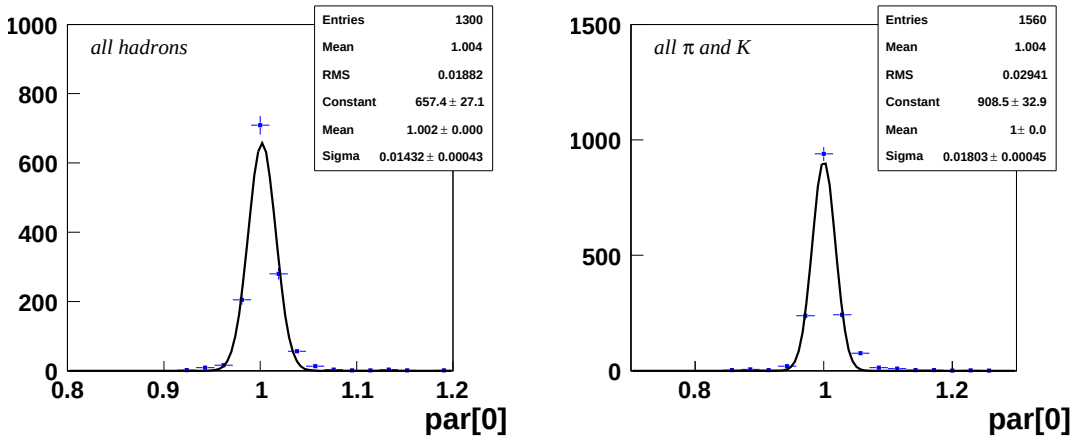

Figure 7.20: The distribution of the $par(0)$ values for *unidentified* hadrons (left) and pions kaons (right) for all the five $W_j(\Phi_j)$ modulations from all data-taking periods (five in 2002-2004 for *unidentified* hadrons, three in 2003-2004 for pions and kaons).

7.4.3 Stability of Acceptance Ratios *"R'-test"*

The assumption on acceptance ratios Eq. (7.38) implies their constancy in each Φ_j bin. In the meanwhile more stringent test on Φ_j dependence of the ratio of acceptances (*"R'-test"*) was performed.

In this test the number of events $N^{\pm}_{u/d}$ used to construct the ratio product quantities (see eq: 7.31):

$$R(\Phi_j) = \frac{N^+_u(\Phi_j)N^+_d(\Phi_j)}{N^-_u(\Phi_j)N^-_d(\Phi_j)},$$

are rearranged to create a ratio

$$R'(\Phi_j) = \frac{N^+_u(\Phi_j)N^-_d(\Phi_j)}{N^-_u(\Phi_j)N^+_d(\Phi_j)}. \tag{7.49}$$

Assuming the absolute value of the target polarization to be the same in each cell before and after reversal, at the first order it is:

$$R'(\Phi_j) \simeq \frac{F^+_u \cdot F^-_d}{F^-_u \cdot F^+_d} \cdot \frac{a^+_u(\Phi_j) \cdot a^-_d(\Phi_j)}{a^-_u(\Phi_j) \cdot a^+_d(\Phi_j)} \tag{7.50}$$

here the same notation as in Sec. 7.2.1 are used. Using the assumption on ratio of acceptances Eq. (7.38):

$$\frac{a^+_u(\Phi_j)}{a^-_d(\Phi_j)} = \frac{a^-_u(\Phi_j)}{a^+_d(\Phi_j)}$$

we obtain,

$$R'(\Phi_j) \simeq \frac{F_u^+ \cdot F_d^-}{F_u^- \cdot F_d^+} \cdot \left(\frac{a_u^+(\Phi_j)}{a_u^-(\Phi_j)}\right)^2 \quad (7.51)$$

$$\simeq \frac{F_u^+ \cdot F_d^-}{F_u^- \cdot F_d^+} \cdot \left(\frac{a_d^-(\Phi_j)}{a_d^+(\Phi_j)}\right)^2 \quad (7.52)$$

The requirement on $R'(\Phi_j)$ to be constant in Φ_j will serve as a stronger assumption than the required reasonable assumption (see Eq. (7.38)). This will imply for each cell the ratio of the acceptances before and after the polarization reversal to be constant in Φ_j, ensuring that the spectrometer was stable during the running period. The $R'(\Phi_j)$ ratios were evaluated in 16 bins over Φ_j and then fitted with the constant. This was performed for all five Φ_j angles, for positive and negative *unidentified* hadrons, pions and kaons in each kinematical bin of x, z and P_{hT}, separately for each data-taking period.

Figures 7.21, 7.22 and 7.23 show an example of the $R' - test$ for $(3\phi_h - \phi_S)$ angle vs. x for positive *unidentified* hadrons, pions and kaons respectively, for the period W35/W36. The lines are the results of the fit, showing constancy. The quality of these $R' - test$ constant fits as well as quality of the double ratio fits which evaluate the asymmetry values have been tested by looking at the χ^2 distribution (see next section).

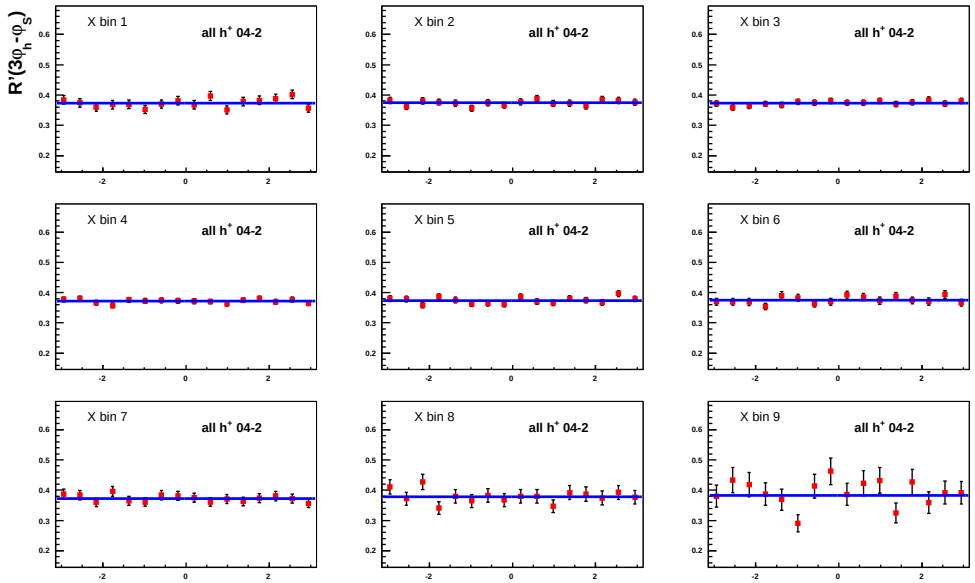

Figure 7.21: Distribution of the R'-Values for $(3\phi_h - \phi_S)$ modulation vs. x for the period W35/W36 for positive *unidentified* hadrons.

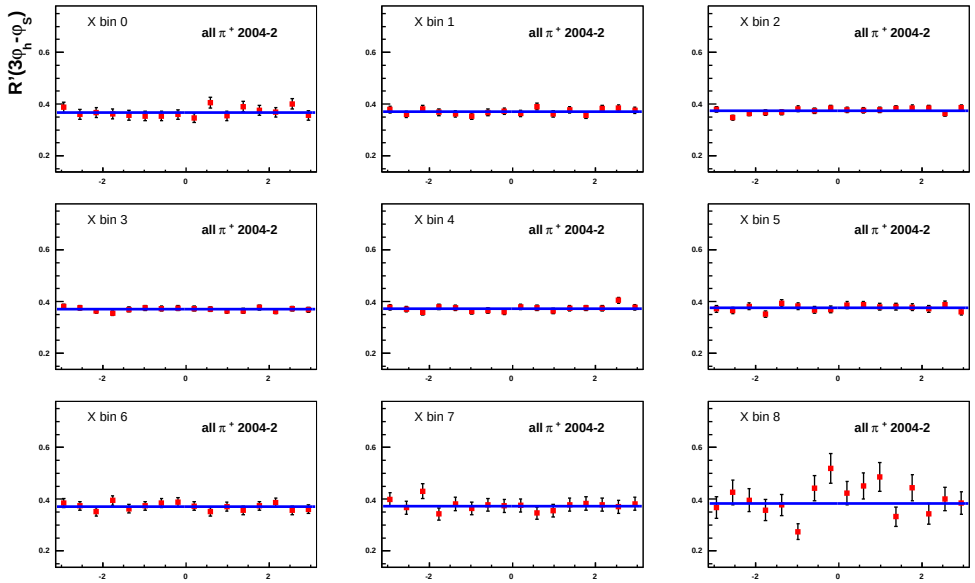

Figure 7.22: Distribution of the R'-Values for $(3\phi_h - \phi_S)$ angle vs. x for the period W35/W36 for positive pions.

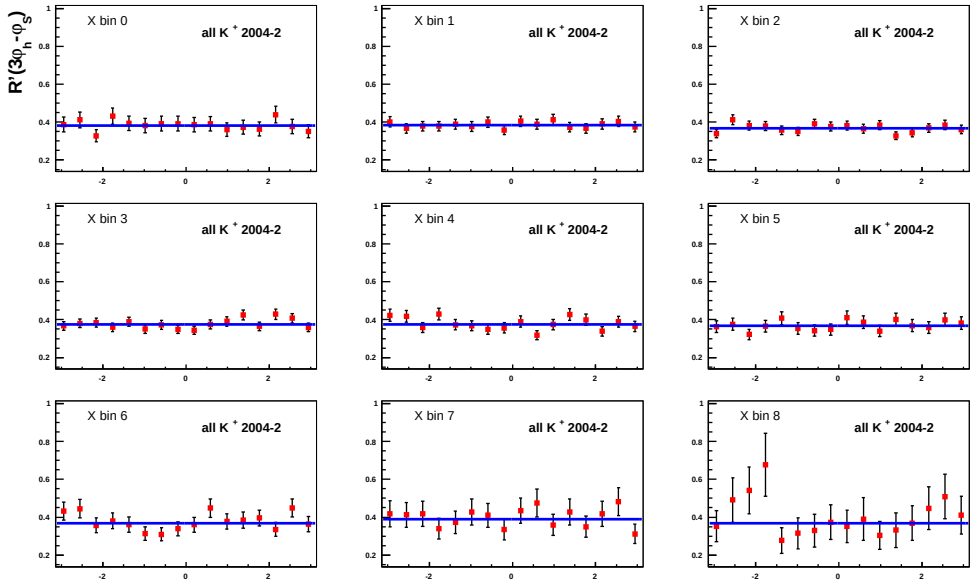

Figure 7.23: Distribution of the R'-Values for $(3\phi_h - \phi_S)$ angle vs. x for the period W35/W36 for positive kaons.

7.4.4 Quality of the Fit

The quality of the fits have been checked by constructing the distribution of χ^2 values from each fit. They should follow the theoretical χ^2 distribution with the corresponding number of degree of freedom (ndf).

The left plot in figure 7.24 shows the distribution of the χ^2 values of the constant fits on $R'(\Phi_j)$ quantities evaluated for positive and negative *unidentified* hadrons, in all kinematical bins from all data taking periods for $(3\phi_h - \phi_S)$ angle. For comparison theoretical χ^2 distribution for 15 degrees of freedom (we have 16 Φ bins and one parameter fit, $ndf = 15$) is also plotted. The right plot present distribution of the χ^2 values of two parameter fit on double ratio $R(\Phi_j)$ quantities evaluated for positive and negative *unidentified* hadrons, in all kinematical bins from all data taking periods for $(3\phi_h - \phi_S)$ angle and theoretical χ^2 distribution for 14 degrees of freedom ($ndf = 16 - 2 = 14$). The figure 7.24 include same distributions evaluated for $RICH - identified$ pions and kaons. One can see good agreement between expected and observed χ^2 distributions.

At this point all the performed tests did not reveal any evidence of systematic effects present in the analysis. So the conclusion to be drawn is that systematic errors due to acceptance and efficiency effects are considerably smaller than statistical ones.

The asymmetry scale uncertainty due to the uncertainties on target polarization S_T (see Sec. 7.1.4) and dilution factor f (see Sec. 7.1.5), which are 5% and 6% respectively. Combined in quadrature, these errors give a global asymmetry scale uncertainty of 8%.

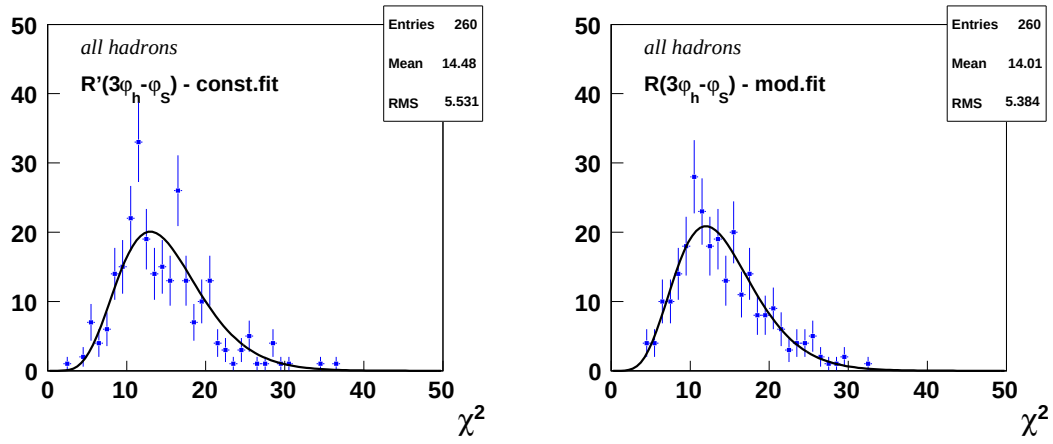

Figure 7.24: Right plot: χ^2 distribution of the constant fit on $R'(\Phi)$ values for $(3\phi_h - \phi_S)$ angle compared to the normalized χ^2 distribution for $ndf = 15$ for all hadrons. Left plot: χ^2 distribution of the two parameter fit on $R(\Phi)$ values (DR) for $(3\phi_h - \phi_S)$ angle compared to the normalized χ^2 distribution for $ndf = 14$ for all hadrons. In both plots theoretical χ^2 distribution is normalized by the number of entries in the histogram.

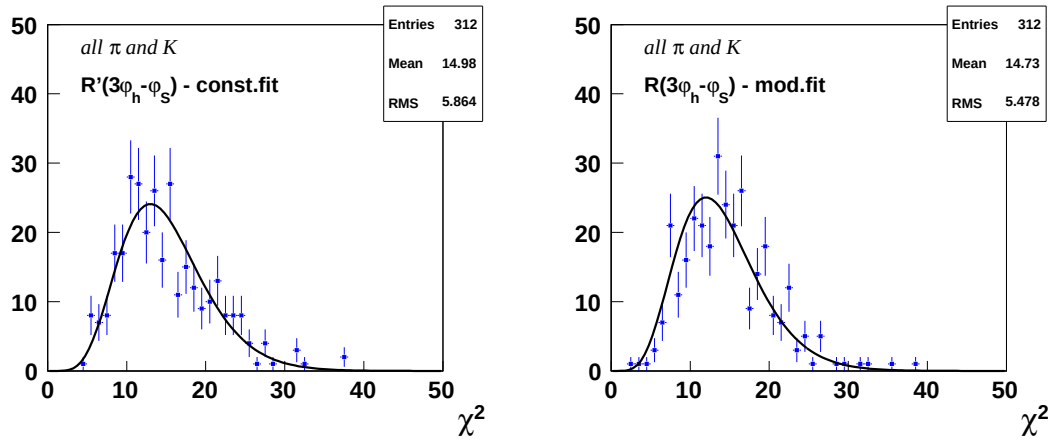

Figure 7.25: Right plot: χ^2 distribution of the constant fit on $R'(\Phi)$ values for $(3\phi_h - \phi_S)$ angle compared to the normalized χ^2 distribution for $ndf = 15$ for all pions and kaons. Left plot: χ^2 distribution of the two parameter fit on $R(\Phi)$ values (DR) for $(3\phi_h - \phi_S)$ angle compared to the normalized χ^2 distribution for $ndf = 14$ for all pions and kaons. In both plots theoretical χ^2 distribution is normalized by the number of entries in the histogram.

7.5 Acceptance Effects in One-Dimensional Analysis

The COMPASS results on Collins and Sivers asymmetries published in Refs. [5],[6], as well as results on all eight target transverse spin dependent asymmetries presented in this thesis in Sec. 7.2.2 (figures 7.4 - 7.11) have been obtained by using the described so far one-dimensional ratio product method.

In this method only the acceptance dependence on target cell, target polarization and Φ_j was taken into account. The expression for number of event dependence on Φ_j was defined by Eq. (7.30):

$$N^{\pm}_{u/d}(\Phi_j) = F^{\pm}_{u/d} n^{\pm}_{u/d} a^{\pm}_{u/d}(\Phi_j)\sigma(1 \pm W_j(\Phi_j))$$

where $a^{\pm}_{u/d}(\Phi_j)$ is Φ_j dependent acceptance in upstream or downstream cell, with "up" or "down" target polarization. Using the double ratio quantities Eq. (7.31) as an estimator for the asymmetry evaluation and making assumption on the acceptance ratios Eq. (7.38) we end up with canceled out acceptances.

The week point of this method is that the possible acceptance dependencies on kinematic variables and azimuthal angles are not taken into account. In Ref. [103] it was demonstrated that the asymmetries extracted using one-dimensional ratio product method will have systematic deviations due to the strong non-uniformity of acceptance on spin azimuthal angle ϕ_S (see ϕ_S distribution presented in the figure 7.2). For the simplicity it was assumed that acceptance is independent of the target cell, target polarization and x, y, z and P_{hT} kinematical variables. Only the dependence of the acceptance on azimuthal angles ϕ_h and ϕ_S was considered. Additional assumptions on beam flux, target polariza-

tion and dilution factor to be constant and independent of target cell were also applied. In this case the expression for the number of event dependence on kinematic variables and azimuthal angles for each target polarization is given by:

$$N_{\pm}(x, y, z, P_{hT}, \phi_h, \phi_S) \propto A(\phi_h, \phi_S)\sigma_{\pm}(x, y, z, P_{hT}, \phi_h, \phi_S), \tag{7.53}$$

where $\sigma_{\pm}(x, y, z, P_{hT}, \phi_h, \phi_S)$ is a target transverse spin dependent cross-section, which can be represented as:

$$\begin{aligned} \sigma_{\pm} \propto 1 \quad &\pm \quad [a_1 \sin(\phi_h - \phi_S) + a_2 \sin(\phi_h + \phi_S) \\ &+ \quad a_3 \sin(3\phi_h - \phi_S) + a_4 \sin(\phi_S) \\ &+ \quad a_5 \sin(2\phi_h - \phi_S) + a_6 \cos(\phi_h - \phi_S) \\ &+ \quad a_7 \cos(\phi_S) + a_8 \cos(2\phi_h - \phi_S)], \end{aligned} \tag{7.54}$$

where the amplitudes $a_i,\ i = 1, 8$ depend on x, y, z and P_{hT}. The eight modulations present in cross-section are based on five combination of azimuthal angles:

$$\Phi_1 = \phi_h - \phi_S = \Phi_S - Sivers\ angle \tag{7.55}$$
$$\Phi_2 = \phi_h + \phi_S = \Phi_C - Collins\ angle \tag{7.56}$$
$$\Phi_3 = 3\phi_h - \phi_S \tag{7.57}$$
$$\Phi_4 = \phi_S \tag{7.58}$$
$$\Phi_5 = 2\phi_h - \phi_S \tag{7.59}$$

In order to extract the amplitudes $a_i,\ i = 1, 8$ as a function of variable $v = x, y, z, P_{hT}$ in COMPASS one-dimensional analysis we need first to construct the double ratio quantities in which the acceptance effects are canceling out:

$$R(v, \Phi_j) = \frac{N_+(v, \Phi_j)N_+(v, \Phi_j)}{N_-(v, \Phi_j)N_-(v, \Phi_j)} \tag{7.60}$$

where $N_{\pm}(v, \Phi_j)$ are obtained from Eq. (7.53) by integrating over all phase space variables except v and Φ_j. To perform this integration one has to change the azimuthal variables

$$(\phi_h, \phi_S) \rightarrow (\phi_h, \Phi_j) \tag{7.61}$$

and then integrate over ϕ_h. For example, for x-dependence one obtains the integral

$$N_{\pm}(x, \Phi_j) \propto \int_{-\pi}^{\pi} d\phi_h \int dydzdP_{hT} A(\phi_h, \phi_{si}(\phi_h, \Phi_j))\sigma_{\pm}(x, y, z, P_{hT}, \phi_h, \phi_{si}(\phi_h, \Phi_j)), \tag{7.62}$$

where $j = 1, .., 5$ and

$$\phi_{s1}(\phi_h, \Phi_1) = \phi_h - \Phi_1, \tag{7.63}$$
$$\phi_{s2}(\phi_h, \Phi_2) = -\phi_h + \Phi_2, \tag{7.64}$$
$$\phi_{s3}(\phi_h, \Phi_3) = 3\phi_h - \Phi_3, \tag{7.65}$$
$$\phi_{s4}(\phi_h, \Phi_4) = \Phi_4, \tag{7.66}$$
$$\phi_{s5}(\phi_h, \Phi_5) = 2\phi_h - \Phi_5. \tag{7.67}$$

Important remark is that, acceptance function entering in Eq. (7.62) as integrand, in general, cannot be factorized, since integral of product of two function is not equal to product of integrals of these two functions.

7.5.1 Constant Acceptance

Considering the case when the acceptance is independent of the azimuthal angles, $A(\phi_h, \phi_S) = A_0 = const$, from the counting rate expression (7.62) one will obtain:

$$N_{\pm}(x, \Phi_j) \propto A_0 \int_{-\pi}^{\pi} d\phi_h \int dy dz dP_{hT} \sigma_{\pm}(x, y, z, P_{hT}, \phi_h, \phi_{si}(\phi_h, \Phi_j)), \tag{7.68}$$

For example, the counting rate dependence for x variable and $\Phi_1 = \Phi_S$ (Sivers angle) will contain only the amplitudes a_1 and a_6

$$N_{\pm}(x, \Phi_S) \propto 1 \pm [a_1(x) \sin(\Phi_S) + a_6(x) \cos(\Phi_S)] \tag{7.69}$$

since all other modulations presented in the cross-section 7.54 after integration over ϕ_h will give zero and thus will not contribute.

Then the usual COMPASS ratio product method can be applied. Within an assumption that a_1 and a_6 are small the double ratio quantities will give:

$$R(x, \Phi_S) = 1 + 4[a_1(x) \sin(\Phi_S) + a_6(x) \cos(\Phi_S)]. \tag{7.70}$$

and acceptances will be canceled out. Now amplitudes $a_1(x)$ and $a_6(x)$ can be extracted by fitting the $R(x, \Phi_S)$ with the appropriate function (see Sec. 7.2.1). This was the case of constant acceptance in ϕ_S. Now lets discuss the COMPASS situation with the non-uniform ϕ_S distribution. For this purpose some model of the COMPASS ϕ_S-acceptance is needed.

7.5.2 Model of Non-uniform COMPASS Acceptance

The distributions of the azimuthal angles ϕ_h and ϕ_S in COMPASS have been presented in Sec. 7.1.2. The acceptance dependence on ϕ_h can be considered as week and can be neglected in the first approximation, while the ϕ_S dependence is much stronger and must be taken into account. Thus in $A(\phi_h, \phi_S)$ we will keep only ϕ_S dependence:

$$A(\phi_h, \phi_S) = \mathcal{A}(\phi_S). \tag{7.71}$$

In order to simulate acceptance function $\mathcal{A}(\phi_S)$ we used its Fourier decomposition which can be presented like:

$$\mathcal{A}(\phi_S) = c_0 \left(1 + 2 \sum_{n=1}^{n=\infty} [c_n \cos(n\phi_S) + s_n \sin(n\phi_S)] \right). \tag{7.72}$$

The sum limit was set at five and the obtained expression was used as an analyzer of harmonics. The ϕ_S distribution of all events (from both cells with both target polarizations) entering in particular bin of x ($0.05 < x < 0.1$) was fitted by this function with free

parameters c_i^{fit} and s_i^{fit} giving the amplitudes of corresponding cos and sin harmonics. The ϕ_S distribution with the plotted fitting function is presented in figure 7.26 and the fit parameters are given in Tab. 7.2.

i	c_i^{fit}	s_i^{fit}
1	0.025935	0.208876
2	0.173028	0.007965
3	-0.001848	-0.061086
4	-0.042701	0.002011
5	0.000329	0.000378

Table 7.2: Fitted parameters for acceptance dependence on ϕ_S

As one can see in this table at least two of relevant fit parameters are large enough: $c_2^{fit} \approx s_1^{fit} \approx 0.2$, each corresponding to 40% modulations (factor 2 in front of the sum in Eq. (7.72) doubles all amplitudes).

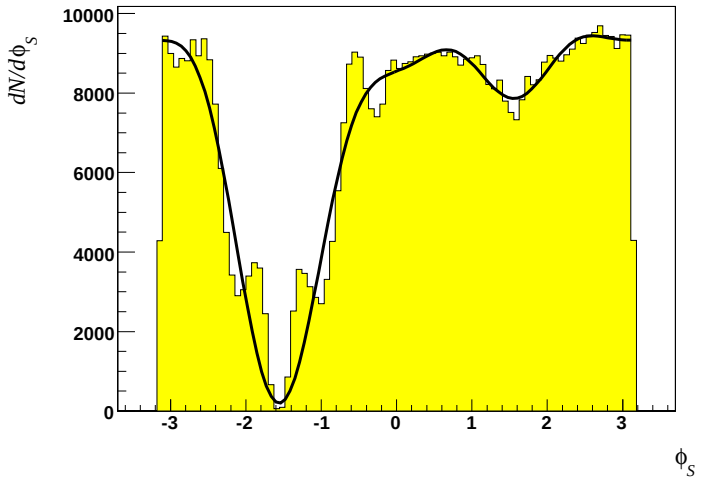

Figure 7.26: ϕ_S distribution in $0.05 < x < 0.1$ bin at COMPASS. The solid line represents the fitting function.

7.5.3 The Systematic Deviations in Asymmetries

Using number of events expression (Eq. (7.62)) and Fourier decomposition of acceptance $\mathcal{A}(\phi_S)$, one can calculate the double ratio quantities for all five Φ_j angles. Since the dependence on kinematic variables is not essential for this discussion for the certainty we will consider extraction of asymmetries as a function of x. As the first case to be discussed we choose the simplest one which is the Φ_4 angle.

- $\mathbf{\Phi_4 = \phi_S}$

For Φ_4 calculations are the most simple because it doesn't include ϕ_h. The counting rate expression will be presented like:

$$N_{\pm}(x,\Phi_4) \propto \int_{-\pi}^{\pi} d\phi_h \mathcal{A}(\Phi_4)\sigma_{\pm}(x,\phi_h,\Phi_4), \tag{7.73}$$

where $\sigma_{\pm}(x,\phi_h,\Phi_4)$ is defined by Eq. (7.54) with a_i integrated over y, z and P_{hT}. Since $\mathcal{A}(\Phi_4)$ does not depend on ϕ_h acceptance term will factor out. After the integration over ϕ_h all the modulations presented in the cross-section will vanish except two which depend on Φ_4:

$$N_{\pm}(x,\Phi_4) \quad \propto \quad \mathcal{A}(\Phi_4)(1 \pm [a_4 \sin(\Phi_4) + a_7 \cos(\Phi_4)]). \tag{7.74}$$

Using the double ratio quantities $R(x,\Phi_4)$ the acceptances will cancel out and for small asymmetries a_4 and a_7 one can obtain:

$$R(x,\Phi_4) \quad = \quad 1 + 4[a_4 \sin(\Phi_4) + a_7 \cos(\Phi_4)]. \tag{7.75}$$

So in this case usual one-dimensional ratio product method is valid and result is not changed by non-uniform acceptance in Φ_S.

- $\mathbf{\Phi_1 = \phi_h - \phi_S = \Phi_S}$ – Sivers angle

Here the situation is different and the definition of Sivers angle includes ϕ_h. The number of events dependence on x and Φ_S can be represented according to Eq. (7.62) like:

$$N_{\pm}(x,\Phi_S) \propto \int_{-\pi}^{\pi} d\phi_h A(\phi_h, \phi_h - \Phi_S)\sigma_{\pm}(x,\phi_h,\phi_h - \Phi_S), \tag{7.76}$$

where $\sigma_{\pm}(x,\phi_h,\phi_h - \Phi_S)$ is defined by Eq. (7.54) with corresponding change of variables $\phi_S \longrightarrow \phi_h - \Phi_S$:

$$\begin{aligned} \sigma_{\pm}(x,\phi_h,\phi_h - \Phi_S) \propto 1 \quad \pm \quad & [a_1 \sin(\Phi_S) + a_2 \sin(2\phi_h - \Phi_S) \\ + \quad & a_3 \sin(2\phi_h + \Phi_S) + a_4 \sin(\phi_h - \Phi_S) \\ + \quad & a_5 \sin(\phi_h + \Phi_S) + a_6 \cos(\Phi_S) \\ + \quad & a_7 \cos(\phi_h - \Phi_S) + a_8 \cos(\phi_h + \Phi_S)], \end{aligned} \tag{7.77}$$

here the amplitudes a_i now depend only on x. Inserting this expression and the Fourier decomposition of acceptance into Eq. (7.76) we have:

$$\begin{aligned} N_{\pm}(x,\Phi_S) \quad \propto \quad & \int_{-\pi}^{\pi} d\phi_h \left(1 + 2\sum_{n=1}^{n=\infty} [c_n \cos(n\phi_h - n\Phi_S) + s_n \sin(n\phi_h - n\Phi_S)]\right) \times \\ & \times \sigma_{\pm}(x,\phi_h,\phi_h - \Phi_S), \end{aligned}$$

After integrating the *r.h.s* over ϕ_h we obtain:

$$\begin{aligned} N_{\pm}(x,\Phi_S) &\propto 1 \pm [a_4 s_1 + a_7 c_1 + (a_1 + a_2 c_2)\sin(\Phi_S) \\ &+ (a_6 + a_3 s_2)\cos(\Phi_S) + (a_5 s_1 + a_8 c_1)\cos(2\Phi_S) \\ &+ (a_5 c_1 - a_8 s_1)\sin(2\Phi_S) + a_3 c_2 \sin(3\Phi_S) + a_3 s_2 \cos(3\Phi_S)]. \end{aligned} \tag{7.78}$$

The comparison of this equation with Eq. (7.69) (written for the constant acceptance) clearly reveals that non-uniformity of the acceptance induces *non-physical* $2\Phi_S$ and $3\Phi_S$ modulations and target transverse spin dependent but azimuth independent asymmetry, moreover it changes the amplitudes of *real-physical* $sin(\Phi_S)$ and $cos(\Phi_S)$ modulations.

For small asymmetries $a_i,\ i = 1, 8$ the double ratio quantities Eq. (7.60) can be represented as:

$$\begin{aligned} R(x,\Phi_S) &= 1 + 4[a_4 s_1 + a_7 c_1 + (a_1 + a_2 c_2)\sin(\Phi_S) \\ &+ (a_6 + a_3 s_2)\cos(\Phi_S) + (a_5 s_1 + a_8 c_1)\cos(2\Phi_S) \\ &+ (a_5 c_1 - a_8 s_1)\sin(2\Phi_S) + a_3 c_2 \sin(3\Phi_S) + a_3 s_2 \cos(3\Phi_S)]. \end{aligned} \tag{7.79}$$

Keeping only the terms which includes large modulations of acceptance function – s_1 and c_2, we obtain:

$$\begin{aligned} R(x,\Phi_S) &\approx 1 + 4[0.2a_4 + [(a_1 + 0.2a_2)\sin(\Phi_S) + a_6 \cos(\Phi_S) \\ &+ 0.2a_5 \cos(2\Phi_S) - 0.2a_8 \sin(2\Phi_S) + 0.2a_3 \sin(3\Phi_S)]. \end{aligned} \tag{7.80}$$

According to one-dimensional method in order to extract the amplitudes of Φ_S modulations (a_1 and a_6) this expression must be fitted by a function given by Eq. (7.41):

$$R(\Phi_j) = par(0)(1 + 4[par(1)\sin(\Phi_j) + par(2)\cos(\Phi_j)]).$$

In this case the extracted amplitude of $\sin(\Phi_S)$ modulation (the Sivers asymmetry) will be sifted from its original value a_1 by 20% of amplitude of real (physics) Collins asymmetry (a_2). The $par(0)$ will also be shifted form its expected value 1 by almost 80% of amplitude of $\sin(\phi_S)$ modulation (a_4). In addition the a_5, a_8 and a_3 amplitudes can be extracted from the data by adding to the fitting function Eq. (7.41) the *non-physical* $cos(2\Phi_S)$, $\sin(2\Phi_S)$ and $\sin(3\Phi_S)$ modulations.

- $\mathbf{\Phi_2 = \phi_h + \phi_S = \Phi_C}$ – Collins angle

Using the same procedure for Φ_C angle the double ratio quantities will be represented as:

$$\begin{aligned} R(x,\Phi_C) &= 1 + 4[a_4 s_1 + a_7 c_1 + (a_1 c_2 + a_6 s_2 + a_2)\sin(\Phi_C) \\ &+ (a_1 s_2 + a_6 c_2)\cos(\Phi_C) + (a_5 s_3 + a_8 c_3)\cos(2\Phi_C) \\ &+ (a_5 c_3 + a_8 s_3)\sin(2\Phi_C) + a_3 c_4 \sin(3\Phi_C) + a_3 s_4 \cos(3\Phi_C)] \\ &\approx 1 + 4[0.2a_4 + (0.2a_1 + a_2)\sin(\Phi_C) + 0.2a_6 \cos(\Phi_C)]. \end{aligned} \tag{7.81}$$

Again we see that extracted amplitude of $\sin(\Phi_C)$ modulation (the Collins asymmetry) will be shifted from its original value (a_2) by 20% of amplitude of Sivers asymmetry (a_1). In addition the $\cos(\Phi_C)$ *non-physical* modulation and $0.8a_4$ constant term appear in the expression.

- $\mathbf{\Phi_3 = 3\phi_h - \phi_S}$

In this case only the $0.8a_4$ *non-physical* constant term appear in the expression.

$$\begin{aligned} R(x,\Phi_3) &= 1 + 4[a_4 s_1 + a_7 c_1 + a_3 \sin(\Phi_4)] \\ &\approx 1 + 4[0.2a_4 + a_3 \sin(\Phi_4)]. \end{aligned} \tag{7.82}$$

- $\mathbf{\Phi_5 = 2\phi_h - \phi_S}$

Here also the same as for Φ_3 case only the $0.8a_4$ *non-physical* constant term appear in the double ratio expression.

$$\begin{aligned} R(x,\Phi_5) &= 1 + 4[a_4 s_1 + a_7 c_1 + a_5 \sin(\Phi_3) + a_8 \cos(\Phi_3)] \\ &\approx 1 + 4[0.2a_4 + a_5 \sin(\Phi_3) + a_8 \cos(\Phi_3)]. \end{aligned} \tag{7.83}$$

7.6 Concluding Remarks on One-Dimensional Method

As it was demonstrated in Sec. 7.5 the disadvantage of the one-dimensional analysis method is that it gives distorted results in case of non-uniform azimuthal acceptance in ϕ_S. Using the realistic model of non-uniform COMPASS ϕ_S distribution (see Sec. 7.5.2) it was shown that in such a case amplitudes of different azimuthal modulations extracted with one-dimensional method are mixed and even non-physical modulations arise in double ratio expressions. Thus the results obtained with one-dimensional ratio product method have to be corrected for azimuthal acceptance effects.

In case of small asymmetries a_i the distortions are not changing results essentially and thus may be accounted in the systematic errors. This is actually the case of COMPASS results, due to the fact that all the measured asymmetries are small additional *"acceptance-induced"* terms entering in double ratio expressions with small ($\simeq 0.2 - 0.3$) scaling factor can be even neglected within statistical accuracy. As opposed to this in the case of large asymmetries the deviations may change the results drastically, and one-dimensional method will not be valid without necessary acceptance corrections.

Anyway there exist another, more elegant way to avoid such a complications. The so-called two-dimensional analysis method does not suffer at all from the azimuthal acceptance effects, since in this case asymmetries are evaluated in two-dimensional (ϕ_h, ϕ_S) bins without performing an integration over the azimuthal angles and acceptances are canceled out in each bin. The two-dimensional analysis method and results obtained using this technic are presented in next section.

7.7 Two-Dimensional Analysis *(2D)*

The two-dimensional analysis method allows to extract all the eight target transverse spin dependent asymmetries (see Sec. 2.2) simultaneously. In addition this method is not affected by the systematic effects caused by non-uniformity of the COMPASS acceptance on ϕ_S described in Sec. 7.5. Two-dimensional fit also provides the information about the correlation between different asymmetries extracted as a parameters of the fit. In this section the description of the two-dimensional analysis procedure and the results on asymmetries evaluated using this method in each kinematical bin of x, z and P_{hT} (see Sec. 6.4) for positive and negative *unidentified* hadrons, and for positive and negative pions and kaons are presented.

7.7.1 Ratio Product Method (RPM) in Two-Dimensional Analysis

In the two-dimensional analysis we applied the same Ratio Product Method (RPM) method which was used in one-dimensional analysis (see Sec. 7.2.1) with only difference that now the double ratio quantities instead of being calculated in 16 Φ_j bins have been evaluated in 8×8 equal-size bins in two-dimensional (ϕ_h,ϕ_S) space. This allows simultaneous extraction of all eight asymmetries and also avoid the integration over azimuthal angles which as it was demonstrated in the section Sec. 7.5 cause some acceptance effects.

The counting rate dependence on ϕ_h and ϕ_S analogously to the one-dimensional case can be represented as:

$$N^{\pm}_{u/d}(\phi_h,\phi_S) = F^{\pm}_{u/d} n^{\pm}_{u/d} a^{\pm}_{u/d}(\phi_h,\phi_S)\sigma\{1 \pm \sum_{i=1}^{8} A_{raw}^{w_i(\phi_h,\phi_S)} w_i(\phi_h,\phi_S)\} \tag{7.84}$$

where $+(-)$ indicate up (down) target polarization, $u(d)$ the upstream and downstream target cells. The $F^{\pm}_{u/d}$ is the flux and $n^{\pm}_{u/d}$ is the target density for the given cell (u/d) and polarization ($\pm$). The σ is the unpolarized cross-section and $a^{\pm}_{u/d}(\phi_h,\phi_S)$ is the azimuthal angles dependent acceptance for the corresponding cell and polarization state. And finally $A_{raw}^{w_i(\phi_h,\phi_S)}$ are the *raw* asymmetries extracted as amplitudes of the corresponding modulations $w_i(\phi_h,\phi_S)$.

The double ratio quantities in each (ϕ_h,ϕ_S) bin are calculated similarly to one-dimensional analysis procedure (see Sec. 7.2.1) as:

$$R(\phi_h,\phi_S) = \frac{N^+_u(\phi_h,\phi_S) N^+_d(\phi_h,\phi_S)}{N^-_u(\phi_h,\phi_S) N^-_d(\phi_h,\phi_S)}, \tag{7.85}$$

and the respective error propagation is:

$$\sigma_R(\phi_h,\phi_S) = \sqrt{\frac{1}{N^+_u(\phi_h,\phi_S)} + \frac{1}{N^+_d(\phi_h,\phi_S)} + \frac{1}{N^-_u(\phi_h,\phi_S)} + \frac{1}{N^-_d(\phi_h,\phi_S)}}. \tag{7.86}$$

The ratios are calculated in 8×8 equal bins over the range of (ϕ_h,ϕ_S). The reasonable assumption on acceptances Eq. (7.38) is applied in two-dimensional case as well and can be represented as:

$$\frac{a_u^+(\phi_h,\phi_S)}{a_d^-(\phi_h,\phi_S)} = \frac{a_u^-(\phi_h,\phi_S)}{a_d^+(\phi_h,\phi_S)}. \tag{7.87}$$

Similarly to the Eqs. (7.33–7.39) under the assumption of smallness of asymmetries making the Taylor expansion of double ratios one can obtain:

$$R(\phi_h,\phi_S) = const \cdot (1 + 4 \cdot \sum_{i=1}^{8} A_{raw}^{w_i(\phi_h,\phi_S)} w_i(\phi_h,\phi_S)). \tag{7.88}$$

The corresponding nine-parameter fitting function used to extract simultaneously all eight $A_{raw}^{w_i(\phi_h,\phi_S)}$ values is the following one:

$$\begin{aligned} R(\phi_h,\phi_S) = par(0)[1 + 4[&par(1)sin(\phi_h+\phi_S-\pi) + par(2)sin(3\phi_h-\phi_S) + \\ &par(3)sin(\phi_h-\phi_S) + par(4)cos(\phi_h-\phi_S) + par(5)sin(\phi_S) + \\ &par(6)sin(2\phi_h-\phi_S) + par(7)\cos(\phi_S) + par(8)cos(2\phi_h-\phi_S)]]. \end{aligned} \tag{7.89}$$

where the parameters $par(1)$ to $par(8)$ give the "raw asymmetries", while $par(0)$ represents the constant term in Eq. (7.88) and is expected to be ≈ 1 confirming the validity of the acceptance assumption Eq. (7.87). So, summarizing one can conclude that the two-dimensional analysis method take all the advantages of the one-dimensional one, namely:

- method combines information from both target cells from both sub-periods of one data-taking period;
- it implies only a "soft" assumptions on acceptances;
- at first order (for small values of the involved asymmetries) all spin-independent effects, e.g. Cahn asymmetry, are factored out

in addition to these:

- two-dimensional method is free from systematic deviations caused by the non-uniform acceptance in ϕ_S (see, Sec. 7.5);
- and finally it allows to reveal the possible correlations between asymmetries (see, Sec. 7.7.4).

Anyway method has some requirements on minimal statistics entering in the analysis. The reason is that in case of kinematical bins with low statistics (usually last bins) it may happen that no events will fall in some of the 64 (ϕ_h,ϕ_S) bins. In such a cases the χ^2-minimization fails and fit does not converge. Due to this the optimal for COMPASS statistics binning was chosen to be 8×8 and not more. In a fact even with this binning the data from both periods in 2002 which contain much less events compared to other periods in 2003 and 2004 (see Table 6.2) have been excluded in two-dimensional analysis because of problems during the fit. Another aspect to be discussed for two dimensional method is the "binning effect", described in the next section.

7.7.2 Binning effect

The "Binning effect" is an important issue related to the extraction of the asymmetries which have to be mentioned especially for the case of two-dimensional asymmetry evaluation procedure. In general, using the histogram-fitting technic for the extraction of the amplitudes of the modulations one has to take into account that the obtained values differ from the real ones by the factor related to the bin-width.

As the first example Let us consider the one-dimensional case of extraction of the amplitudes a and b of a modulation:

$$f(\varphi) = 1 + a\cos(\varphi) + b\sin(\varphi) \tag{7.90}$$

Lets consider the n-bin histogram filled with N events ($N \to \infty$) according to this distribution. The mean value of $f(\varphi)$ in a bin (ϕ_i, ϕ_{i+1}) is given by:

$$\langle f(\varphi)\rangle_{i,i+1} = \frac{1}{\Delta\varphi}\int_{\varphi_i}^{\varphi_{i+1}} f(\varphi)d\varphi, \tag{7.91}$$

where the bin width $\Delta\varphi = 2\pi/n$. In case of infinite statistics this value is equal to the number of the events entering in i-th bin (N_i) and during the standard histogram-fitting procedure it will be taken by the fitter as an input in the center of the bin, while the "true" height of the function in the center of the bin is given by

$$f(\varphi_i + \Delta\varphi/2) = 1 + a\cos(\varphi_i + \Delta\varphi/2) + b\sin(\varphi_i + \Delta\varphi/2). \tag{7.92}$$

These two values, $\langle f(\phi)\rangle_{i,i+1}$ and $f(\varphi_i + \Delta\varphi/2)$ are not equal, and the difference between them depends on the number of bins. Thus, since the amplitudes extracted from the fit are evaluated using $\langle f(\phi)\rangle_{i,i+1}$ values in the center of the bins ($\varphi_i + \Delta\varphi/2$), they will differ from actual amplitudes which correspond to $(\varphi_i + \Delta\varphi/2; f(\varphi_i + \Delta\varphi/2))$ points. Simple calculations reveal the following relation between extracted amplitudes and *real* ones:

$$\begin{aligned} a_{fit} &= a\frac{2}{\Delta\varphi}\sin\frac{\Delta\varphi}{2} \\ b_{fit} &= b\frac{2}{\Delta\varphi}\sin\frac{\Delta\varphi}{2} \end{aligned} \tag{7.93}$$

In Table 7.7.2 we present the numerical values of the ratios between extracted (a_{fit}, b_{fit}) and actual (a, b) amplitudes calculated for the different number of the bins n:

n	2	4	8	16
$a_{fit}/a = b_{fit}/b$	0.6366	0.9003	0.9745	0.9936

Table 7.3: Dependence of the ratio of extracted and actual amplitudes on the number of the bins in one-dimensional analysis

As we see from this table in case of COMPASS one-dimensional analysis with $n = 16$ the bias is very small $\simeq 0.6\%$ and thus can be neglected.

In two-dimensional analysis method the situation is different. In this case we deal with the following general function:

$$f(\varphi_h, \varphi_S) = 1 + \sum_{k=-1}^{3} (a_k \sin(k\varphi_h - \varphi_S) + b_k \cos(k\varphi_h - \varphi_S)). \tag{7.94}$$

Using the same logic one can obtain the following relations for the ratios between extracted and actual amplitudes:

$$a_{k,fit} = a_k \frac{2}{k\Delta\varphi_h} \sin\frac{k\Delta\varphi_h}{2} \frac{2}{\Delta\varphi_S} \sin\frac{\Delta\varphi_S}{2} \tag{7.95}$$

$$b_{k,fit} = b_k \frac{2}{k\Delta\varphi_h} \sin\frac{k\Delta\varphi_h}{2} \frac{2}{\Delta\varphi_S} \sin\frac{\Delta\varphi_S}{2}. \tag{7.96}$$

The relevant values for the biases are listed in Table 7.7.2.
In order to have reasonable statistics in angular bins we use 8×8 binning in $(\phi_h; \phi_S)$ space. As it can be seen from the above table in this case extracted amplitudes will have a sizable bias, comparing with the actual ones. For example, the real amplitude of the $\sin(3\phi_h - \phi_S)$ modulation differs from the extracted one by more than 20%. Which means that these deviations cannot be neglected and asymmetries extracted by two-dimensional analysis method must be corrected using the corresponding relations Eq. (7.96) and Eq. (7.96).

$n_1 \cdot n_2$	$2 \cdot 2$	$4 \cdot 4$	$8 \cdot 8$	$16 \cdot 16$
$a_{1,fit}/a = b_{1,fit}/b$	0.81057	0.87735	0.94964	0.99180
$a_{2,fit}/a = b_{2,fit}/b$	0.57316	0.81057	0.87735	0.97959
$a_{3,fit}/a = b_{3,fit}/b$	0.2702.	0.70604	0.76421	0.95944

Table 7.4: Dependence of the ratio of extracted and actual amplitudes on number of the bins in two-dimensional analysis

7.7.3 Evaluation of the Asymmetries and Results

Similarly to the one-dimensional analysis the target transverse spin dependent asymmetries were evaluated as a functions of x, z and P_{hT} kinematical variables separately for positive and negative *unidentified* hadrons, and for positive and negative *RICH-identified* pions and kaons.

The event selection, binning over x,z and P_{hT}, evaluation of the correction factors and subsequent correction of the *raw* asymmetries as well as calculation of the weighted mean asymmetries are absolutely identical in one- and two-dimensional analyses and are described in Sec. 6.3, Sec. 6.4, Sec. 7.1 and Sec. 7.2.2.

The difference in the *raw* asymmetries evaluation procedures is that instead of 16 bins over Φ_j the double ratio quantities are now filled in $8 \times 8 = 64$ bins of two-dimensional (ϕ_h, ϕ_S) histogram which is then fitted by two-dimensional function Eq. (7.89). With this fit the values of all eight asymmetries are calculated simultaneously as opposed to one-dimensional case where the fitting was done separately for each of five $W_j(\Phi_j)$ modulations. Analogously to one-dimensional fitting procedure the two-dimensional fit was performed also using MINUIT with χ^2-minimization.

Similarly to one-dimensional case the asymmetries for *RICH-identified* pions and kaons have been evaluated from COMPASS "transverse" 2003-2004 data which have passed the RICH-stability criteria described in Sec. 6.3.10. Since the data from both two periods in 2002 (P2B-P2C and P2H1-P2H2) was rejected due to the low statistics and following from this problems with the fit convergence in two dimensional analysis (see Sec. 7.7.1) the *unidentified* hadron asymmetries with this method have been evaluated only using the 2003-2004 COMPASS data.

In the figures 7.27 - 7.34 the extracted with two-dimensional method eight transverse momentum dependent asymmetries for positive and negative unidentified hadrons, and for positive and negative *RICH-identified* pions and kaons are presented as a function of x, z and P_{hT}.

The red circles indicates the results for positive hadrons, (pions and kaons) while the blue triangles correspond to negative hadrons, (pions and kaons). The error bars shown in all the plots are statistical only. In all the plots the blue triangles are slightly shifted horizontally with the respect to the measured value.

The same preliminary conclusion as one made on results from one-dimensional method about the smallness of the asymmetries measured with the deuteron target and agreement with theory predictions can be drawn here.

$A_{UT}^{-\sin(\phi_h+\phi_S)}$ **(Collins) asymmetry with COMPASS data. Two-dimensional fit.**

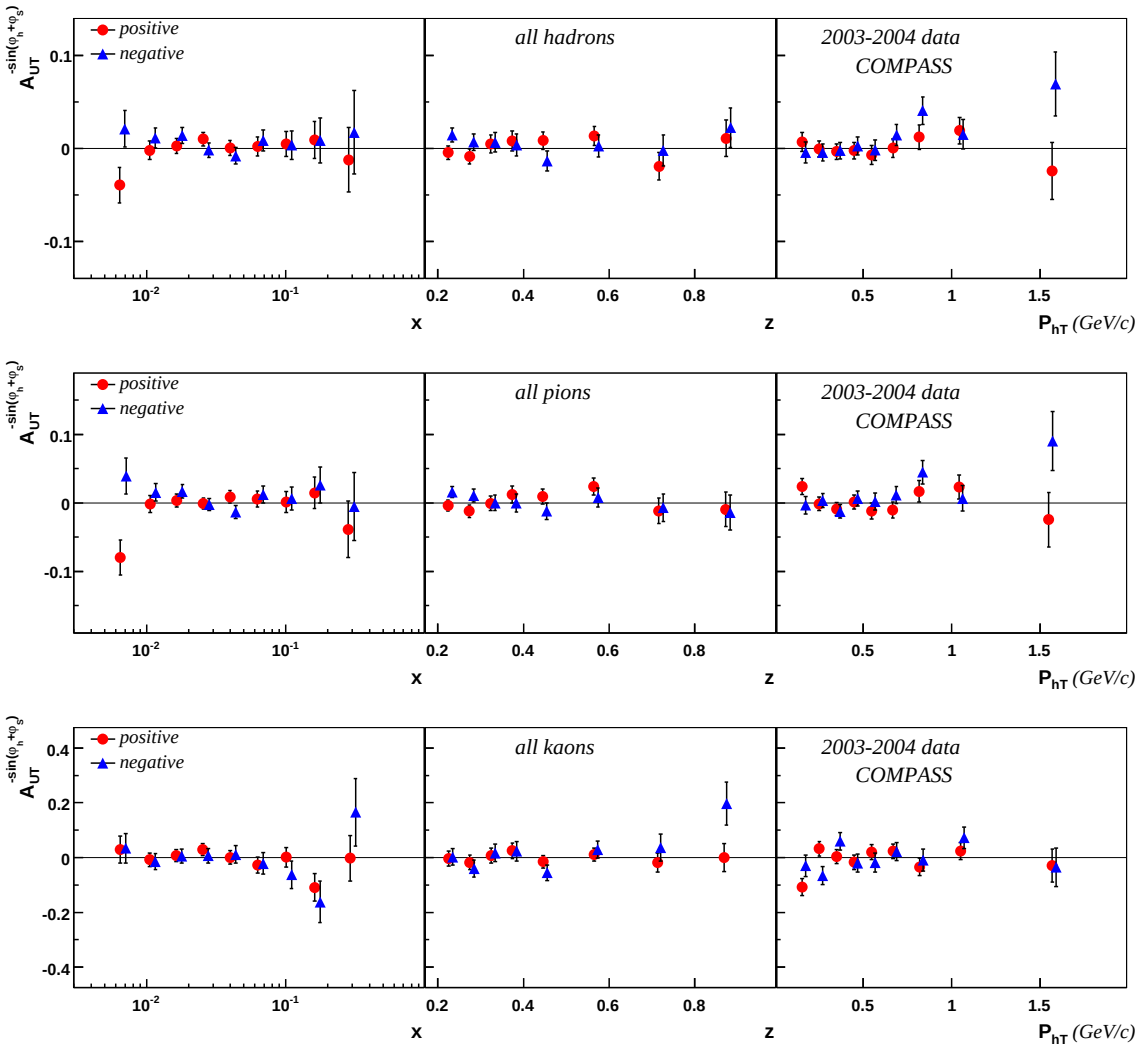

Figure 7.27: Extracted $A_{UT}^{-\sin(\phi_h+\phi_S)}$ (Collins) asymmetry for unidentified hadrons (top row), pions (middle row) and kaons (bottom row) as a function of x, z and P_{hT}

$A_{UT}^{\sin(3\phi_h-\phi_S)}$ **asymmetry with COMPASS data. Two-dimensional fit.**

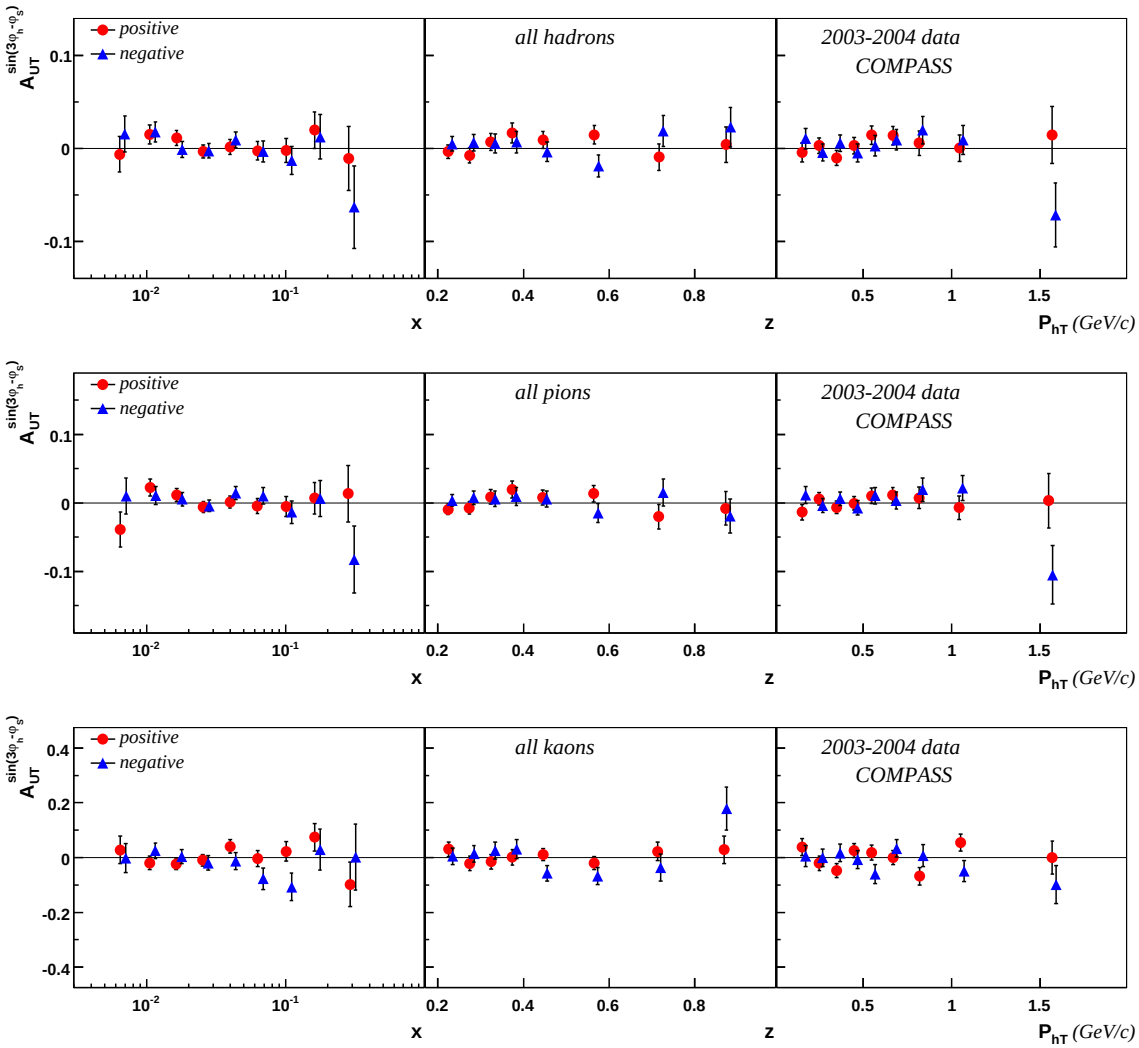

Figure 7.28: Extracted $A_{UT}^{\sin(3\phi_h-\phi_S)}$ asymmetry for unidentified hadrons (top row), pions (middle row) and kaons (bottom row) as a function of x, z and P_{hT}

$A_{UT}^{\sin(\phi_h-\phi_S)}$ **(Sivers) asymmetry with COMPASS data. Two-dimensional fit.**

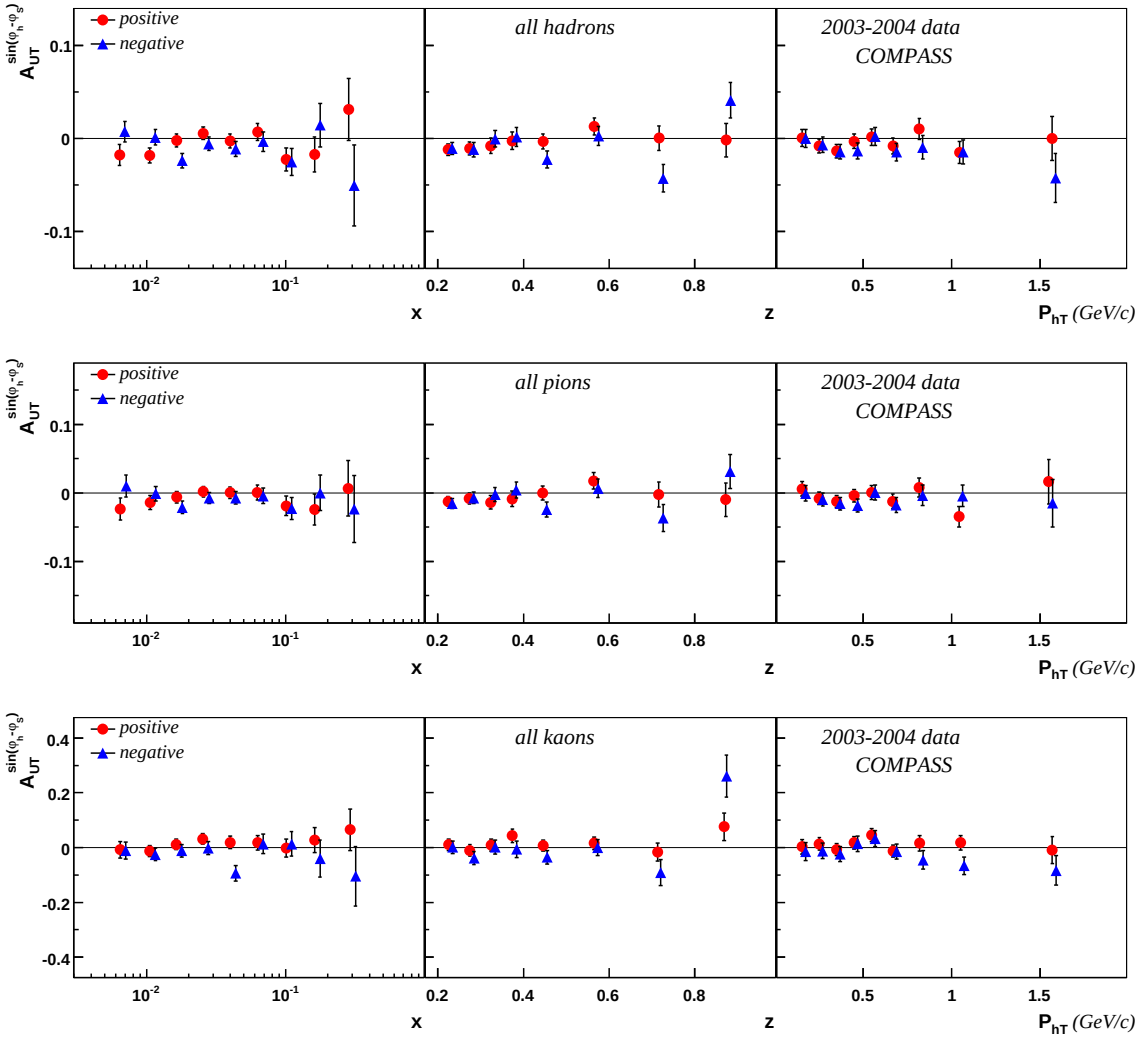

Figure 7.29: Extracted $A_{UT}^{\sin(\phi_h-\phi_S)}$ (Sivers) asymmetry for unidentified hadrons (top row), pions (middle row) and kaons (bottom row) as a function of x, z and P_{hT}

$A_{LT}^{\cos(\phi_h-\phi_S)}$ asymmetry with COMPASS data. Two-dimensional fit.

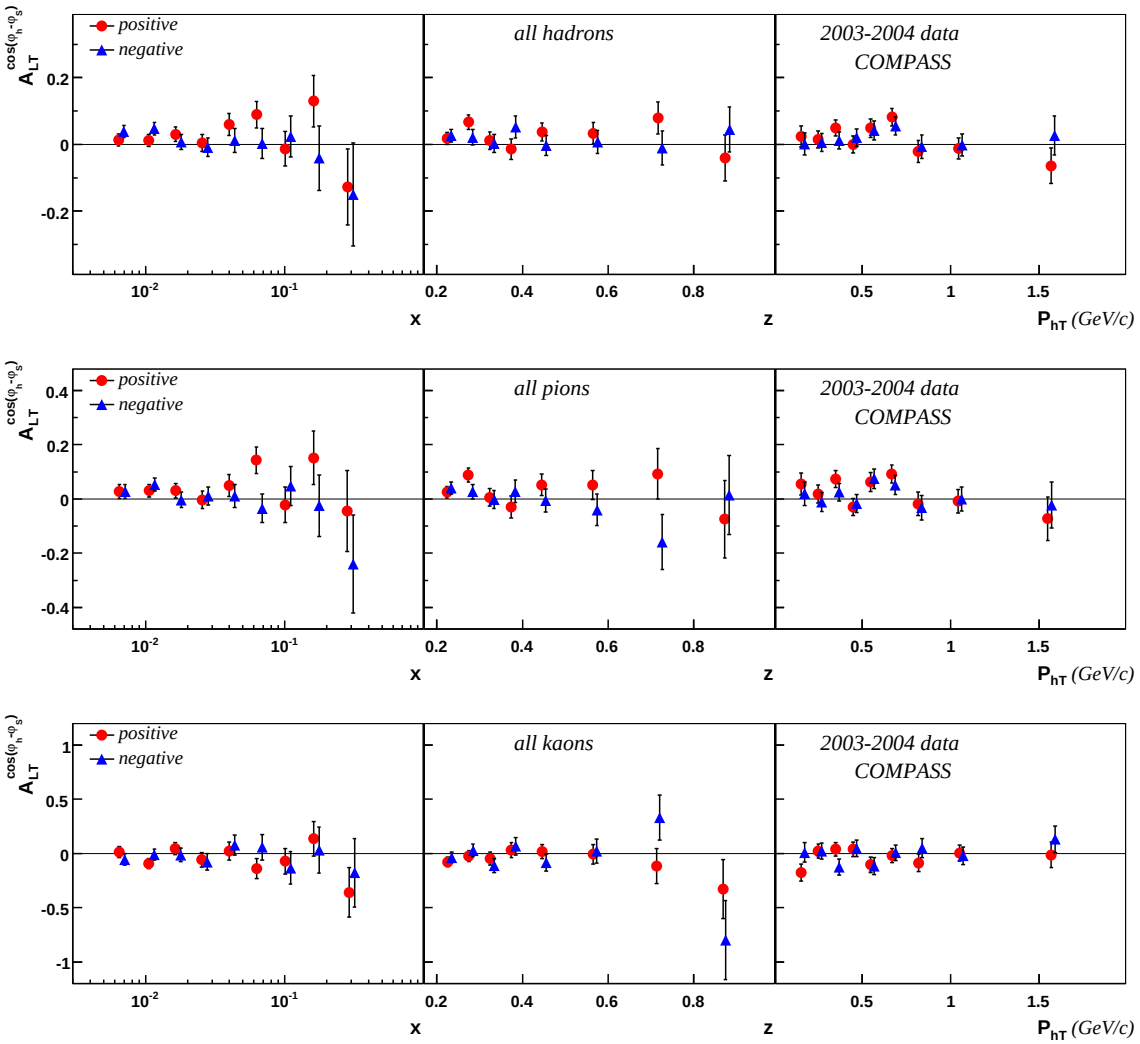

Figure 7.30: Extracted $A_{LT}^{\cos(\phi_h-\phi_S)}$ asymmetry for unidentified hadrons (top row), pions (middle row) and kaons (bottom row) as a function of x, z and P_{hT}

$A_{UT}^{\sin(\phi_S)}$ asymmetry with COMPASS data. Two-dimensional fit.

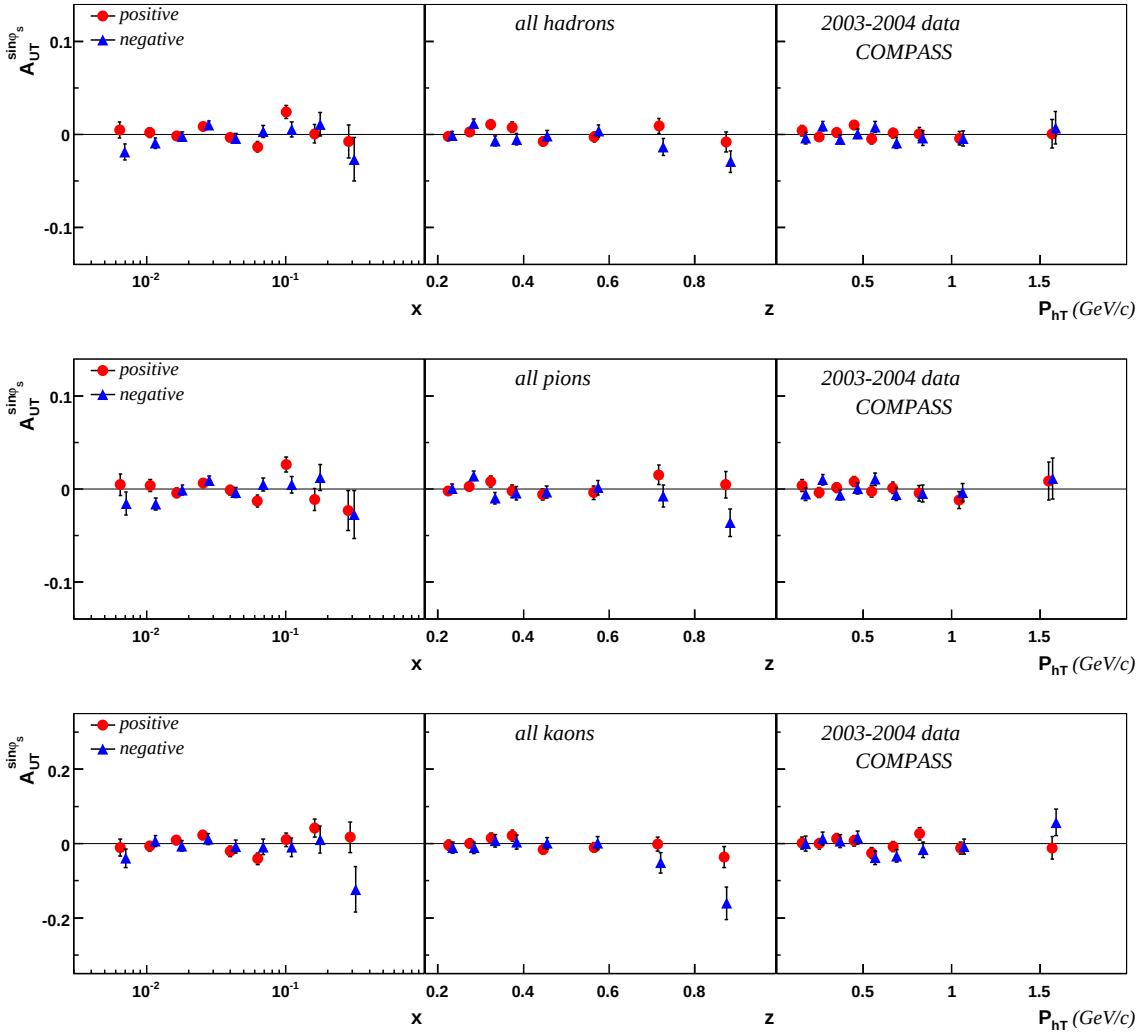

Figure 7.31: Extracted $A_{UT}^{\sin(\phi_S)}$ asymmetry for unidentified hadrons (top row), pions (middle row) and kaons (bottom row) as a function of x, z and P_{hT}

$A_{UT}^{\sin(2\phi_h-\phi_S)}$ **asymmetry with COMPASS data. Two-dimensional fit.**

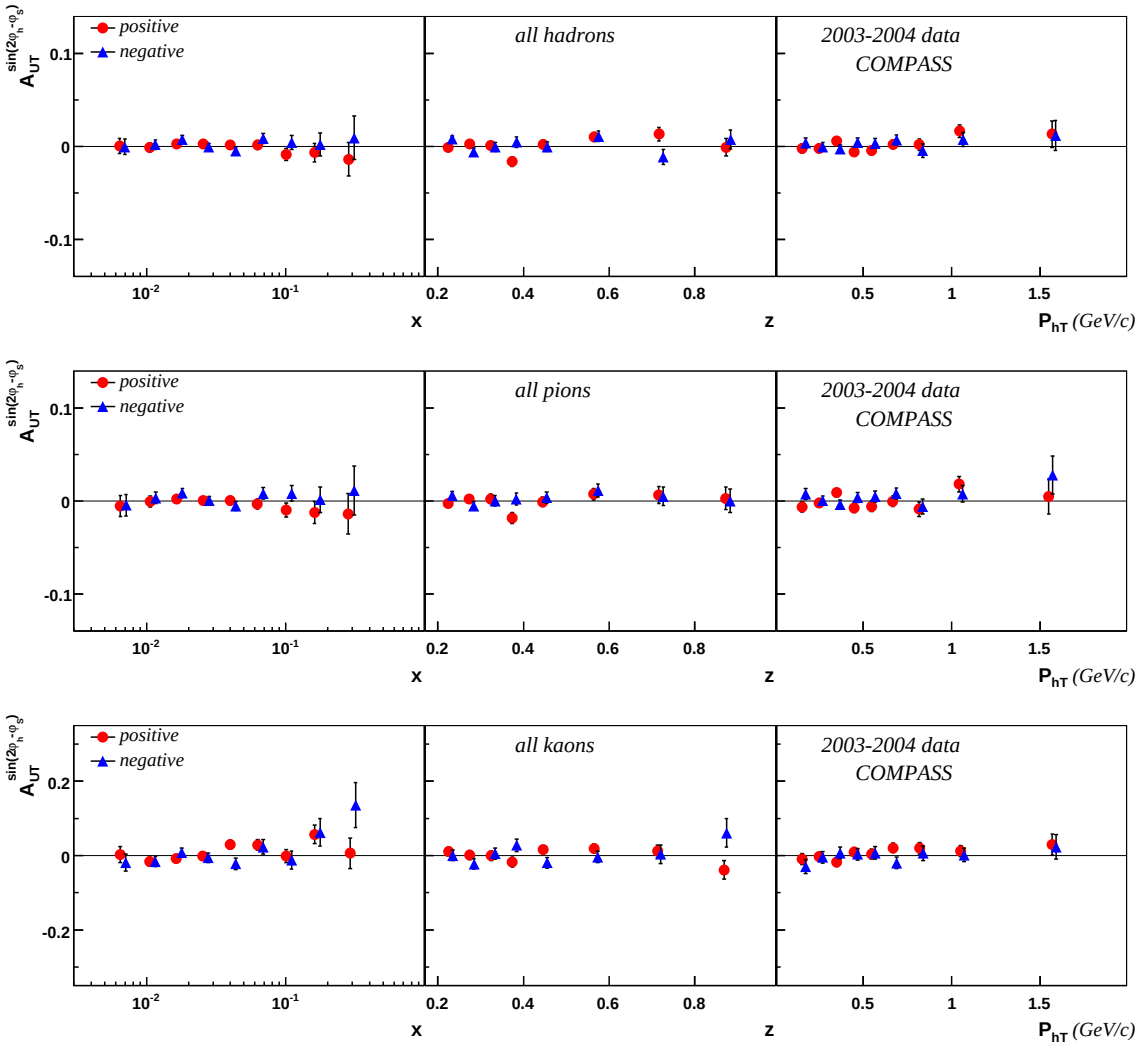

Figure 7.32: Extracted $A_{UT}^{\sin(2\phi_h-\phi_S)}$ asymmetry for unidentified hadrons (top row), pions (middle row) and kaons (bottom row) as a function of x, z and P_{hT}

$A_{LT}^{\cos(\phi_S)}$ asymmetry with COMPASS data. Two-dimensional fit.

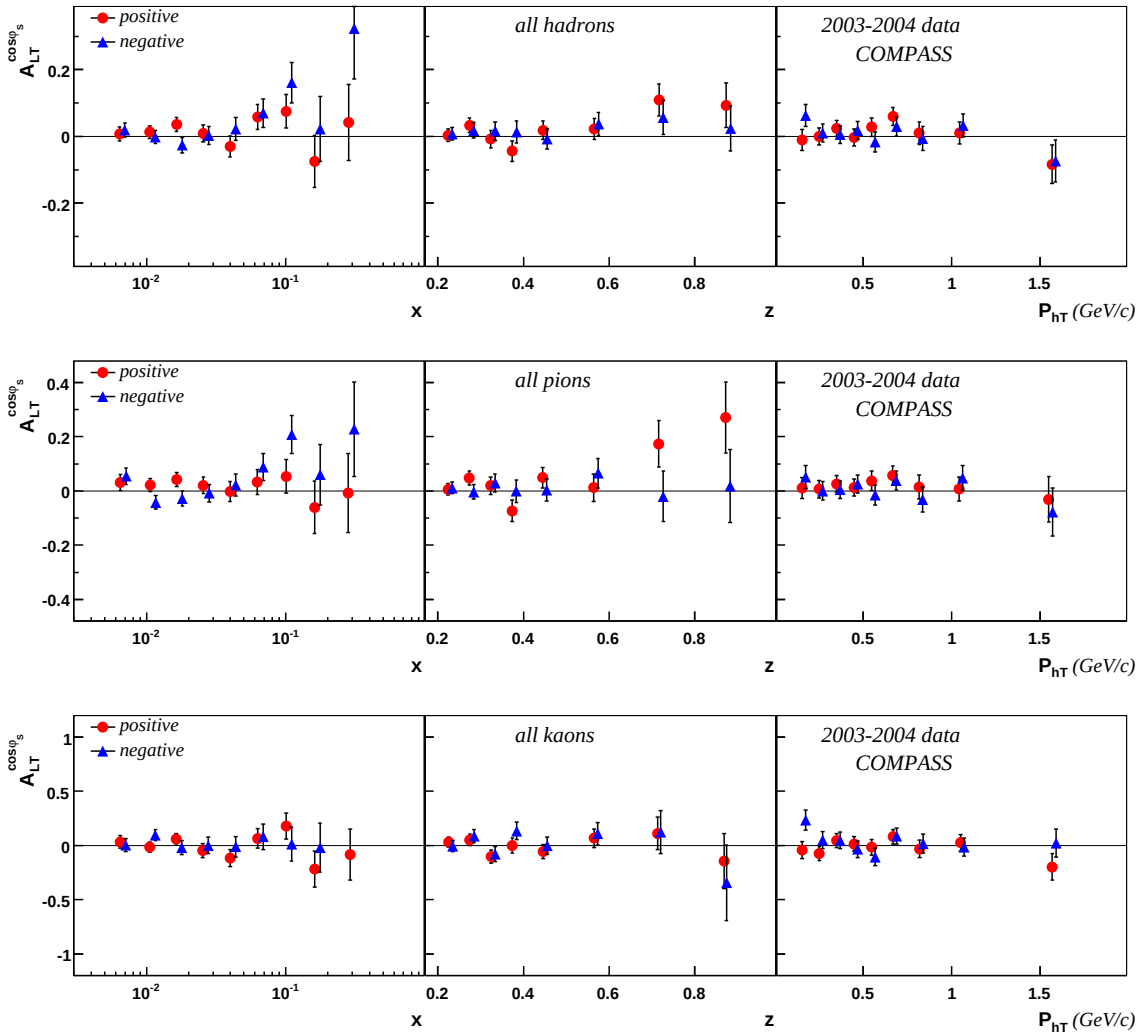

Figure 7.33: Extracted $A_{LT}^{\cos(\phi_S)}$ asymmetry for unidentified hadrons (top row), pions (middle row) and kaons (bottom row) as a function of x, z and P_{hT}

$A_{LT}^{\cos(2\phi_h-\phi_S)}$ asymmetry with COMPASS data. Two-dimensional fit.

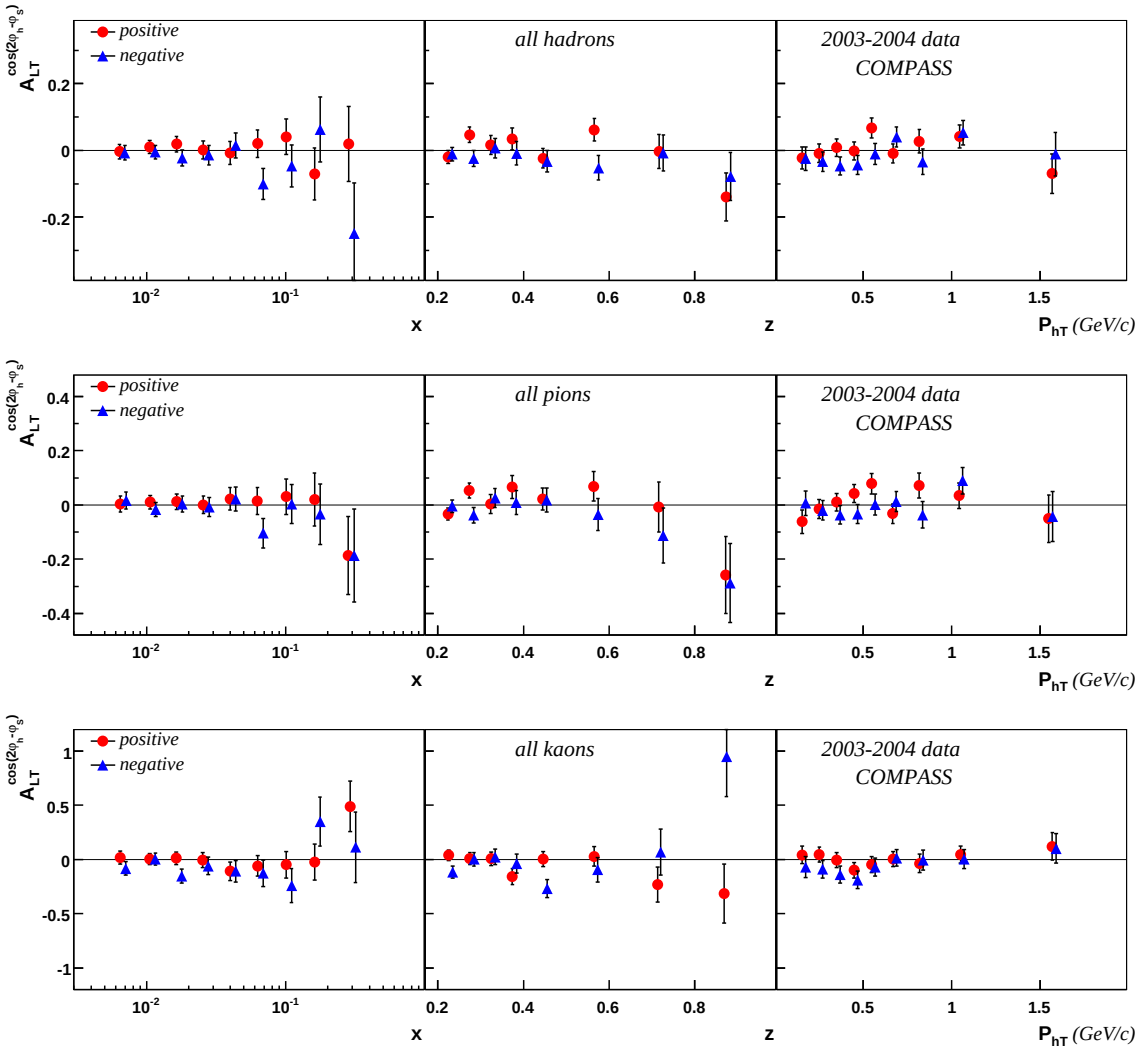

Figure 7.34: Extracted $A_{LT}^{\cos(2\phi_h-\phi_S)}$ asymmetry for unidentified hadrons (top row), pions (middle row) and kaons (bottom row) as a function of x, z and P_{hT}

7.7.4 Correlation Coefficients

One of the advantages of the two-dimensional analysis method is that it gives access to the correlations between the extracted asymmetries. Performing the fit with two-dimensional function MINUIT calculates the $n \times n$ covariance matrix $A_{[i,j]}$ ($i = 1, .., n$; $\text{J} = 1, .., n$), with n being the number of parameters in fitting function which in our case is nine. The correlations ρ between any two pairs of parameters are then calculated through the expression:

$$\frac{covariance_{[i,j]}}{\sqrt{variance_{[i,i]} \cdot variance_{[j,j]}}} \tag{7.97}$$

For nine parameters in total we have 36 pairs of parameters and thus 36 correlation coefficients to be calculated for positive and negative *unidentified* hadrons and positive and negative pions and kaons, in each kinematical bin over x, z and P_{hT} and for each data-taking period. In most of the cases correlation coefficients are negligible (≈ 0), only for seven pairs of parameters correlations larger than 0.1 have been revealed, though even they remains in a maximum smaller than 0.4, which is again indication of negligible correlations. Performed Monte-Carlo studies have shown that such ($0.4 > \rho > 0.1$) correlations can be caused by the *non-uniformity* of acceptance in ϕ_S in COMPASS. During the evaluation of the two-dimensional fit by MINUIT, the covariances (correlations) between each pairs of parameters are automatically taken into account in the calculation of the fit parameters and their errors. Since in one-dimensional fit the asymmetries are evaluate separately no information about correlations between them is available and thus covariances are not taken into account. Anyway since the correlations are found to be small they can be neglected in one-dimensional analysis.

As an example we present in figures 7.35, 7.36 and 7.37 the correlation coefficients with absolute values larger than 0.1 for unidentified hadrons, pions and kaons respectively [1]. All three plots correspond to second data-taking period in 2004 (W35-W36), for other periods situation is very similar. In all the plots the top row is for positive hadrons, the bottom row is for the negative hadrons, and correlation coefficients are shown (from left to right) for x, z and P_{hT}. The notation of symbols in the plots are the following:

- Red solid square indicates the correlation between $A_{UT}^{-\sin(\phi_h+\phi_S)}$ and $A_{UT}^{\sin(\phi_h-\phi_S)}$
- Green upper solid triangle indicates the correlation between $A_{UT}^{-\sin(\phi_h+\phi_S)}$ and $A_{UT}^{\sin(\phi_S)}$
- Blue lower solid triangle indicates the correlation between $A_{UT}^{\sin(3\phi_h-\phi_S)}$ and $A_{UT}^{\sin(2\phi_h-\phi_S)}$
- Yellow hollow circle indicates the correlation between $A_{UT}^{\sin(\phi_h-\phi_S)}$ and $A_{UT}^{\sin(\phi_S)}$
- Violet hollow square indicates the correlation between $A_{UT}^{\sin(\phi_h-\phi_S)}$ and $A_{UT}^{\sin(2\phi_h-\phi_S)}$
- Blue upper hollow triangle indicates the correlation between $A_{UT}^{\cos(\phi_h-\phi_S)}$ and $A_{UT}^{\cos(\phi_S)}$
- Green hollow diamond indicates the correlation between $A_{UT}^{\cos(\phi_h-\phi_S)}$ and $A_{UT}^{\cos(2\phi_h-\phi_S)}$

[1] For complete set of correlation coefficients see Appendix (Sec. 9.2.1 – 9.2.3)

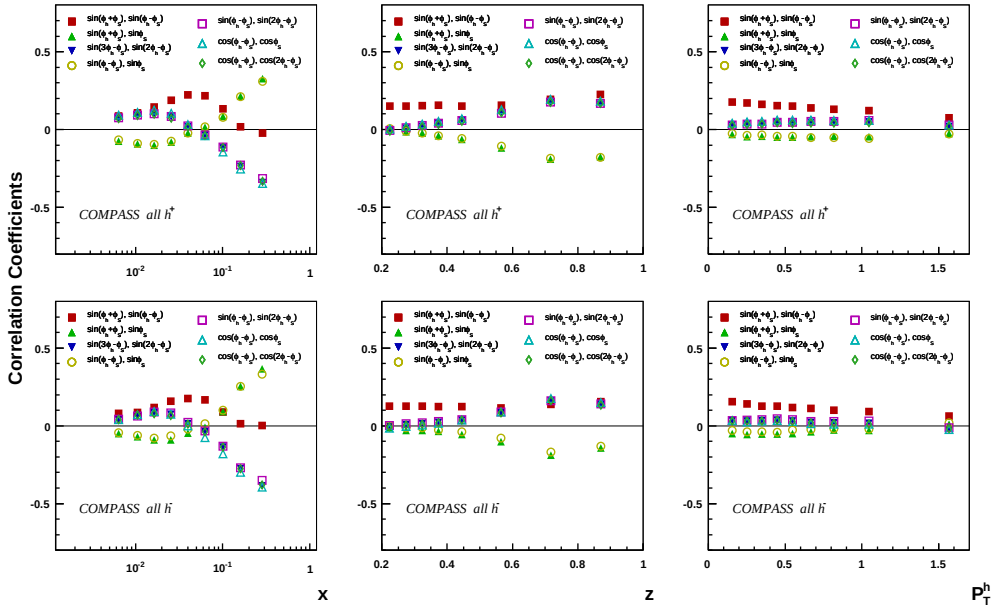

Figure 7.35: *Unidentified* hadron - sample: Correlation between parameters, where the correlation is in the range above $\pm$ 0.1 in any one of the x, z and P_{hT} bin.

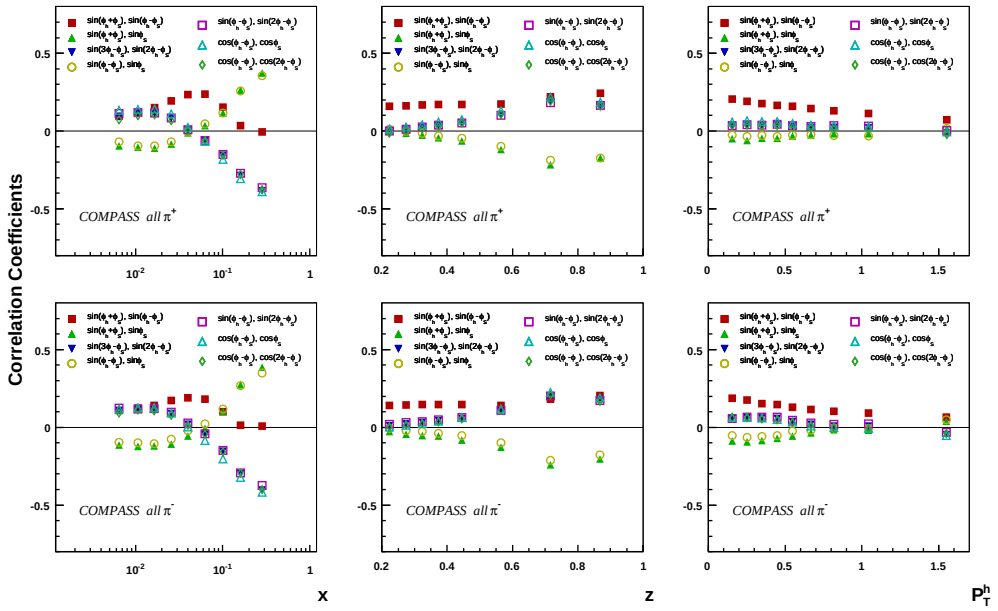

Figure 7.36: Pion - sample: Correlation between parameters, where the correlation is in the range above $\pm$ 0.1 in any one of the x, z and P_{hT} bin.

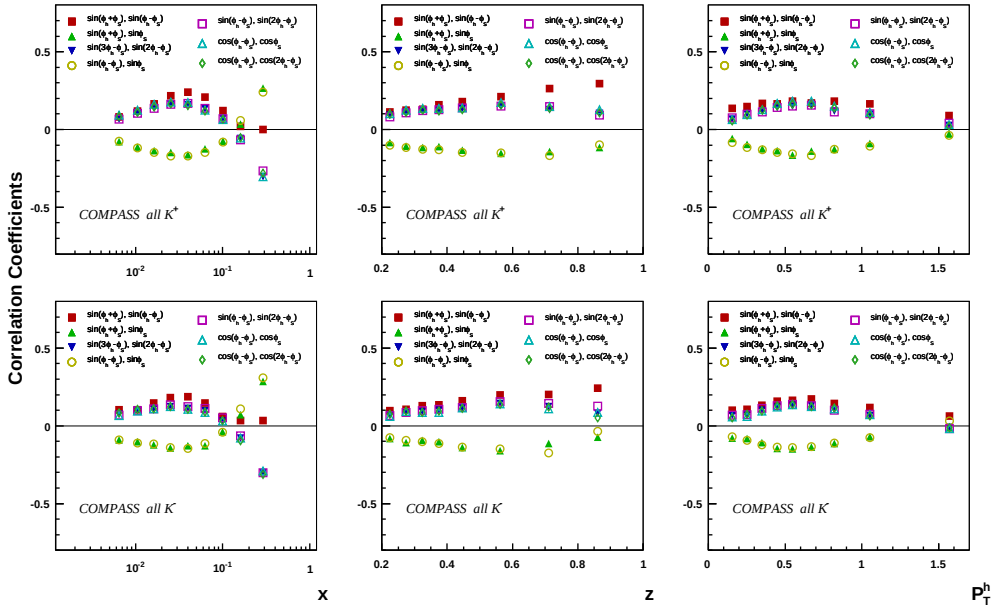

Figure 7.37: Kaon - sample: Correlation between parameters, where the correlation is in the range above $\pm$ 0.1 in any one of the x, z and P_{hT} bin.

7.8 Cross-check Between the Independent Analyses *(2D)*

Similarly to one-dimensional case, all the results obtained using two-dimensional analysis method have been cross-checked with the results obtained independently (using the same method) by COMPASS group in Bonn. As an estimate of the difference between two results we use the same quantity as one used in one-dimensional case (see Sec. 7.3, Eq. (7.47)) which is:

$$\frac{A^m_{To} - A^m_{Bn}}{\sigma_{A^m_{To}}}$$

where A^m_{To} indicates asymmetry value obtained by Torino group and A^m_{Bn} is the same value extracted by Bonn group, their difference is divided by the statistical error calculated by Torino (or by Bonn).

The cross-check have been performed for all eight asymmetries, separately for *unidentified* hadrons and *RICH-identified* pions and kaons. The "pulls" distributions (see Sec. 7.3) between two analysis are shown in figure 7.38 for *unidentified* hadrons and in figure 7.39 for pions and kaons. "Pulls" are constructed separately for x, z and P_{hT} variables and for overall difference between two analyses. The mean difference between the two analyses is given by the average RMS of performed gauss-fits which is approximately of 0.0004 which indicates the perfect agreement.

The number of entries for *unidentified* hadron histograms are:

432 – for x and P_{hT} histograms (8 (asymmetries) $\times$ 2 ($\pm$ hadrons) $\times$ 9 (x or P_{hT} bins) $\times$ 3 (data-taking periods) $= 432$);

384 – for z histogram (8 (asymmetries) $\times$ 2 ($\pm$ hadrons) $\times$ 8 (z bins) $\times$ 3 (data-taking periods) $= 384$);

and correspondingly 1248 entries in overall $x : z : P_{hT}$ histogram ($432 + 384 + 432 = 1248$).

The number of entries for *RICH-identified* pion-kaon histograms are:

864 – for x and P_{hT} histograms (8 (asymmetries) $\times$ 2 ($\pm$ hadrons) $\times$ 2 (π/K) $\times$ 9 (x or P_{hT} bins) $\times$ 3 (data-taking periods) $= 864$);

768 – for z histogram (8 (asymmetries) $\times$ 2 ($\pm$ hadrons) $\times$ 2 (π/K) $\times$ 8 (z bins) $\times$ 3 (data-taking periods) $= 768$);

and as a summary 2496 entries in overall $x : z : P_{hT}$ histogram ($864 + 768 + 864 = 2496$).

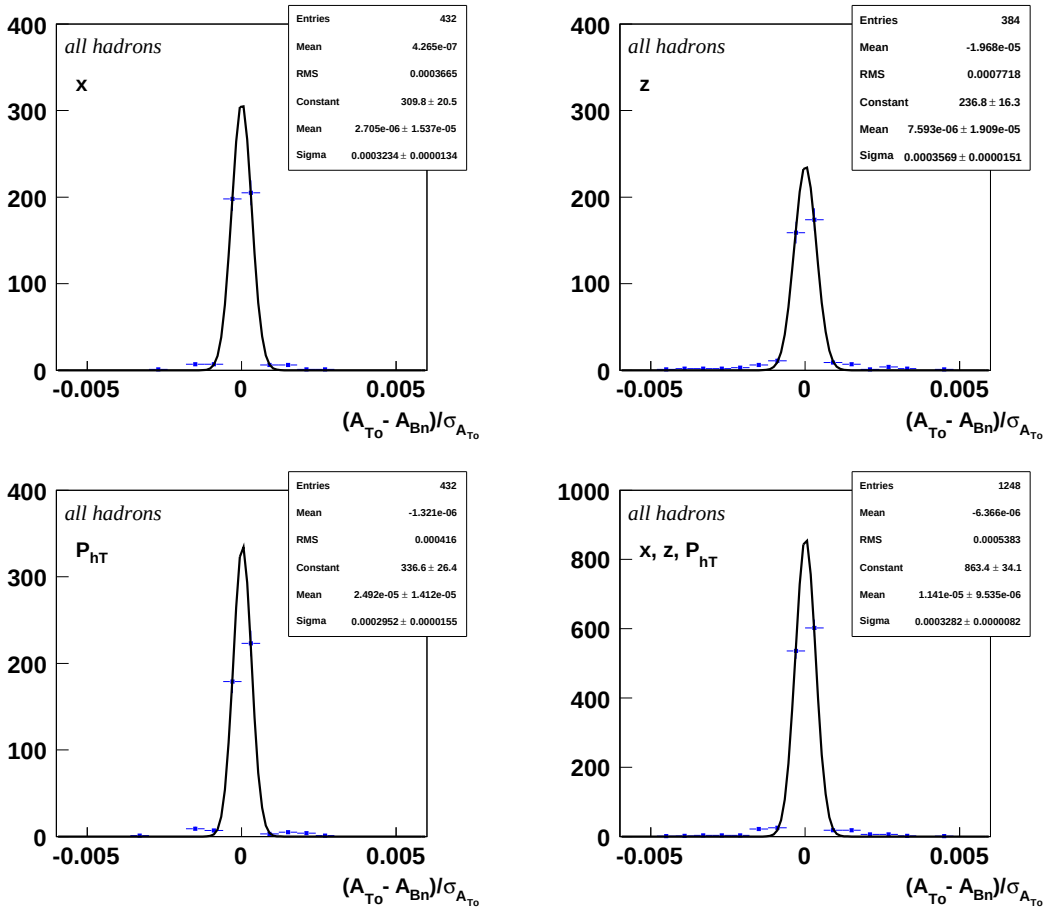

Figure 7.38: Cross check between Bonn and Torino analysis for *unidentified* hadron asymmetries with two-dimensional fit: "pulls" distribution for x (top left), z (top right) and P_{hT} (bottom left) variables, and for all variables (bottom right).

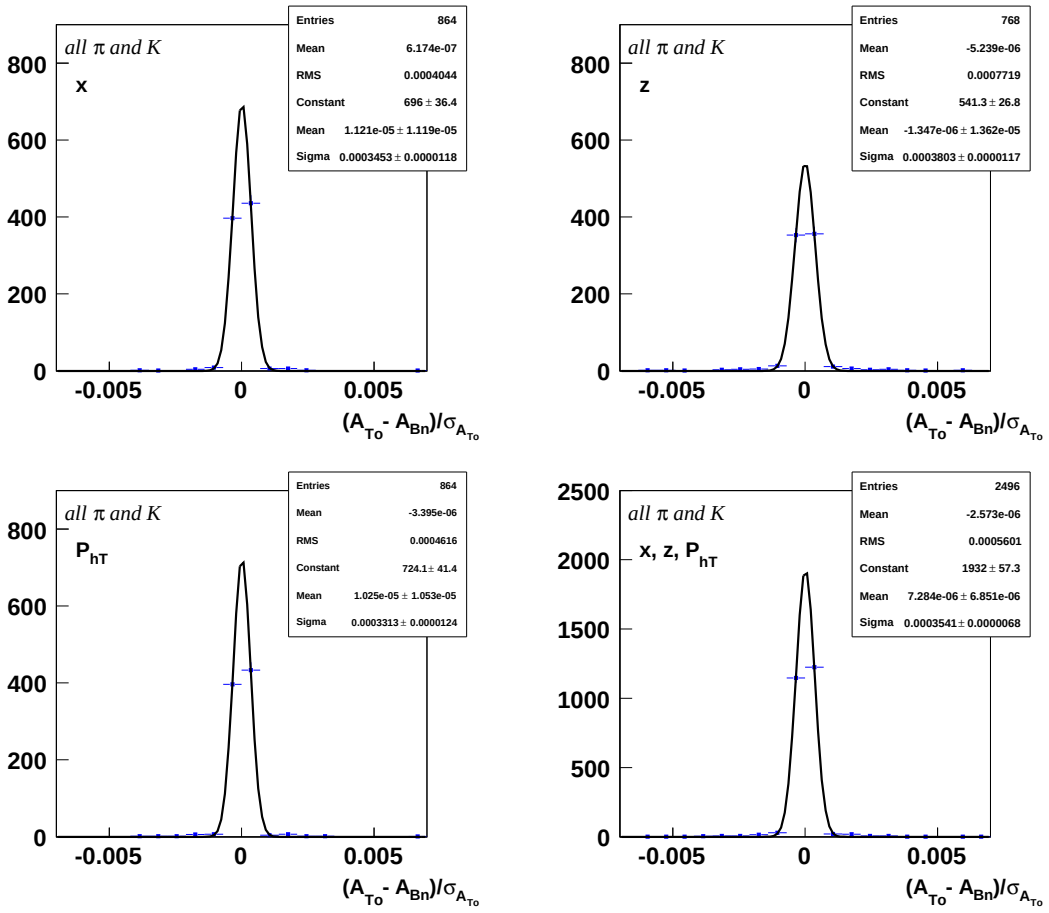

Figure 7.39: Cross check between Torino and Bonn analysis for pion and kaon asymmetries with two-dimensional fit: "pulls" distribution for x (top left), z (top right) and P_{hT} (bottom left) variables, and for all variables (bottom right).

7.9 Systematic Studies *(2D)*

Results obtained using the two-dimensional analysis have been scrutinized for the systematic deviations using the same tests as ones used in one-dimensional analysis. These are namely periods compatibility test, *"par(0)-test"*, *"R'-test"* and fit quality test. None of these checks revealed any systematic deviations, which shows that possible systematic errors of measurement are much smaller than statistical ones. Here in order to reduce the amount of similar plots we present only the results for periods compatibility test.

Another study have been performed in order to check the agreement between the results obtained with two methods. Special Monte-Carlo tests dedicated to this subject are presented in Sec. 7.9.3. Performed studies demonstrated that the difference between the two methods can be explained by the statistical fluctuations present in low-statistical bins.

7.9.1 Compatibility of the Results from Different Periods

The test have been performed similarly to its analogue in one-dimensional analysis (see Sec. 7.4.1). The compatibility of the results obtained in different periods have been tested by constructing the P_i^m estimator presented in Eq. (7.48):

$$P_i^m = \frac{A_i^m - < A^m >}{\sqrt{\sigma^2_{A_i^m} - \sigma^2_{<A^m>}}}$$

where A_i^m indicates the result obtained from i-th period and $< A^m >$ is the weighted mean of A_i^m values over all periods while the $\sigma^2_{A_i^m}$ and $\sigma^2_{<A^m>}$ are respective variances. The P_i^m values were evaluated for positive and negative *unidentified* hadrons, from three data-taking periods in 2003-2004 and filled in the histograms separately for x, z and P_{hT} asymmetries, and one common histogram for all three variables. Analogous procedure was done for P_i^m values for positive and negative combined pion and kaon asymmetries from three $RICH$-periods in 2003-2004. The gauss-fits of the histograms reveal the expected standard normal distributions demonstrating that the differences between the results from different periods has purely a statistical origin.

Results of the period compatibility tests are presented in figures 7.40 and 7.41 respectively for *unidentified* hadron and combined pion and kaon asymmetries.

The number of entries for *unidentified* hadron histograms are:
432 – for x and P_{hT} histograms (8 (asymmetries) $\times$ 2 ($\pm$ hadrons) $\times$ 9 (x or P_{hT} bins) $\times$ 3 (data-taking periods) $= 432$);
384 – for z histogram (8 (asymmetries) $\times$ 2 ($\pm$ hadrons) $\times$ 8 (z bins) $\times$ 3 (data-taking periods) $= 384$);
and correspondingly 1248 entries in overall $x : z : P_{hT}$ histogram ($432 + 384 + 432 = 1248$).

The number of entries for *RICH-identified* pion-kaon histograms are:
864 – for x and P_{hT} histograms (8 (asymmetries) $\times$ 2 ($\pm$ hadrons) $\times$ 2 (π/K) $\times$ 9 (x or P_{hT} bins) $\times$ 3 (data-taking periods) $= 864$);
768 – for z histogram (8 (asymmetries) $\times$ 2 ($\pm$ hadrons) $\times$ 2 (π/K) $\times$ 8 (z bins) $\times$ 3 (data-taking periods) $= 768$);
and as a summary 2496 entries in overall $x : z : P_{hT}$ histogram ($864 + 768 + 864 = 2496$).

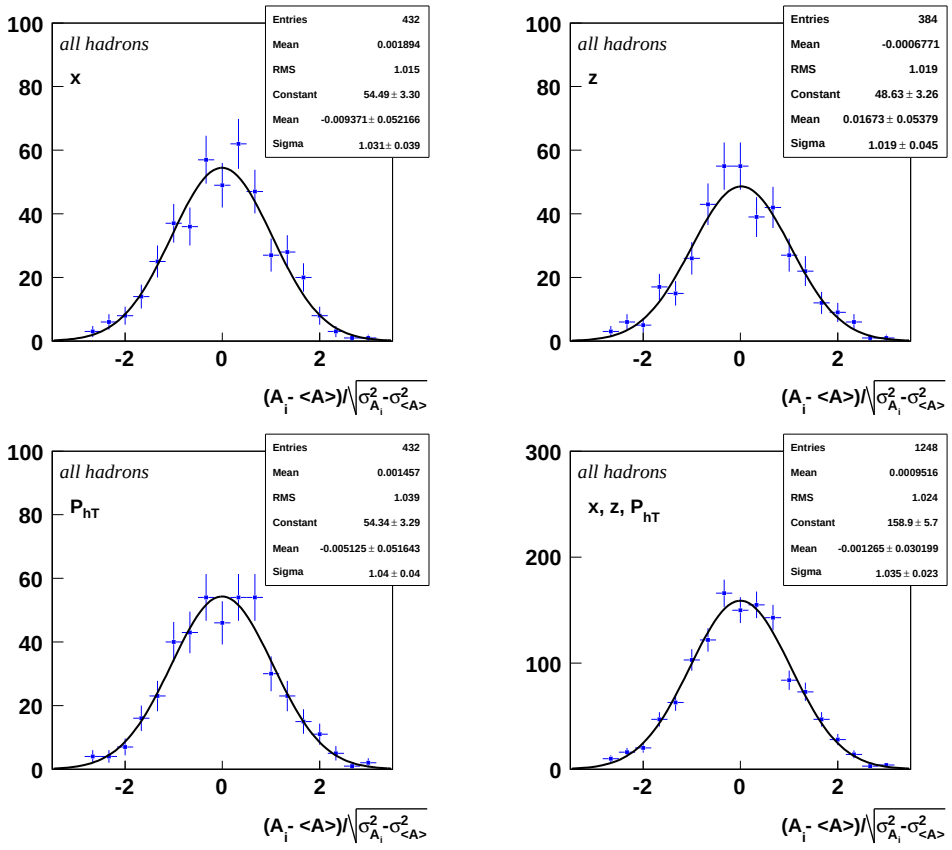

Figure 7.40: Compatibility of the results from different periods: "pulls" distributions to see the compatibility of the results from different periods with x (top left), z (top right), P_{hT} (bottom left) and combined x, z, P_{hT} (bottom right).

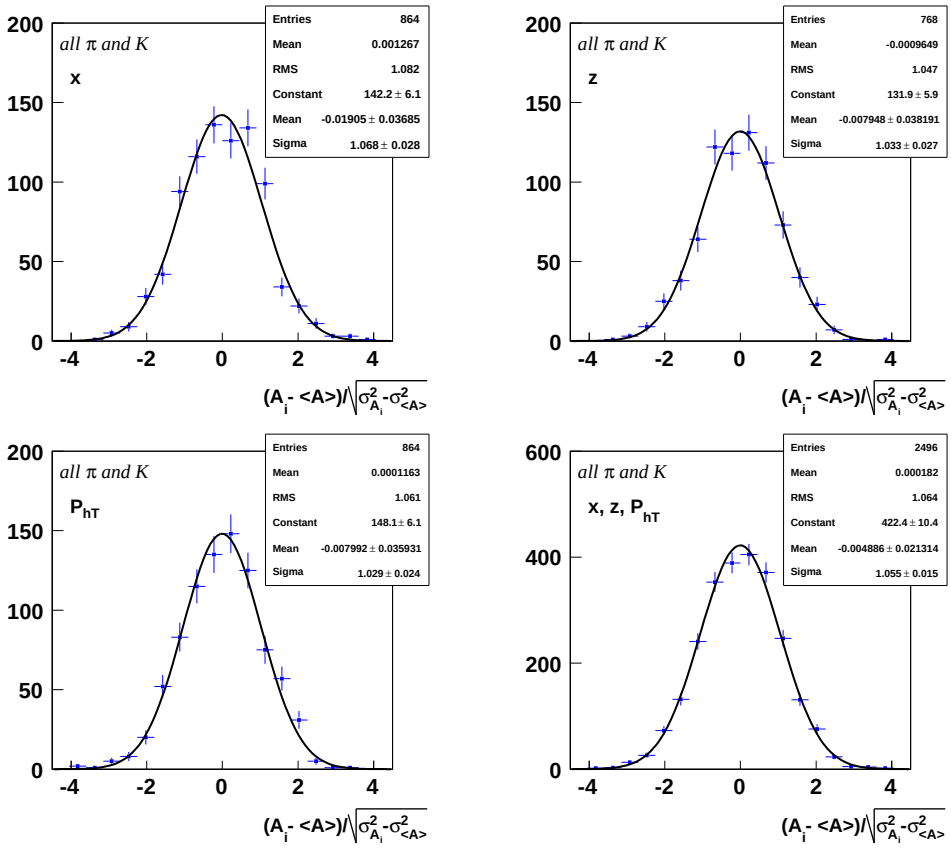

Figure 7.41: Compatibility of the results from different periods: "pulls" distribution to see the compatibility of the results from different periods with x (top left), z (top right), P_{hT} (bottom left) and combined x, z, P_{hT} (bottom right).

7.9.2 Comparison between the Asymmetries Extracted with One- and Two- Dimensional Analyses

We have presented asymmetries extracted with two different methods, one- and two- dimensional analyses. As it was shown in Sec. 7.5 the first method (*1D*) may give slightly distorted results for measured in COMPASS *small* asymmetries due to the not accounted in method ϕ_S-acceptance effects, while the second method may fail to give correct result in low statistical bins. Now it becomes necessary to compare the results from two analyses in order to check if possible differences have statistical or systematic origin.

Figures 7.42 show the cross-check between the results on Sivers asymmetry from one- and two-dimensional methods for positive hadrons (left) and negative hadrons (right) vs. x, z and P_{hT} – top, medium and bottom plots respectively. Similarly figures 7.43 and 7.44 show the cross-check between the results on Sivers asymmetry from two methods for pions and kaons. In all the cross-check plots the red squares correspond to results obtained using one-dimensional and blue triangles using two-dimensional analysis methods.

Figures 7.45 (*unidentified* hadrons), 7.46 (pions) and 7.47 (kaons) show the "pulls" distribution, evaluated similarly to the cross-checks between Torino and Bonn results (see Sec. 7.3 and Sec. 7.8) with the given formula:

$$\frac{A^m_{1D} - A^m_{2D}}{\sigma_{A^m_{1D}}} \tag{7.98}$$

where the A^m_{1D} and A^m_{2D} indicate the results from one- and two- dimensional methods respectively and $\sigma_{A^m_{1D}}$ is the corresponding statistical error calculated in one-dimensional analysis.

Looking to the cross-check plots in figures 7.42 - 7.44 one can see that in general points corresponding to both methods follow the same trend and are very close to each other despite some rare cases in which points differ by more than one σ. Mostly all such a cases correspond to the low-statistical bins, as an example: the last bin in x for positive hadrons and the last bin in z for negative hadrons (fig.7.42), the last bin in P_{hT} for positive pions (fig.7.43), almost all the last bins for positive and negative kaons (fig.7.44).

Also in "pulls" we see that average RMS is of $\simeq 0.40 - 0.50$ which indicates that in average results differs by $\simeq 40 - 50\%$ of statistical error. In order to understand the origin of the differences between the results from two analysis the special Monte-Carlo studies have been performed, which are described in next section.

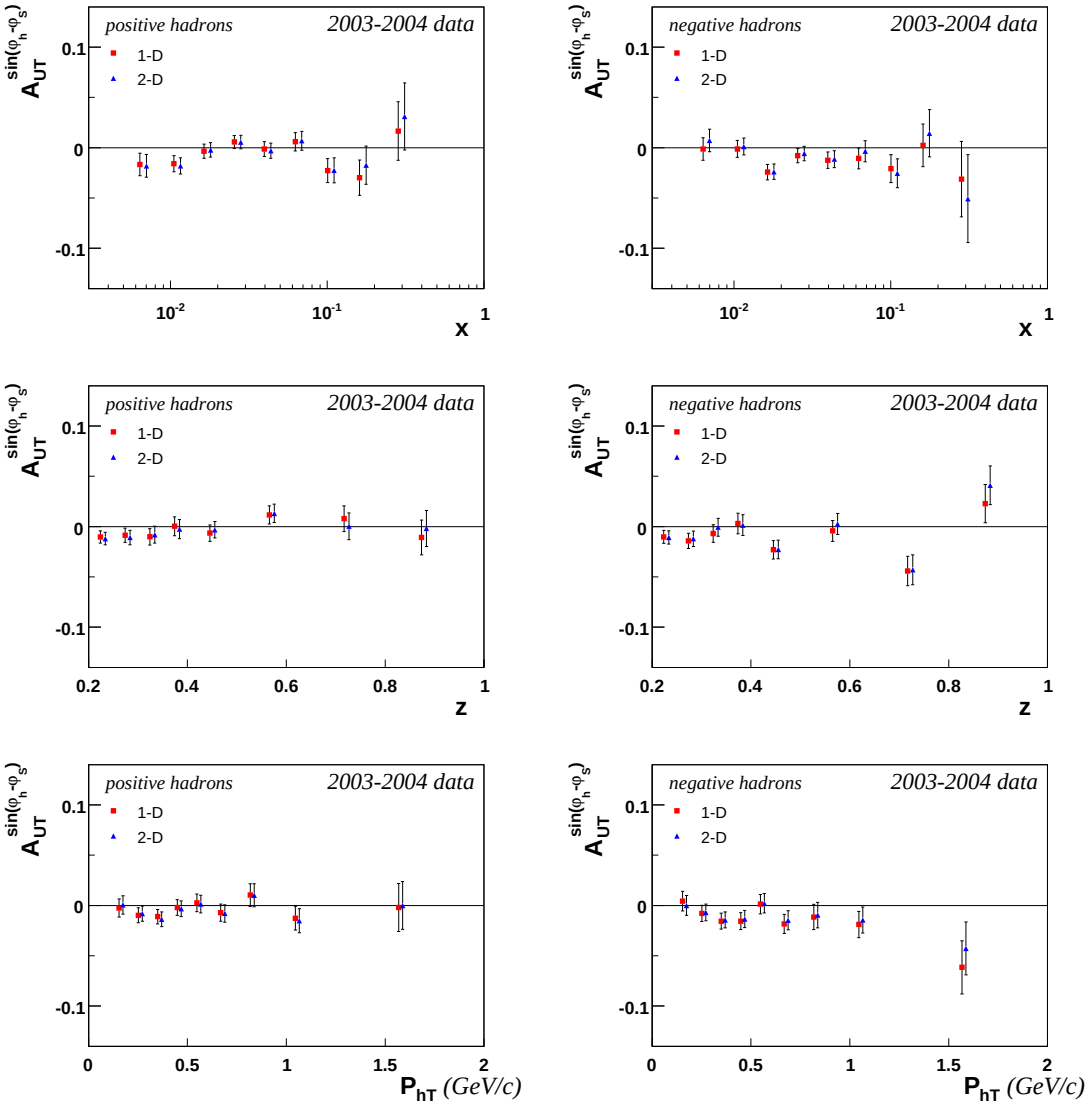

Figure 7.42: Cross check between 1D and 2D analysis for $A_{UT}^{\sin(\phi_h - \phi_S)}$ asymmetry for the periods in 2003 - 2004, all positive hadrons vs. x, z and P_{hT}(left) and all negative hadrons vs. x, z and P_{hT}(right).

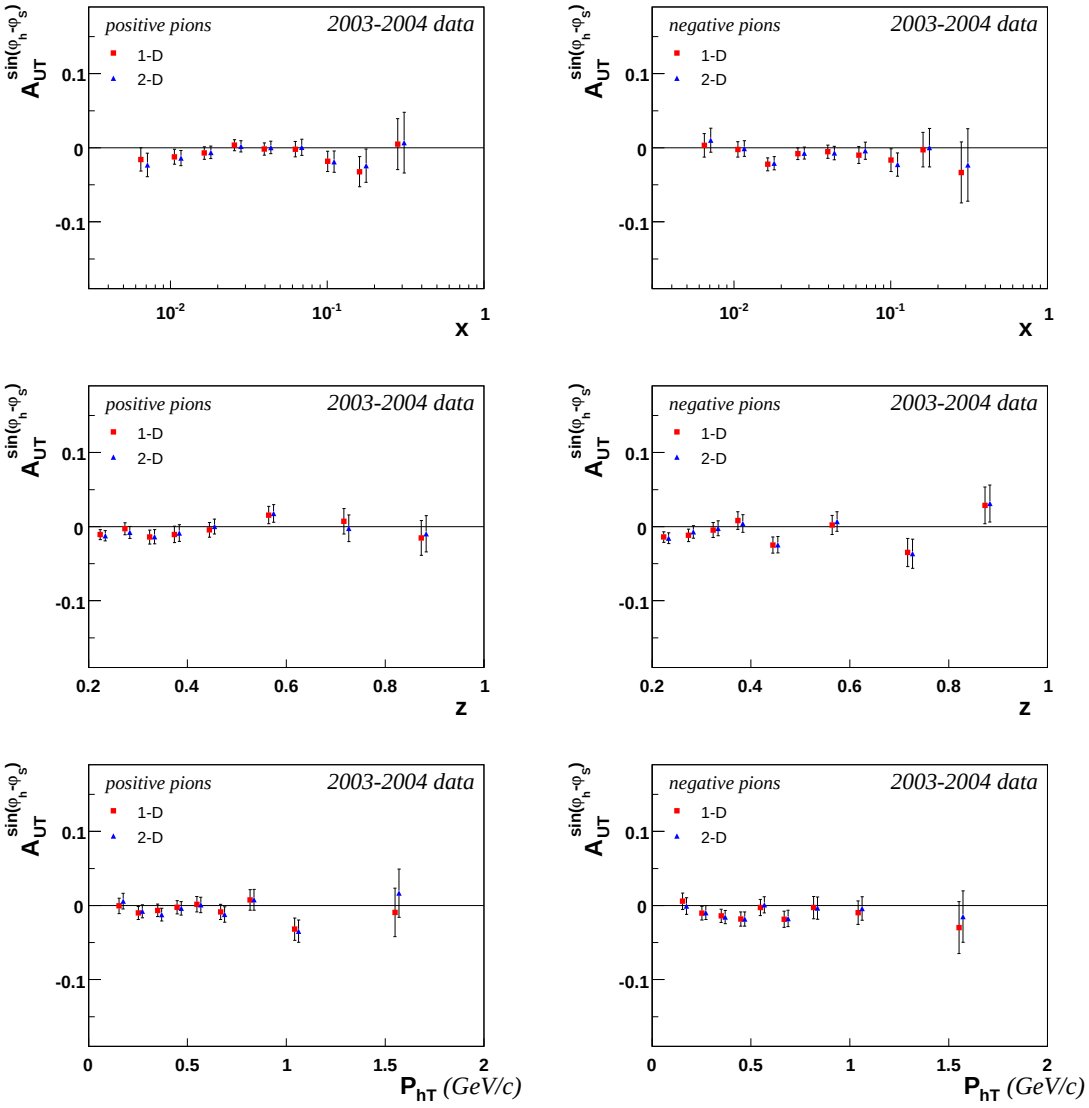

Figure 7.43: Cross check between 1D and 2D analysis for $A_{UT}^{\sin(\phi_h-\phi_S)}$ asymmetry for the periods in 2003 - 2004, all positive pions vs. x, z and P_{hT}(left) and all negative pions vs. x, z and P_{hT}(right).

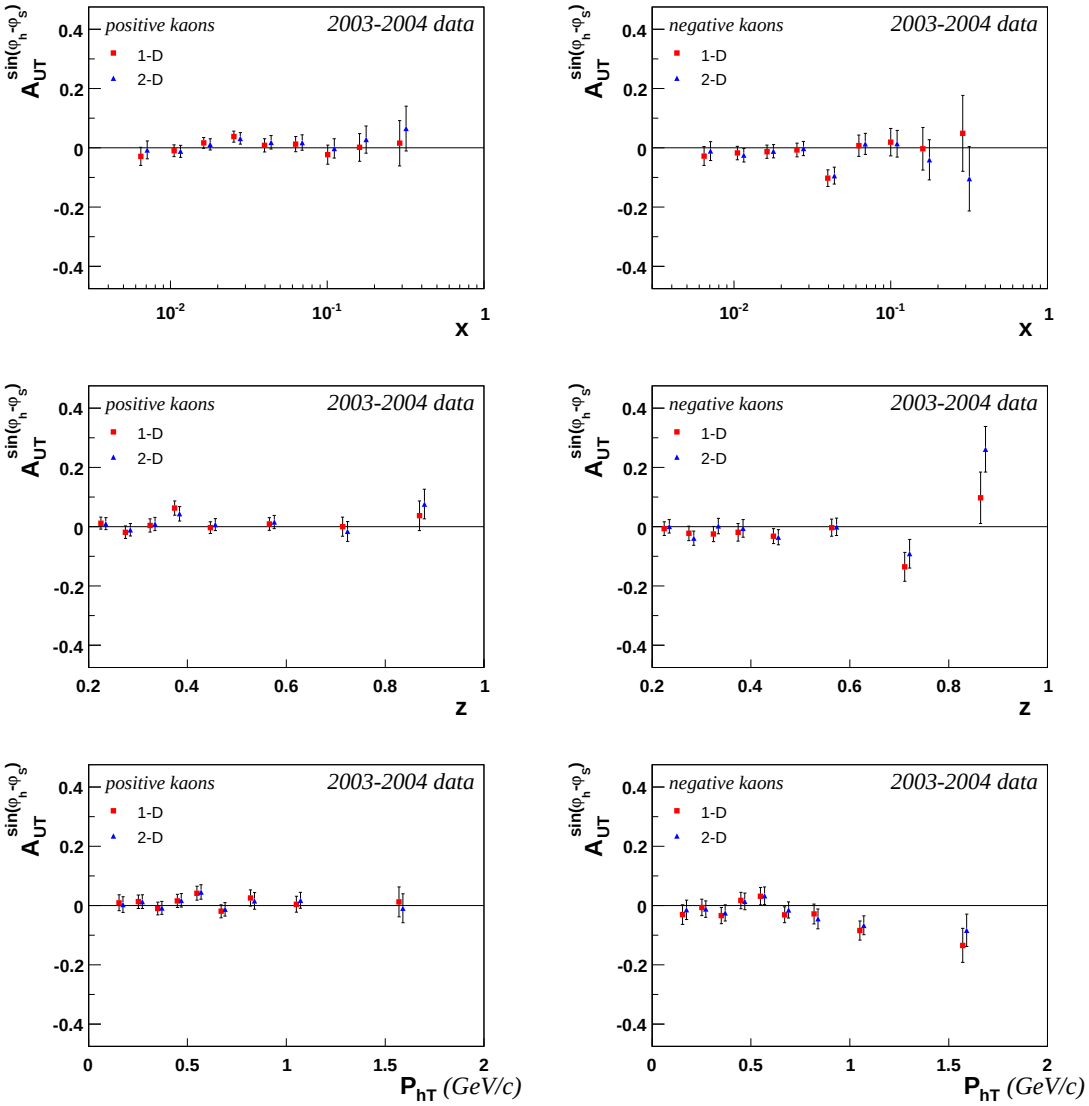

Figure 7.44: Cross check between 1D and 2D analysis for $A_{UT}^{\sin(\phi_h - \phi_S)}$ asymmetry for the periods in 2003 - 2004, all positive kaons vs. x, z and P_{hT}(left) and all negative kaons vs. x, z and P_{hT}(right).

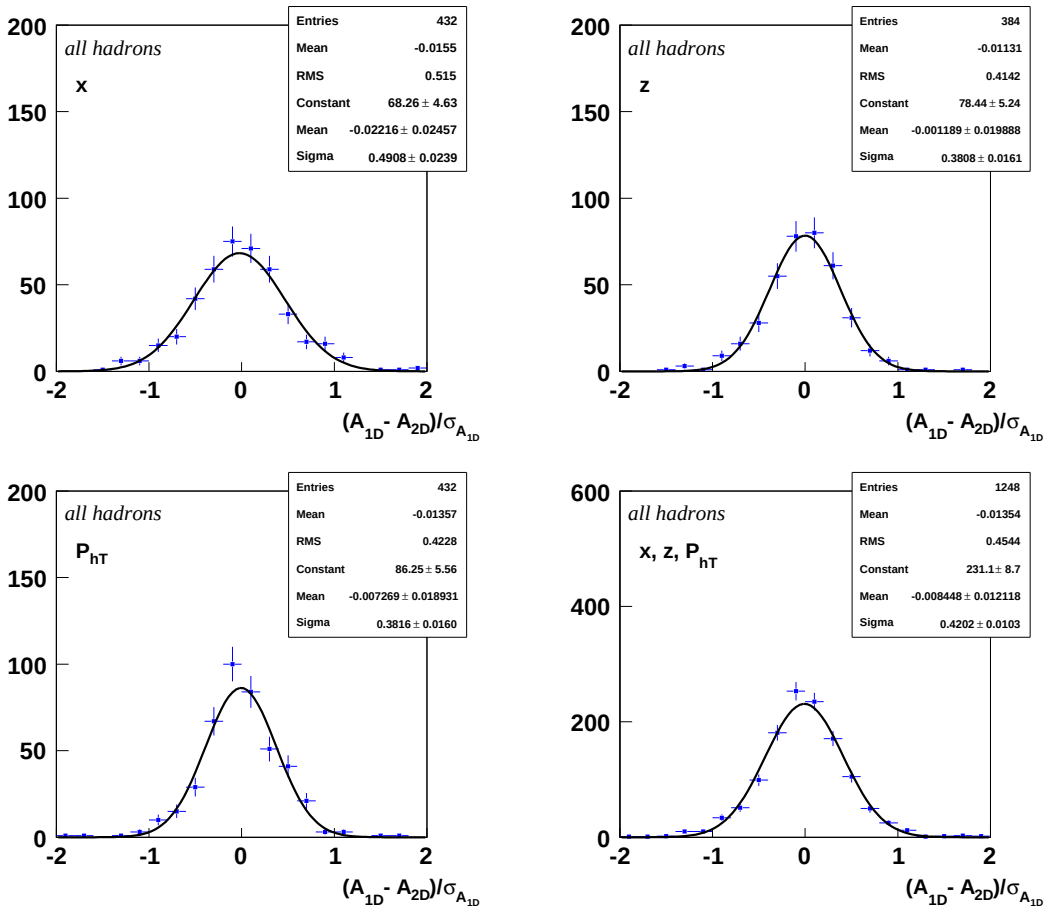

Figure 7.45: Cross check between one-dimensional analysis and two-dimensional analysis for *unidentified* hadron asymmetries with two-dimensional fit: "pulls" distribution for x(top left), z(top right) and P_{hT}(bottom left) variables, and for all variables (bottom right).

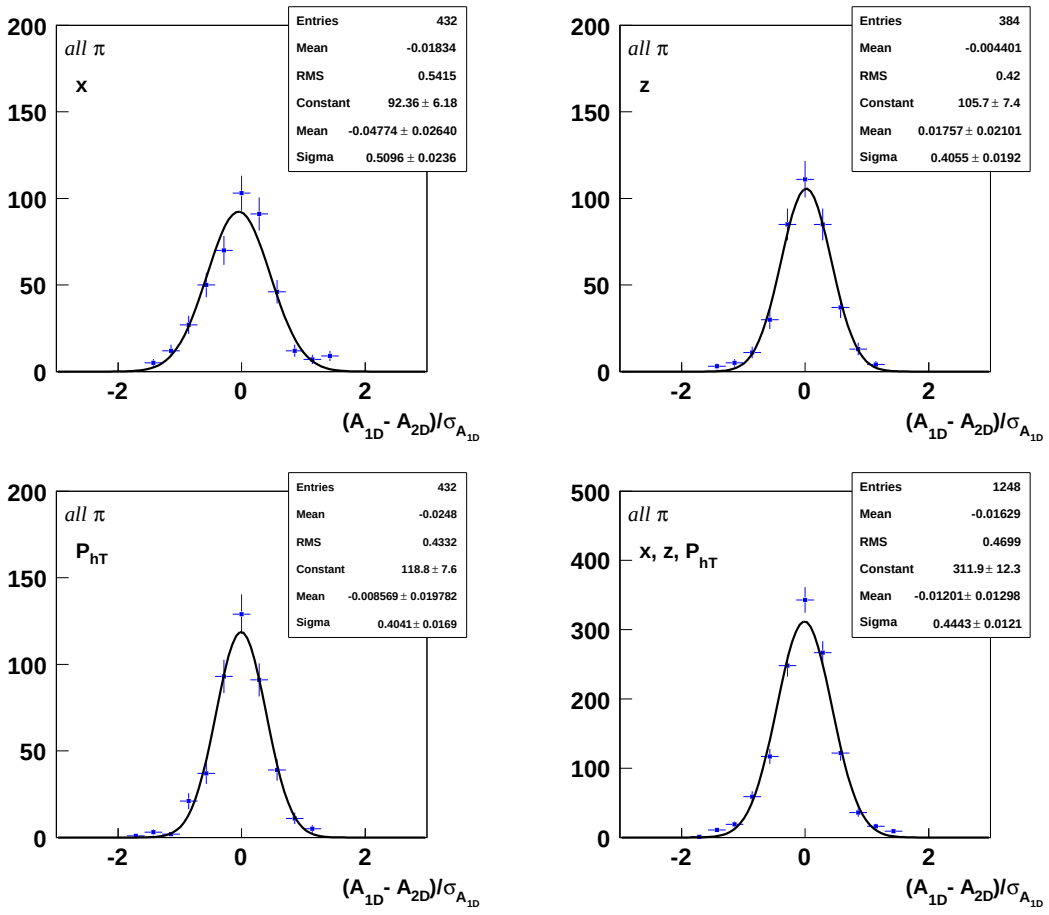

Figure 7.46: Cross check between one-dimensional analysis and two-dimensional analysis for pion asymmetries with two-dimensional fit: "pulls" distribution for x(top left), z(top right) and P_{hT}(bottom left) variables, and for all variables (bottom right).

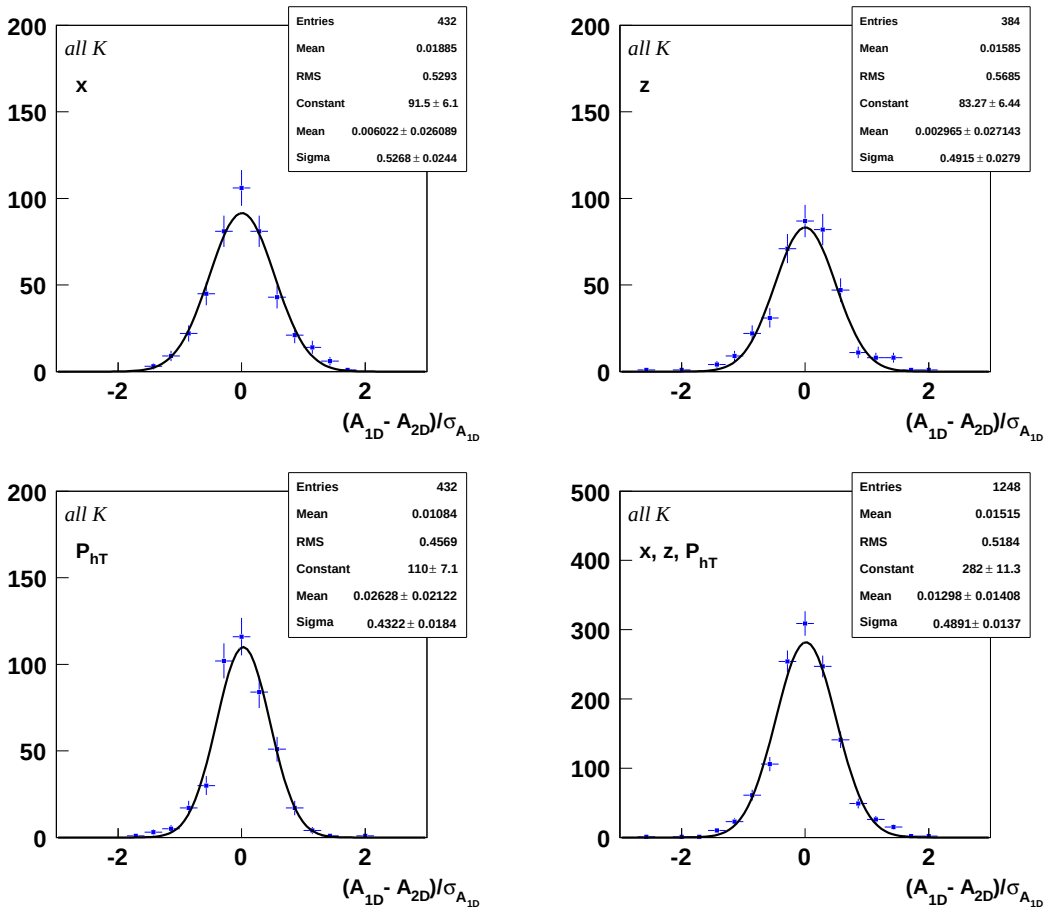

Figure 7.47: Cross check between one-dimensional analysis and two-dimensional analysis for kaon asymmetries with two-dimensional fit: "pulls" distribution for x(top left), z(top right) and P_{hT}(bottom left) variables, and for all variables (bottom right).

7.9.3 Monte-Carlo studies on One- and Two- Dimensional Analyses

As it was shown in the previous section results from two analysis may differ by more than one σ, and usually these are the cases of low statistical bins, mostly for negative particles and specially for kaons (since the kaon sample contains much less statistics compared to pion or *unidentified* hadron samples see Table 6.5). From one side we know that one-dimensional analysis is caused by the systematic effects due to the *non-uniformity* of acceptance over ϕ_S (see Sec. 7.5), from the other we know that in case of insufficient statistics two-dimensional fit may fail. The second aspect was checked by having a look to the distribution of the χ^2 values of the fits. No evidence of failed fits for 2003-2004 data have been detected, while 2002 data did not pass this test. In order to check the first aspect and understand the difference between the results obtained using one-dimensional and two-dimensional methods, some Monte-Carlo studies have been performed.

We simulated 155 independent samples in two dimensional (ϕ_h, ϕ_S) space according to eight target transverse spin modulations Eq. (7.99) with values of the amplitudes $A_i(i = 1,..8)$ set to be of $\approx 0.001 - 0.01$ which represents the *small* transverse asymmetries measured in COMPASS with deuteron target.

$$\begin{aligned} F(\phi_h,\phi_S) = 1 + S_T[&A_1 sin(\phi_h+\phi_S) + A_2 sin(3\phi_h-\phi_S) + \\ &A_3 sin(\phi_h-\phi_S) + A_4 cos(\phi_h-\phi_S) + A_5 sin(\phi_S) + \\ &A_6 sin(2\phi_h-\phi_S) + A_7\cos(\phi_S) + A_8 cos(2\phi_h-\phi_S)]. \end{aligned} \tag{7.99}$$

Each sample has four sub-samples corresponding to positive ($S_T = +1$) and negative ($S_T = -1$) target polarization and Up (Down)-stream target cell. So the sub-samples are:

1. (Upstream, $S_T > 0$)
2. (Upstream, $S_T < 0$)
3. (Downstream, $S_T > 0$)
4. (Downstream, $S_T < 0$).

In order to simulate difference of the acceptances in two target cells we generated 20% less events in samples 1 and 2 compared to samples 3 and 4. Sub-samples imitating same cell but different polarization sign has approximately same statistics, which corresponds two the COMPASS case where approximately equal statistics are collected in two sub-periods of one data-taking period. Number of the events in each sample varies between $\approx 4 \cdot 10^3$ and $\approx 4 \cdot 10^5$ which imitates the COMPASS statistics in different kinematical bins for +/- pions and different data taking periods. The overall statistics of the simulated events is close to COMPASS statistics for pions collected in transverse runs in 2003-2004 years. After the simulation we extracted the Collins and Sivers amplitudes using one-dimensional (16 $\phi_{Collins}$(ϕ_{Sivers}) bins) and two-dimensional (8·8 ϕ_h,ϕ_S bins) ratio product methods and constructed the "pulls" distributions for difference between them. In the figures 7.48 difference between Collins and Sivers asymmetries from one- and two-dimensional methods for "all" pion data (left) and simulated data (right) is presented.

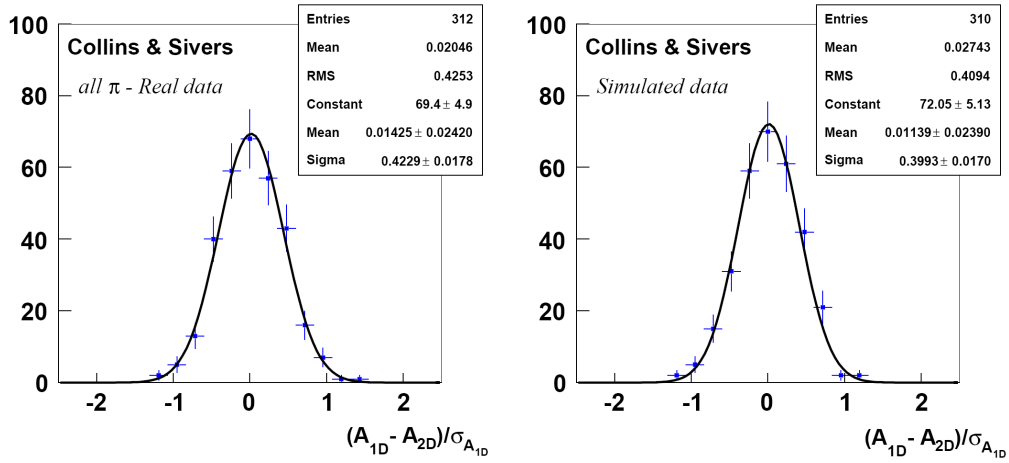

Figure 7.48: The "pulls" distributions describing the difference between results for the Collins and Sivers asymmetries obtained from 1D and 2D methods for real (all pions) data (left) and for Monte-Carlo simulated data (right).

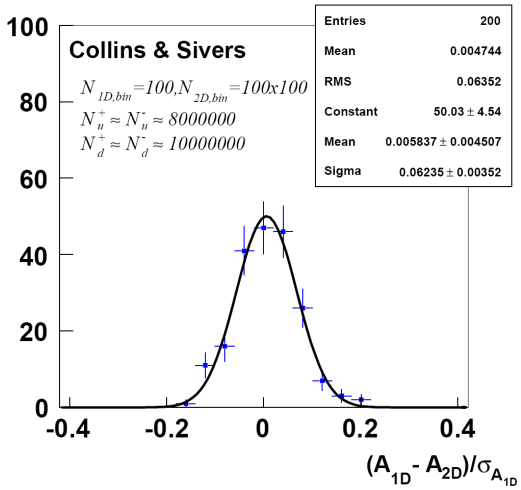

Figure 7.49: The "pull" distribution describing the difference between results for the Collins and Sivers asymmetries obtained from 1D with 100 bins and 2D with 100×100 bins methods for Monte-Carlo simulated data ($4 \cdot 10^7$ events in each of the generated 100 samples).

One can see that the difference between two methods is present in case of both real and simulated data and plots and RMS values look quite similar.

In the performed simulations the ϕ_h and ϕ_S was generated uniformly according to Eq. (7.99), and thus acceptance dependence on ϕ_S present in the data was not taken into account in the generator. Anyway the difference between the results of two analysis is very similar for *real* and *simulated* data. This means that the systematic deviations caused by *non-uniform* ϕ_S-acceptance does not play an essential role and are much smaller than the statistical error, while the main reason of the difference between two methods are the statistical fluctuations in both analysis caused by the low number of events in some kine-

matic bins. In this case deviation between the two methods should vanish with increase of the statistics. In the plot 7.49 we present "pulls" distribution of difference between Collins and Sivers asymmetries extracted using one- and two- dimensional fit methods for the case of very high statistics ($4 \cdot 10^7$ events in each of the generated 100 samples) and high number of the bins (100 bins in one-dimensional and 100×100 in case of two-dimensional fit). As it was expected the difference in this case is very small.

So the conclusion is that both methods give the correct results within statistical accuracy. Anyway one should mention that in the case of high statistics the two-dimensional method is more preferable since it is free from distortions present in one dimensional case and caused by non-uniformity of the azimuthal acceptance in COMPASS.

7.10 Concluding Remarks on Two-Dimensional Method

The two-dimensional method allows to extract all the eight target transverse spin dependent asymmetries simultaneously and gives access to correlation coefficients between the parameters of the fit (For complete set of correlation coefficients see Appendix (Sec. 9.2.1 – 9.2.3)). Method is free from distortions due to the non-uniformity of COMPASS acceptance over ϕ_S present in one-dimensional analysis (see Sec. 7.5). The only disadvantage of the method is that it fails to give correct results in case of low statistical bins when no events fall in some of (ϕ_h,ϕ_S) bins. Due to this reason the data from both periods in 2002 have been excluded from two-dimensional analysis.

Chapter 8

Conclusions

The main goal of this thesis was the extraction of target transverse spin dependent azimuthal asymmetries from COMPASS experimental data and their interpretation within the QCD approach of polarized SIDIS.

There are in total of eight target transverse polarization dependent asymmetries allowed in semi-inclusive deep inelastic scattering of polarized leptons on a transversely polarized nucleons. Within the QCD parton model they can be presented in a form of convolutions of twist-two Transverse Momentum Dependent (TMD) parton Distribution Functions (DF) and Fragmentation Functions (FF). Using this framework the measurement of all possible azimuthal effects present in SIDIS, and these are not only *transverse* spin dependent but also *unpolarized* and *longitudinal* polarization dependent phenomena, will allow us to access the parameters of TMD DFs and FFs from experimental data.

As an example we made a phenomenological calculations on target transverse spin dependent A_{LT} and target longitudinal spin dependent A_{LL} double-spin effects showing that their measurement will give us access to the TMD DFs g^q_{1T} and g^q_{1L} respectively. The predictions for x, y,z and P_{hT} dependence of these asymmetries for different types of hadrons production in proton, deuteron and neutron (only for JLab) targets have been done for COMPASS, HERMES and JLab experiments (see Sec. 3 and 4).

The A_{LT} asymmetry is one of the full set of eight transverse spin asymmetries which we have extracted from COMPASS experimental data collected in 2002-2004 years with a transversely polarized target. A part of Collins and Sivers effects which have been already measured by HERMES and COMPASS collaborations the remaining six new asymmetries (including A_{LT}) have been extracted for the first time by COMPASS collaboration. Asymmetries were evaluated as a functions of x, z and P_{hT} kinematical variables for positive and negative *unidentified* hadrons and for positive and negative *RICH-identified* pions and kaons productions.

Analysis was done using two different – one-dimensional and two-dimensional extraction methods. The results obtained from two analysis methods are in agreement and point to the same physical result within the statistical accuracy. According to COMPASS general policy all the asymmetries have been cross-checked with the independent analysis done by COMPASS-Bonn group. Results obtained in two groups were found to be in a perfect agreement. Performed systematic checks demonstrated that systematic errors as well as correlations between different asymmetries are negligible.

All measured in COMPASS with deuteron target transverse spin asymmetries appear to be small. The smallness of azimuthal effects for deuteron target is interpreted by the partial cancelation of u- and d- quarks contributions into the asymmetry like it was demonstrated on an example of A_{LT} (see Sec. 3.1).

In figures 8.2 and 8.1 we compare the curves plotting the calculated x-dependence of the $A_{LT}^{cos(\phi_h-\phi_s)}$ asymmetry in the COMPASS kinematical region, with our experimental measurements. The blue line corresponds to the asymmetry calculated for the proton target and the red dashed line is for the deuteron target. Experimental observations do not contradict the predictions, and the theoretical curve lies within experimental error bands. Results for other asymmetries obtained with TMD DFs from quark-diquark model are also in agreement with extracted asymmetries Ref. [102].

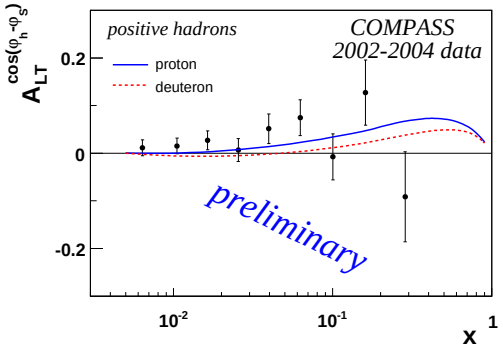

Figure 8.1: $A_{LT}^{cos(\phi_h-\phi_s)}$ asymmetry, positive hadrons vs. x.

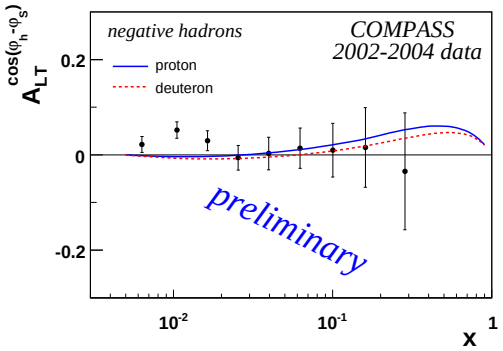

Figure 8.2: $A_{LT}^{cos(\phi_h-\phi_s)}$ asymmetry, positive hadrons vs. x.

Although the measured asymmetries are small this in no way affects the significance of the obtained result. As it was shown in recent global analysis by Anselmino et. al. Ref. [16] the d-quark DFs cannot be well defined without using COMPASS data.

Soon new results on transverse-asymmetries are expected from COMPASS (2007 - proton), HERMES (proton, deuteron) and JLab (proton, deuteron and neutron). Together with COMPASS deuteron results these measurements will allow to perform more general global analysis comprising all TMD DFs.

Chapter 9

Appendix

9.1 Numerical Values of the Asymmetries

Preliminary $A_{UT}^{\sin(\varphi_h-\varphi_S)}$ asymmetry, vs x, z and p_T from COMPASS 2002-2004 data

Positive hadrons					Negative hadrons			
N bin	<x>	Asymmetry	stat. error		N bin	<x>	Asymmetry	stat. error
1	0.006375	-0.007406	0.010228		1	0.006338	-0.008943	0.010288
2	0.010526	-0.018839	0.007348		2	0.010502	-0.003363	0.007744
3	0.016375	-0.001258	0.006535		3	0.016350	-0.025057	0.007036
4	0.025522	0.006757	0.005979		4	0.025482	-0.006161	0.006527
5	0.039677	0.000001	0.006798		5	0.039630	-0.006964	0.007550
6	0.062522	0.006032	0.008508		6	0.062428	-0.009756	0.009631
7	0.100434	-0.017211	0.011325		7	0.100160	-0.018994	0.013150
8	0.160878	-0.025140	0.016833		8	0.160560	0.005574	0.020189
9	0.285412	0.010362	0.027829		9	0.284620	-0.043600	0.035426

Positive hadrons					Negative hadrons			
N bin	<z>	Asymmetry	stat. error		N bin	<z>	Asymmetry	stat. error
1	0.223813	-0.009123	0.005707		1	0.223673	-0.009670	0.006023
2	0.273849	-0.006805	0.006538		2	0.273677	-0.015617	0.007017
3	0.323834	-0.012114	0.007569		3	0.323703	-0.015559	0.008170
4	0.373882	0.007337	0.008642		4	0.373771	0.005244	0.009540
5	0.445566	-0.005399	0.007493		5	0.445216	-0.020142	0.008438
6	0.565748	0.013966	0.008287		6	0.565371	-0.000036	0.009549
7	0.716789	0.005016	0.011944		7	0.717162	-0.031286	0.013513
8	0.874184	-0.003190	0.015912		8	0.874513	0.021087	0.017551

Positive hadrons					Negative hadrons			
N bin	$<p_T>$	Asymmetry	stat. error		N bin	$<p_T>$	Asymmetry	stat. error
1	0.154506	0.001300	0.008287		1	0.154439	0.002910	0.009021
2	0.251820	-0.006094	0.006924		2	0.251855	-0.008257	0.007476
3	0.349692	-0.010842	0.006685		3	0.349610	-0.016495	0.007238
4	0.448378	-0.001370	0.007118		4	0.448348	-0.007071	0.007755
5	0.547677	0.002451	0.008052		5	0.547549	-0.006754	0.008786
6	0.668573	-0.005029	0.007924		6	0.668253	-0.018438	0.008772
7	0.817555	0.008896	0.010474		7	0.817350	-0.012181	0.011707
8	1.045961	-0.010031	0.010960		8	1.045210	-0.017367	0.012138
9	1.566275	-0.001776	0.022356		9	1.564970	-0.053123	0.024632

Preliminary $A_{UT}^{\sin(\varphi_h+\varphi_S)}$ asymmetry, vs x, z and p_T from COMPASS 2002-2004 data

Positive hadrons					Negative hadrons			
N bin	<x>	Asymmetry	stat. error		N bin	<x>	Asymmetry	stat. error
1	0.006375	-0.028478	0.017481		1	0.006338	0.016734	0.017954
2	0.010526	-0.003410	0.009306		2	0.010502	0.012709	0.009881
3	0.016375	-0.000188	0.007394		3	0.016350	0.018786	0.008000
4	0.025522	0.004245	0.006462		4	0.025482	0.001087	0.007064
5	0.039677	0.006025	0.007295		5	0.039630	-0.001879	0.008110
6	0.062522	0.002478	0.009135		6	0.062428	0.010711	0.010400
7	0.100434	0.001703	0.012182		7	0.100160	0.006039	0.014209
8	0.160878	0.009375	0.018280		8	0.160560	-0.014379	0.022099
9	0.285412	0.001623	0.030862		9	0.284620	0.025804	0.038983

Positive hadrons					Negative hadrons			
N bin	<z>	Asymmetry	stat. error		N bin	<z>	Asymmetry	stat. error
1	0.223813	-0.001694	0.006650		1	0.223673	0.010599	0.007082
2	0.273849	-0.010244	0.007532		2	0.273677	0.015863	0.008145
3	0.323834	0.006609	0.008653		3	0.323703	0.010213	0.009435
4	0.373882	0.002673	0.009828		4	0.373771	-0.001003	0.010972
5	0.445566	0.005992	0.008476		5	0.445216	-0.007150	0.009670
6	0.565748	0.003475	0.009339		6	0.565371	0.002035	0.010897
7	0.716789	-0.004993	0.013349		7	0.717162	0.013701	0.015366
8	0.874184	0.019663	0.017647		8	0.874513	0.018914	0.019718

Positive hadrons					Negative hadrons			
N bin	$<p_T>$	Asymmetry	stat. error		N bin	$<p_T>$	Asymmetry	stat. error
1	0.154506	0.002928	0.009318		1	0.154439	0.003424	0.010262
2	0.251820	0.006078	0.007784		2	0.251855	-0.000451	0.008499
3	0.349692	-0.002201	0.007561		3	0.349610	-0.001005	0.008285
4	0.448378	-0.007886	0.008084		4	0.448348	0.003653	0.008914
5	0.547677	-0.008085	0.009215		5	0.547549	0.002773	0.010156
6	0.668573	-0.001409	0.009138		6	0.668253	0.017725	0.010251
7	0.817555	0.018919	0.012253		7	0.817350	0.036073	0.013856
8	1.045961	0.016751	0.013138		8	1.045210	0.017284	0.014750
9	1.566275	-0.038102	0.028824		9	1.564970	0.064040	0.032189

Preliminary $A_{UT}^{\sin(3\varphi_h-\varphi_S)}$ asymmetry, vs x, z and p_T from COMPASS 2002-2004 data

Positive hadrons					Negative hadrons			
N bin	<x>	Asymmetry	stat. error		N bin	<x>	Asymmetry	stat. error
1	0.006375	-0.021234	0.017438		1	0.006338	0.031248	0.017914
2	0.010526	0.011279	0.009293		2	0.010502	0.014132	0.009863
3	0.016375	-0.002592	0.007382		3	0.016350	-0.000132	0.007985
4	0.025522	0.004603	0.006446		4	0.025482	-0.002370	0.007041
5	0.039677	-0.003732	0.007284		5	0.039630	-0.004469	0.008071
6	0.062522	0.003021	0.009131		6	0.062428	-0.009611	0.010333
7	0.100434	-0.000836	0.012075		7	0.100160	0.010247	0.014028
8	0.160878	-0.012905	0.018097		8	0.160560	0.006693	0.021617
9	0.285412	-0.012497	0.030465		9	0.284620	-0.024671	0.038035

Positive hadrons					Negative hadrons			
N bin	<z>	Asymmetry	stat. error		N bin	<z>	Asymmetry	stat. error
1	0.223813	-0.003137	0.006642		1	0.223673	0.002127	0.007057
2	0.273849	-0.008710	0.007519		2	0.273677	0.003919	0.008131
3	0.323834	0.003748	0.008634		3	0.323703	0.001876	0.009412
4	0.373882	0.009172	0.009804		4	0.373771	0.001506	0.010945
5	0.445566	0.010726	0.008456		5	0.445216	-0.003058	0.009628
6	0.565748	0.004575	0.009304		6	0.565371	-0.007034	0.010843
7	0.716789	-0.034273	0.013289		7	0.717162	0.022607	0.015283
8	0.874184	0.026254	0.017575		8	0.874513	0.004165	0.019632

Positive hadrons					Negative hadrons			
N bin	$<p_T>$	Asymmetry	stat. error		N bin	$<p_T>$	Asymmetry	stat. error
1	0.154506	-0.008666	0.009316		1	0.154439	0.002978	0.010236
2	0.251820	0.005291	0.007772		2	0.251855	0.008356	0.008467
3	0.349692	-0.007320	0.007531		3	0.349610	0.006154	0.008239
4	0.448378	0.009269	0.008056		4	0.448348	-0.001304	0.008878
5	0.547677	0.009886	0.009185		5	0.547549	-0.013260	0.010130
6	0.668573	0.003450	0.009123		6	0.668253	-0.000602	0.010229
7	0.817555	-0.009567	0.012234		7	0.817350	0.018087	0.013843
8	1.045961	-0.001018	0.013147		8	1.045210	0.005776	0.014721
9	1.566275	-0.040067	0.028845		9	1.564970	-0.044883	0.032126

Preliminary $A_{UT}^{\sin(\varphi_S)}$ asymmetry, vs x, z and p_T from COMPASS 2002-2004 data

Positive hadrons					Negative hadrons			
N bin	<x>	Asymmetry	stat. error		N bin	<x>	Asymmetry	stat. error
1	0.006375	0.001205	0.008053		1	0.006338	-0.011446	0.008210
2	0.010526	0.002151	0.004814		2	0.010502	-0.007225	0.005082
3	0.016375	-0.003425	0.004044		3	0.016350	-0.006225	0.004368
4	0.025522	0.007967	0.003734		4	0.025482	0.005437	0.004093
5	0.039677	0.000322	0.004263		5	0.039630	-0.007274	0.004739
6	0.062522	-0.010437	0.005267		6	0.062428	0.004243	0.006041
7	0.100434	0.023772	0.006615		7	0.100160	0.005689	0.007696
8	0.160878	0.001827	0.009257		8	0.160560	0.013029	0.011233
9	0.285412	-0.026290	0.015052		9	0.284620	-0.034938	0.019170

Positive hadrons					Negative hadrons			
N bin	<z>	Asymmetry	stat. error		N bin	<z>	Asymmetry	stat. error
1	0.223813	-0.002029	0.003594		1	0.223673	-0.003177	0.003830
2	0.273849	0.004333	0.004116		2	0.273677	0.009049	0.004469
3	0.323834	0.006444	0.004746		3	0.323703	-0.007134	0.005142
4	0.373882	0.010786	0.005433		4	0.373771	-0.007562	0.005998
5	0.445566	-0.007793	0.004653		5	0.445216	0.001460	0.005331
6	0.565748	0.001845	0.005165		6	0.565371	-0.000644	0.006007
7	0.716789	0.005329	0.007444		7	0.717162	-0.013510	0.008469
8	0.874184	-0.001486	0.009917		8	0.874513	-0.012312	0.011026

Positive hadrons					Negative hadrons			
N bin	$<p_T>$	Asymmetry	stat. error		N bin	$<p_T>$	Asymmetry	stat. error
1	0.154506	0.003392	0.005228		1	0.154439	-0.004591	0.005703
2	0.251820	0.000816	0.004339		2	0.251855	0.005899	0.004735
3	0.349692	0.004315	0.004187		3	0.349610	-0.005798	0.004557
4	0.448378	0.006570	0.004443		4	0.448348	0.000269	0.004900
5	0.547677	-0.004045	0.005010		5	0.547549	0.001257	0.005546
6	0.668573	0.002280	0.004949		6	0.668253	-0.008169	0.005523
7	0.817555	-0.000821	0.006577		7	0.817350	-0.003576	0.007438
8	1.045961	-0.009766	0.006931		8	1.045210	-0.005144	0.007755
9	1.566275	0.011923	0.014812		9	1.564970	0.010837	0.016449

Preliminary $A_{UT}^{\sin(2\varphi_h-\varphi_S)}$ asymmetry, vs x, z and p_T from COMPASS 2002-2004 data

Positive hadrons					Negative hadrons			
N bin	<x>	Asymmetry	stat. error		N bin	<x>	Asymmetry	stat. error
1	0.006375	0.007525	0.007520		1	0.006338	-0.002065	0.007698
2	0.010526	0.002175	0.004373		2	0.010502	-0.002254	0.004634
3	0.016375	0.001477	0.003577		3	0.016350	0.006697	0.003865
4	0.025522	0.005913	0.003174		4	0.025482	-0.004288	0.003460
5	0.039677	-0.003380	0.003594		5	0.039630	0.000483	0.003982
6	0.062522	0.002937	0.004493		6	0.062428	-0.000327	0.005086
7	0.100434	-0.007034	0.005942		7	0.100160	0.007271	0.006892
8	0.160878	-0.001335	0.008863		8	0.160560	0.003694	0.010598
9	0.285412	-0.005847	0.014821		9	0.284620	-0.005106	0.018614

Positive hadrons					Negative hadrons			
N bin	<z>	Asymmetry	stat. error		N bin	<z>	Asymmetry	stat. error
1	0.223813	0.001330	0.003198		1	0.223673	0.003485	0.003395
2	0.273849	0.000085	0.003636		2	0.273677	-0.005118	0.003924
3	0.323834	-0.000099	0.004185		3	0.323703	-0.003063	0.004547
4	0.373882	-0.012853	0.004759		4	0.373771	-0.000533	0.005293
5	0.445566	0.005348	0.004109		5	0.445216	0.003166	0.004664
6	0.565748	0.009707	0.004530		6	0.565371	0.009503	0.005261
7	0.716789	0.014028	0.006498		7	0.717162	-0.010345	0.007414
8	0.874184	-0.003078	0.008576		8	0.874513	0.001513	0.009555

Positive hadrons					Negative hadrons			
N bin	$<p_T>$	Asymmetry	stat. error		N bin	$<p_T>$	Asymmetry	stat. error
1	0.154506	-0.001569	0.004532		1	0.154439	-0.000488	0.004963
2	0.251820	-0.001343	0.003779		2	0.251855	-0.002337	0.004107
3	0.349692	0.004904	0.003660		3	0.349610	-0.001646	0.003994
4	0.448378	-0.006932	0.003911		4	0.448348	-0.000926	0.004300
5	0.547677	0.000938	0.004454		5	0.547549	0.004247	0.004894
6	0.668573	0.003191	0.004410		6	0.668253	0.006076	0.004933
7	0.817555	0.006711	0.005900		7	0.817350	-0.007592	0.006641
8	1.045961	0.016854	0.006294		8	1.045210	0.006655	0.007020
9	1.566275	0.007556	0.013541		9	1.564970	0.007393	0.015019

Preliminary $A_{LT}^{\cos(\varphi_h-\varphi_S)}$ asymmetry, vs x, z and p_T from COMPASS 2002-2004 data

Positive hadrons					Negative hadrons			
N bin	<x>	Asymmetry	stat. error		N bin	<x>	Asymmetry	stat. error
1	0.006375	0.011287	0.016539		1	0.006338	0.021700	0.016679
2	0.010526	0.015086	0.016425		2	0.010502	0.052199	0.017139
3	0.016375	0.026839	0.019772		3	0.016350	0.029665	0.021086
4	0.025522	0.006671	0.024169		4	0.025482	-0.006047	0.026003
5	0.039677	0.051399	0.031157		5	0.039630	0.002944	0.034162
6	0.062522	0.074437	0.037706		6	0.062428	0.014001	0.042428
7	0.100434	-0.007604	0.048171		7	0.100160	0.009948	0.056391
8	0.160878	0.127177	0.068363		8	0.160560	0.015479	0.083581
9	0.285412	-0.091356	0.094309		9	0.284620	-0.034605	0.122522

Positive hadrons					Negative hadrons			
N bin	<z>	Asymmetry	stat. error		N bin	<z>	Asymmetry	stat. error
1	0.223813	0.022905	0.016709		1	0.223673	0.032228	0.017425
2	0.273849	0.056677	0.020156		2	0.273677	0.029903	0.021275
3	0.323834	0.008795	0.024251		3	0.323703	-0.010544	0.025546
4	0.373882	-0.015792	0.028550		4	0.373771	0.033831	0.030507
5	0.445566	0.032447	0.025471		5	0.445216	0.013520	0.027570
6	0.565748	0.032428	0.029409		6	0.565371	0.021746	0.031718
7	0.716789	0.047485	0.044468		7	0.717162	0.010144	0.046446
8	0.874184	-0.037239	0.062967		8	0.874513	-0.008253	0.062840

Positive hadrons					Negative hadrons			
N bin	$<p_T>$	Asymmetry	stat. error		N bin	$<p_T>$	Asymmetry	stat. error
1	0.154506	0.018739	0.029173		1	0.154439	0.016459	0.030688
2	0.251820	0.025834	0.023957		2	0.251855	0.011259	0.025070
3	0.349692	0.054649	0.022600		3	0.349610	0.006969	0.023694
4	0.448378	0.001168	0.023463		4	0.448348	0.032006	0.024659
5	0.547677	0.026319	0.025854		5	0.547549	0.037651	0.027015
6	0.668573	0.077578	0.024431		6	0.668253	0.025958	0.025876
7	0.817555	-0.011809	0.030748		7	0.817350	0.025423	0.032827
8	1.045961	-0.023142	0.029717		8	1.045210	0.009536	0.031529
9	1.566275	-0.039312	0.051119		9	1.564970	0.017665	0.055302

Preliminary $A_{LT}^{\cos(\varphi_S)}$ asymmetry, vs x, z and p_T from COMPASS 2002-2004 data

Positive hadrons					Negative hadrons			
N bin	<x>	Asymmetry	stat. error		N bin	<x>	Asymmetry	stat. error
1	0.006375	-0.007566	0.019045		1	0.006338	0.006404	0.019208
2	0.010526	-0.008992	0.017152		2	0.010502	-0.004771	0.017909
3	0.016375	0.021560	0.019775		3	0.016350	-0.015132	0.021160
4	0.025522	0.003123	0.023412		4	0.025482	0.017415	0.025349
5	0.039677	-0.011592	0.029508		5	0.039630	0.027087	0.032812
6	0.062522	0.036543	0.035745		6	0.062428	0.079288	0.041079
7	0.100434	0.066251	0.047493		7	0.100160	0.116239	0.056410
8	0.160878	-0.022743	0.070316		8	0.160560	0.081331	0.086720
9	0.285412	0.002619	0.097732		9	0.284620	0.243327	0.126986

Positive hadrons					Negative hadrons			
N bin	<z>	Asymmetry	stat. error		N bin	<z>	Asymmetry	stat. error
1	0.223813	0.008229	0.016964		1	0.223673	0.008328	0.017860
2	0.273849	0.007318	0.020434		2	0.273677	0.016210	0.021773
3	0.323834	-0.014267	0.024462		3	0.323703	0.034701	0.025994
4	0.373882	-0.043652	0.028789		4	0.373771	0.024977	0.030933
5	0.445566	0.016827	0.025486		5	0.445216	-0.004998	0.028075
6	0.565748	0.016163	0.029316		6	0.565371	0.027647	0.032235
7	0.716789	0.071475	0.044052		7	0.717162	0.046923	0.046892
8	0.874184	0.100567	0.061717		8	0.874513	0.039084	0.062813

Positive hadrons					Negative hadrons			
N bin	$<p_T>$	Asymmetry	stat. error		N bin	$<p_T>$	Asymmetry	stat. error
1	0.154506	-0.009852	0.028842		1	0.154439	0.069617	0.030678
2	0.251820	-0.010521	0.023841		2	0.251855	0.018324	0.025314
3	0.349692	0.015347	0.022588		3	0.349610	-0.002861	0.023986
4	0.448378	0.005474	0.023567		4	0.448348	0.018643	0.025092
5	0.547677	0.020156	0.026073		5	0.547549	-0.009262	0.027649
6	0.668573	0.035975	0.024871		6	0.668253	0.039047	0.026553
7	0.817555	-0.006459	0.031540		7	0.817350	-0.004077	0.033966
8	1.045961	0.018493	0.030691		8	1.045210	0.022061	0.033086
9	1.566275	-0.080586	0.054858		9	1.564970	0.000662	0.059494

Preliminary $A_{LT}^{\cos(2\varphi_h-\varphi_S)}$ asymmetry, vs x, z and p_T from COMPASS 2002-2004 data

Positive hadrons					Negative hadrons			
N bin	<x>	Asymmetry	stat. error		N bin	<x>	Asymmetry	stat. error
1	0.006375	-0.016082	0.019985		1	0.006338	0.003895	0.020154
2	0.010526	0.018072	0.018011		2	0.010502	-0.012760	0.018814
3	0.016375	-0.006125	0.021043		3	0.016350	-0.025649	0.022470
4	0.025522	0.022666	0.025179		4	0.025482	-0.022432	0.027153
5	0.039677	0.010228	0.032115		5	0.039630	0.015568	0.035417
6	0.062522	-0.018460	0.038915		6	0.062428	-0.095548	0.044005
7	0.100434	0.028208	0.049974		7	0.100160	-0.031445	0.058987
8	0.160878	-0.049302	0.071589		8	0.160560	0.093417	0.087791
9	0.285412	-0.067310	0.099071		9	0.284620	-0.067232	0.128555

Positive hadrons					Negative hadrons			
N bin	<z>	Asymmetry	stat. error		N bin	<z>	Asymmetry	stat. error
1	0.223813	-0.021592	0.018120		1	0.223673	-0.013044	0.018957
2	0.273849	0.037489	0.021769		2	0.273677	-0.035830	0.023053
3	0.323834	-0.004163	0.026099		3	0.323703	0.012122	0.027656
4	0.373882	0.029039	0.030667		4	0.373771	-0.015127	0.032971
5	0.445566	-0.020425	0.027315		5	0.445216	-0.001739	0.029811
6	0.565748	0.053909	0.031343		6	0.565371	-0.041392	0.034282
7	0.716789	-0.006113	0.047085		7	0.717162	-0.008967	0.050178
8	0.874184	-0.089256	0.066125		8	0.874513	-0.025526	0.067328

Positive hadrons					Negative hadrons			
N bin	$<p_T>$	Asymmetry	stat. error		N bin	$<p_T>$	Asymmetry	stat. error
1	0.154506	-0.018011	0.031190		1	0.154439	-0.018100	0.033058
2	0.251820	-0.013071	0.025677		2	0.251855	-0.023989	0.027034
3	0.349692	-0.003919	0.024227		3	0.349610	-0.041059	0.025560
4	0.448378	0.005701	0.025179		4	0.448348	-0.017851	0.026613
5	0.547677	0.051532	0.027737		5	0.547549	-0.029524	0.029261
6	0.668573	0.002203	0.026316		6	0.668253	0.049203	0.028094
7	0.817555	0.007915	0.033233		7	0.817350	-0.047234	0.035825
8	1.045961	0.025709	0.032386		8	1.045210	0.018157	0.034723
9	1.566275	-0.085886	0.057057		9	1.564970	-0.038115	0.062054

9.2 Correlation Coefficients

9.2.1 Correlation Coefficients for *Unidentified* Hadron Asymmetries

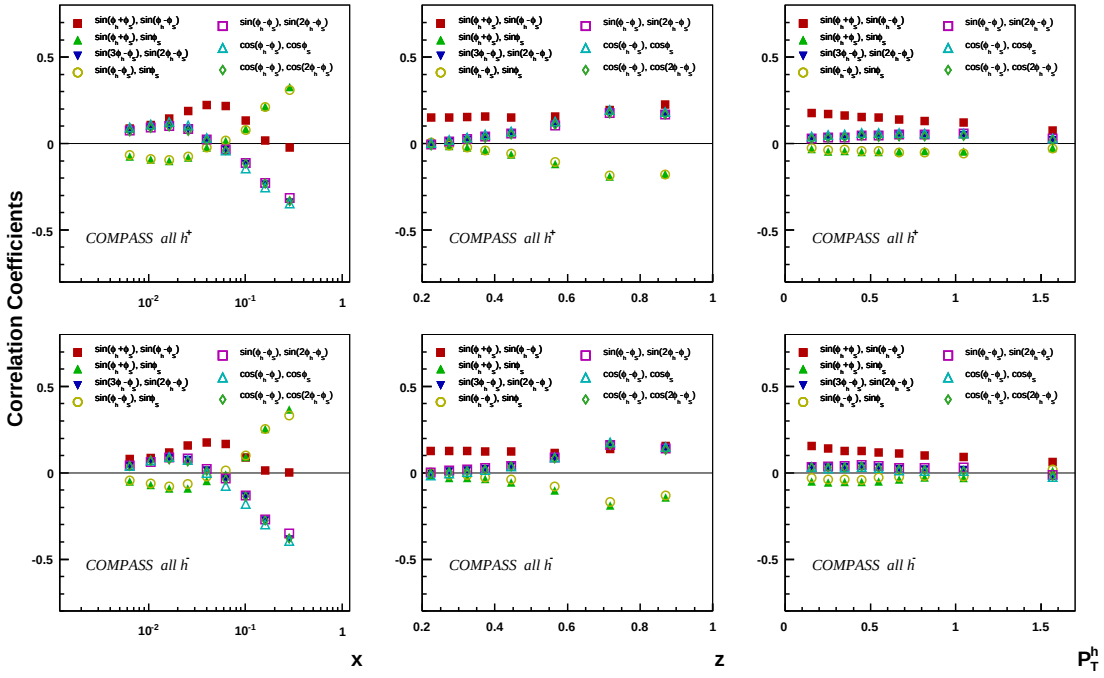

Figure 9.1: Correlation between parameters, where the correlation is in the range above $\pm$ 0.1 in any one of the x, z and P_{hT} bin.

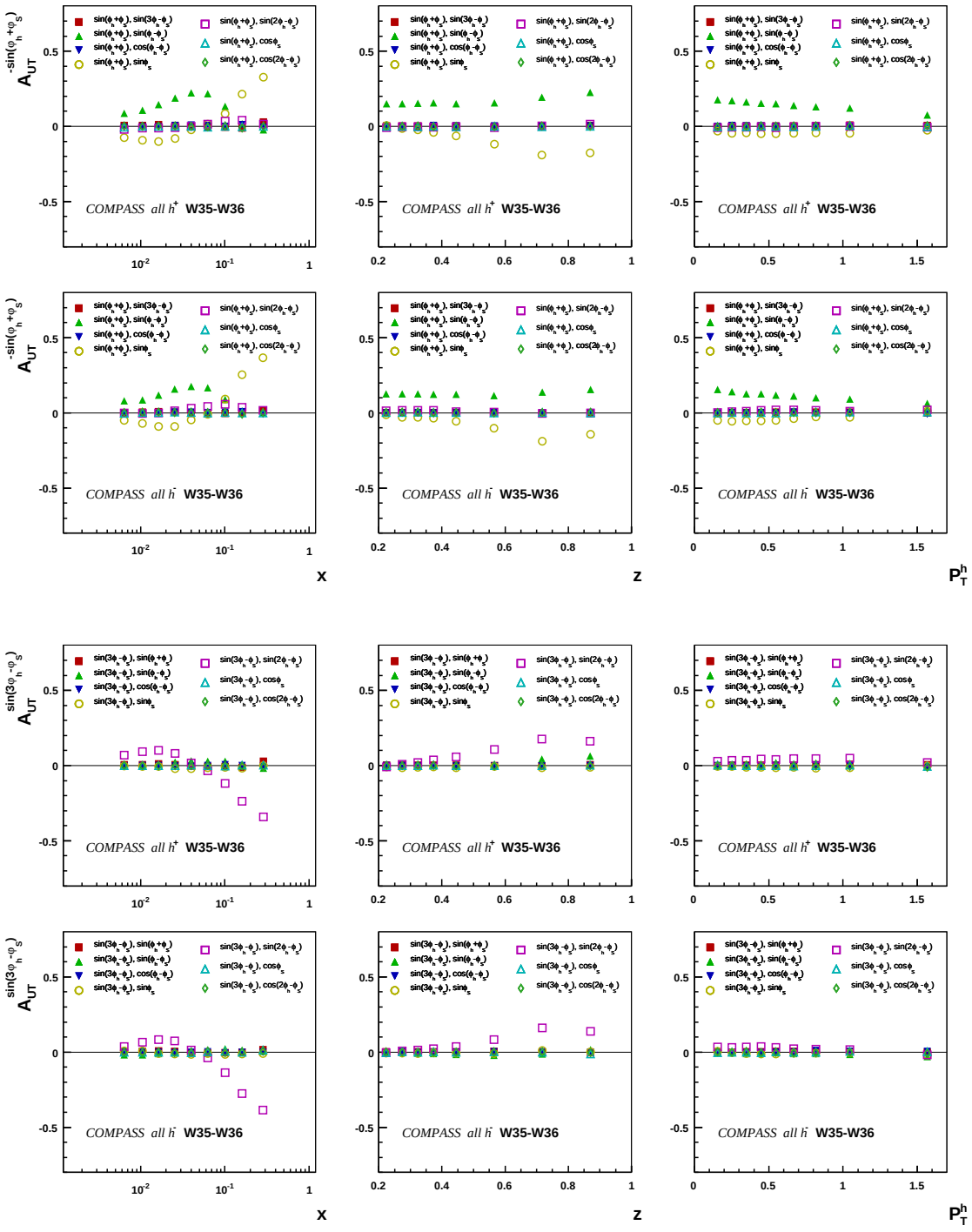

Figure 9.2: Correlation between $A_{UT}^{\sin(\phi_h+\phi_s)}$ and rest of the parameters (two plots on top). Correlation between $A_{UT}^{\sin(3\phi_h-\phi_s)}$ and rest of the parameters (two plots in bottom) vs. x, z and P_{hT}.

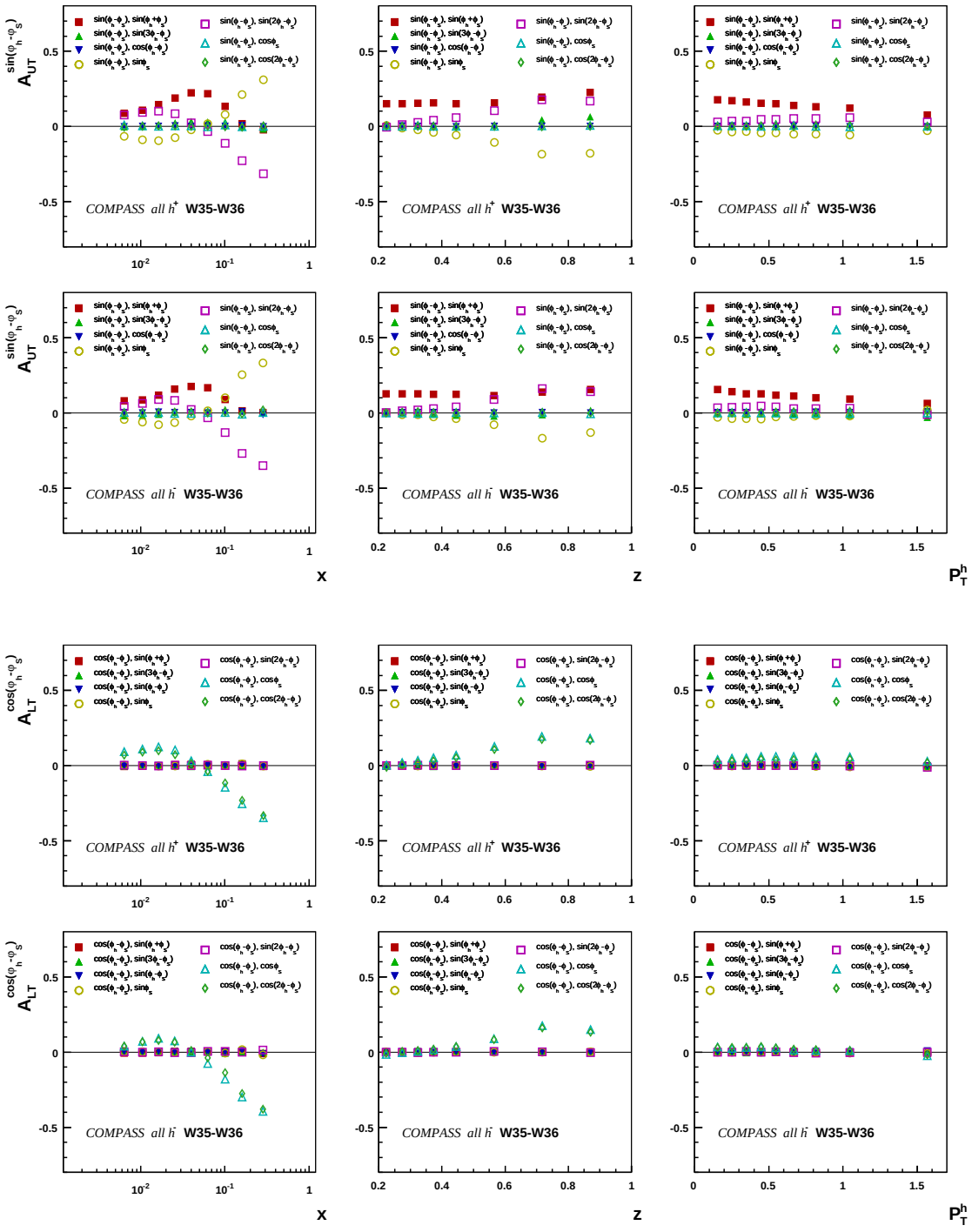

Figure 9.3: Correlation between $A_{UT}^{\sin(\phi_h-\phi_s)}$ and rest of the parameters (two plots on top). Correlation between $A_{LT}^{\cos(\phi_h-\phi_s)}$ and rest of the parameters (two plots in bottom) vs. x, z and P_{hT}.

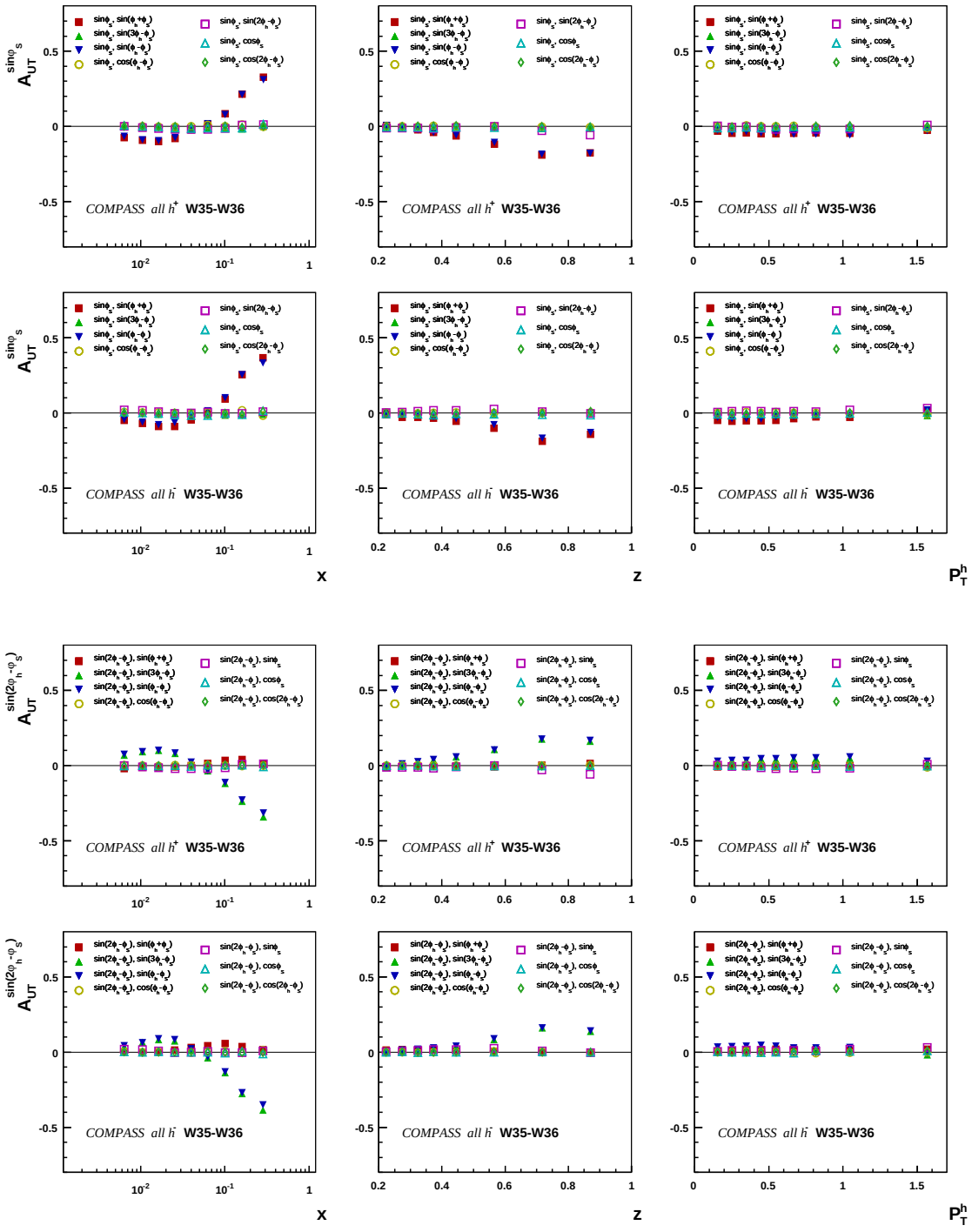

Figure 9.4: Correlation between $A_{UT}^{\sin(\phi_s)}$ and rest of the parameters (two plots on top). Correlation between $A_{UT}^{\sin(2\phi_h-\phi_s)}$ and rest of the parameters (two plots in bottom) vs. x, z and P_{hT}.

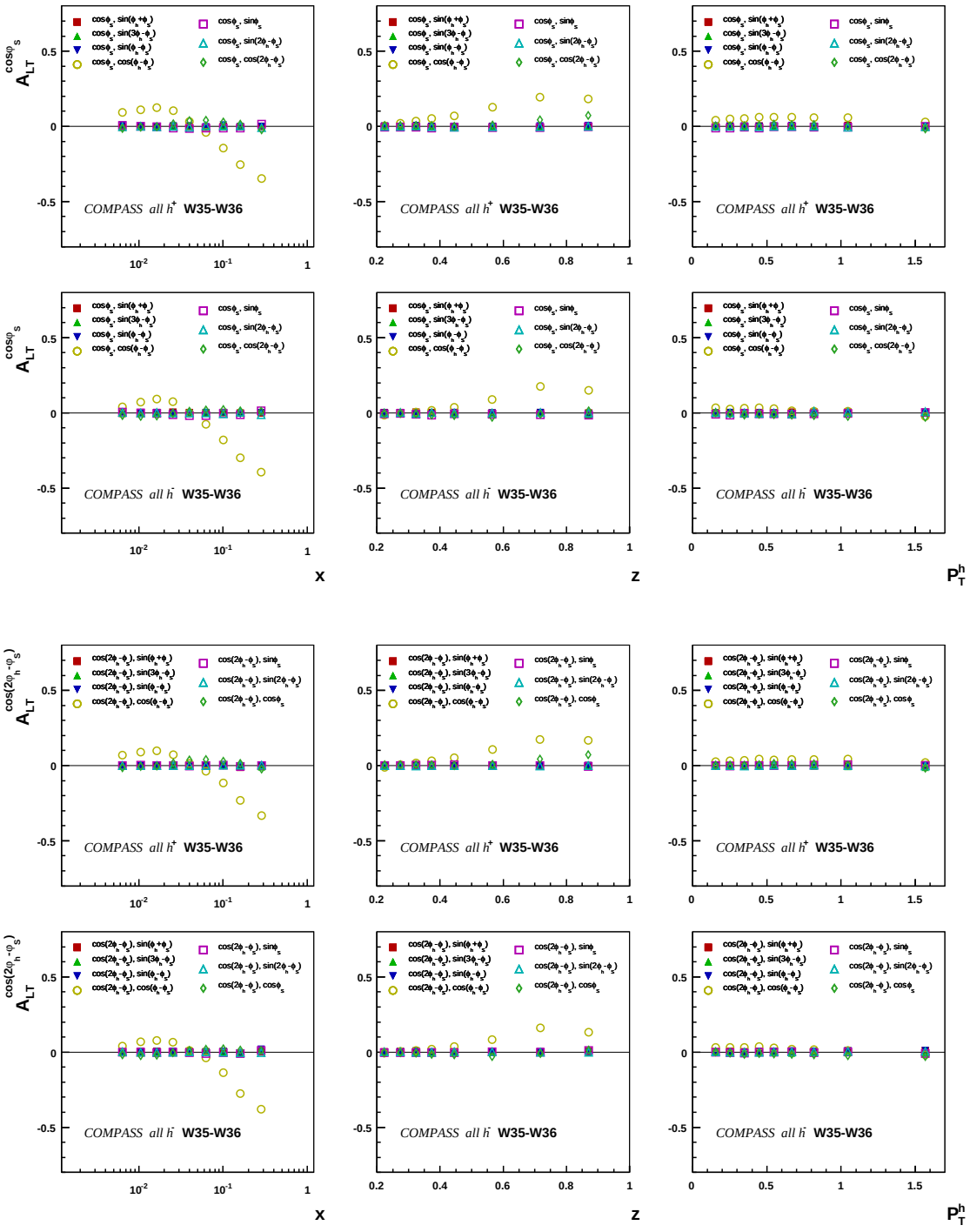

Figure 9.5: Correlation between $A_{LT}^{\cos(\phi_s)}$ and rest of the parameters (two plots on top). Correlation between $A_{LT}^{\cos(2\phi_h-\phi_s)}$ and rest of the parameters (two plots in bottom) vs. x, z and P_{hT}.

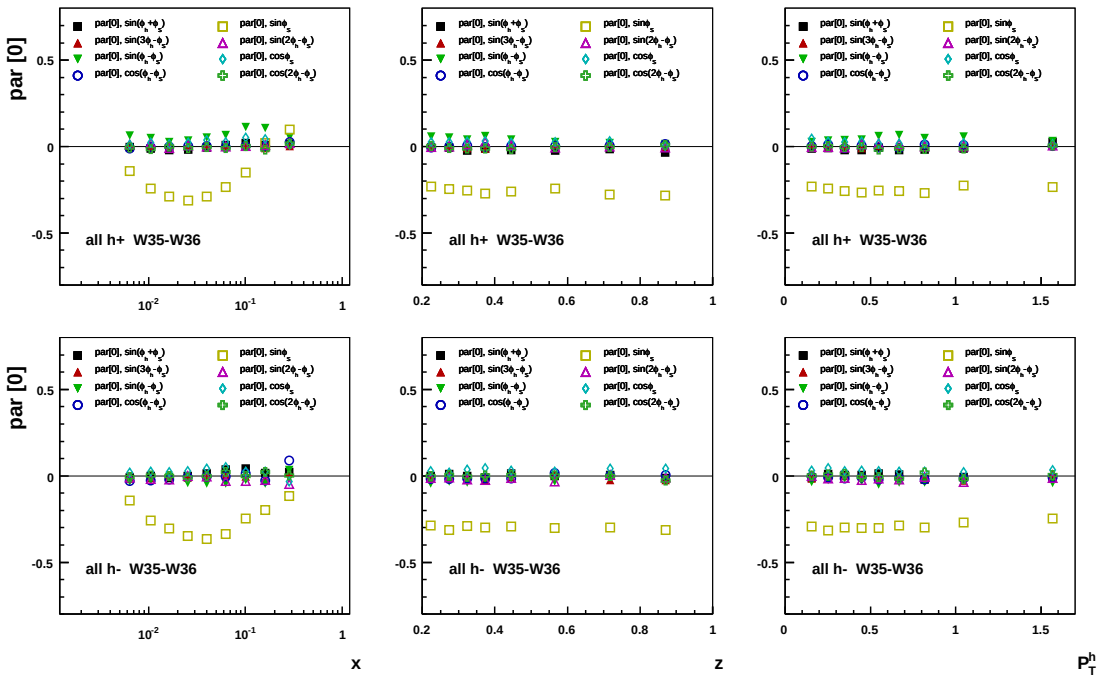

Figure 9.6: Correlation between par(0) and rest of the parameters vs. x, z and P_{hT}.

9.2.2 Correlation Coefficients for Pion Asymmetries

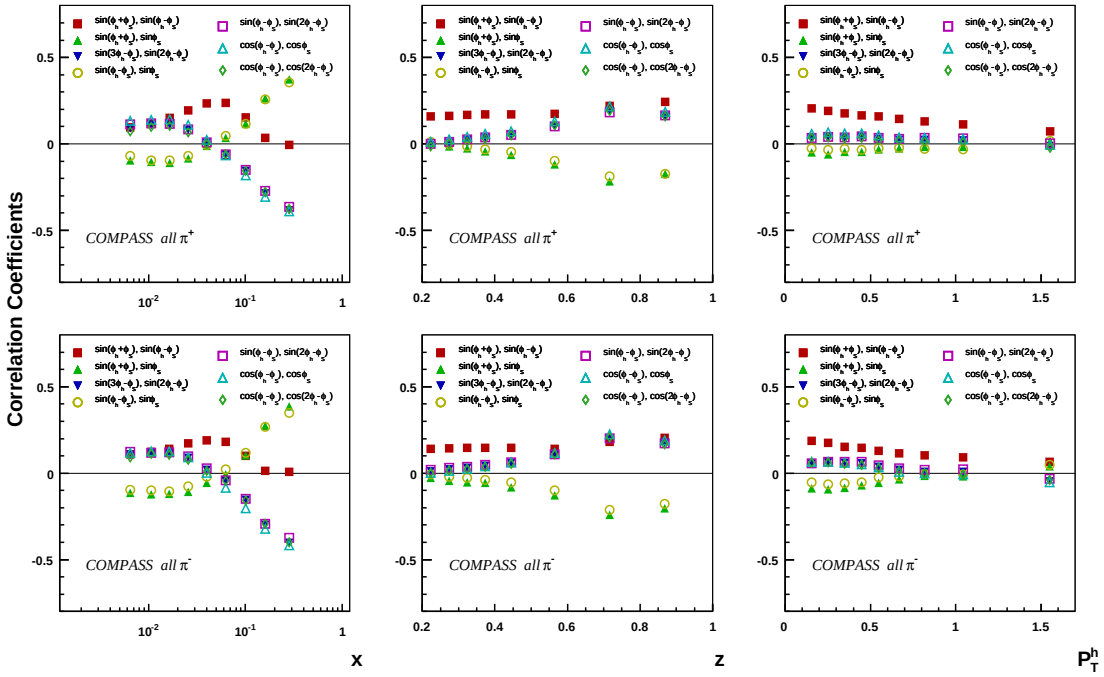

Figure 9.7: Correlation between parameters, where the correlation is in the range above $\pm$ 0.1 in any one of the x, z and P_{hT} bin.

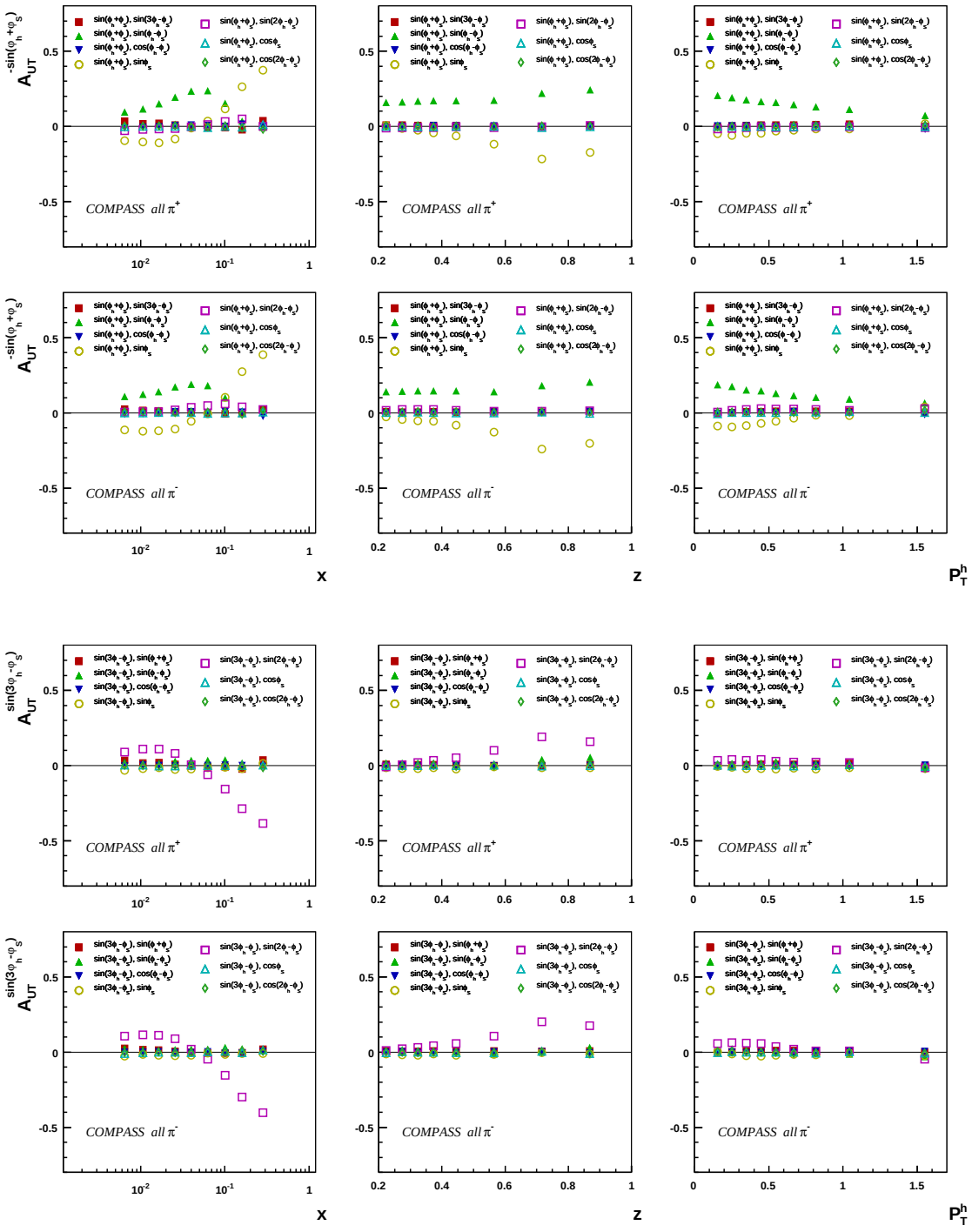

Figure 9.8: Correlation between $A_{UT}^{\sin(\phi_h+\phi_s)}$ and rest of the parameters (two plots on top). Correlation between $A_{UT}^{\sin(3\phi_h-\phi_s)}$ and rest of the parameters (two plots in bottom) vs. x, z and P_{hT}.

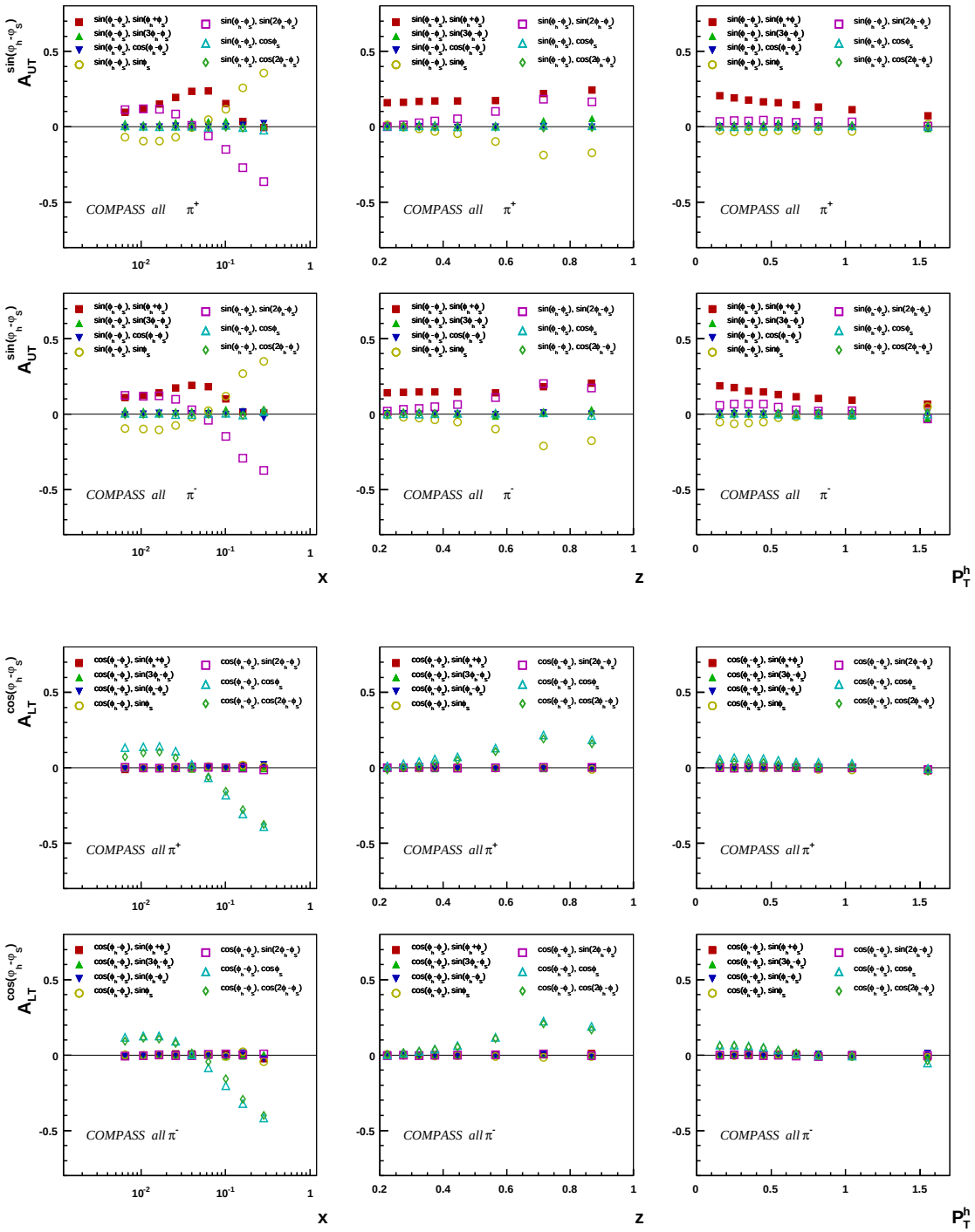

Figure 9.9: Correlation between $A_{UT}^{\sin(\phi_h-\phi_s)}$ and rest of the parameters (two plots on top). Correlation between $A_{LT}^{\cos(\phi_h-\phi_s)}$ and rest of the parameters (two plots in bottom) vs. x, z and P_{hT}.

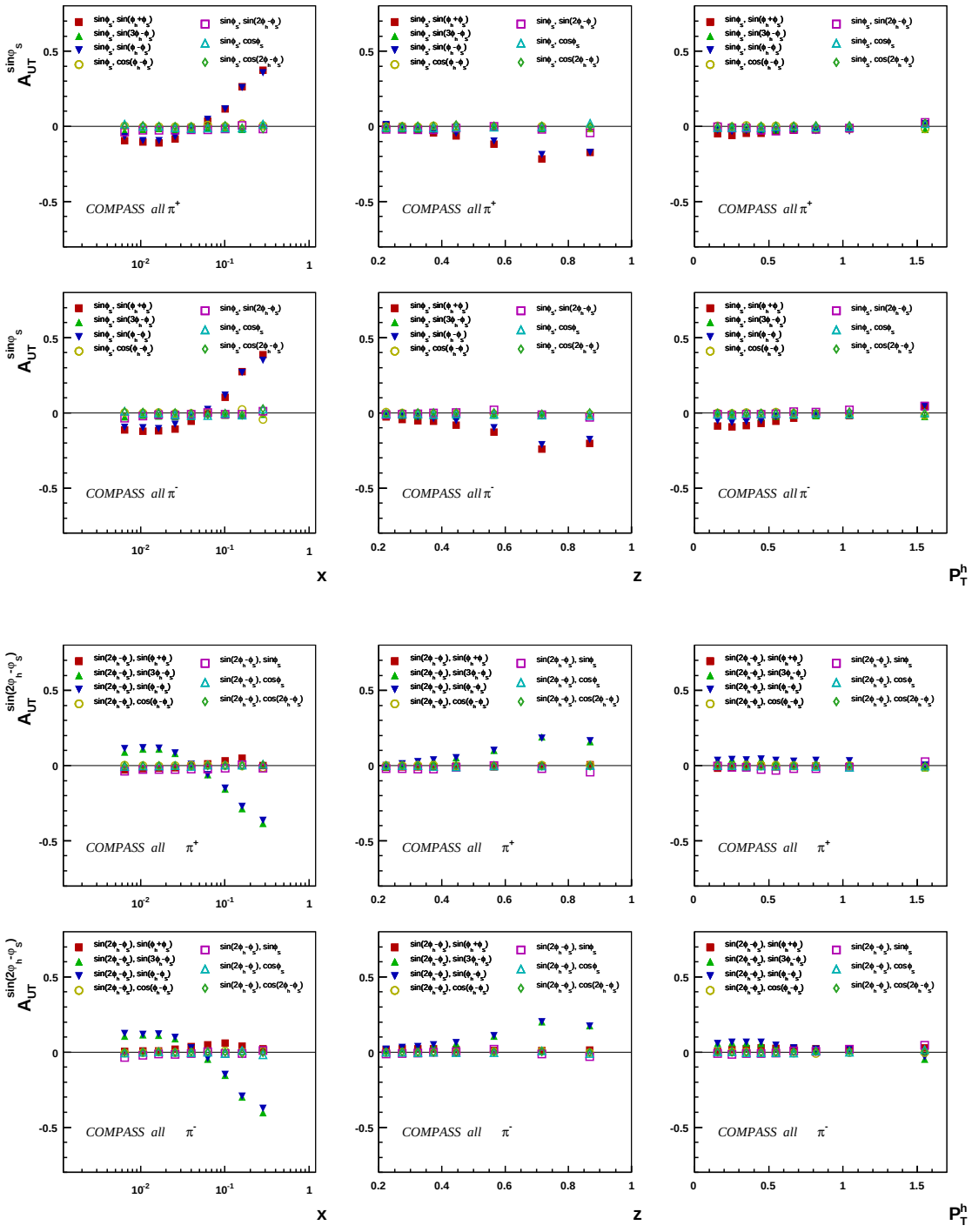

Figure 9.10: Correlation between $A_{UT}^{\sin(\phi_s)}$ and rest of the parameters (two plots on top). Correlation between $A_{UT}^{\sin(2\phi_h-\phi_s)}$ and rest of the parameters (two plots in bottom) vs. x, z and P_{hT}.

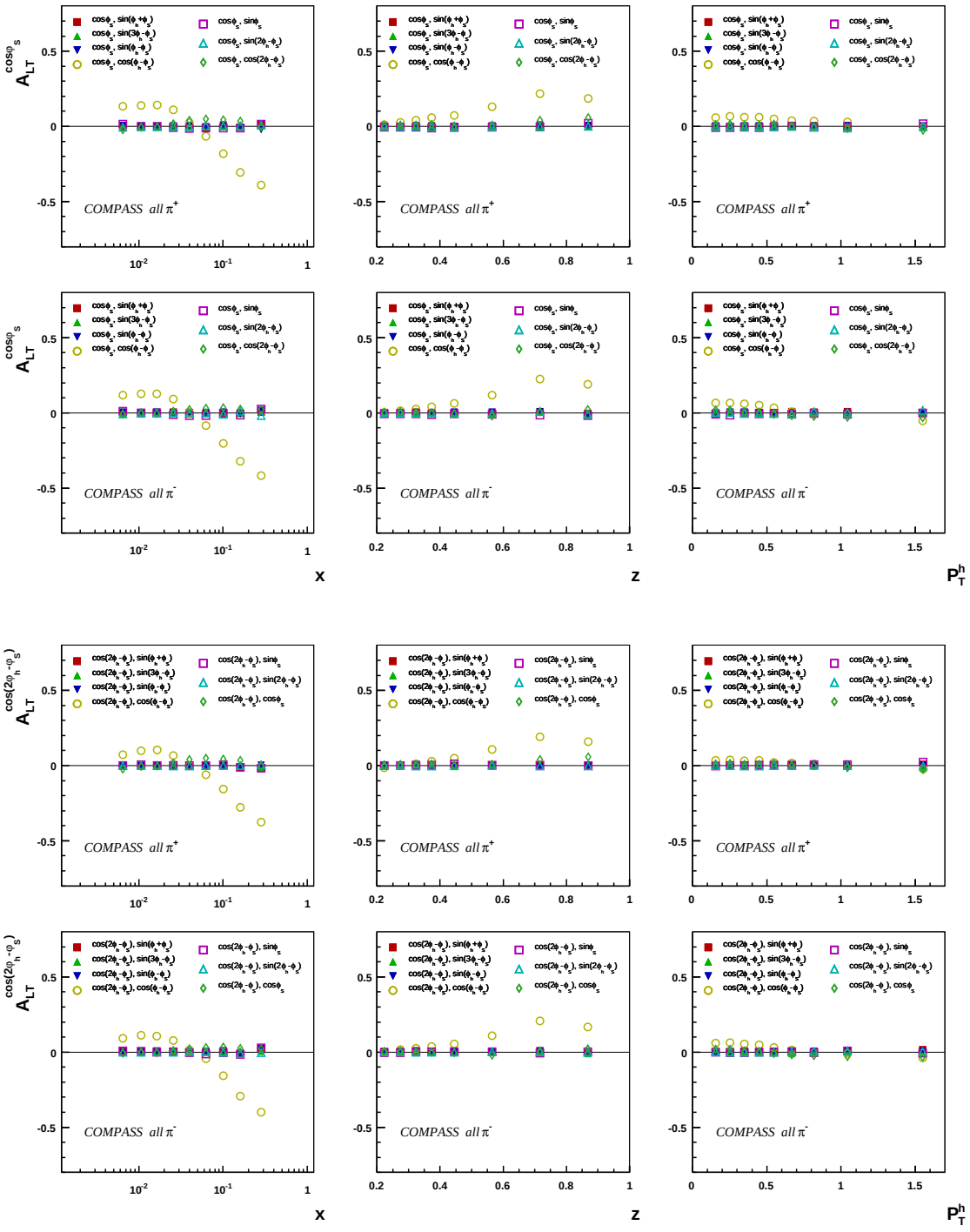

Figure 9.11: Correlation between $A_{LT}^{\cos(\phi_s)}$ and rest of the parameters (two plots on top). Correlation between $A_{LT}^{\cos(2\phi_h-\phi_s)}$ and rest of the parameters (two plots in bottom) vs. x, z and P_{hT}.

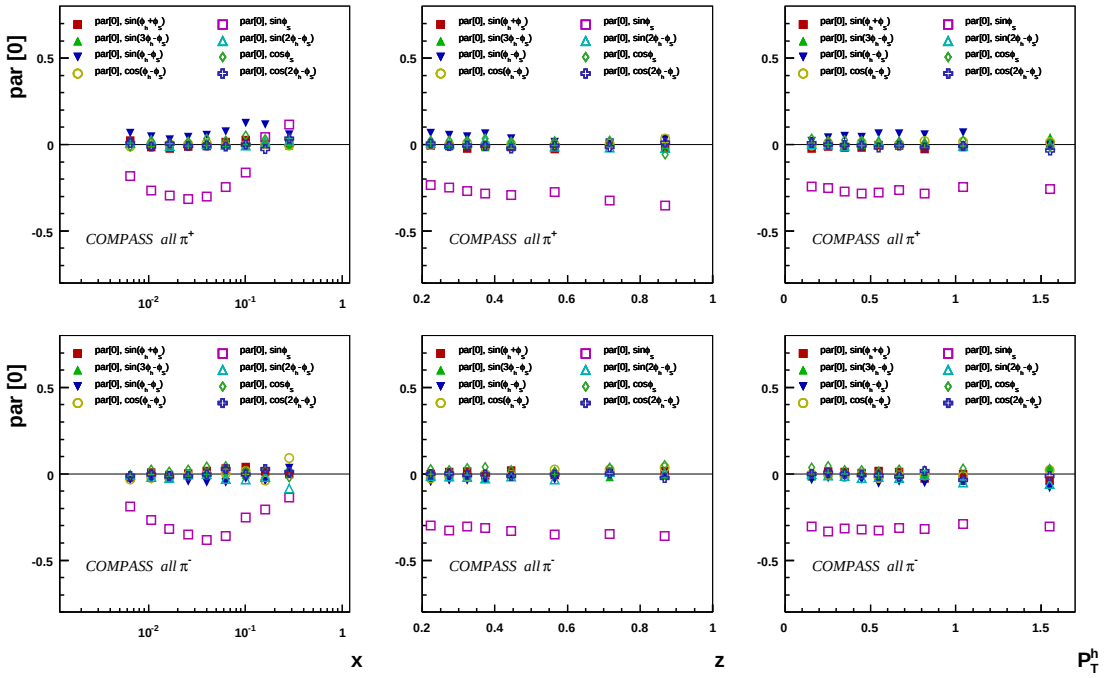

Figure 9.12: Correlation between par(0) and rest of the parameters vs. x, z and P_{hT}.

9.2.3 Correlation Coefficients for Kaon Asymmetries

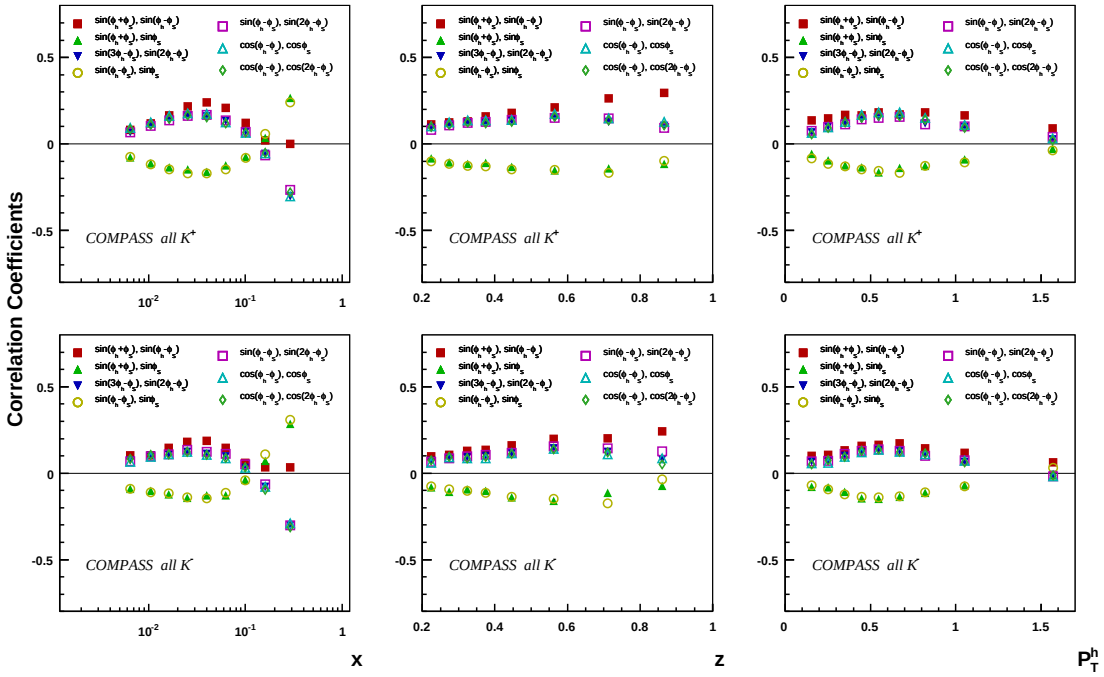

Figure 9.13: Correlation between parameters, where the correlation is in the range above $\pm$ 0.1 in any one of the x, z and P_{hT} bin.

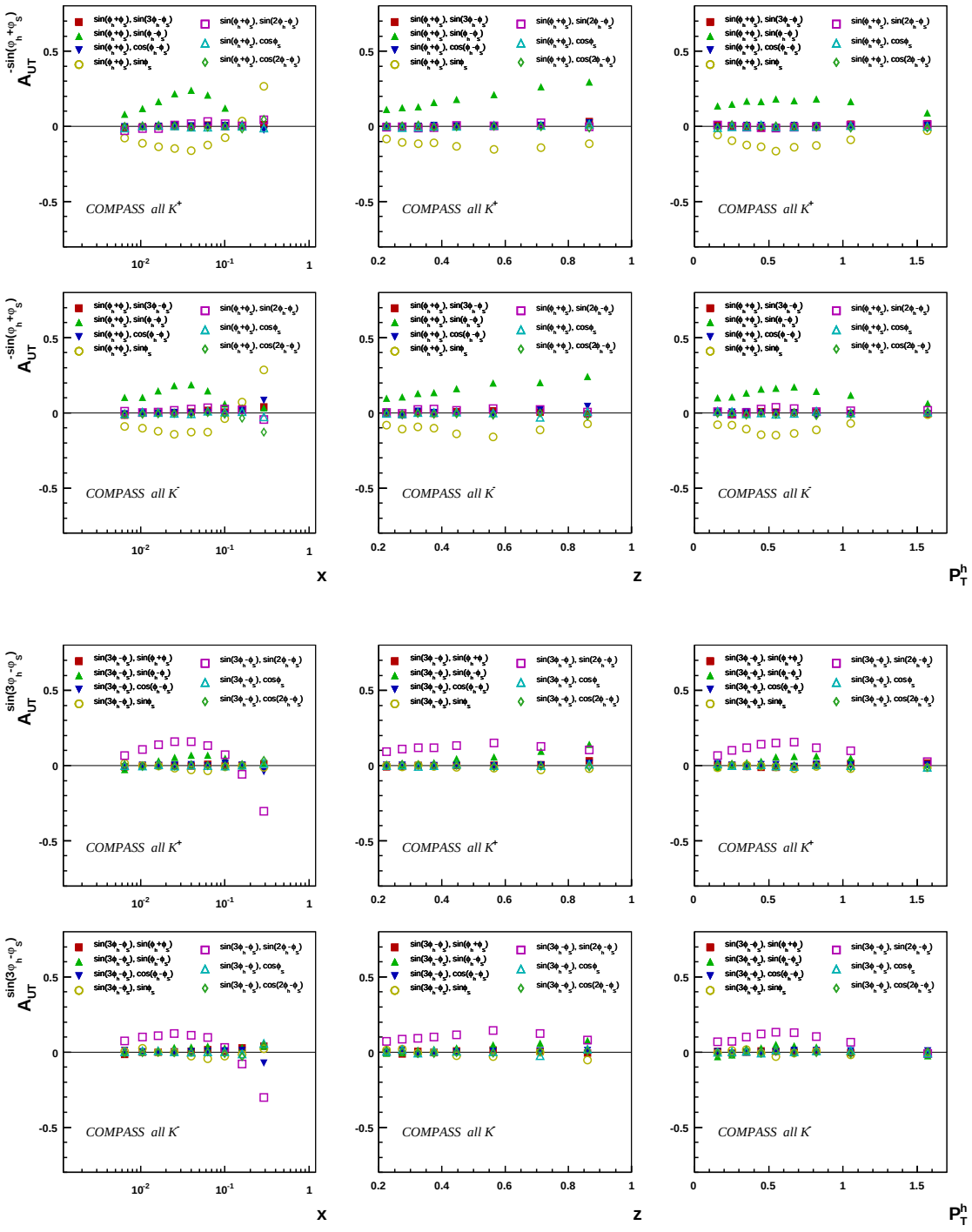

Figure 9.14: Correlation between $A_{UT}^{\sin(\phi_h+\phi_s)}$ and rest of the parameters (two plots on top). Correlation between $A_{UT}^{\sin(3\phi_h-\phi_s)}$ and rest of the parameters (two plots in bottom) vs. x, z and P_{hT}.

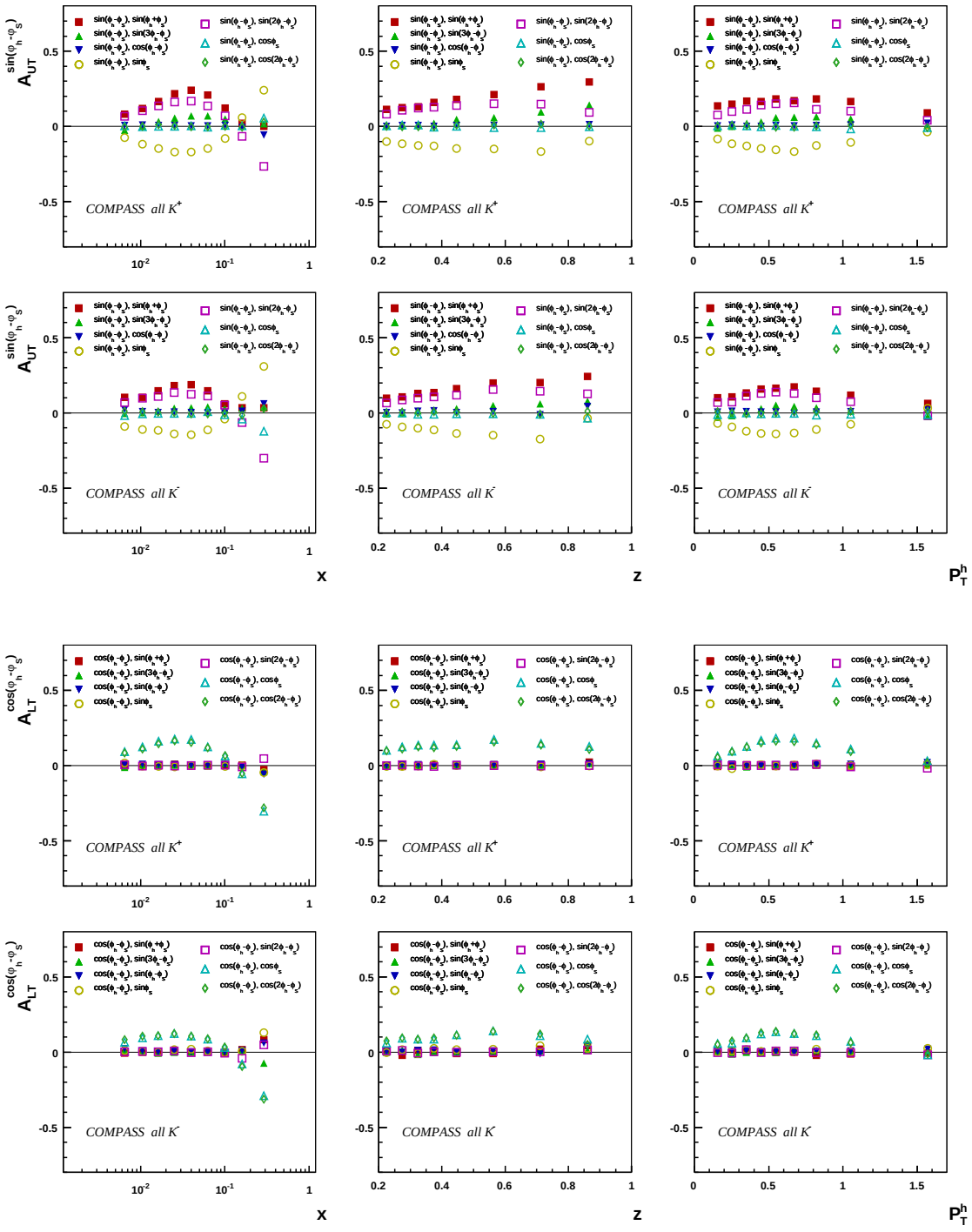

Figure 9.15: Correlation between $A_{UT}^{\sin(\phi_h-\phi_s)}$ and rest of the parameters (two plots on top). Correlation between $A_{LT}^{\cos(\phi_h-\phi_s)}$ and rest of the parameters (two plots in bottom) vs. x, z and P_{hT}.

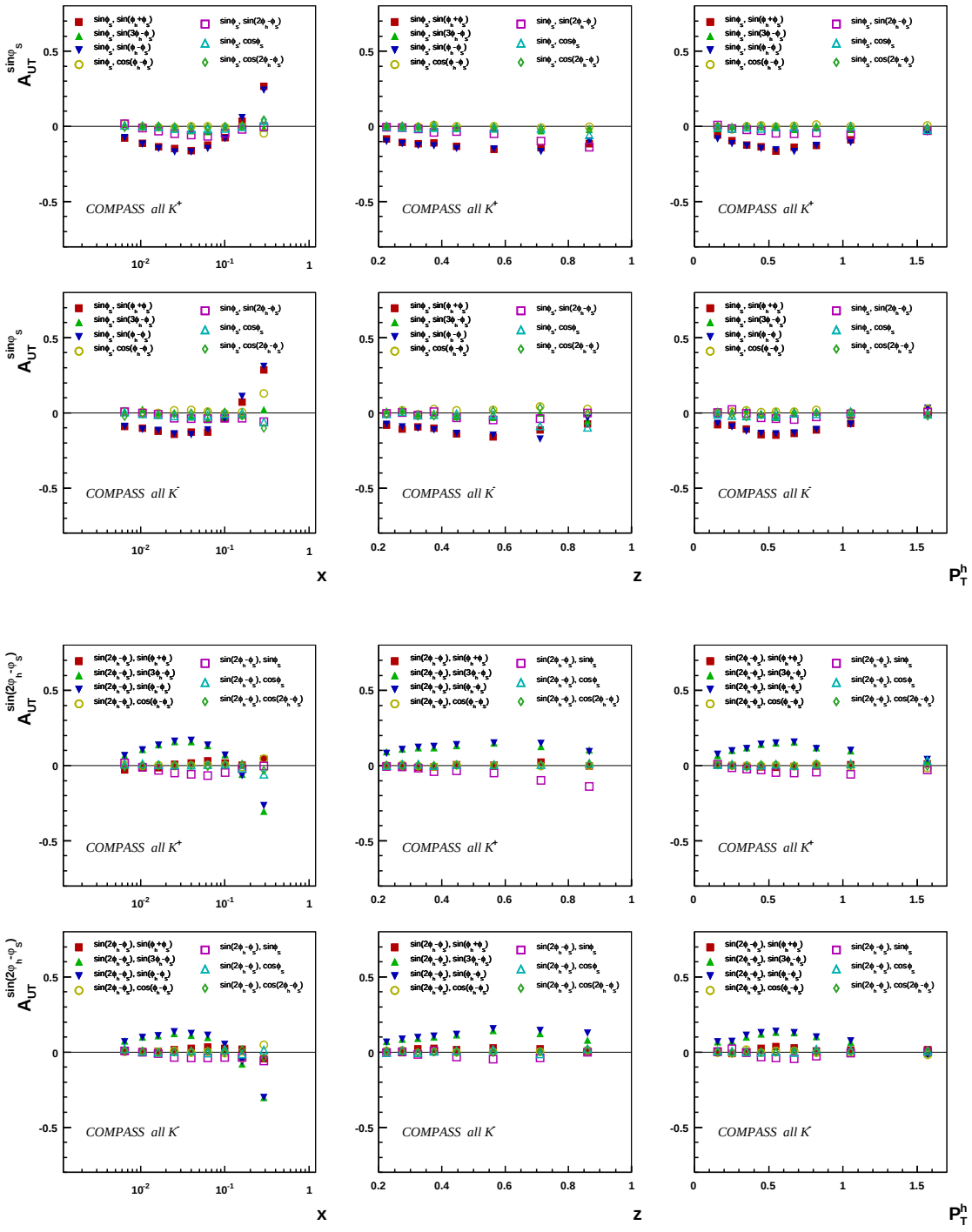

Figure 9.16: Correlation between $A_{UT}^{\sin(\phi_s)}$ and rest of the parameters (two plots on top). Correlation between $A_{UT}^{\sin(2\phi_h-\phi_s)}$ and rest of the parameters (two plots in bottom) vs. x, z and P_{hT}.

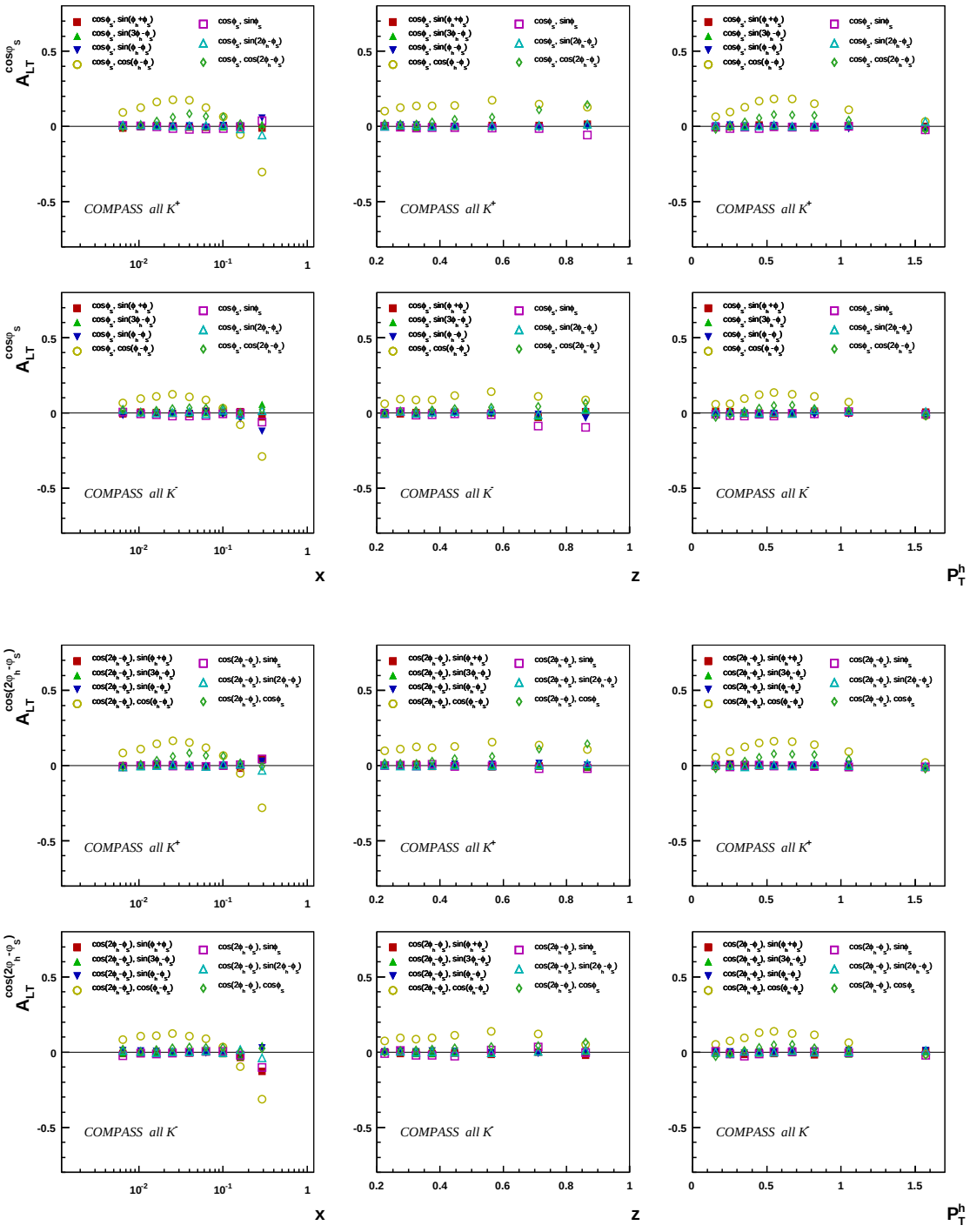

Figure 9.17: Correlation between $A_{LT}^{\cos(\phi_s)}$ and rest of the parameters (two plots on top). Correlation between $A_{LT}^{\cos(2\phi_h-\phi_s)}$ and rest of the parameters (two plots in bottom) vs. x, z and P_{hT}.

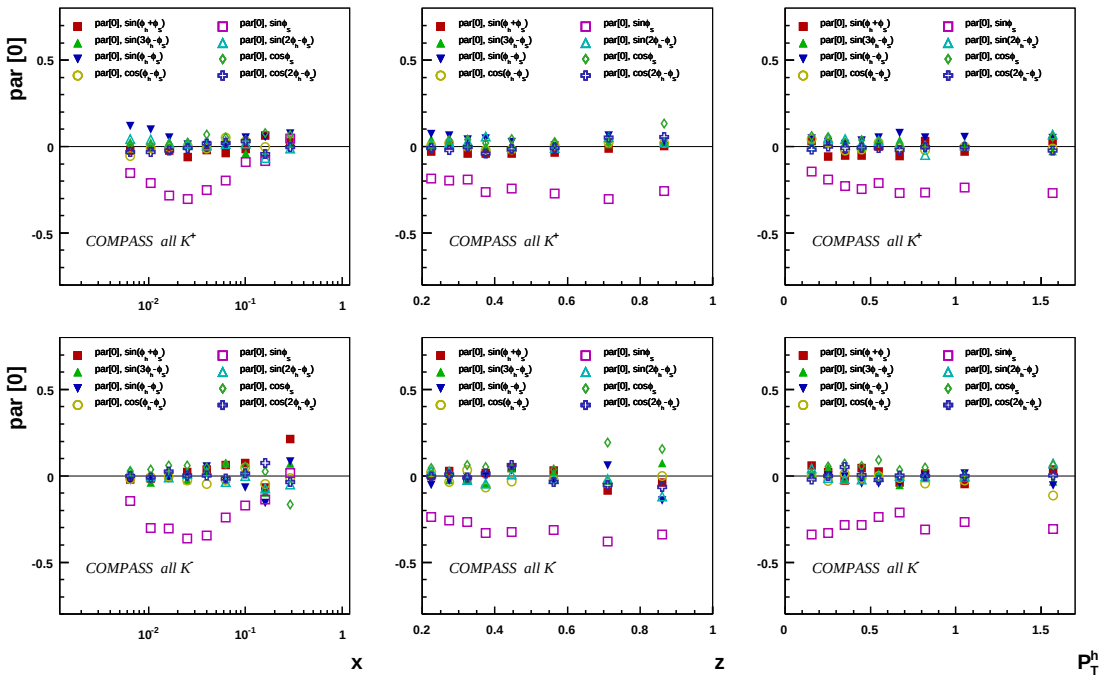

Figure 9.18: Correlation between par(0) and rest of the parameters vs. x, z and P_{hT}.

List of Tables

List of Figures

Bibliography

[1] European Muon Collaboration, J. Ashman *et al.*, Phys. Lett. B **206** (1988) 364; Nucl. Phys. B **328** (1989) 1.

[2] A. Kotzinian, Nucl. Phys. B **441** (1995) 234 [arXiv:hep-ph/9412283].

[3] P.J. Mulders and R.D. Tangerman, Nucl. Phys. **B461**, 197 (1996), [Erratum-ibid. B **484**, 538 (1997)].

[4] J. C. Collins and D. E. Soper, Nucl. Phys. B **193**, 381 (1981) [Erratum-ibid. B **213**, 545 (1983)]; Nucl. Phys. B **194**, 445 (1982).

[5] V. Y. Alexakhin *et al.* [**COMPASS** Collaboration], Phys. Rev. Lett. **94**, 202002 (2005) [arXiv:hep-ex/0503002].

[6] E. S. Ageev *et al.* [**COMPASS** Collaboration], Nucl. Phys. B **765**, 31 (2007) [arXiv:hep-ex/0610068];

[7] A. Airapetian *et al.* [**HERMES** Collaboration], Phys. Rev. Lett. **94**, 012002 (2005) [arXiv:hep-ex/0408013].

[8] H. Avakian *et al.* [**CLAS** Collaboration], Phys. Rev. D **69**, 112004 (2004).

[9] H. Avakian, P. Bosted, V. Burkert and L. Elouadrhiri [**CLAS** Collaboration], AIP Conf. Proc. **792**, 945 (2005) [arXiv:nucl-ex/0509032].

[10] X. D. Ji, J. P. Ma and F. Yuan, Phys. Rev. D **71**, 034005 (2005) [arXiv:hep-ph/0404183], Phys. Lett. B **597**, 299 (2004) [arXiv:hep-ph/0405085].

[11] J. C. Collins and A. Metz, Phys. Rev. Lett. **93**, 252001 (2004) [arXiv:hep-ph/0408249].

[12] M. Anselmino, M. Boglione, U. D'Alesio, A. Kotzinian, F. Murgia and A. Prokudin, Phys. Rev. D **71**, 074006 (2005) [arXiv:hep-ph/0501196]; Phys. Rev. D **72**, 094007 (2005) [Erratum-ibid. D **72**, 099903 (2005)] [arXiv:hep-ph/0507181].

[13] M. Anselmino *et al.*, arXiv:hep-ph/0511017.

[14] M. Anselmino *et al.*, arXiv:hep-ph/0511017.

[15] R. Seidl *et al.* [Belle Collaboration], Phys. Rev. Lett. **96**, 232002 (2006) [arXiv:hep-ex/0507063].

[16] M. Anselmino, M. Boglione, U. D'Alesio, A. Kotzinian, F. Murgia, A. Prokudin and C. Turk, arXiv:hep-ph/0701006.

[17] A. Bacchetta, M. Boglione, A. Henneman and P. J. Mulders, Phys. Rev. Lett. **85**, 712 (2000) [arXiv:hep-ph/9912490].

[18] A. Kotzinian, B. Parsamyan and A. Prokudin, Phys. Rev. D **73**, 114017 (2006) [arXiv:hep-ph/0603194].

[19] A. Bacchetta, M. Diehl, K. Goeke, A. Metz, P. Mulders and M. Schlegel, arXiv:hep-ph/0611265.

[20] J. C. Collins and D. E. Soper, *Back-to-back jets in qcd*, *Nucl. Phys.* **B193** (1981) 381.

[21] X. Ji, J.-P. Ma, and F. Yuan, *QCD factorization for semi-inclusive deep-inelastic scattering at low transverse momentum*, *Phys. Rev.* **D71** (2005) 034005, arXiv:hep-ph/0404183.

[22] X. Ji, J.-P. Ma, and F. Yuan, *QCD factorization for spin-dependent cross sections in DIS and Drell-Yan processes at low transverse momentum*, *Phys. Lett.* **B597** (2004) 299–308, arXiv:hep-ph/0405085.

[23] J. C. Collins and A. Metz, *Universality of soft and collinear factors in hard- scattering factorization*, *Phys. Rev. Lett.* **93** (2004) 252001, arXiv:hep-ph/0408249.

[24] M. Anselmino *et al.*, *The role of Cahn and Sivers effects in deep inelastic scattering*, *Phys. Rev.* **D71** (2005) 074006, arXiv:hep-ph/0501196.

[25] M. Anselmino, A. Efremov, A. Kotzinian, and B. Parsamyan, *Transverse momentum dependence of the quark helicity distributions and the Cahn effect in double-spin asymmetry A(LL) in semi inclusive DIS*, arXiv:hep-ph/0608048.

[26] R. Jakob, P. J. Mulders and J. Rodrigues, Nucl. Phys. A **626**, 937 (1997) arXiv:hep-ph/9704335.

[27] **HERMES** Collaboration, A. Airapetian *et al.*, *Subleading-twist effects in single-spin asymmetries in semi-inclusive deep-inelastic scattering on a longitudinally polarized hydrogen target*, *Phys. Lett.* **B622** (2005) 14–22, arXiv:hep-ph/0505042.

[28] **EMC** Collaboration, M. Arneodo *et al.*, *Measurement of hadron azimuthal distributions in deep inelastic muon proton scattering*, *Z. Phys.* **C34** (1987) 277.

[29] **E665** Collaboration, M. R. Adams *et al.*, *Perturbative QCD effects observed in 490-GeV deep inelastic muon scattering*, *Phys. Rev.* **D48** (1993) 5057–5066.

[30] D. Boer and P. J. Mulders, *Time-reversal odd distribution functions in leptoproduction*, *Phys. Rev.* **D57** (1998) 5780–5786, arXiv:hep-ph/9711485.

[31] J. C. Collins, *Fragmentation of transversely polarized quarks probed in transverse momentum distributions*, *Nucl. Phys.* **B396** (1993) 161–182, arXiv:hep-ph/9208213.

[32] **ZEUS** Collaboration, J. Breitweg *et al.*, *Measurement of azimuthal asymmetries in deep inelastic scattering*, *Phys. Lett.* **B481** (2000) 199–212, arXiv:hep-ph/0003017.

[33] **ZEUS** Collaboration, S. Chekanov *et al.*, *Measurement of azimuthal asymmetries in neutral current deep inelastic scattering at HERA*, arXiv:hep-ph/0608053.

[34] **CLAS** Collaboration, H. Avakian *et al.*, *Measurement of beam-spin asymmetries for deep inelastic π^+ electroproduction*, *Phys. Rev.* **D69** (2004) 112004, arXiv:hep-ph/0301005.

[35] V. A. Korotkov, W. D. Nowak, and K. A. Oganessyan, *Transversity distribution and polarized fragmentation function from semi-inclusive pion electroproduction*, *Eur. Phys. J.* **C18** (2001) 639–644, arXiv:hep-ph/0002268.

[36] K. A. Oganessyan, P. J. Mulders, E. De Sanctis, and L. S. Asilyan, *Kinematical contributions to the transverse asymmetry in semi-inclusive DIS*, *Nucl. Phys.* **A711** (2002) 89–92, arXiv:hep-ph/0208207.

[37] A. Bacchetta, P. J. Mulders, and F. Pijlman, *New observables in longitudinal single-spin asymmetries in semi-inclusive DIS*, *Phys. Lett.* **B595** (2004) 309–317, arXiv:hep-ph/0405154.

[38] M. Diehl and S. Sapeta, *On the analysis of lepton scattering on longitudinally or transversely polarized protons*, *Eur. Phys. J.* **C41** (2005) 515–533, arXiv:hep-ph/0503023.

[39] **HERMES** Collaboration, A. Airapetian *et al.*, *Observation of a single-spin azimuthal asymmetry in semi-inclusive pion electro-production*, *Phys. Rev. Lett.* **84** (2000) 4047–4051, arXiv:hep-ph/9910062.

[40] **HERMES** Collaboration, A. Airapetian *et al.*, *Single-spin azimuthal asymmetries in electroproduction of neutral pions in semi-inclusive deep-inelastic scattering*, *Phys. Rev.* **D64** (2001) 097101, arXiv:hep-ph/0104005.

[41] **HERMES** Collaboration, A. Airapetian *et al.*, *Measurement of single-spin azimuthal asymmetries in semi- inclusive electroproduction of pions and kaons on a longitudinally polarised deuterium target*, *Phys. Lett.* **B562** (2003) 182–192, arXiv:hep-ph/0212039.

[42] A. V. Efremov, K. Goeke, and P. Schweitzer, *Azimuthal asymmetry in electroproduction of neutral pions in semi-inclusive DIS*, *Phys. Lett.* **B522** (2001) 37–48, arXiv:hep-ph/0108213. Erratum-ibid. **B544** (2002) 389.

[43] A. V. Efremov, K. Goeke, and P. Schweitzer, *Predictions for azimuthal asymmetries in pion and kaon production in SIDIS off a longitudinally polarized deuterium target at HERMES*, *Eur. Phys. J.* **C24** (2002) 407–412, arXiv:hep-ph/0112166.

[44] A. V. Efremov, K. Goeke, and P. Schweitzer, *Azimuthal asymmetries at CLAS: Extraction of $e^a(x)$ and prediction of A_{UL}*, *Phys. Rev.* **D67** (2003) 114014, arXiv:hep-ph/0208124.

[45] B.-Q. Ma, I. Schmidt, and J. J. Yang, *Reanalysis of azimuthal spin asymmetries of meson electroproduction*, *Phys. Rev.* **D66** (2002) 094001, arXiv:hep-ph/0209114.

[46] A. V. Efremov, K. Goeke, and P. Schweitzer, *Collins effect and single spin azimuthal asymmetries in the HERMES and COMPASS experiments*, *Eur. Phys. J.* **C32** (2003) 337–346, arXiv:hep-ph/0309209.

[47] A. V. Efremov, K. Goeke, and P. Schweitzer, *Sivers vs. Collins effect in azimuthal single spin asymmetries in pion production in SIDIS*, *Phys. Lett.* **B568** (2003) 63–72, arXiv:hep-ph/0303062.

[48] P. Schweitzer and A. Bacchetta, *Azimuthal single spin asymmetries in SIDIS in the light of chiral symmetry breaking*, *Nucl. Phys.* **A732** (2004) 106–124, arXiv:hep-ph/0310318.

[49] D. W. Sivers, *Single spin production asymmetries from the hard scattering of point-like constituents*, *Phys. Rev.* **D41** (1990) 83.

[50] J. P. Ralston and D. E. Soper, *Production of dimuons from high-energy polarized proton- proton collisions*, *Nucl. Phys.* **B152** (1979) 109.

[51] V. Barone, A. Drago, and P. G. Ratcliffe, *Transverse polarisation of quarks in hadrons*, *Phys. Rept.* **359** (2002) 1–168, arXiv:hep-ph/0104283.

[52] **HERMES** Collaboration, A. Airapetian *et al.*, *Single-spin asymmetries in semi-inclusive deep-inelastic scattering on a transversely polarized hydrogen target*, *Phys. Rev. Lett.* **94** (2005) 012002, arXiv:hep-ph/0408013.

[53] M. Anselmino *et al.*, *Extracting the Sivers function from polarized SIDIS data and making predictions*, *Phys. Rev.* **D72** (2005) 094007, arXiv:hep-ph/0507181.

[54] W. Vogelsang and F. Yuan, *Single-transverse spin asymmetries: From DIS to hadronic collisions*, *Phys. Rev.* **D72** (2005) 054028, arXiv:hep-ph/0507266.

[55] J. C. Collins *et al.*, *Sivers effect in semi-inclusive deeply inelastic scattering*, *Phys. Rev.* **D73** (2006) 014021, arXiv:hep-ph/0509076.

[56] A. V. Efremov, K. Goeke, and P. Schweitzer, *Collins effect in semi-inclusive deeply inelastic scattering and in e^+e^- annihilation*, *Phys. Rev.* **D73** (2006) 094025, arXiv:hep-ph/0603054.

[57] **BELLE** Collaboration, K. Abe *et al.*, *Measurement of azimuthal asymmetries in inclusive production of hadron pairs in e^+e^- annihilation at BELLE*, *Phys. Rev. Lett.* **96** (2006) 232002, arXiv:hep-ph/0507063.

[58] A. Kotzinian [on behalf of the **COMPASS** Collaboration], arXiv:0705.2402 [hep-ex].

[59] B. Parsamyan [**COMPASS** Collaboration], arXiv:0709.3440 [hep-ex].

[60] A. M. Kotzinian and P. J. Mulders, Phys. Rev. D **54** (1996) 1229 [arXiv:hep-ph/9511420].

[61] R.D. Tangerman and P.J. Mulders, hep-ph/9408305.

[62] S. Wandzura and F. Wilczek, Phys. Lett. **B72**, 195 (1977).

[63] M. Gluck, E. Reya and A. Vogt, Eur. Phys. J. C **5**, 461 (1998) [arXiv:hep-ph/9806404].

[64] M. Gluck, E. Reya, M. Stratmann and W. Vogelsang, Phys. Rev. D **63**, 094005 (2001) [arXiv:hep-ph/0011215].

[65] S. Kretzer, Phys. Rev. D **62**, 054001 (2000) [arXiv:hep-ph/0003177].

[66] E155 Collaboration, Phys. Lett. **B553**, 18 (2003);
JLab Hall A Collaboration, Phys. Rev **C70**, 065207 (2004).

[67] R. Kundu and A. Metz, Phys. Rev. D **65** (2002) 014009 [arXiv:hep-ph/0107073].

[68] M. Schlegel and A. Metz, arXiv:hep-ph/0406289.

[69] K. Goeke, A. Metz, P. V. Pobylitsa and M. V. Polyakov, Phys. Lett. B **567** (2003) 27 [arXiv:hep-ph/0302028].

[70] A. Kotzinian, Eur. Phys. J. C **44**, 211 (2005) [arXiv:hep-ph/0410093]; arXiv:hep-ph/0504081.

[71] R. N. Cahn, *Azimuthal dependence in leptoproduction: a simple parton model calculation*, *Phys. Lett.* **B78** (1978) 269.

[72] R. N. Cahn, *Critique of parton model calculations of azimuthal dependence in leptoproduction*, *Phys. Rev.* **D40** (1989) 3107–3110.

[73] M. Anselmino, M. Boglione, U. D'Alesio, E. Leader, S. Melis and F. Murgia, Phys. Rev. D **73** (2006) 014020.

[74] M. Anselmino, M. Boglione, A. Prokudin and C. Türk, e-Print Archive: hep-ph/0606286.

[75] The **COMPASS** Collaboration, E. S. Ageev *et al.*, Phys. Lett. B **633** (2006) 25.
the **COMPASS** Collaboration, V. Y. Alexakhin *et al.*, "The Deuteron Spin Dependent Structure Function g_1^d and its First Moment", in preparation.

[76] E. S. Ageev *et al.* [**COMPASS** Collaboration], Eur. Phys. J. C **41** (2005) 469 [arXiv:hep-ex/0503033].

[77] E. S. Ageev *et al.* [**COMPASS** Collaboration], Phys. Lett. B **612** (2005) 154 [arXiv:hep-ex/0501073].

[78] E. S. Ageev *et al.* [**COMPASS** Collaboration], Phys. Lett. B **647** (2007) 330 [arXiv:hep-ex/0701014].

[79] M. Alekseev *et al.* [**COMPASS** Collaboration], arXiv:0707.4077 [hep-ex].

[80] P. Abbon *et al.* [**COMPASS** Collaboration], Nucl. Instrum. Meth. A **577** (2007) 455 [arXiv:hep-ex/0703049].

[81] J. Ball, Nucl. Instr. and Meth. A 526 (2004) 7.

[82] S. Goertz, et al., Nucl. Instr. and Meth. A 356 (1995) 20.

[83] S. Bültmann, et al., Nucl. Instr. and Meth. A 425 (1999) 23.

[84] J. Bisplinghoff, et al., Nucl. Instr. and Meth. A 490 (2002) 101.

[85] S. Horikawa, et al., Nucl. Instr. and Meth. A 516 (2004) 34.

[86] D. Thers, et al., Nucl. Instr. and Meth. A 469 (2001) 133.

[87] F. Kunne, Nucl. Phys. A 721 (2003) 1087c.

[88] C. Bernet, et al., Nucl. Instr. and Meth. A 536 (2005) 61.

[89] F. Sauli, Nucl. Instr. and Meth. A 386 (1997) 531.

[90] V. N. Bychkov, et al., Nucl. Instr. and Meth. A 556 (2006) 66.

[91] E. Albrecht, et al., Nucl. Instr. and Meth. A 553 (2005) 215, and references therein.

[92] C. Bernet, et al., Nucl. Instr. and Meth. A 550 (2005) 217.

[93] J.-P. Baud, et al., CASTOR status and evolution, in: Computing in high energy and nuclear physics (CHEP03), La Jolla, CA, USA, 2003, arXiv:cs.oh/0303241.

[94] ALICE DAQ and ECS user's guide, ALICE-INT-2005-015 v.1.

[95] R. Brun, et al., Nucl. Instr. and Meth. A 389 (1997) 81, http://root.cern.ch.

[96] R. Frühwirth, Nucl. Instr. and Meth. A 262 (1987) 444.

[97] E. J. Wolin, et al., Nucl. Instr. and Meth. A 329 (1993) 493.

[98] GEANT - detector description and simulation tool, CERN Program Library Long Writeup W5013, http://wwwasdoc.web.cern.ch/wwwasdoc /geant_html3/geantall.html.

[99] G. Ingelman, et al., Comput. Phys. Commun. 101 (1997) 108.

[100] G. Ingelman, et al., Comput. Phys. Commun. 101 (1997) 135.

[101] T. Sjöstrand, et al., Comput. Phys. Commun. 135 (2001) 238.

[102] A. Kotzinian, ”Spin and TMD azimuthal asymmetries in SIDIS”, presentation given in Trento-workshop on ’Transverse momentum, spin, and position distributions of partons in hadrons’ 11-15 June 2007, ECT* Trento, Italy.

[103] A. Kotzinian, ”Remarks on acceptance effects in asymmetry extraction”, COMPASS Internal Note, 27/02/2007.

Acknowledgments

Finishing the thesis I would like to express my sincere gratitude to all the people with whose help and support I successfully completed my doctorate.

Firstly I wish to thank my scientific supervisor, Prof. Aram Kotzinian. Without his teaching and help this work simply would not be possible. In the past three years of my PhD we worked together in dynamical and friendly atmosphere and I really enjoined my scientific and human communication with him.

Next, I want to thank my tutor, Prof. Ferruccio Balestra, for his helpfulness and support and continual interest in the progress of my work. My very special thanks goes to Prof. Guido Piragino. He always was a constant source of good advices and warm encouragement.

My gratefulness is addressed to Profs. Daniele Panzieri and Angelo Maggiora. I appreciate very much all the support lent by them during my doctorate. Many thanks also to my colleagues from our Torino group for their helpfulness and friendly environment. Speaking about the friends from Torino I would like to name specially: Gil Pontecorvo, Vladimir Frolov, Ivan Gnesi and his wife Elisa, Maxim Alekseev and his wife Natasha, Alexey Prokudin and Sergey Senyukov. Thank to them I never felt myself alone in Torino.

Next, I wish to thank all the members of COMPASS-Transversity group for all our fruitful discussions and many helpful and inspiring comments and suggestions and specially for friendliness. In particular I would like to thank Andrea Bressan and Federica Sozzi who helped me a lot when I was just starting the analysis and Girisan Venugopal for the good professional and personal cooperation.

Finally I would like to thank all my friends and relatives from different countries and cities and above all, a heartfelt thanks to my family whose moral support was always encouraging me during these long three years far away from them.

Շնորհակալություն!!!

Grazie Mille!!!

Спасибо!!!

Thank you!!!